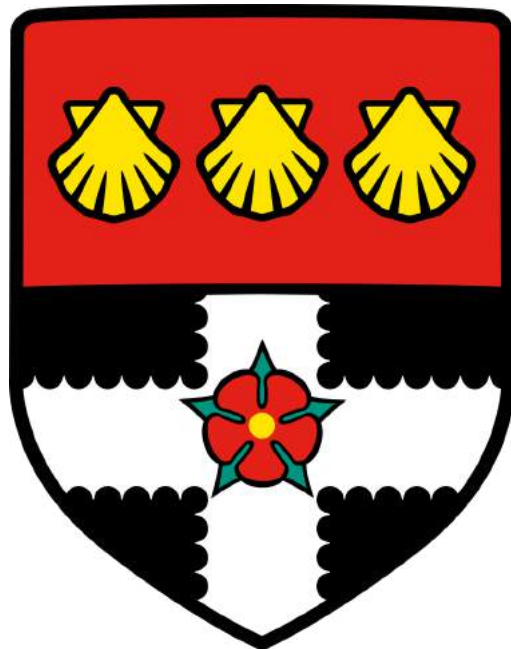


UNIVERSITY OF READING

Department of Meteorology



# Extinction of Microwave Radiation in Snow

WILLIAM MICHAEL MASLANKA

*A thesis submitted for the degree of Doctor of Philosophy*

April 2017

---

---

# Declaration

I confirm that this is my own work and the use of all material from other sources has been properly and fully acknowledged.

William Maslanka

---

---

# Abstract

Global observations of snow cover and snow water equivalent are vitally important for climatological and hydrological studies, at both global and local scales. Passive microwave remote sensing techniques have been used over the past 30 years to produce global estimations of snow water equivalent through empirical calculations. However, the uncertainties surrounding the influence of snow microstructure has led to large errors in snow water equivalent estimation.

This study examined the extinction properties of the natural snowpack and produced a new extinction coefficient, for use with the semi-empirical multiple layer Helsinki University of Technology (n-HUT) snow emission model. Snow slabs from the natural snowpack were extracted and observed radiometrically upon bases of different reflectivities, as part of the Arctic Snow Microstructure Experiment (ASMEEx). Snow parameters were characterised via traditional snowpit observation techniques, as well as with modern high resolution methods, such as with the SnowMicroPen and X-Ray Computer Tomography analysis.

The ASMEEx snow slab data were used with a flux coefficient model to calculate six flux absorption and scattering coefficients. The six flux scattering coefficients in the vertical polarization were used with a theoretical absorption coefficient model to create a new empirical extinction coefficient, eliminating the need to use subjective observations.

The new extinction coefficient was compared to the original n-HUT extinction coefficient model, through the observation and simulation of snowpack brightness temperatures, obtained as part of the Sodankylä Radiometer Experiment (SoRaX). The derived extinction coefficient produced more accurate simulated brightness temperatures at vertical polarizations, especially at 36.5 GHz. The ability to include snow specific surface area data within the n-HUT model has greatly increased its capability; by increasing the breadth of microstructure parameters to include objective observations of specific surface area, and by increasing the accuracy of simulations of the natural snowpack.

---

---

# Acknowledgements

This work owes a lot of thanks for the assistance, guidance, and help from a great number of people, all of which were vital in the completion of this work. The research presented in this thesis was jointly funded by the University of Reading and the Finnish Meteorology Institute.

A huge thank you goes to my supervisors, Melody Sandells, Robert Gurney, and Juha Lemmetyinen for all the help and guidance that they have given me throughout the course of this PhD. Their insight and instinct helped improve my research phenomenally and have been crucial throughout my PhD.

I would like to thank all those at the Finnish Meteorological Institute Arctic Research Centre in Sodankylä, Finland, as the Arctic Snow Microstructure Experiment field campaign would not have been possible without both the infrastructure and the technical support that was offered. Particular thanks goes to Riitta, Timo, Leena, Tiina, Heena, and Anna for making my stay unforgettable!

The fieldwork would not have been possible without the provision of the SMP and  $\mu$ CT analysis by the WSL Institute for Snow and Avalanche Research SLF, in Davos, Switzerland. The research would not have been possible without the training and data analysis performed by Maritn Schneebeli, Martin Proksch, Henning Löwe, and Margret Matzl,

The provision of the Sodankylä Radiometer Experiment dataset by Juha, Nick Rutter, Richard Kelly, Tom Watts, and Anna Kontu was vital for the validation of the extinction coefficient. The extent and quality of the data collected made the validation possible.

I also want to thank the PhDs within the department, who have all contributed in some form or another. Special thanks go to current office-mates Matt, Hannah and Liz, who have been there for me through the highs and lows, but especially been with me for tea and snack breaks! None of this would have been possible without the encouragement and support of my family, who were there to celebrate with me when things were going well, and to comfort me when things were going less well. Finally, a massive thank you to Luisa, for her unwavering love and support throughout my PhD, and her constant reminder that the cold shouldn't bother me anyway.

# Contents

<b>Declaration</b>	i
<b>Abstract</b>	ii
<b>Acknowledgements</b>	iii
<b>Table of contents</b>	vi
<b>List of Acronyms</b>	vii
<b>1 Introduction</b>	1
1.1 The Importance of Snow . . . . .	1
1.2 Global Observations of Snow Depth . . . . .	4
1.3 Aims of the Thesis . . . . .	6
1.4 Thesis Outline . . . . .	8
<b>2 Microwave Remote Sensing of Snow</b>	10
2.1 Theory of Microwave Radiation . . . . .	10
2.2 Radiative Transfer Theory . . . . .	12
2.3 Snow Properties . . . . .	16
2.3.1 Physical Properties of Snow . . . . .	17
2.3.2 Microwave Properties of Snow . . . . .	20
2.4 Earth Observation of Snow . . . . .	22
2.4.1 Visible, Infrared, and Microwave Remote Sensing of Snow Mass . .	22
2.4.2 Passive Microwave Observation Contributions . . . . .	28
2.5 Snow Emission Models . . . . .	30
2.5.1 Empirical Models . . . . .	30
2.5.2 Theoretical Models . . . . .	31
2.5.3 Semi-empirical Models . . . . .	32
2.5.4 Helsinki University of Technology Snow Emission Model . . . . .	33
2.6 Chapter Summary . . . . .	43
<b>3 Arctic Snow Microstructure Experiment (ASMEx)</b>	45
3.1 Chapter Introduction . . . . .	45

3.2	FMI Arctic Research Centre . . . . .	46
3.3	SodRad Radiometers . . . . .	47
3.3.1	Technical Details . . . . .	47
3.3.2	SodRad Calibration . . . . .	49
3.4	ASMEEx Principle Set-up . . . . .	50
3.5	Experimental Proceedings . . . . .	54
3.5.1	Slab Extraction and Transportation . . . . .	54
3.5.2	Radiometric Measurements . . . . .	57
3.5.3	Snow Characteristic Measurements . . . . .	60
3.6	Problems faced during ASMEEx . . . . .	71
3.6.1	Climatic Problems . . . . .	73
3.6.2	Equipment Problems . . . . .	74
3.7	Chapter Summary . . . . .	76
<b>4</b>	<b>ASMEEx Results and Single Layer HUT Model Simulations</b>	<b>78</b>
4.1	Chapter Introduction . . . . .	78
4.2	Fieldwork Data . . . . .	79
4.2.1	Slab Metadata . . . . .	79
4.2.2	Radiometric Results . . . . .	80
4.2.3	Snow Characteristics Results . . . . .	89
4.2.4	Stratigraphic Results . . . . .	100
4.2.5	Fieldwork Data Discussion . . . . .	111
4.3	Comparison of HUT Simulations: ASMEEx . . . . .	113
4.4	Chapter Summary . . . . .	121
<b>5</b>	<b>Extinction Coefficient Calculation</b>	<b>124</b>
5.1	Chapter Introduction . . . . .	124
5.2	Flux Coefficient Model . . . . .	125
5.2.1	Snow Slab Reflectivities . . . . .	125
5.2.2	Calculating the absorption and scattering flux coefficients . . . . .	127
5.3	Applying ASMEEx data to Wiesmann et al. (1998) Methodology . . . . .	132
5.3.1	Flux Coefficient Model: Absorption Coefficient . . . . .	136
5.3.2	Flux Coefficient Model: Scattering Coefficient . . . . .	139
5.4	Extinction Coefficient Model . . . . .	148
5.4.1	Frequency Dependency . . . . .	149
5.4.2	Optical Diameter Dependency . . . . .	152
5.4.3	$\alpha$ Calculation . . . . .	153
5.4.4	Development of the Scattering Coefficient Model . . . . .	154
5.4.5	Extinction Coefficient Model . . . . .	156

---

5.4.6 Implementation of the Derived Extinction Coefficient Model into the n-HUT Model . . . . .	156
5.5 Chapter Summary . . . . .	158
<b>6 Sodankylä Radiometer Experiment (SoRaX)</b>	<b>161</b>
6.1 Chapter Introduction . . . . .	161
6.2 Sodankylä Radiometer Experiment . . . . .	162
6.2.1 SoRaX: Location . . . . .	164
6.2.2 SoRaX: Radiometers . . . . .	164
6.2.3 SoRaX: Experimental Proceedings . . . . .	165
6.3 SoRaX Observations . . . . .	171
6.3.1 Radiometric Observations . . . . .	173
6.3.2 Snow Characteristic Observations . . . . .	176
6.4 HUT Simulations of the SoRaX Trenches . . . . .	188
6.4.1 Aligning SoRaX Radiometric Data with Snowpit Observations .	188
6.4.2 n-HUT Model Parameter Selection . . . . .	191
6.4.3 Original and Adapted n-HUT Model Simulation . . . . .	193
6.5 Discussion . . . . .	198
6.6 Chapter Summary . . . . .	199
<b>7 Conclusion</b>	<b>201</b>
7.1 Summary of Main Findings . . . . .	201
7.2 Research Significance . . . . .	203
7.3 Research Limitations . . . . .	204
7.4 Future Work . . . . .	205
<b>A ASMEx Radiometric Data</b>	<b>206</b>
<b>B ASMEx Physical Slab Data</b>	<b>213</b>
<b>C Two- to- Six-Flux Coefficient conversion</b>	<b>216</b>
<b>D SoRaX Radiometric Data</b>	<b>219</b>
<b>References</b>	<b>221</b>

# List of Acronyms

---

Acronym	Definition
ACF	Auto-Correlation Function
AMSR-E	Advanced Microwave Scanning Radiometer Earth Observing System
ARC	Arctic Research Centre
ASME <sub>x</sub>	Arctic Snow Microstructure Experiment
DEP	Diethyl-Phthalate
DMRT Model	Dense Medium Radiative Theory model
DMSP	Defence Meteorological Satellite Program
DUFISSS	Dual Frequency Integrating Sphere for Snow SSA measurement
ELBARA-II	ETH L-Band Radiometer
FCM	Flux Coefficient Model
FMI	Finnish Meteorological Institute
GDP	Gross Domestic Product
HPBW	Half Power Beam Width
HUT	Helsinki University of Technology
IOA	Intensive Observation Area
n-HUT Model	Multiple Layer HUT snow emission Model
NIR	Near Infrared
RMSE	Root Mean Squared Error
SEM	Standard Error of the Mean
SMMR	Scanning Multichannel Microwave Radiometer
SMP	SnowMicroPentrometer
SoRaX	Sodankylä Radiometer Experiment
SodRad	Sodankylä Radiometers
SSA	Specific Surface Area
SSM/I	Special Sensor Microwave/Imager
SWE	Snow Water Equivalent
T <sub>B</sub>	Brightness Temperature
WSL SLF	WSL Institute for Snow and Avalanche Research SLF
$\mu$ CT	X-ray Computer Tomography

---

## Chapter 1:

# Introduction

### 1.1 The Importance of Snow

Snow cover covers a considerable area of the Northern Hemisphere; at its peak in January covering approximately 47 million square kilometres ([Frei and Robinson \[1999\]](#)). Snow cover is also the largest varying land surface type, ranging from approximately 47 to approximately 3 million squared kilometres at its lowest ([Robinson et al. \[2012\]](#), Figure 1.1). This magnitude of snow cover is very important for numerous climatological and hydrological processes, such as global estimates of albedo, monsoon duration forecasting, surface temperature forecasting, and irrigation management.

Knowledge of the total snow extent is very important within the field of climate research, especially for its role in controlling the Earth's seasonal albedo (the ratio of the solar energy (at ultraviolet, visible, and near-infrared wavelengths) reflected by the surface to that incident upon it, [Barry \[1996\]](#)), as well as for its use as a proxy for studies into climate change. The change in seasonal snow extent in the Northern Hemisphere, as shown in Figure 1.1, is responsible for large variations of land surface albedo experienced across the year ([Armstrong and Brodzik \[2001\]](#)), due to the snows much higher values of albedo, compared to that of the surfaces that it covers (such as soil, vegetation, etc., Figure 1.2). In a warming global climate with reduced snow extent ([Collins et al. \[2013\]](#)), the average surface albedo would ultimately decrease, due to the reducing extent of snow cover. This would occur as a result of the exposed underlying surface (that would normally be covered with seasonal snow) having a lower albedo than that of the snow cover. This would lead to an increase in the amount of absorbed radiation at the surface, which would then be re-emitted back into the atmosphere, thus warming the atmosphere further. This cycle would continue, setting up a positive feedback loop ([Qu and Hall \[2014\]](#)).

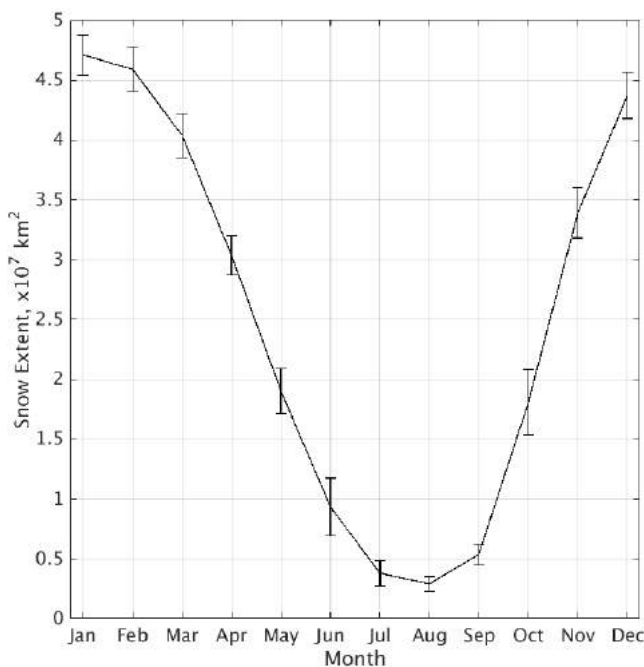


**Figure 1.1:** Monthly mean Northern Hemispheric maximum snow extent, in the period 1975 – 2016, as determined by [Robinson et al. \[2012\]](#). Error bars show the monthly standard deviation values over the same period.

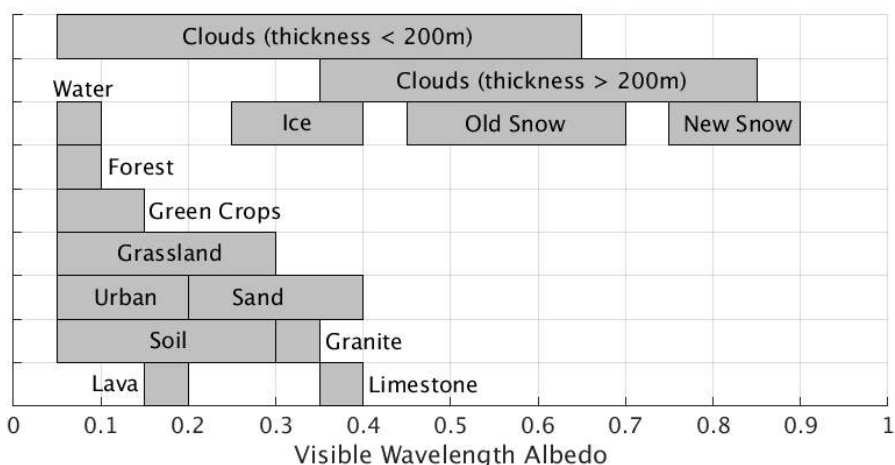


**Figure 1.2:** Typical values of albedo for different land surface types, integrated over visible wavelengths, for normally incident radiation. Taken from [Rees \[2012\]](#).

Snow mass and snow extent observations are also vitally important for hydrological processes and forecasting, as well as on economics and industry on the local scale. As over a billion people rely on snow and glacier melt for their freshwater drinking supply (Figure 1.3, [Barnett et al. \[2005\]](#)), it is critically important that the amount of potential water that is locked as snow is known. In a similar theme to this, the amount of water that is locked as snow is also important for governing the effectiveness of irrigation schemes ([Benson and Williams \[2013\]](#)), hydropower generation ([Kulkarni et al. \[2002\]](#)), and flood forecasts ([Stanzel et al. \[2008\]](#)). [Carroll et al. \[2003\]](#) calculated that snowmelt contributes \$1.7 trillion annually to the United States Gross Domestic Product (GDP, 2002 Dollars) of \$10.7 trillion (16%). Of this \$1.7 trillion, \$1.6 trillion is contributed through industrial use of snowmelt. Snow itself is a source of economic revenue, as winter sports and tourism relies on snow to be successful. [Burakowski and Magnusson \[2012\]](#) found that more than 23 million people participated in winter sports in the US annually, adding a further \$12.2 billion to the US economy annually (2012 Dollars).

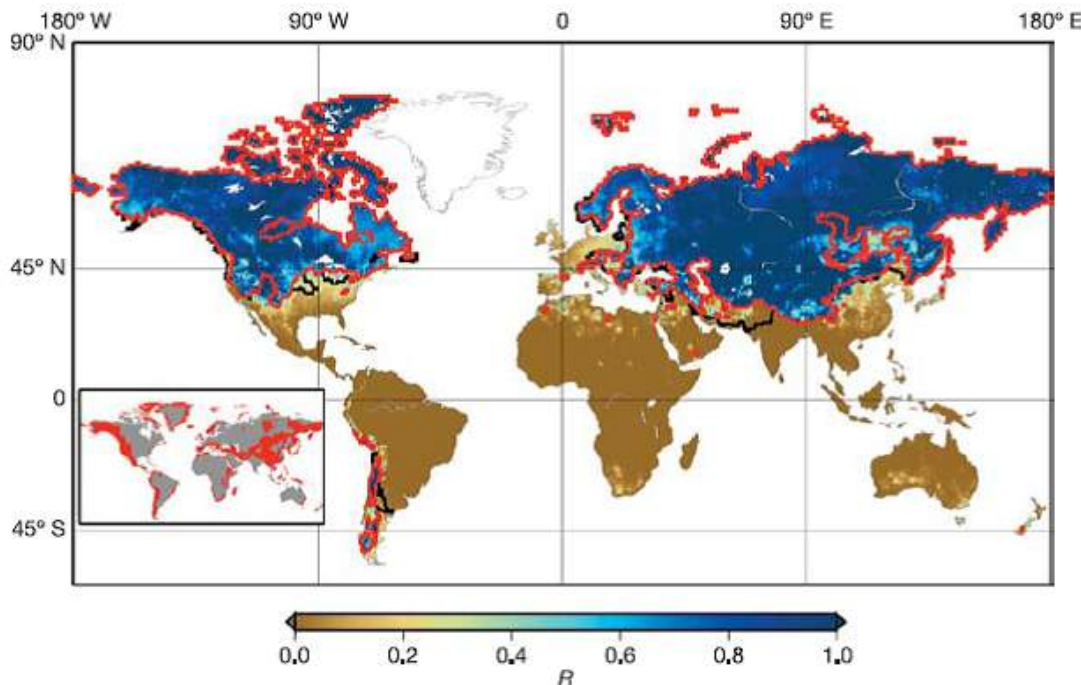


**Figure 1.3:** Accumulated annual snowfall divided by annual runoff over the global land regions. The value of this dimensionless ratio lies between 0 and 1 and is given by the colour scale, R. The red lines indicate the regions where streamflow is snowmelt-dominated, and where there is not adequate reservoir storage capacity to buffer shifts in the seasonal hydrograph. The black lines indicate additional areas where water availability is predominantly influenced by snowmelt generated upstream (but runoff generated within these areas is not snowmelt-dominated). Taken from [Barnett et al. \[2005\]](#)

It is therefore clear that global observations and estimations of total snow cover and snow mass are vitally important quantities to be known. Through reliable estimates and

observations of snow mass and snow extent, the relationships between snow extent and meteorological phenomena and global atmospheric systems ([Blanford \[1884\]](#), [Leathers and Robinson \[1993\]](#), and [Orsolini and Kvamstø \[2009\]](#)) can be better understood. In a changing global climate, better estimations of snow mass and snow extent will allow for hydrological forecasts to highlight regions at risk of drought and flooding ([Takala et al. \[2009\]](#)). Reduced snow extent and snow mass will alter hydrological systems, in terms of both the quality and quantity of the water resource ([Jimenez Cisneros et al. \[2014\]](#)).

## 1.2 Global Observations of Snow Depth

Obtaining a global observation of snow depth is not straight forward. Whilst global networks of manual and automatic observations of snow depth do exist ([Brown et al. \[2003\]](#)), these observations tend to be located close to urban populations centres, and are less likely to be located at higher latitudes ([Brown et al. \[2003\]](#) and [Rees et al. \[2014\]](#)). This would lead to an under sampling of observations, as the manual and automatic point-observations of snow depth are not sufficient.

Satellite remote sensing methods, through the utilization of passive microwave retrievals, are the most practical means of global snow mass estimation ([Rees \[2006\]](#) and [Amlien \[2008\]](#)), due to the ability to penetrate through clouds, the lack of need of illumination from an external source, and the ability of microwave wavelengths to penetrate the snow cover; three of the major drawbacks for using visible and near-infrared wavelengths ([Foster et al. \[1987\]](#), [Chang et al. \[2005\]](#), and [Rees \[2006\]](#)). This is most effective for observations at polar latitudes, as observations during the polar night are still possible. Passive microwave observations of snow mass have been made since the 1980's ([Rango et al. \[1979\]](#)), with the frequency range of 19 – 37 GHz being of most interest, due to the relationships that occur between snow depth and emitted radiation ([Amlien \[2008\]](#)). At the upper end of this frequency range, the snowpack is able to effectively scatter the naturally emitted radiation from the underlying surface. At the lower end of the frequency range, snow is not able to scatter effectively. A comparison between observations at these frequencies provide an estimation of snow depth; as increasing snow depths impose an increasing difference in observed microwave radiation ([Chang et al. \[1987\]](#), [Mätzler \[1994\]](#), [Tait \[1998\]](#), [Amlien \[2008\]](#), [Kelly et al. \[2003\]](#), and [Takala et al. \[2011\]](#)).

Initially, a large amount of research was dedicated towards empirical models of snow depth estimation, using a radiation difference observed across different frequencies, to linearly estimate snow depth. One of the empirical algorithms, by [Chang \[1986\]](#), used to

derive snow depth is:

$$SD = 1.59 \times (T_{B18H} - T_{B37H}) \quad (1.1)$$

where  $T_{B18H}$  and  $T_{B37H}$  are the brightness temperatures at 18 and 37 GHz respectively, at horizontal polarizations. This empirical formula was developed for use with radiometric data collected using the Nimbus-7 Scanning Multiple-channel Radiometer (SMMR, described further in Section 2.4.1). However, as shown by [Davenport et al. \[2012\]](#), large variations in estimated snow depth and snow water equivalent values can be attributed to variations of density and snow grain diameter within the snowpack being observed (Figure 1.4).

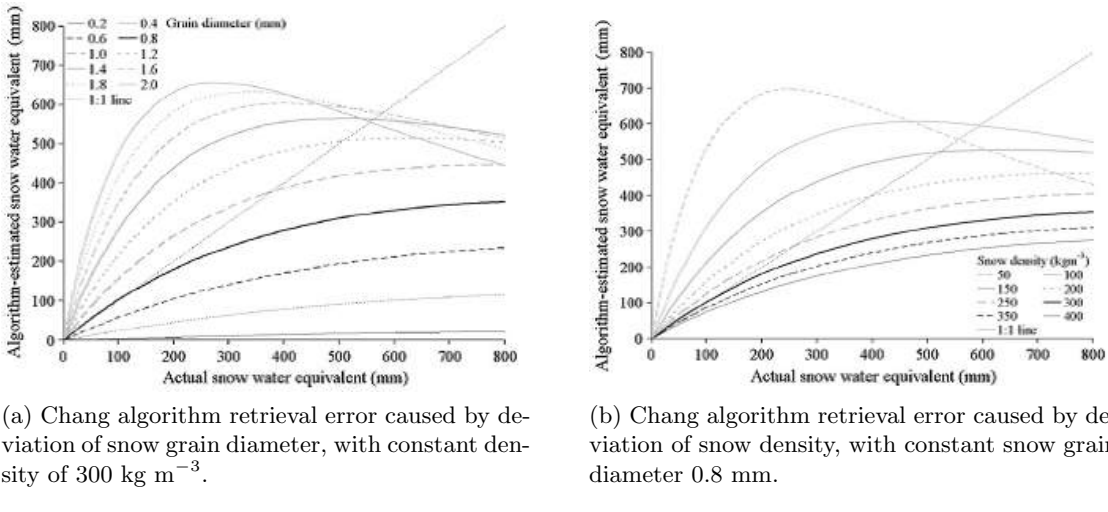


**Figure 1.4:** Chang algorithm retrieval error caused by deviation of snow grain diameter and density from ideal values. Taken from [Davenport et al. \[2012\]](#).

More recently, new snow mass estimates are made using the inversion of semi-empirical snow emission models, which depend on the understanding of the physics of the snow and electromagnetic processes at the snow microstructure level. One such semi-empirical model is the Helsinki University of Technology (HUT) snow emission model ([Pulliainen et al. \[1999\]](#) and [Lemmettyinen et al. \[2010\]](#), Section 2.5.4), which describes the modelled snowpack in terms of a stack of homogeneous layers with individual physical temperature, thickness, density, and traditional grain size (as described by [Fierz et al. \[2009\]](#)). At the heart of the HUT snow emission model is the assumption that forward scattering is dominant ([Pulliainen et al. \[1999\]](#)), and that the level of extinction (the sum of the absorptive and scattering processes) within the snowpack is calculated by the empirical expression ([Hallikainen et al. \[1987\]](#)):

$$k_e = 0.0018F^{2.8}d_o^{2.0} \quad (1.2)$$

where the extinction coefficient,  $k_e$ , is dependent on both the observed values of frequency,  $F$ , in GHz, and the traditional grain size,  $d_o$ , in mm.

### 1.3 Aims of the Thesis

The original empirical model for the extinction of microwave radiation used by the HUT snow emission model was developed to use the traditional grain size as an input parameter. The traditional grain size is defined by [Fierz et al. \[2009\]](#) to be the measurement of the grains greatest extension, often expressed in millimetres. However, manual sampling of a vertical profile of traditional grain size is subject to a mixture of resolution and time constraints, as well as issues surrounding the observers level of expertise. Modern observation techniques, such as through observations using the IceCube instrument ([Zuanon \[2013\]](#)), the SnowMicroPentrometer (SMP, [Schneebeli and Johnson \[1998\]](#)), and X-ray microcomputer tomography ( $\mu$ CT, [Seidler et al. \[2001\]](#)) are able to quantify the snowpack in terms of its physical properties. All four techniques mentioned have their own advantages and disadvantages, however, the objective nature of observations using the SMP,  $\mu$ CT, and IceCube instruments are an improvement over the more subjective traditional grain size observations. The SMP and  $\mu$ CT techniques are also able to produce profiles at a much higher resolution than those produced with traditional snowpit techniques.

This thesis will use modern observation techniques, such as those mentioned above, to produce a new modern extinction coefficient model, for use within the HUT snow emission model. This will be done by completing three individual thesis aims (listed below); each progressing one step further towards creation and evaluation of a new extinction coefficient model.

In order to begin to derive a new empirical extinction coefficient for microwave radiation in snow, observations of the radiometric properties and snow characteristics must be made. These observations form the first thesis aim:

#### Aim 1

Creation of the Arctic Snow Microstructure Experiment (ASMEEx) dataset; comprising of radiometric and snow characteristic properties of snow slabs, extracted from the

natural snowpack.

## Goals

1. Complete the Arctic Snow Microstructure Experiment (ASMEEx); in which radiometric and snow characteristic properties of snow slabs upon two bases of differing reflectivities.
2. Analyse the ASMEEx dataset; comparing the different instrumentation techniques used, as well as their affect upon the simulated brightness temperatures, using the single layer HUT snow emission model.

Upon the completion of the ASMEEx field campaign, the resulting ASMEEx dataset will be used to derive a new empirical extinction coefficient, leading to the second thesis aim:

## Aim 2

Derivation of a new extinction coefficient model, using the ASMEEx dataset.

## Goals

1. Calculate individual absorption and scattering coefficients of the ASMEEx snow slab dataset, using a flux coefficient model.
2. Derive an empirical extinction coefficient model, using ASMEEx absorption and scattering coefficients.
3. Implement the newly derived extinction coefficient model in the HUT snow emission model.

After the derivation of a new empirical extinction coefficient model, and implementing it into the HUT snow emission model, it is to be evaluated against brightness temperature observations from an independent natural snowpack. Thus, the third and final thesis aim is:

## Aim 3

Validate the new extinction coefficient with independent natural snowpack data.

## Goals

1. Analyse data collected as part of the Sodankylä Radiometer Experiment (SoRaX), to assess the usability of the SoRaX snowpit observations.
2. Simulate the brightness temperature, using both the original and the newly derived extinction coefficients.
3. Compare and contrast the brightness temperature errors from both extinction coefficient models.

## 1.4 Thesis Outline

The structure of the thesis is as follows:

**Chapter 2** reviews microwave radiation theory, as well as discussing its use with respect to snow remote sensing. Different forms of snow retrieval techniques are discussed, focusing on the semi-empirical HUT snow emission model.

**Chapter 3** introduces the first of the two field campaigns used in this thesis; the Arctic Snow Microstructure Experiment (ASMEEx). The experimental proceedings (including snow slab extraction, radiometric, and physical snow parameter observation) are detailed, as well as the problems experienced during the ASMEEx campaign.

**Chapter 4** describes the data collected during the ASMEEx campaign, in terms of the radiometric, snow characteristic, and stratigraphic data. Observations of snow characteristics (such as density and specific surface area) using different observation techniques (snowpit, SMP, and  $\mu$ CT analysis) are compared and contrasted. Snow slabs were then simulated using the single layer HUT snow emission model, with simulations being compared to the corresponding observed brightness temperatures.

**Chapter 5** uses the data shown in Chapter 4, in conjunction with a flux coefficient model, to produce six-flux scattering coefficients. These coefficients were then used to form an empirical extinction coefficient model, using both frequency and optical grain size (derived from values of Specific Surface Area) as inputs.

**Chapter 6** introduces the second of the two field campaigns used in this thesis; the Sodankylä Radiometer Experiment (SoRaX). The SoRaX experiment proceedings and collected data are shown, with snowpit observations being used with the multiple layer HUT snow emission model. Simulations of brightness temperature using

both the original extinction coefficient of the HUT snow emission model and the newly derived extinction coefficient model of Chapter 5 are compared to observed values of brightness temperatures.

**Chapter 7** draws together the main conclusions, presents a summary of the work completed, and suggests avenues of future work to be completed.

## Chapter 2:

# Microwave Remote Sensing of Snow

## 2.1 Theory of Microwave Radiation

All natural matter both absorbs and emits electromagnetic radiation, as a result of having a physical temperature ( $T_{phys}$ ) greater than 0 K. This naturally emitted electromagnetic radiation originates as thermal radiation within the matter. If an object, under thermodynamic equilibrium, were to perfectly absorb and radiate radiation at all frequencies, it would be classified as a blackbody object ([Ulaby et al. \[1986a\]](#)).

According to Planck's radiation law, the electromagnetic radiation of a blackbody in thermal equilibrium with its surroundings can be calculated for a given frequency,  $f$ , if the value of  $T_{phys}$  is known. The blackbody spectral brightness,  $B_f$ , will radiate uniformly in all directions, according to:

$$B_f = \frac{2hf^3}{c^2} \left( \frac{1}{e^{\frac{hf}{k_b T_{phys}}} - 1} \right) \quad (2.1)$$

where  $h$  is Planck's constant ( $6.626 \times 10^{-34}$  Js $^{-1}$ ),  $c$  is the speed of electromagnetic radiation through a vacuum ( $2.998 \times 10^8$  ms $^{-1}$ ),  $k_b$  is the Boltzmann constant ( $1.381 \times 10^{-23}$  JK $^{-1}$ ), and all other variables are previously defined. In the microwave region (between 1 and 300 GHz),  $hf \ll k_b T_{phys}$ . This leads to the Rayleigh-Jeans approximation ([Mätzler \[2006\]](#)), which states that:

$$B_f \approx \frac{2k_b T_{phys} f^2}{c^2} = \frac{2k_b T_{phys}}{\lambda^2} \quad (2.2)$$

where  $\lambda$  is the radiation wavelength (measured in metres). Figure 2.1 shows the values of  $B_f$  for an object at 300 K, between 0.1 GHz and 1 PHz, using both Planck's law and the Rayleigh-Jeans approximation. It can be seen that the spectral brightness calculated by the two separate regimes are comparable up to approximately 1 THz, where the Rayleigh-Jean approximation diverges from Planck's law. Figure 2.1 shows that the Rayleigh-Jeans approximation is indeed valid across the microwave region.

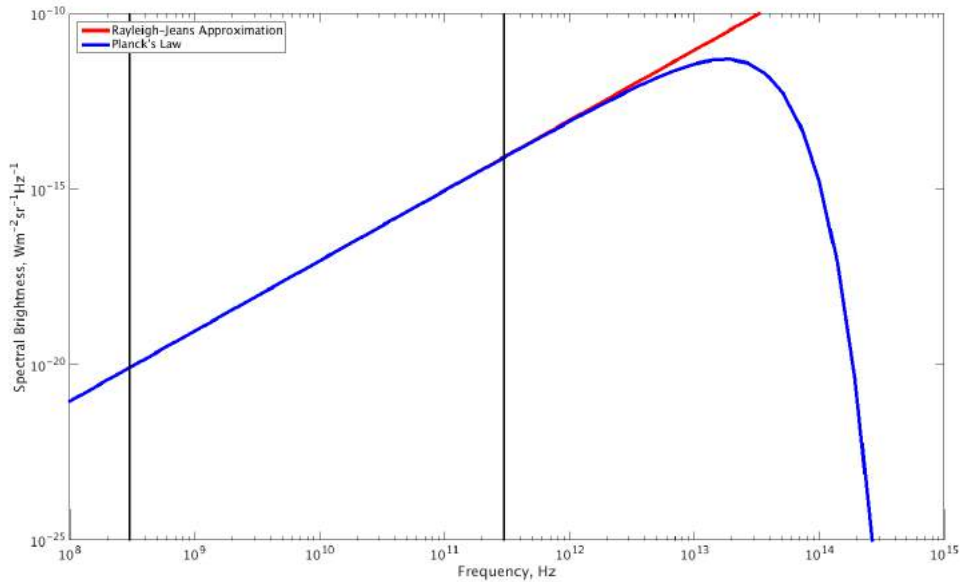


**Figure 2.1:** Comparison of Planck's law (blue) and the Rayleigh-Jeans approximation (red) over frequencies above 100 MHz, for a blackbody with a physical temperature of 300K. The microwave frequency range (300 MHz to 300 GHz) is shown by the black vertical lines.

The emissivity,  $\varepsilon$ , of a grey body object (an object that does not perfectly absorb or radiate radiation at all frequencies) can now be defined as the ratio between the spectral brightness of the grey body object ( $B_{gb}$ ) to the spectral brightness of a blackbody at the same physical temperature ( $B_{bb}$ ), such that:

$$\varepsilon = \frac{B_{gb}}{B_{bb}} \quad (2.3)$$

The Rayleigh-Jeans approximation can be applied to Eqn. 2.3, such that the emissivity is calculated via the ratio of two temperatures; the physical temperature  $T_{phys}$ , and parameter known as the brightness temperature,  $T_B$ , such that Eqn. 2.4 holds. The brightness temperature is the value of temperature that a blackbody would have to be in order to duplicate the radiometric emissions of a grey body at that frequency (Rees [2006]).

$$\varepsilon = \frac{T_B}{T_{phys}} \quad (2.4)$$

## 2.2 Radiative Transfer Theory

Using the knowledge of microwave brightness temperature theory, initially discussed in Section 2.1, it is possible to calculate the microwave brightness temperature of a medium, with known absorption and scattering properties, as well as from its physical temperature, through the utilization of Radiative Transfer Theory.

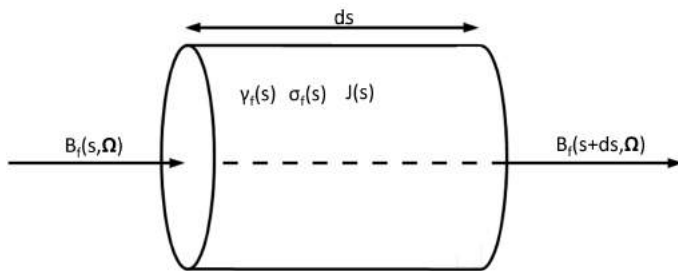


**Figure 2.2:** Schematic of the radiative transfer situation. The medium is characterised by an emission source function  $J(s)$ , spectral absorption coefficient  $\gamma_f(s)$ , and spectral scattering coefficient  $\sigma_f(s)$ .

Consider a beam of monochromatic radiation passing through a medium in direction  $\Omega$  from point  $s$  to point  $s+ds$ , as shown in Figure 2.2. The medium is capable of both absorbing and scattering the beam as it passes through. As the medium has a physical temperature greater than 0 K, it also is capable of emitting microwave radiation. It is therefore clear that the energy of the monochromatic radiation beam would be altered as it passes through the medium (Ulaby et al. [1986a] and Sharkov [2003]). This alteration in energy would be the sum of the processes providing a positive alteration (emission and scattering into the beam) and negative alteration (absorption and scattering out of the beam).

$B_f(s, \Omega)$  and  $B_f(s + ds, \Omega)$  in Figure 2.2 show values of spectral brightness along the beam, prior to and after the medium respectively. The medium is characterised as having a length of  $ds$ , and has spectral absorption and scattering properties of  $\gamma_f(s)$  and  $\sigma_f(s)$  respectively, and an emission source term of  $J(s)$ . The change in spectral brightness prior to and after leaving the medium is defined as  $\frac{dB_f}{ds}$ .

As previously stated, the change in spectral brightness from the medium can be accredited to processes that provide positive ( $M_+$ ) and negative ( $M_-$ ) alterations to the energy of the monochromatic radiation beam (Ulaby et al. [1986a] and Sharkov [2003]).

By assuming that the medium only affects the radiation beam through its absorption, scattering, and emission properties, the change in spectral brightness can be described through these terms, as shown in Eqn. 2.6, with the individual terms being described below:

$$\frac{dB_f}{ds} = M_+ - M_- \quad (2.5)$$

$$\Rightarrow \frac{dB_f}{ds} = (M_{EM} + M_{SI}) - (M_{AB} + M_{SO}) \quad (2.6)$$

As the beam of monochromatic radiation,  $B_f(s, \Omega)$ , propagates through the medium (as shown in the Schematic from Figure 2.2), part of the radiation is absorbed by the medium. The spectral absorption coefficient is designated by  $\gamma_f(s)$ , and is equal to the fraction of incident radiation absorbed by the medium over unit of the radiation propagation path length. The value  $M_{AB}$  represents the radiation energy loss caused by radiation absorption, and can be written as:

$$M_{AB} = \gamma_f(s)B_f(s, \Omega) \quad (2.7)$$

If the medium in question is in local thermodynamic equilibrium, then the emission of radiation can be described, through Kirchhoffs Law ([Ulaby et al. \[1986a\]](#)), by the amount of absorption. If the emission source term is designated by  $J_s$ , then  $M_{EM}$ , the emission alteration term in Eqn. 2.6 can be written as:

$$M_{EM} = J_s = \gamma_f(s)B_f(T_{phys}) \quad (2.8)$$

where  $B_f(T_{phys})$  is the spectral brightness of the medium if it were a blackbody at  $T_{phys}$  (from Eqn. 2.2).

If the medium includes small particulate matter (in the instance of snow, the small particulate matter would be ice crystals), then the propagating beam of monochromatic radiation will be scattered in all directions ([Ulaby et al. \[1986a\]](#) and [Sharkov \[2003\]](#)). However, the medium may be considered electromagnetically homogeneous if the linear size of the particulate matter is considerably smaller than that of the radiation wavelength. However, when the particulate matter is comparable to the radiation wavelength, two types of scattering can take place. Classical scattering occurs if the scattered radiation has the same frequency as that of the original radiation beam, while non-classical scattering occurs

when the frequency of the scattered radiation is different to that of the original beam. Only classical scattering is considered in this radiative transfer section.

As the beam of monochromatic radiation,  $B_f(s, \Omega)$ , propagates through the medium, some of the radiation is scattered away from the beam, reducing its intensity and negatively altering the energy of the beam. By defining the spectral scattering coefficient, the fraction of incident radiation scattered away in all directions over the unit length of the propagation path, as  $\sigma_f(s)$ , the amount of radiation scattered away from the beam,  $M_{SO}$ , can be expressed as:

$$M_{SO} = \sigma_f(s)B_f(s, \Omega) \quad (2.9)$$

Scattering into the beam has not yet been considered. While Eqn. 2.9 considers radiation that has effectively been removed via scattering, it does not include radiation that has been included via scattering. This can be calculated using the normalised phase function:

$$\frac{1}{4\pi} \int \int \Psi(\Omega, \Omega') d\Omega' \quad (2.10)$$

which allows for calculation of the fraction of radiation that enters solid angle  $\Omega$  from direction  $\Omega'$ . Using the normalised phase function, the amount of radiation that is scattered into the beam,  $M_{SI}$  can be calculated as:

$$M_{SI} = \frac{\sigma_f(s)}{4\pi} \iint_{\Omega=4\pi} \Psi(\Omega, \Omega') B_f(s, \Omega') d\Omega' \quad (2.11)$$

Thus, by substituting Eqns. 2.7, 2.8, 2.9, and 2.11 into Eqn. 2.6, the radiative transfer equation can be written in the form:

$$\begin{aligned} \frac{dB_f}{ds} = & \left( \gamma_f(s)B_f(T_{phys}) + \frac{\sigma_f(s)}{4\pi} \iint_{\Omega=4\pi} \Psi(\Omega, \Omega') B_f(s, \Omega) d\Omega' \right) \\ & - \left( \gamma_f(s)B_f(s, \Omega) + \sigma_f(s)B_f(s, \Omega) \right) \end{aligned} \quad (2.12)$$

This radiative transfer equation can also be written in terms of brightness temperature, rather than spectral difference, using Eqn. 2.2. This gives:

$$\frac{dT_B(s, \Omega)}{ds} = k_a(s)T_{phys} + \frac{k_s(s)}{4\pi} \iint_{\Omega=4\pi} \Psi(\Omega, \Omega') T_B(s, \Omega') d\Omega' - k_e(s)T_B(s, \Omega) \quad (2.13)$$

where  $k_a(s)$  is the absorption coefficient at point  $s$ ,  $k_s(s)$  is the scattering coefficient at point  $s$ , and  $k_e(s)$  is the extinction coefficient ( $k_a(s) + k_s(s)$ ) at point  $s$ . Eqn. 2.13 shows the radiative transfer equation in its general form. While Eqn. 2.13 deals with the beam's path length and solid angles, it is possible to convert the radiative transfer equation into a form which uses azimuth and elevation angles, and the Cartesian co-ordinate system. This is possible, as  $\Omega$  can be converted into values of elevation ( $\theta$ ) and azimuth ( $\Phi$ ), and  $d\Omega$  can be equated to (using Figure 2.3):

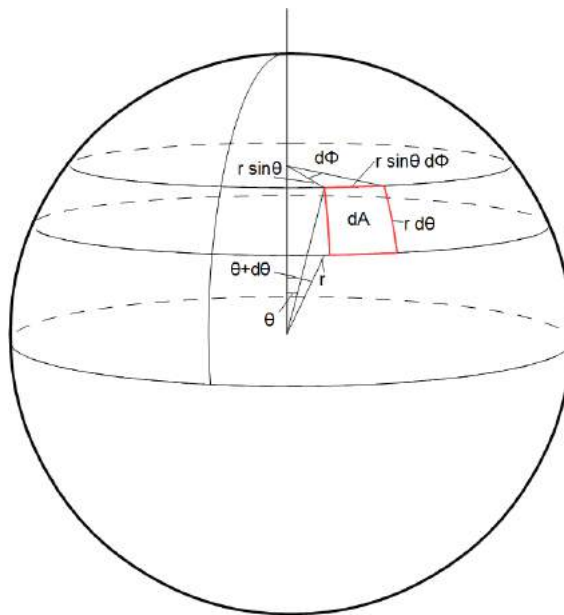


**Figure 2.3:** Schematic of the solid body calculation for a sphere of radius  $r$ , with elevation angle  $\theta$  and azimuth angle  $\Phi$ .

$$\begin{aligned} dA &= (rd\theta)(r \sin \theta d\Phi) = r^2 \sin \theta d\theta d\Phi \\ d\Omega &= \frac{dA}{r^2} \\ \Rightarrow d\Omega &= \frac{r^2 \sin \theta d\theta d\Phi}{r^2} = \sin \theta d\theta d\Phi \end{aligned} \quad (2.14)$$

The path length  $ds$  can be converted into the Cartesian co-ordinate system, using Figure 2.4 and Eqn. 2.15:

$$ds = \frac{dz}{\cos \theta} \quad (2.15)$$

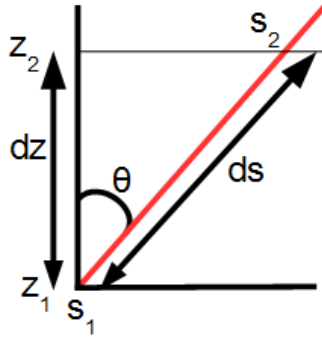


**Figure 2.4:** Converting direction  $s$  into Cartesian Coordinates.

By integrating Eqn. 2.13 over  $\Phi$ , and using Eqns. 2.14 and 2.15, a beam of radiation travelling in direction  $\theta_d$  through a medium, will be affected via:

$$\frac{dT_B}{dz} = -k_e(z) \sec(\theta) T_B(z, \theta_d) + k_s(z) \frac{\sec(\theta)}{2} \int_0^{\pi} \Psi(\theta') T_B(z, \theta') \sin \theta' d\theta' + k_a(z) \sec(\theta) T_{phys}$$
(2.16)

## 2.3 Snow Properties

If radiative transfer theory is to be used for the monitoring of snow (treating snow as the medium in which the radiation propagates through) via passive microwave radiation observations, a mixture of physical and microwave properties of snow must be discussed and detailed. The physical characteristics of the snow can have a large effect upon the scattering experienced by the microwave radiation (Bernier [1987], Chang et al. [1987], Foster et al. [1987], and Hallikainen et al. [1987]) and the fundamental makeup of the snow can influence the dominant processes occurring as the microwave radiation is transmitted through the snow. Snow is a highly porous, fine grained media, consisting of a mixture of ice and air (when the snow is dry), or ice, air and liquid water (when the snow is wet, Amlien [2008]). From its deposition as frozen precipitation, the snowpack is in a constant state of changing and evolution, known as metamorphism (Colbeck [1983]). When manually observing the snowpack properties, it is important to measure numerous physical characteristics (Section 2.3.1), which affect its microwave properties.

Therefore, it is important to state the internal characteristics at the time of observation, when discussing the snowpack. Each snowpack will have physical characteristics associated with it, which will in turn affect its microwave characteristics.

### 2.3.1 Physical Properties of Snow

Snow on the ground is often summarised by its total height, or by its Snow Water Equivalent, often abbreviated to SWE. SWE is a measure of the depth of water that would result if the snow mass were to melt completely ([Fierz et al. \[2009\]](#)), and can be calculated via:

$$SWE = H \frac{\rho_{snow}}{\rho_w} \quad (2.17)$$

where SWE is the Snow Water Equivalent, H is the total height of the snowpack (in metres),  $\rho_{snow}$  is the snow density ( $\text{kgm}^{-3}$ ), and  $\rho_w$  is the density of water ( $1000 \text{ kgm}^{-3}$ ). The SWE is the most commonly used output from microwave remote sensing of snow, as the constant monitoring of the snow hydrology is important for management of water in hydrological models and flood forecasting.

The physical temperature,  $T_{phys}$ , of the snowpack is an important variable to measure, as the physical temperature of the snowpack directly governs the amount of microwave radiation emitted by the snowpack, as shown by Eqn. [2.2](#) and the third term of Eqn. [2.16](#). As the observed microwave signature from a snowpack is produced from numerous contributions (Figure [2.9](#) in Section [2.4.2](#)), knowledge of the physical temperature of the snowpack allows for the calculation of the emission by the snowpack.

The snow density,  $\rho_{snow}$ , is measured by weighing snow of a known volume, giving units of mass of snow per unit volume (commonly  $\text{kgm}^{-3}$ ). The total snow density is a bulk average of the entire snowpack, taking a vertically averaged value for the density of the snowpack. In porous material, such as snow, density generally refers to its bulk density, which takes into account both solid material (ice) and pore space (air, [Fierz et al. \[2009\]](#)). The snow density is highly dependent on numerous different factors, such as compaction, snow metamorphism, and phase change ([Doesken and Judson \[1997\]](#), [Judson and Doesken \[2000\]](#), and [Rees \[2006\]](#)). The density tends to increase with age and compaction underneath the weight of fresh snow being deposited at the surface. "Fresh snow" has a density within the range of  $10\text{-}200 \text{ kgm}^{-3}$ , with older snow having increasingly larger densities associated with them ([Doesken and Judson \[1997\]](#)). As the snowpack ages, its density increases, due to compaction by wind and gravity, as well as through thermal metamorphism ([Rees \[2006\]](#)). This is shown in Table [2.1](#), which shows the typical densities of different snow and ice types, as well as the density for pure water. The ambient temperature at the time of deposition can also influence the density of the

freshly deposited snow. If the ambient temperature is greatly below freezing, then the snow would typically have a low density, while close to freezing temperatures favours high density ([Doesken and Judson \[1997\]](#)).

**Table 2.1:** Typical densities, taken from [Cuffey and Patterson \[2010\]](#).

Snow Type	Density range (kgm <sup>-3</sup> )
New snow	50 - 70
Damp new snow	100 - 200
Settled snow	200 - 300
Depth hoar	100 - 300
Wind-packed snow	350 - 450
Firn	400 - 830
Very wet snow and firn	700 - 800
Ice	917
Water	1000

An understanding of the size of the snow crystals within the snowpack is very important with regards to understanding microwave processes within the snowpack (see [Section 2.3.2](#)). There are numerous different parameters which come under the umbrella term of snow microstructure, with each parameter corresponding to a unique concept and definition.

One simple parameter is the maximum extent of the prevailing grains, or the grain size,  $D_{max}$  ([Mätzler \[2002\]](#)). It is defined as the "average size of its prevailing grains or characteristic grains, the size of the grain or particle being its greatest extension (diameter) measured in millimetres" from within a homogeneous snowpack ([Armstrong et al. \[1993\]](#), [Mätzler \[2002\]](#), [Fierz et al. \[2009\]](#)).  $D_{max}$  has long been used as a classical parameter for determining size and shape ([Montpetit et al. \[2011\]](#)), due to the ease at which the measurement can be made in the field (see [Section 3.5.3](#)). It has been shown, however, that using the maximum extent of characteristic grains, such as  $D_{max}$  can lead to an overestimation within scattering models ([Toure et al. \[2008\]](#), [Mätzler \[2002\]](#)). Another parameter that can be measured to help quantify the characteristics of the snowpack is the Specific Surface Area, or SSA, which is defined by [Legagneux et al. \[2002\]](#), [Gallet et al. \[2009\]](#), and [Montpetit et al. \[2012\]](#) as the surface area per unit mass (m<sup>2</sup> kg<sup>-1</sup>), such that:

$$SSA = \frac{S}{M} = \frac{S}{\rho_{ice}V} \quad (2.18)$$

where S is the surface area of a given snow mass, M is the mass of the snow, V is the volume of the snow particles, and  $\rho_{ice}$  is the density of ice (917 kgm<sup>-3</sup> at 273 K). The

SSA parameter is interesting, as it is a better parameter for representing non-spherical snow crystals; such as needles ([Toure et al. \[2008\]](#)). Measurements of SSA can be used to calculate other parameters, such as the optical grain size ([Mätzler \[2002\]](#)), such that:

$$D_o = \frac{6}{\rho_{ice}SSA} \quad (2.19)$$

The optical grain size is the diameter that an ice sphere would have with the same optical properties as the snowpack that is being modelled ([Mätzler \[2002\]](#)), as many snow emission models model snow as a collection of ice spheres.

The correlation length,  $p_c$ , and corresponding autocorrelation function (ACF, [Weise \[1996\]](#)), are also associated with the physical size and structure of the media; in this instance, the ice crystals within the snow. In the ACF of snow, the correlation length corresponds to the scale of permittivity fluctuations in the snow ([Arslan \[2006\]](#)).

Generally, a spatial autocorrelation function  $ACF(\vec{x})$  in three dimensions is defined by [Mätzler \[1997\]](#) as:

$$ACF(\vec{x}) = \frac{1}{V} \iiint f(\vec{x}')f(\vec{x}' - \vec{x})d^3x' \quad (2.20)$$

where  $V$  is the total volume of the medium under investigation,  $f(\vec{x}')$  is the spatially fluctuating function of  $\vec{x}$ , and  $\vec{x}'$  is the displacement. The ACF is a measure of similarity between the permittivity at point  $\vec{x}$  and point  $\vec{x}'$  away from  $\vec{x}$  ([Arslan \[2006\]](#)).

In the instance of snow,  $f(\vec{x}')$  represents the snow's permittivity for a given location in space.  $f(\vec{x}')$  is normalised, so that  $ACF(0) = 1$ . Many ACFs are assumed to be exponential, and can be written as ([Weise \[1996\]](#)):

$$ACF(x) = \exp\left(\frac{-x}{p_{ex}}\right) \quad (2.21)$$

where  $p_{ex}$  is the exponential correlation length. The exponential correlation length can also be calculated empirically ([Mätzler \[2002\]](#)) from values of snow density and SSA, or from values of the correlation length, such that:

$$p_{ex} \approx 0.75p_c = \frac{3(1 - \frac{\rho_{snow}}{\rho_{ice}})}{SSA} \quad (2.22)$$

The physical properties of the snow vary spatially both horizontally and vertically. The vertical distribution of physical properties within the snowpack results in the snow-

snowpack being characterised by many horizontal layers, where a layer is defined by its boundaries of differing physical snow properties ([Weise \[1996\]](#)). By analysing the internal horizontal layers, or stratigraphy, of the snowpack, it is possible to read into the snowpack's history. The snowpack is formed from fresh snow being precipitated during different time periods and during different atmospheric conditions (wind, humidity, air temperature, etc). Different metamorphosis processes will also change the stratigraphy of the snowpack. One such process is the formation of melt-freeze crusts, which form during diurnal above-below freezing temperatures. This commonly occurs during the spring months, as the air temperature will be above freezing during the day, thus slightly melting the surface of the snow. Then, as the temperature drops to below freezing during the night, the melted surface would freeze, forming a hard crust layer ([Montpetit et al. \[2013\]](#)). If fresh snow was to be deposited on the melt-freeze crust, then the crust would remain buried, and would be a very obvious layer within the snowpack.

### 2.3.2 Microwave Properties of Snow

As previously stated in Section [2.3.1](#), snow is a mixture of ice and air, and in the case of wet snow, liquid water. The propagation of microwaves through a snowpack is governed by the different dielectric properties of these three components of snow ([Bernier \[1987\]](#)).

#### 2.3.2.1 Dry Snow

In dry snow (where liquid water is not present), the propagation of microwaves is highly dependent on the dielectric properties of the ice and air that makes up the snow. The real part of the dielectric constant of air is 1;  $\epsilon'_{air} = 1$ , while the real part of the dielectric constant of ice has a typical value of  $\epsilon'_{ice} \approx 3.17$  ([Mätzler \[1987\]](#) and [Rees \[2006\]](#)). The imaginary part of the dielectric constant of ice is very small;  $\epsilon''_{ice} \approx 0$  in the microwave region ([Rees \[2006\]](#) and [Amlien \[2008\]](#)). Partnered with a very small imaginary part of the dielectric constant of air ( $\epsilon''_{air} \approx 0$ ), this suggests that the absorption of microwaves in dry snow is very low ([Mätzler \[1987\]](#), [Rees \[2006\]](#) and [Amlien \[2008\]](#)).

Scattering will occur in any inhomogeneous dielectric medium ([Amlien \[2008\]](#)); caused by differences in dielectric properties between the ice crystals and the air ([Bernier \[1987\]](#)). As dry snow absorbs very little of the microwave radiation, the microwaves are able to penetrate the snowpack, and scatter into the snowpack.

The amount of scattering is highly dependent on two factors; the wavelength (there-

fore frequency) of the microwave frequencies, and the ice crystals grain size (Mätzler [1987], Foster et al. [1987], Chang et al. [1987], Hallikainen et al. [1987], Roy et al. [2004], and Amlien [2008]). If the wavelengths are smaller than the snow grains, then the snow grains will act like quasi-diffuse Rayleigh scattering centres (Amlien [2008]). This means that the microwave radiation is strongly scattered by the snow crystals, even by a thin snowpack. The penetration depth of microwaves in snow is defined as the point where the power is reduced by the factor e, and is given by (Amlien [2008]):

$$\delta_p = \frac{\lambda \sqrt{\epsilon'_{snow}}}{2\pi \epsilon''_{snow}} \quad (2.23)$$

where  $\lambda$  is the wavelength of the microwaves, in metres. This expression states that higher frequencies (and therefore smaller wavelengths) cannot penetrate as deeply as lower frequencies. This is true, as lower frequency microwaves can penetrate much deeper into the dry snowpack, with the lowest frequency microwaves (1–2 GHz) being able to travel almost unaffected through the dry snowpack (Mätzler [1987], Bernier [1987], Amlien [2008], Chang et al. [1987], Hallikainen et al. [1986], and Sorman and Beser [2013]). It is this relationship between snow and microwave frequencies that allows estimations of snow depth via microwave radiation remote sensing (see Section 2.4.1).

Typically, comparing the observed brightness temperatures of snowpacks at frequencies above 25 GHz (where scattering is dominant; therefore only the contributions from the snowpack are visible) with those from below 25 GHz (where scattering is less dominant, allowing the ground emission contribution to also be visible) makes up the basis of passive microwave remote sensing (Foster et al. [2005], Chang et al. [1987], Mätzler [1994], Amlien [2008], Kelly et al. [2003], Mätzler [1987], and Takala et al. [2011]).

### 2.3.2.2 Wet Snow

When the snow is wet, the snow is made up of ice, air, and liquid water. The addition of liquid water to the medium changes the microwave properties of the snow immensely. Even in small amounts, the presence of liquid water will increase the imaginary part of the dielectric constant of snow, turning it into a “lossy” medium (Bernier [1987]). This means that the wet snow readily absorbs and emits microwave radiation, reducing the amount of scattering present. The absorption in wet snow is several orders of magnitude higher than that of dry snow (Amlien [2008]), greatly reducing the scattering in the snowpack to near-zero (Mätzler [1987]).

As the research presented in this thesis focuses on the derivation of a new empirical extinction coefficient for use with the n-HUT model (discussed later in Section 2.5.4, with the empirical extinction coefficient derivation being shown in Chapter 5), any wet snow observations will be neglected. This is because wet snow observations would hinder progress, as observed brightness temperatures from wet snow tend to be dominated by the absorption and emission by liquid water, rather than from scattering of snow crystals.

## 2.4 Earth Observation of Snow

Observations with electromagnetic radiation via space borne remote sensing techniques have become a vital method in Earth observation ([Sharkov \[2003\]](#), [Rees \[2006\]](#), [Frei et al. \[2012\]](#), and [Rees \[2012\]](#)), due to its ability to cover large regions of the Earth in a relatively short period of time ([Chang et al. \[1987\]](#), [Hollinger et al. \[1990\]](#), [Kelly et al. \[2003\]](#), [Sharkov \[2003\]](#), [Takala et al. \[2011\]](#), and [Rees \[2012\]](#)). This allows for constant observations of many different parameters that are vital in the understanding and forecasting of the current state of the atmosphere and oceans, including but not limited to water vapour ([Mätzler \[2006\]](#)), sea surface temperature ([Merchant and Le Borgne \[2004\]](#)), severe storm monitoring ([Chang and Guo \[2007\]](#)), and snow mass estimates ([Takala et al. \[2011\]](#)).

Remote sensing can be performed in two separate ways; active or passive techniques. *Passive* techniques sense only the radiation that is naturally emitted by an object or scene ([Amlien \[2008\]](#)). *Active* techniques provide a source of electromagnetic radiation, to illuminate the object or scene, and the strength of returned signal is measured. A common use of active remote sensing in meteorology is RADAR measurements of precipitation ([Rees \[2006\]](#)). The focus of the research shown in Chapters 3 – 6 is the observation of microwave brightness temperatures of natural snow through passive microwave remote sensing techniques, and simulating the microwave signature with the n-HUT model. This is due to the n-HUT model being a semi-empirical model which simulates the passive microwave signature of a multiple layered snowpack. Therefore, passive microwave remote sensing is discussed below.

### 2.4.1 Visible, Infrared, and Microwave Remote Sensing of Snow Mass

Figure 2.5, taken from [Rees \[2006\]](#), shows the atmospheric transparency (also known as atmospheric “windows”) at different wavelengths. There are three main regions of

the electromagnetic spectrum that can propagate through the atmosphere where the atmospheric transparency is high enough to be useful for remote sensing purposes; visible ( $0.35 - 0.70 \mu\text{m}$ ), near infrared ( $0.7 - 1.4 \mu\text{m}$ ), thermal infrared ( $8 - 14 \mu\text{m}$ ), and microwave ( $0.1 \text{ cm} - 30 \text{ cm}$ ) wavelengths.

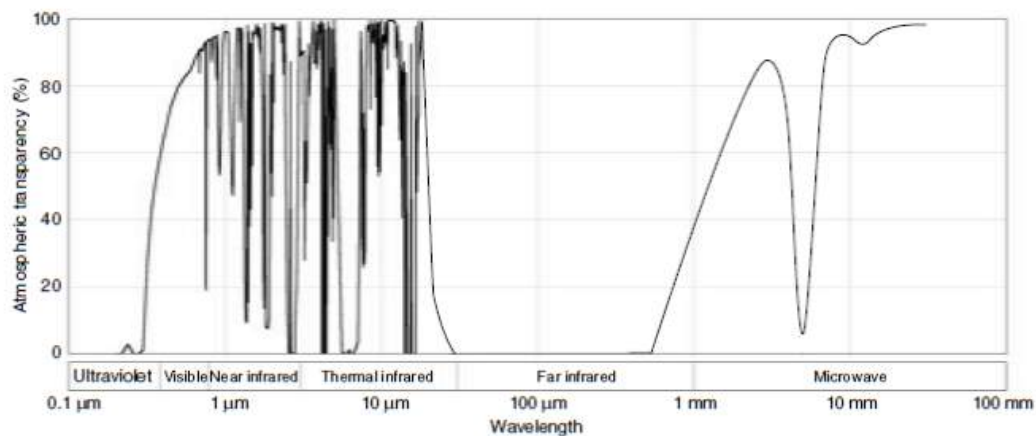


**Figure 2.5:** Typical atmospheric transparency and principle regions of the electromagnetic spectrum, taken from [Rees \[2006\]](#).

Passive remote sensing techniques, therefore, tend to use one of the three wavelength regions stated above. Each region has its advantages and disadvantages when discussing remote sensing; however when discussing the remote sensing of snow, microwave frequencies provide the best platform for remote sensing observation.

Passive remote sensing techniques using visible wavelengths are relatively straightforward with respect to snow observations, as these techniques are very similar to using aerial photographs. Due to the high albedo of snow compared to snow-free ground, as shown in Figure 1.2 ([Warren \[1982\]](#), [Schanda \[1986\]](#), and [Rees \[2012\]](#)), it is relatively easy to distinguish snow extent at these wavelengths.

However, measurements using visible wavelengths (such as albedo) rely on reflected solar radiation in the visible part of the electromagnetic spectrum ([Foster et al. \[1987\]](#)). Thus, remote sensing techniques using visible wavelengths are limited to regions that are illuminated by the sun, making measurements of snow during the night impossible. This impossibility would make continuous snow observations over Polar Regions difficult, as the polar winter suffers from a greatly reduced exposure to the sun.

A second major limitation of remote sensing with visible wavelengths is cloud cover. All but the thinnest cloud will block any upwelling radiation at these wavelengths ([Foster et al. \[1987\]](#) and [Frei et al. \[2012\]](#)), making any observations of the state of the ground

useless when cloud cover is present.

Thermal infrared wavelengths can also be used in the passive remote sensing of the Earth ([Foster et al. \[1987\]](#) and [Frei et al. \[2012\]](#)). Using this region of the electromagnetic spectrum, the infrared brightness temperatures are observed, which can be used to measure the physical skin temperature of the snow, using Eqn. 2.4. The emissivity of dry snow in the thermal infrared region ranges from 0.965 – 0.995 ([Warren \[1982\]](#) and [Rees \[2006\]](#)). In this region of the electromagnetic spectrum, the absorption of the ice is high, which increases its tendency to act like a blackbody. As the emissivity of water is not substantially different to that of snow, the effect from the presence of liquid water in snow is negligible. Due to the small penetration depth of infrared radiation, thermal infrared radiation cannot give any information about the internal properties of the snowpack, but can give information about the physical skin temperature of the snow ([Foster et al. \[1987\]](#)).

Thermal infrared wavelengths are an improvement upon visible wavelengths for the remote sensing of snow at night, as thermal infrared radiation is not dependent on reflected solar radiation. This allows for satellite scans to be completed during both the day and night, regardless of the lighting conditions. This makes observations over the Arctic winter night possible, unlike at visible wavelengths ([Frei et al. \[2012\]](#)).

Remote sensing using thermal infrared wavelengths require cloud-free skies, as infrared radiation cannot penetrate through clouds ([Foster et al. \[1987\]](#), [Foster et al. \[2005\]](#), [Chang et al. \[2005\]](#), and [Rees \[2006\]](#)). A second issue relating to remote sensing using thermal infrared wavelengths is atmospheric attenuation, due to the presence of water vapour, atmospheric gases, and aerosols in the atmosphere ([Foster et al. \[1987\]](#)). These absorb some thermal infrared radiation, causing the measured radiative temperature to be lower than the actual temperature of the surface ([Barnes et al. \[1981\]](#)).

Remote sensing techniques using near-infrared wavelengths do allow for the differentiation between the cloud tops and the snow surface; as the near-infrared reflectance of most clouds is high ([Frei et al. \[2012\]](#)), whilst the near-infrared reflectance between 1.55 and  $1.75 \mu\text{m}$  drops to almost zero ([Konig et al. \[2001\]](#)). Therefore, using this wavelength range, it is possible to discriminate between snow and cloud, as well as detecting cirrus, stratus, and cumulus clouds ([Konig et al. \[2001\]](#)).

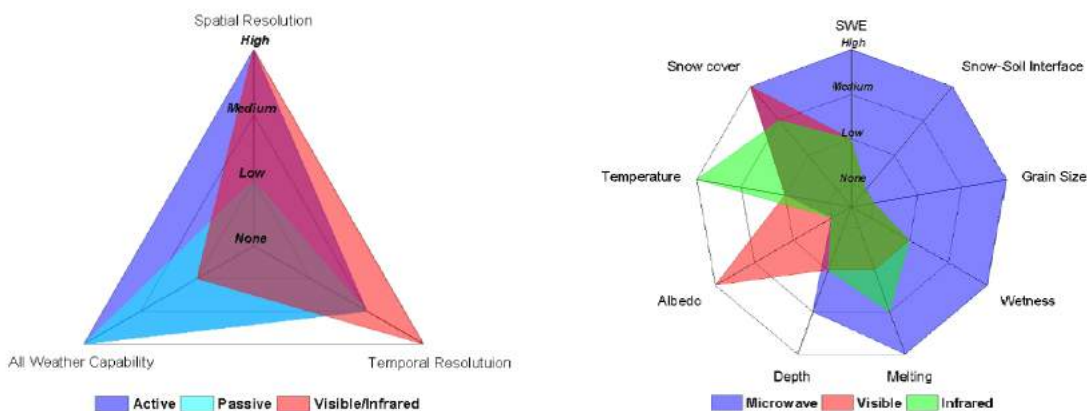
Near-infrared wavelengths are sensitive to “grain size”; a feature that is heavily used in the observation of SSA in snowpit observation (Section 2.3.1). Satellite remote sensing of snow using near-infrared wavelengths do allow for the estimation of SSA, and

thus surface optical diameter ([Dozier et al. \[1981\]](#), [Tedesco and Kokhanovsky \[2007\]](#), and [Mary et al. \[2013\]](#)). However, like visible and thermal infrared wavelengths, near-infrared wavelengths are only capable of retrieving information from the surface of the snowpack, due to the small penetration depth ([Foster et al. \[1987\]](#) and [Aoki et al. \[2007\]](#)).

Microwave radiation is extremely useful in the passive remote sensing of snow, due to differences with visual and thermal infrared radiation. This is due to the nature of the radiation characteristics. Unlike remote sensing techniques at visible or thermal infrared wavelengths, passive remote sensing techniques at microwave wavelengths are able to penetrate through (almost) all non-precipitating clouds, making microwave observations independent of cloud cover ([Foster et al. \[1987\]](#), [Tait \[1998\]](#), [Rees \[2006\]](#), and [Frei et al. \[2012\]](#)). This, along with being independent of current levels of reflected solar radiation, makes microwave observations possible at virtually any time of year, regardless if the snow could be visually seen or not. This is most effective when observing in Polar Regions, as observations can be made during the polar night, regardless of the weather conditions.

Figure 2.6, taken from [Muñoz et al. \[2013\]](#), graphically shows the advantages and disadvantages of different remote sensing techniques for the remote sensing of snow.

Snow is very efficient at scattering microwave radiation at some frequencies, due to the similarity between the crystal sizes within the snow and the wavelengths of the microwave frequencies in question ([Chang et al. \[1976\]](#), [Mätzler \[1994\]](#), and [Tait \[1998\]](#)). As the microwave emission is directly related to snow cover (which will be discussed in more detail in Section 2.3.2), it is possible to use microwave radiation to determine snow cover



(a) Capabilities of spatial and temporal resolution of snow remote sensing with active and passive Microwave and Visible/Infrared wavelengths. Taken from [Muñoz et al. \[2013\]](#).

(b) Passive sensor responses to snowpack properties. Taken from [Muñoz et al. \[2013\]](#).

**Figure 2.6:** Qualitative assessment of different snow remote sensing techniques, taken from [Muñoz et al. \[2013\]](#).

extent (Chang et al. [1976], Mätzler [1994], Tait [1998], and Grody [2008]). As the amount of scattering is proportional to the number of snow grains (acting as scattering centres), microwave remote sensing can be used to determine numerous different parameters of the snow from the observed brightness temperature, such as bulk density, bulk snow grain size, and Snow Water Equivalent (Foster et al. [1987], Rees [2006], Tait [1998], Tedesco and Kim [2006], and Chang et al. [1987]). Due to the difficulties that arise from passive microwave remote sensing of snow (discussed in Section 2.5), not all snow parameters can be determined at the same time, as some information on the other parameters is needed first.

Scattering is not only dependent on the snow grain size, but on the electromagnetic frequency (Hallikainen et al. [1987], Roy et al. [2004], Kontu and Pulliainen [2010], Chang et al. [1987], Rees [2006], and Grody [2008]). Higher frequencies are more effectively scattered by snow grains, when compared to the scattering at lower frequencies. Thus by comparing two different frequencies, it is possible to estimate snow depth (Foster et al. [1987], Rees [2006], Tait [1998], Tedesco and Kim [2006], Chang et al. [1987], Takala et al. [2011], Walker and Goodison [1993], Kelly et al. [2003], and Pulliainen [2006]).

Passive microwave remote sensing isn't without limitations. Snow cover with liquid water content (present during melting or during rain-on-snow events, also known as *wet* snow, Section 2.3.1) will greatly hinder snow depth retrieval, as emitted microwaves from the liquid water will mask signals coming from the surrounding snow mass (discussed further in Section 2.3.2). Therefore areas of wet snow will not be as easily measured as regions of dry snow. This means that snow cover and snow mass estimates during the autumn and spring will be difficult to produce, when temperatures are close to zero during the day (Ulaby et al. [1986b], Rott [1986], and Koike and Suhama [1993]), as the liquid water present in the snow will mask the signal, giving an incorrect observation.

A second limitation of passive microwave remote sensing of snow is with measuring snow depth. Due to attenuation of the ground contribution of microwave emission (discussed further in Section 2.3.2), the observed microwave emission at higher frequencies will plateau above certain depths (Chang et al. [1987]).

A further limitation of passive microwave remote sensing of snow involves the spatial resolution of satellite observations. Due to the relatively low levels of naturally emitted microwave energy (Rees et al. [2006]), the antenna size must therefore be large in order to observe the low levels of passive microwave radiation. This antenna size limits the spatial resolution of spaceborne observations of passive microwaves to approximately 25

km x 25 km ([Foster et al. \[1984\]](#), [Rees et al. \[2006\]](#), [Amlien \[2008\]](#), and [Takala et al. \[2011\]](#)). Having a single value of brightness temperature for a 25 km x 25 km grid box can hinder the retrieval of estimated snow mass, as the land type, vegetation, and snow cover area within the grid box may include fractional cover (e.g. if the grid box was made of a mixture of farm land and forest). Numerous different methods of solving fractional land type forest cover ([Foster et al. \[1991\]](#), [Pullainen and Hallikainen \[1997\]](#), and [Kelly et al. \[2003\]](#)) exist for use with passive microwave remote sensing techniques.

The use of passive microwave remote sensing for the monitoring of Snow Water Equivalent and snow depth became possible with the launch of the first satellite with multiple-channel radiometers ([Chang et al. \[1987\]](#)), with records of Snow Water Equivalent and snow depth measurements from passive microwave remote sensing satellites going back over 35 years ([Chang et al. \[1987\]](#), [Hollinger et al. \[1990\]](#), [Kelly et al. \[2003\]](#), [Takala et al. \[2011\]](#)).

Long data series are vital for meteorological and climatological studies (Section 1.1), as historical data must be used to monitor long term trends ([Takala et al. \[2011\]](#)). Table 2.2 provides a summary of satellites with passive microwave radiometers on-board, from the first set of radiometers upon the Scanning Multichannel Microwave Radiometer, as described in [Chang et al. \[1987\]](#). As the satellites are set up in a near-polar orbit, large regions of the Earth are able to be measured in a very short period of time. Figure 2.7, taken from [Hollinger et al. \[1990\]](#) shows the 24 hour coverage of the Special Sensor Microwave/Imager (SSM/I). It can be seen that the Arctic has got very good coverage; being completely scanned at least once in a 24 hour period.



**Figure 2.7:** Earth coverage of the SSM/I in a 24 hour period. Only the shaded areas are not observed. Taken from [Hollinger et al. \[1990\]](#).

**Table 2.2:** Summary of satellite microwave sensors, taken from [Takala et al. \[2011\]](#)

Platform	Sensor	Frequency (GHz)	Swath (km)	Incidence angle (°)	Field of view (km)
Nimbus-7 (1978)	SMMR	6.6	800	50.3	95 x 148
		10.69			70 x 109
		18.0			43 x 68
		21.0			36 x 56
		37.0			18 x 27
DMSP F8 to F15 (1987)	SSM/I	19.4	1400	53	45 x 70
		22.2			40 x 60
		37.0			30 x 38
		85.5			14 x 16
Aqua (2002)	AMSR-E	6.9	1445	54.8	43 x 75
		10.7			29 x 51
		18.7			16 x 27
		23.8			18 x 32
		36.5			8 x 14
		89.0			4 x 6

#### 2.4.2 Passive Microwave Observation Contributions

The microwave emission measured by the spaceborne passive microwave radiometers have contributions from different components within the radiometer footprint. Figure 2.8 displays a simplified scenario of the different contributions of the microwave emission. These contributions include:

- (A) The upwelling emission from the atmosphere,
- (B) Cosmic background/solar radiation reflected from the atmosphere,
- (C) Cosmic background/solar radiation reflected from the ground surface and attenuated throughout the atmosphere,
- (D) Downwelling emission from the atmosphere, reflected by the ground, and attenuated throughout the atmosphere,
- (E) Upwelling emission from the ground surface, attenuated throughout the atmosphere.

For spaceborne retrievals, the wanted parameter, typically E (the upwelling emission from the surface) is embedded within the sum of all the five components. For airborne and ground-based retrievals, the contributions from components A and B can be neglected, as can the atmospheric attenuation factors within components C, D, and E. For retrievals using ground-based radiometers, components C and D can be measured, by taking mea-

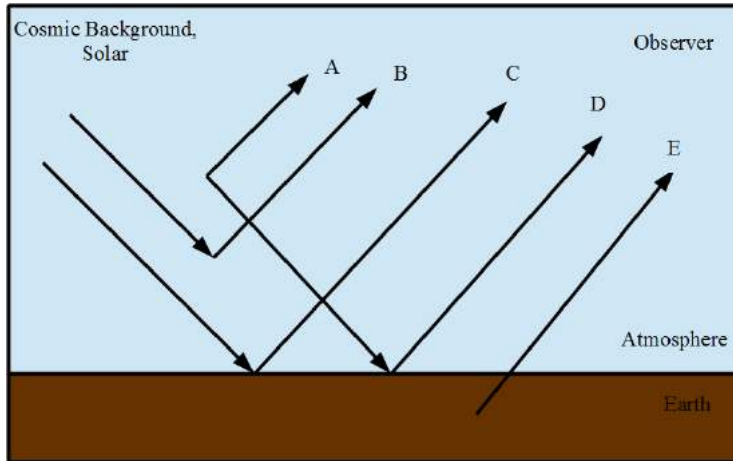


**Figure 2.8:** Diagram of the passive microwave remote sensing scenario. The brightness temperature observed by spaceborne radiometers is a sum of all five components.

surements of the downwelling sky brightness temperature at the opposite inclination angle to the surface measurements.

For snow covered ground, component E in Figure 2.8 is made up of three separate contributions. These contributions are discussed in Section 2.3.2, and are shown in Figure 2.9. These contributions include:

1. Emission from the snow, attenuated through the snow
2. Emission from the ground, attenuated through the snow
3. Emission from the snow, attenuated through the snow, reflected by the ground.

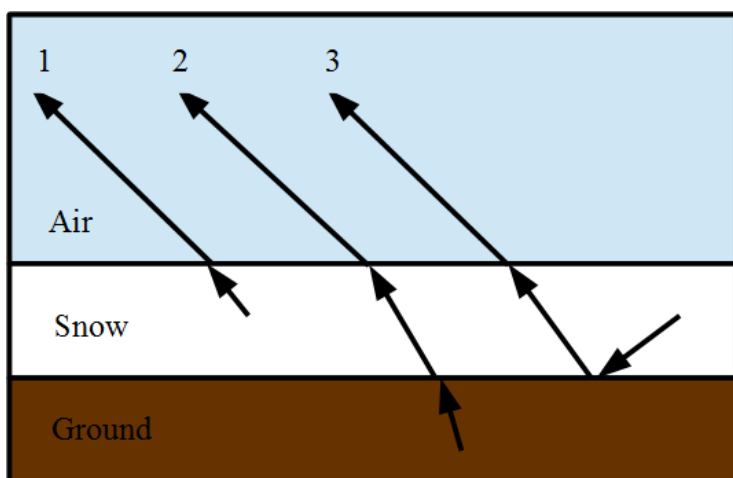


**Figure 2.9:** Diagram of component E in Figure 2.8 for a snow covered ground.

Typically, these contributions are simplified, by adding together components 1 and 3 from Figure 2.9. Therefore, the observed microwave signature of the snowpack can be

described in terms of two separate contributions: a source from the snow itself (components 1 and 3) and a source from the underlying ground (component 2) ([Foster et al. \[1984\]](#), [Chang et al. \[1987\]](#), [Armstrong et al. \[1993\]](#), [Chang et al. \[1997\]](#), [Amlien \[2008\]](#), and [Davenport et al. \[2012\]](#)).

## 2.5 Snow Emission Models

As microwave wavelengths are sensitive to snow mass, passive microwave observations can be used to retrieve information regarding snow variables, such as depth, snow water equivalent, and snow extent. Such variables can be estimated, using relationships between microwave brightness temperature, radiometer instrumentation settings (such as frequency and polarizations), and the snow variables in question. A large amount of literature has been focused on the different forms of relationships regarding snow variables and estimation techniques. Such techniques can be categorised into one of three different types: empirical, theoretical, and semi-empirical models.

### 2.5.1 Empirical Models

Empirical models use a very simple framework as a basis. By exploiting relationships between differences in brightness temperature at different frequencies (known as the spectral difference) and snow properties, such as snow depth and SWE, simple empirical model can be built to estimate SWE and snow depth from the spectral difference observed from spaceborne radiometers. The advantage of this form of model is that it allows for fast and direct retrieval of simple snow properties. However, empirical relationships are very limited in use, as they rely on assumptions. They are also highly restricted to geographical locations ([Amlien \[2008\]](#)).

Most empirical models which allow for estimation of snow cover extent use spectral difference. By using a threshold value of spectral difference, the empirical models can estimate if the surface is snow covered. [Kunzi et al. \[1982\]](#) initially produced an empirical model using SMMR data, to map the snow cover extent greater than 5 cm in depth, using:

$$(T_{B18H} - T_{B37H}) > 3.8K \quad (2.24)$$

across the whole Northern Hemisphere.

Empirical snow depth and snow water equivalent retrieval methods also use spectral

differences in order to estimate the snow depth and amount of snow water equivalent present. [Kunzi et al. \[1982\]](#) initially suggested an empirical algorithm from SSMR data, for snow depth (in the range 5 – 50 cm), given by:

$$SD = 1.46(T_{B18H} - T_{B37H}) + 2.46 \quad (2.25)$$

where SD is snow depth (in cm). [Chang et al. \[1987\]](#) also uses a simple spectral difference algorithm, derived from snow data taken from Eurasia and the Canadian high plains. By using the horizontally polarized 18 GHz and 37 GHz spectral difference, the snow depth is estimated, valid within the range of 2.5 – 100 cm, by:

$$SD = 1.59(T_{B18H} - T_{B37H}) \quad (2.26)$$

An empirical SWE retrieval algorithm has also been calculated from [Chang et al. \[1987\]](#), which states that:

$$SWE = 4.8(T_{B18H} - T_{B37H}) \quad (2.27)$$

where SWE is snow water equivalent (in mm). The algorithm corresponds well with available snow data in large flat uniform places ([Amlien \[2008\]](#)), but does not work effectively in forest or mountainous areas ([Chang et al. \[1987\]](#)). [Kunzi et al. \[1982\]](#) showed that the spectral difference worked well in flat, uniform plains (with  $R^2$  of 0.71 and 0.66 for Alberta, Canada, and Southern Russia), but did not work as well in forested areas ( $R^2 = 0.56$ ). [Hallikainen and Jolma \[1986\]](#) stated that the reason for the lower  $R^2$  value at Finland is due to the variation of land types and vegetation coverage present. Different regression coefficients were found for Northern and Southern Finland ([Hallikainen and Jolma \[1986\]](#)), as Northern Finland has deeper snow and less forest cover than that of Southern Finland. This need for regional alterations to coefficients show how geographically limited empirical retrieval methods are.

### 2.5.2 Theoretical Models

Another category of snow emission models come in the form of theoretical models. Theoretical radiation models are not built using observational data, but are based on only physical theory. Theoretical models are well based in physical principles, and are very good at snowpack simulation and validation. Unfortunately, purely theoretical radiation

models are extremely difficult to invert ([Amlien \[2008\]](#)), and are not used with satellite retrievals. One such theoretical model which is used to simulate microwave brightness temperatures is the Dense Medium Radiative Theory (DMRT) model ([Tsang \[1992\]](#)). The DMRT model considers a dense medium (where particles occupy more than 10% of the volume of the medium), and assumes that independent scattering is no longer valid when there is more than one scatterer within one wavelength ([Tedesco and Kim \[2006\]](#)). Multiple solutions exist within the DMRT literature, all of which make inversion extremely difficult ([Amlien \[2008\]](#)).

### 2.5.3 Semi-empirical Models

The third type of snow emission model are semi-empirical models. Semi-empirical snow emission models sit between purely empirical models, which are based on purely observational data, and purely theoretical models, which are based on purely physical theory. Semi-empirical models combine theoretical physics with empirical coefficients and regression models. This allows for models to be built based on physical radiative transfer theory, with quick empirical regression models built in for extinction coefficients. Semi-empirical models are designed to simulate the microwave emission from snowpacks, as well as being designed to be inverted, allowing for snow properties to be retrieved from the satellite based brightness temperature observations. The primary disadvantage of using semi-empirical models for retrieval purposes is that they are not as direct or as fast as purely empirical methods, and are not purely based in theoretical physics. One such semi-empirical model is the Helsinki University of Technology (HUT) snow emission model.

The research presented in Chapters [3](#), [4](#), and [6](#) focus on simulating the brightness temperature of individual extracted snow slabs from the natural snowpack as part of the Arctic Snow Microstructure Experiment (Chapters [3](#) and [4](#)), as well as simulating brightness temperatures of the natural snowpack as part of the Sodankylä Radiometer Experiment (Chapter [6](#)) with the HUT snow emission model. The HUT snow emission model is detailed below.

## 2.5.4 Helsinki University of Technology Snow Emission Model

### 2.5.4.1 Original Single Layer HUT Snow Emission Model

The original single layer HUT snow emission model ([Pulliainen et al. \[1999\]](#)) is a semi-empirical, radiative transfer-based model, which simulates the emission of microwaves from a single layer of homogeneous snow. The model itself requires the snowpack and underlying ground layer to be inputted as two separate layers; one depicting the bulk properties of the snowpack, and one of the underlying surface. A schematic of the required input parameters, and various stages within the single layer HUT snow emission model is shown in Figure [2.10](#).

Initially, the complex permittivity of the snow layer is calculated, using empirical formulae with input values of frequency, physical temperature, and bulk density. The real part of the permittivity of dry snow,  $\epsilon'_{snow}$  is calculated, as shown by [Mätzler \[1987\]](#), to be:

$$\epsilon'_{snow} = 1 + \frac{1.58\rho_{snow}}{1 - 0.365\rho_{snow}} \quad (2.28)$$

The imaginary part of the permittivity of dry snow,  $\epsilon''_{snow}$ , is not so readily calculated. As stated by [Mätzler \[1987\]](#),  $\epsilon''_{snow}$  is calculated using a formula based on the Polder-van Santen mixing formula ([Hallikainen et al. \[1986\]](#)), which states that:

$$\epsilon''_{snow} = 3v_i\epsilon''_{ice} \frac{(\epsilon'_{snow})^2(2\epsilon'_{snow} + 1)}{(\epsilon'_{ice} + 2\epsilon'_{snow})(\epsilon'_{ice} + 2(\epsilon'_{snow})^2)} \quad (2.29)$$

where  $v_i$  is the volume fraction of ice within the snow, as calculated by:

$$v_i = \frac{\rho_{snow}}{\rho_{ice}} \quad (2.30)$$

Whilst  $\epsilon'_{snow}$  is easily determined from Eqn. [2.28](#), the real and imaginary parts of the permittivity of ice ( $\epsilon'_{ice}$  and  $\epsilon''_{ice}$  respectively), are calculated through individual empirical models.  $\epsilon'_{ice}$  is calculated via the empirical model stated by [Mätzler and Wegmüller \[1987\]](#):

$$\epsilon'_{ice} = 3.1884 + (9.1 \times 10^{-4})(T_{phys}) \quad (2.31)$$

where  $T_{phys}$  is the physical temperature of the ice crystals ( $^{\circ}\text{C}$ ). The imaginary part of the permittivity of ice was modelled as a function of frequency and temperature by [Hufford \[1991\]](#), using data from [Lamb \[1946\]](#), [Anty and Cole \[1952\]](#), [Mishima et al. \[1983\]](#),

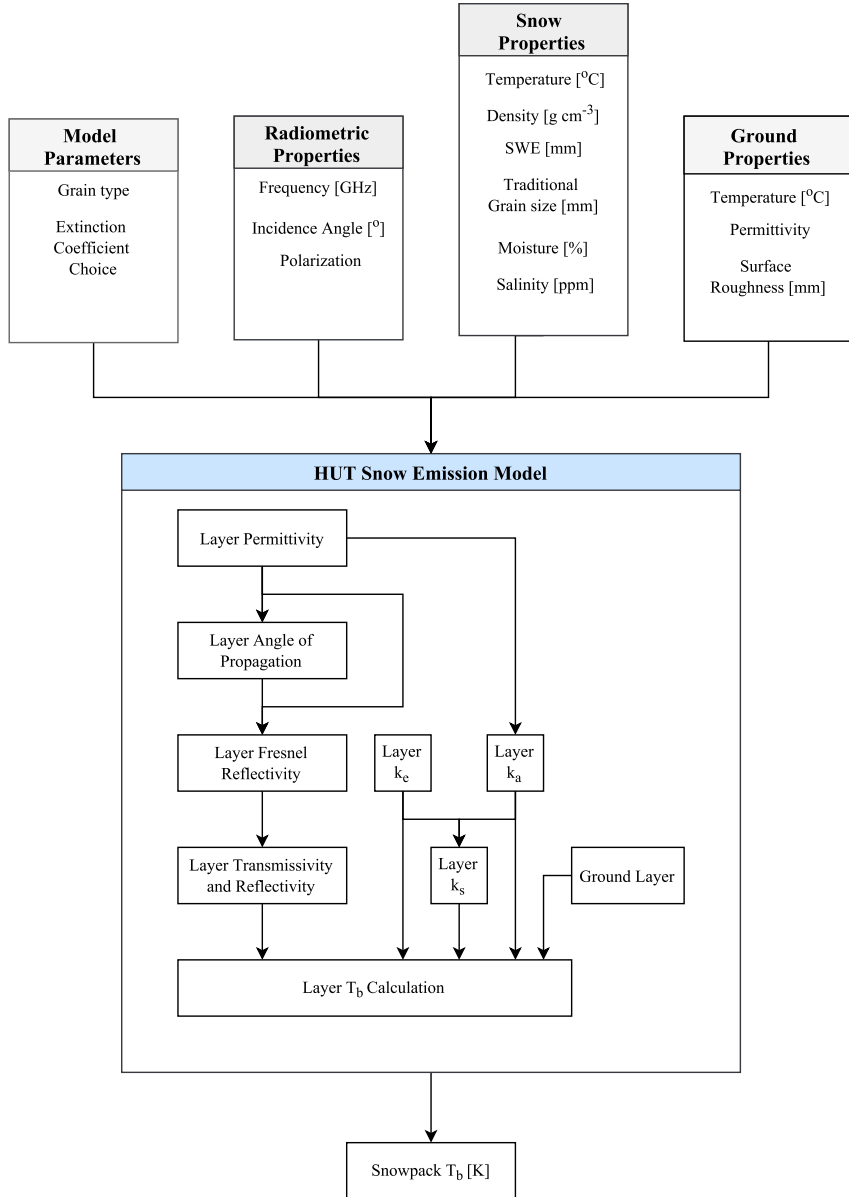


**Figure 2.10:** Schematic diagram of the HUT snow emission model. Model Inputs (grey boxes) are grouped within the four categories. The internal running of the HUT snow emission model is shown within the blue box. This schematic is applicable to both the single layer and the multiple layer HUT snow emission model.

and Mätzler and Wegmüller [1987]. Hufford [1991] stated that  $\epsilon''_{ice}$  can be written in the form:

$$\epsilon''_{ice} = \frac{\alpha}{f} + \beta f \quad (2.32)$$

where  $f$  is the frequency (in GHz). The first term is an unaltered relaxation term (from Anty and Cole [1952]), and the second term is an alteration of the term discussed in Mishima et al. [1983], with a correction applied based on additional losses, observed at temperatures greater than 200K. Using a modified inverse temperature  $\theta_T$ , where  $\theta_T$

is defined as:

$$\theta_T = \frac{T_0}{T_{phys}} - 1 \quad (2.33)$$

where  $T_0 = 300K$ , Hufford [1991] stated that  $\alpha$  can be written as:

$$\alpha = (0.00504 + 0.0062\theta_T)e^{-22.1\theta_T} \quad (2.34)$$

The  $\beta$  coefficient was partially based on a model, produced by Mishima et al. [1983], that considered cold-water ice ( $T_{phys} < 200$  K). However, a correction was applied to allow higher temperatures ( $T_{phys} > 200$  K) to be considered. As such,  $\beta$  can be written, so that:

$$\beta = \beta_M + \Delta\beta \quad (2.35)$$

where  $\beta_M$  is the contribution from Mishima et al. [1983], and  $\Delta\beta$  is the correction for the higher temperatures. Mishima et al. [1983] expressed  $\beta_M$  as:

$$\beta_M = \frac{B_1}{T_{phys}} \frac{\exp(\frac{b}{T_{phys}})}{(\exp(\frac{b}{T_{phys}}) - 1)^2} + B_2 f^2 \quad (2.36)$$

where  $f$  is the frequency (in GHz),  $B_1 = 0.0027GHz^{-1}$ ,  $b = 335K$ , and  $B_2 = 1.16 \times 10^{-11}GHz^{-3}$ .

A correction to allow higher temperatures to be considered ( $\Delta\beta$ ) was proposed by Mätzler [1998] to include the higher temperature permittivities, and is written as:

$$\Delta\beta = \exp(-10.02 + 0.0364(T_{phys} - 273)) \quad (2.37)$$

Therefore, by substituting Eqn. 2.36 and 2.37 into Eqn. 2.35,  $\beta$  can be described as:

$$\beta = \frac{B_1}{T_{phys}} \frac{\exp(\frac{b}{T_{phys}})}{(\exp(\frac{b}{T_{phys}}) - 1)^2} + B_2 f^2 + \exp(-10.02 + 0.0364(T_{phys} - 273)) \quad (2.38)$$

Thus, by using Eqns. 2.28 – 2.38, the complex permittivity of the snow can be calculated empirically. Figure 2.11 shows the spectra of simulated  $\epsilon'_{snow}$  and  $\epsilon''_{snow}$  values for dry snow at 253 K at 36.5 GHz, in the density range  $100 - 300$   $kgm^{-3}$ .

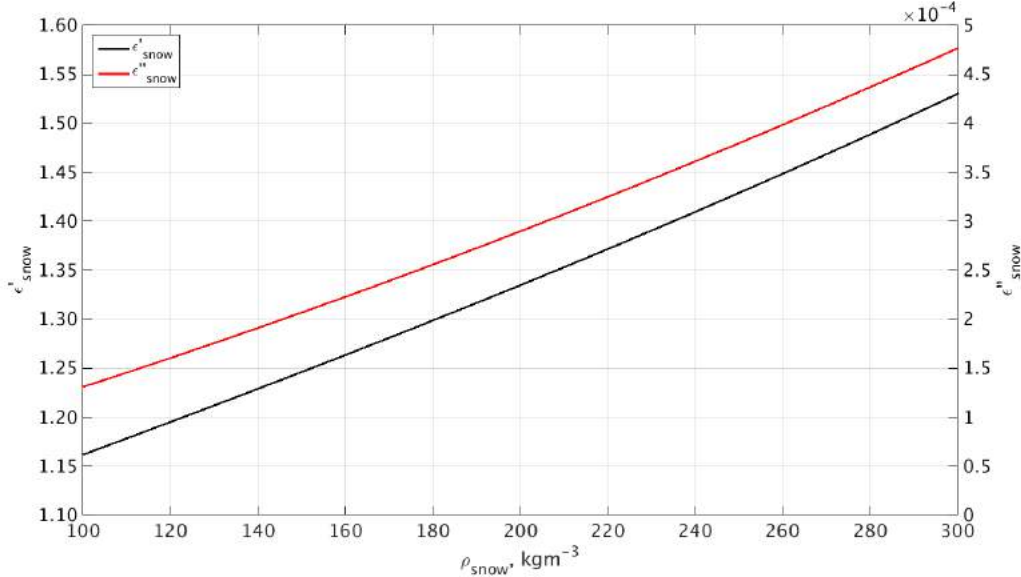


**Figure 2.11:** Spectra of  $\epsilon'_{\text{snow}}$  and  $\epsilon''_{\text{snow}}$  values from  $100 - 300 \text{ kgm}^{-3}$  at  $T_{\text{phys}} = 253 \text{ K}$ , at 36.5 GHz.

The complex dielectric constants of snow are then used to calculate the propagation angle of microwave radiation through the snowpack. This step comes from the fact that the snowpack and overlying air have different dielectric constants, and thus differing refractive indices. These differing refractive indices result in differing angles of propagation, in the air and snowpack. The change in propagation angle through the snowpack is calculated using Snell's Law, which states that:

$$\sqrt{\epsilon_{\text{air}}} \sin(\theta_i) = \sqrt{\epsilon_{\text{snow}}} \sin(\theta_t) \quad (2.39)$$

where  $\theta_i$  and  $\theta_t$  are the angles of incidence and transmissivity respectively, as shown by the schematic in Figure 2.12. The differing permittivities, and thus refractive indices, result in the angle of propagation through the snowpack to be refracted, and ultimately changing the radiation beam length through the snowpack.

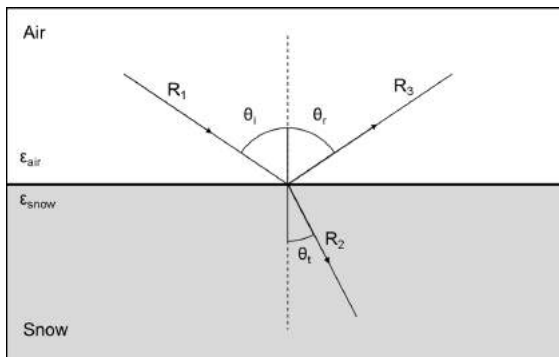


**Figure 2.12:** Air-snow interface schematic.

Upon the calculation of both the complex permittivity of dry snow and the differing angle of propagation through the snowpack, the reflectivity at layer interfaces (in the instance of the single layer HUT snow emission model, the air-snow interface) is calculated, allowing for the amount of radiation to transmit through the layer boundary to be known. These reflectivities, known as Fresnel reflectivities, are calculated separately for each polarization. The Fresnel reflectivity at horizontal ( $r_{ih}$ ) and vertical ( $r_{iv}$ ) polarization are calculated via:

$$r_{ih} = \left| \frac{\sqrt{\epsilon_{air}} \cos(\theta_t) - \sqrt{\epsilon_{snow}} \cos(\theta_i)}{\sqrt{\epsilon_{air}} \cos(\theta_t) + \sqrt{\epsilon_{snow}} \cos(\theta_i)} \right|^2 = \left| \frac{\sqrt{\epsilon_{air}} \sqrt{1 - \frac{\epsilon_{air}}{\epsilon_{snow}} \sin^2(\theta_i)} - \sqrt{\epsilon_{snow}} \cos(\theta_i)}{\sqrt{\epsilon_{air}} \sqrt{1 - \frac{\epsilon_{air}}{\epsilon_{snow}} \sin^2(\theta_i)} + \sqrt{\epsilon_{snow}} \cos(\theta_i)} \right|^2 \quad (2.40)$$

$$r_{iv} = \left| \frac{\sqrt{\epsilon_{snow}} \cos(\theta_i) - \sqrt{\epsilon_{air}} \sin(\theta_t)}{\sqrt{\epsilon_{snow}} \cos(\theta_i) + \sqrt{\epsilon_{air}} \sin(\theta_t)} \right|^2 = \left| \frac{\sqrt{\epsilon_{air}} \cos(\theta_i) - \sqrt{\epsilon_{snow}} \sqrt{1 - \frac{\epsilon_{air}}{\epsilon_{snow}} \sin^2(\theta_i)}}{\sqrt{\epsilon_{air}} \cos(\theta_i) + \sqrt{\epsilon_{snow}} \sqrt{1 - \frac{\epsilon_{air}}{\epsilon_{snow}} \sin^2(\theta_i)}} \right|^2 \quad (2.41)$$

The absorption and scattering properties (collectively known as the extinction properties) of the snowpack are also simulated, for the calculation of the amount of radiation loss present. The absorption coefficient,  $k_a$ , is calculated using the frequency and complex permittivity of the snow layer (Pulliainen et al. [1999]):

$$k_a = (4\pi f)(\sqrt{\mu_0 \epsilon_0 \epsilon'_{snow}}) \left( \sqrt{0.5 \left( \sqrt{1 + \left( \frac{\epsilon''_{snow}}{\epsilon'_{snow}} \right)^2} \right) - 1} \right) \quad (2.42)$$

The total extinction within the snowpack is empirically calculated, from observations of frequency and traditional grain size (as defined by Fierz et al. [2009]). Numerous extinction coefficients have been calculated for use within the single layer HUT snow emission model, as discussed in Section 2.5.4.3. The scattering coefficient is treated as the difference between the total extinction and the absorption coefficient, and is calculated simply as:

$$k_s = k_e - k_a \quad (2.43)$$

Like the transmissivity and reflective properties of the air-snow boundary, the three extinction coefficients ( $k_a$ ,  $k_s$ , and  $k_e$ ) are stored for later use.

The ground layer reflectivity and transmissivity is then calculated, using a rough bare soil reflectivity model created by [Wegmüller and Mätzler \[1999\]](#). The rough bare soil reflectivity model uses values of the ground permittivity and ground roughness observations to calculate the bare soil reflectivities at both horizontal and vertical polarizations. This allows for the calculation of the amount of radiation that is reflected back into the snowpack from the underlying ground layer.

The single layer HUT snow emission model then take the ground layer reflectivity, the snow layer transmissivity, the snow layer reflectivity, the absorption, scattering and extinction coefficients and uses them within the radiative transfer section of the model, to simulate the microwave emission of the homogeneous snowpack over the ground.

The radiative transfer equation for radiation propagating through a snowpack can be written as:

$$\frac{\partial T_B(z, \theta)}{\partial z} = k_a \sec \theta T_{phys} + k_s \sec \theta \frac{1}{4\pi} \iint_{4\pi} \Psi(\bar{r}_\theta, \theta', \phi') T_B(z, \theta', \phi') \sin \theta' d\theta' d\phi' - k_e \sec \theta T_B(z, \theta) \quad (2.44)$$

where  $T_B$  is the brightness temperature,  $T_{phys}$  is the physical snow temperature,  $k_a$  is the absorption coefficient,  $k_s$  is the scattering coefficient,  $k_e$  is the extinction coefficient,  $\Psi$  is the scattering phase function, and  $\bar{r}$  is the unit vector to the angle of observation.

The basic assumption of the HUT snow emission model is that the scattering of propagating radiation can be assumed to be mostly concentrated in the forward direction. As the scattering in the forward direction is assumed to be the dominant direction of scattering, the forward scattering incoherent intensity ( $I_{INC}$ ) for a thin slab with a thickness of  $d$ , and for nominal incidence is ([Ishimaru \[1978\]](#)):

$$I_{INC} = I(0^+) q (e^{-k_a d} - e^{-k_e d}) \quad (2.45)$$

where  $q$  is the constant that describes the fraction of intensity scattered toward the receiver antenna beam. The value of  $q$  was evaluated to be 0.96, constant at all frequencies. This value was determined using measurements of snow packs under controlled-conditions in both Switzerland ([Mätzler \[1987\]](#)) and Finland ([Hallikainen et al. \[1987\]](#)) in the 1980s. Assuming that Eqn. 2.45 holds, then this allows the radiative transfer equation (Eqn. 2.44) to be simplified to:

$$\frac{\partial T_B(z, \theta)}{\partial z} = k_a \sec \theta T_{phys} + \sec \theta (qk_s - k_e) T_B(z, \theta) \quad (2.46)$$

Therefore, the microwave emission of the snow (with a total thickness  $d$ ) at just below the snow surface ( $d^-$ ) can be then obtained from [Pulliainen et al. \[1999\]](#) as:

$$T_B(d^-, \theta) = T_B(0^+, \theta) e^{-(k_e - qk_s) \sec \theta d} + \frac{k_a T_{phys}}{k_e - qk_s} (1 - e^{-(k_e - qk_s) \sec \theta d}) \quad (2.47)$$

$$T_B(d^-, \theta) \equiv T_{B,g} + T_{B,s\uparrow} \quad (2.48)$$

The first term ( $T_{B,g}$ ) corresponds to the brightness temperature contribution originating from below the snow layer, and attenuated by the snow layer. The second term ( $T_{B,s\uparrow}$ ) is the actual thermal emission contribution of the homogeneous snow layer.

#### 2.5.4.2 Multi-layer modification to HUT Snow Emission Model

[Lemmetyinen et al. \[2010\]](#) introduced a multiple layer modification to the HUT model, hereby referred to as the n-HUT model, which allows the simulation of emission from a vertically stacked structure of multiple layers of snow, as shown in Figure 2.13.

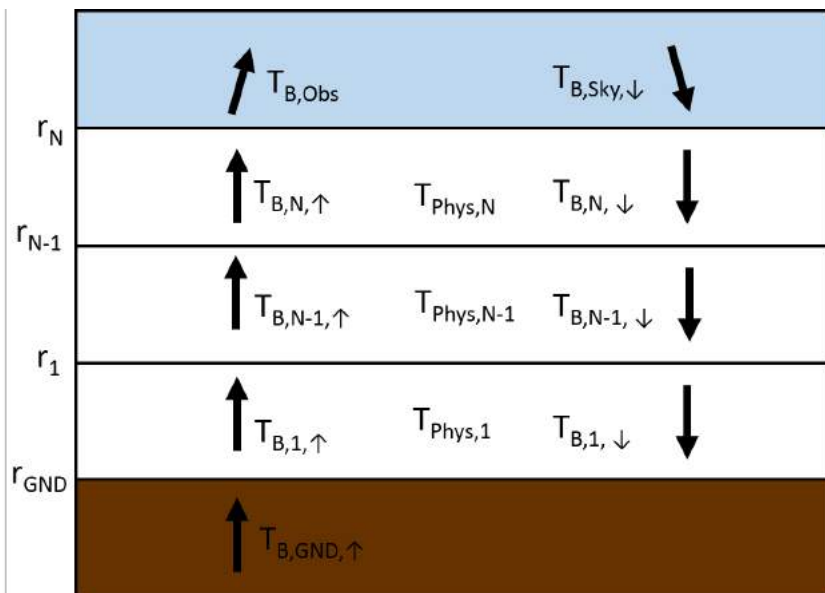


**Figure 2.13:** Diagram of the n-HUT model, with  $N$  layers of snow or ice. Air and ground layers contribute to their respective brightness temperatures with  $T_{B,SKY,\downarrow}$  and  $T_{B,GND,\uparrow}$  respectively. Adapted from [Lemmetyinen et al. \[2010\]](#).

where

$T_{B,obs}$  = Observed brightness temperature;

$T_{B,N,\uparrow}$  = Upwelling Brightness temperature of layer N;

$T_{B,N,\downarrow}$  = Downwelling Brightness temperature of layer N;

$T_{phys,N}$  = Physical snow temperature temperature of layer N;

$r_N$  = Reflection at layer boundary N;

$l_N$  = Attenuation through layer boundary N.

The emission from multiple layers is calculated based on the emission and attenuation properties of the individual layers, and the reflection and transmission properties at the layer interfaces. The upwelling emission of brightness temperature (as shown in Figure 2.13) can be determined as:

$$T_{N,\uparrow} = S_N \left( T_{phys,N} + T_{N+1,\downarrow} \frac{t_N r_{N-1}}{l_N^2} + T_{N-1,\uparrow} \frac{t_{N-1}}{l_N} + T_{S,N} \frac{r_{N-1}}{l_N} \right) \quad (2.49)$$

where

$t_N$  = Fresnel transmission of layer N;

$r_N$  = Fresnel reflectivity of layer N;

$l_N$  = Fresnel loss factor of layer N;

$S_N$  = Geometric sum of multiple reflections in layer N, as shown in Eqn. 2.50.

$$S_N = \frac{1}{1 - \frac{r_N r_{N-1}}{l_N^2}} \quad (2.50)$$

Likewise, downwelling emission of brightness temperature (as shown in Figure 2.13) can be determined as:

$$T_{N,\downarrow} = S_N \left( T_{phys,N} + T_{N+1,\downarrow} \frac{t_N}{l_N} + T_{N-1,\uparrow} \frac{t_{N-1} r_N}{l_N^2} + T_{S,N} \frac{r_N}{l_N} \right) \quad (2.51)$$

Within the n-HUT model schematic (previously shown in Figure 2.10), there is no difference in the order in which the variables are calculated. The n-HUT model treats the

snowpack as a vertical stacked structure of individual homogeneous layers, and thus calculates each of the previously mentioned variables for all individual homogeneous layers within the snowpack. Each individual layer, therefore, has its own set of complex permittivity values, angles of propagation (as radiation passes between two different dielectric mediums), and internal transmissivities and reflectivities. Each layer also has its own set of absorption, scattering, and extinction coefficients. Thus, through Eqns. 2.49 – 2.51, as well as those within [Pulliainen et al. \[1999\]](#) and [Lemmettyinen et al. \[2010\]](#), the n-HUT model is capable of simulating the microwave brightness temperature of a multiple layer snowpack.

#### 2.5.4.3 Extinction Coefficients

Both the single layer and n-HUT model calculates the amount of extinction (the sum of absorption and scattering) taking place within the snowpack through an empirically derived extinction coefficient,  $k_e$ . While the absorption coefficient,  $k_a$ , is calculated using the complex dielectric constant of dry snow (Eqn. 2.42), the scattering coefficient,  $k_s$ , is calculated simply by calculating the difference between  $k_e$  and  $k_a$  ( $k_s = k_e - k_a$ ).

The n-HUT model was initially designed using the extinction coefficient model produced by [Hallikainen et al. \[1987\]](#). In this study, the extinction properties of several dry snow samples were examined, with a traditional grain size range of 0.2 – 1.6 mm. Snow samples were acquired from the natural snowpack, and placed between transmitting and receiving antennas, and microwave radiation, in the range 18.7 – 90 GHz, were transmitted through the snow sample. Transmission losses and surface scattering were calculated from measurements of received microwave radiation, and from these, extinction properties of the snow samples were calculated.

Empirical expressions of extinction coefficients at the different frequencies measured were developed to relate  $k_e$  to the observed traditional grain size  $d$  (in millimetres), such that:

$$k_e = \left\{ \begin{array}{l} 1.5 + 7.4d^{2.3}, \text{ at } 18.7 \text{ GHz} \\ 30d^{2.1}, \text{ at } 35.0 \text{ GHz} \\ 180d^{2.0}, \text{ at } 60 \text{ GHz} \end{array} \right\} \quad (2.52)$$

where  $k_e$  is calculated in decibels per metre ( $dBm^{-1}$ ). These three expressions can be combined into a single equation, which is used within the n-HUT model;

$$k_e = 0.0018f^{2.8}d^{2.0} \quad (2.53)$$

where f is frequency in the range 18 – 60 GHz, and d is the traditional grain size in the range 0.2 – 1.6 mm.

A second extinction coefficient model was designed by [Roy et al. \[2004\]](#). In this study, the original extinction coefficient model was used with the n-HUT model, to test the usability in a Canadian Boreal forest environment. The n-HUT model brightness temperature simulations were compared to brightness temperatures observed using airborne radiometers. [Roy et al. \[2004\]](#) found that at 18.7 GHz (in the vertical polarization), the brightness temperatures were overestimated (bias = +10.7 K) by the snow emission model. At 37.0 GHz (in the vertical polarization), the simulated brightness temperatures were vastly underestimated (bias = -26.9 K). [Roy et al. \[2004\]](#) hypothesised that this large error was an indication that the microwave propagation through the snowpack may be erroneously modelled. Ratios of radiation wavelength and observed grain size (in this study, grain size ranges were in the order of 1 – 4 mm) were assessed, and it was thought that, for 18.7 and 37.0 GHz (wavelengths = 16.7 and 8.1 mm respectively), Rayleigh scattering would be dominant. Classic radiative transfer theory states that, for a spherical particle whose size is smaller than the wavelength in question, Rayleigh scattering is proportional to  $f^4d^6$ . Using experimental data [Roy et al. \[2004\]](#) found a new semi empirical extinction coefficient model, in the form:

$$k_e = \gamma(f^4d^6)^\delta \quad (2.54)$$

where  $\gamma$  and  $\delta$  are constants determined empirically, using a least squares fitting investigation. These empirical constants were found to be  $\gamma = 2 \pm 1$  and  $\delta = 0.20 \pm 0.04$ , across the traditional grain size range of 1.3 – 4.0 mm.

A third extinction coefficient model was designed by [Beser \[2011\]](#). In this study, the new extinction coefficient model was designed to work with maritime snow, which is characterised by deeper, denser snowpack, with larger grainsizes ([Sturm et al. \[1995\]](#) and [Kontu and Pullainen \[2010\]](#)) than the taiga snowpacks found in Finland and Canada; the snowpacks used to design the extinction coefficients of [Hallikainen et al. \[1987\]](#) and [Roy et al. \[2004\]](#). This extinction coefficient was found to be in the form:

$$k_e = 0.08f^{1.75}d^{1.8} \quad (2.55)$$

All three extinction coefficients listed above use traditional grain size (as defined by Fierz et al. [2009]), as one of the two input parameters (the other being frequency). This is due to the amount of scattering occurring with radiation of a certain wavelength being proportional to the size of the scatterer in question (Hallikainen et al. [1987], Roy et al. [2004], Kontu and Pullainen [2010], Chang et al. [1987], Rees [2006], and Grody [2008]). However, the observations of traditional grain size tend to be subjective in nature (as will be discussed in Section 3.5.3), as the observations take place upon a measurement grid and are visually estimated (Leppänen et al. [2016b]). This leads to subjective observations, as the observations are dependent upon observer expertise.

## 2.6 Chapter Summary

Throughout this chapter, the theory behind remote sensing of snow through passive microwave observations have been reviewed and discussed. Different techniques of remote sensing of snow using visible, infrared, and microwave wavelengths were also discussed, with the advantages and disadvantages of each wavelength region being detailed. Ultimately, for snow mass and SWE observations, microwave wavelengths are superior to both visible and infrared wavelengths. This is due to the increased penetration depth possible with the larger wavelength at microwave frequencies. The ability for passive microwave observation to occur regardless of the amount of cloud cover or surface illumination allows for observations of snow mass to occur during the polar night; something that is not possible with visible and infrared wavelengths.

Radiative transfer theory, describing how a beam of monochromatic radiation passes through a dielectric medium and how such a medium would affect the intensity of the radiation beam, was applied to microwave radiation propagating through a snowpack. The change in beam intensity can be accredited to two source terms (emission of radiation by the snowpack, and radiation that has been scattering into the beam by the snowpack) and two loss terms (absorption of radiation by the snowpack, and radiation that has been scattered away from the beam by the snowpack), which produce an increase and decrease in observed microwave intensity respectively; measured in terms of brightness temperature. The amount of absorption and scattering (collectively known as the extinction) that occurs within the snowpack can be calculated through the absorption, scattering, and extinction coefficients. Having knowledge of the values of these radiometric coefficients allow for the calculation and simulation of the propagation of microwave radiation through the snowpack.

The Helsinki University of Technology (HUT) snow emission model uses this radiative transfer theory approach to simulate the microwave brightness temperature of a multiple layer snowpack, with each layer having distinguished values of physical temperature, density, SWE, and traditional grain size, as well as assumptions regarding the layers salinity and moisture content. The n-HUT model is semi-empirical in nature, as the radiative transfer model is coupled with empirical models for calculating absorption, scattering, and extinction coefficients.

Numerous different extinction coefficients have been calculated for use with the n-HUT model. The original, calculated by [Hallikainen et al. \[1987\]](#), coefficient was initially developed for calculating the extinction coefficient in terms of both frequency and traditional grain size in the range 0.4 – 1.6 mm. A second coefficient, developed by [Roy et al. \[2004\]](#), was calculated for a different grain size range of 1.4 – 4.0 mm; the [Roy et al. \[2004\]](#) extinction coefficient model was developed specifically for larger grains than the original [Hallikainen et al. \[1987\]](#) model. A third extinction coefficient, developed by [Beser \[2011\]](#), was calculated for use with maritime snow commonly found in Turkey. All three extinction models, however, use subjective observations of traditional grain size as an input parameter, which results in the calculated values of extinction being dependent on the observer expertise.

The work shown across Chapters 3 – 6 details the effort to produce a new extinction coefficient model, using modern observation techniques, for use within the n-HUT model. The new extinction coefficient model differs from previous extinction coefficient models used by the n-HUT model, as it does not use traditional grain size as an input parameter. Instead, it uses SSA-derived optical diameter values observed from modern and objective techniques as an input parameter.

## **Chapter 3:**

# **Arctic Snow Microstructure Experiment (ASMEEx)**

### **3.1 Chapter Introduction**

Together, Chapters 3 and 4 detail the research needed to complete the first thesis aim, stated in Section 1.3:

#### **Aim 1**

Creation of the Arctic Snow Microstructure Experiment (ASMEEx) dataset; comprising of radiometric and snow characteristic properties of snow slabs, extracted from the natural snowpack.

#### **Goals**

1. Complete the Arctic Snow Microstructure Experiment (ASMEEx); in which radiometric and snow characteristic properties of snow slabs upon two bases of differing reflectivities.
2. Analyse the ASMEEx dataset; comparing the different instrumentation techniques used, as well as their affect upon the simulated brightness temperatures, using the single layer HUT snow emission model.

The work presented in this chapter focuses upon the completion of the first goal stated above; the ASMEEx field campaign, and differing techniques of observation. The second goal of Aim 1, the comparison of observed brightness temperatures with simulated

values using the original n-HUT model, can be found in Chapter 4.

The location of the ASMEEx campaign (Sodankylä, Finland) is discussed in Section 3.2. The key piece of instrumentation for the ASMEEx campaign, the Sodankylä Radiometer (SodRad) platform, is detailed in Section 3.3, focussing on the technical details (Section 3.3.1) and calibration techniques used during the campaign (Section 3.3.2). The radiometric portion of ASMEEx (brightness temperature observations of extracted snow slabs upon two bases with differing reflective qualities) is detailed in Section 3.4. The methodology behind the radiometric portion, along with changes made to the absorbing blackbody base observations during the ASMEEx campaign are also listed. The experimental procedure of the ASMEEx campaign is detailed in Section 3.5. The experimental proceedings includes the method behind the homogeneous slab sample location, extraction from the natural snowpack, and transportation to the SodRad platform (Section 3.5.1), as well as the order of radiometric (Section 3.5.2) and snow characteristic (Section 3.5.3) observations. The two major unavoidable problems that occurred during the ASMEEx campaign are shown in Section 3.6, along with the effects of the problems occurred.

The ASMEEx campaign was the focus of work of [Maslanka et al. \[2016\]](#), which first introduced the ASMEEx campaign, detailed some of the parameters observed, and performed the initial single layer HUT model simulations. Chapter 3 will go into the ASMEEx campaign in more detail than [Maslanka et al. \[2016\]](#), with Chapter 4 providing a more in-depth analysis of the results.

## 3.2 FMI Arctic Research Centre

ASMEEx took place over two winter periods (January – April, 2014 and 2015) at the Finnish Meteorological Institute Arctic Research Centre (FMI ARC). Situated in Sodankylä, Finland ( $67^{\circ} 22' N$ ,  $26^{\circ} 39' E$ ), the FMI ARC is a typical representation of the Eurasian taiga belt, which is characterised by sparse conifer-dominated forests, open forested bogs and small lakes. The FMI ARC completes weekly snowpit observations of the natural snowpack (using techniques shown in Section 3.5.3), meaning that specialist equipment is not needed to be brought on site. FMI ARC also houses a set of passive microwave radiometers (as discussed in Section 3.3), allowing for radiometric measurements of the natural snowpack to take place. This combination of passive microwave radiometers and snowpit instrumentation, as well as the experience of on-site scientists and technicians, allow for such campaigns as ASMEEx and the Sodankylä Radiometer Experiment (SoRaX, Chapter 6) to take place. The surrounding landscape around the

FMI ARC is generally relatively flat; with the FMI ARC being located 179m above sea level. The site used for experimental activities (the Intensive Observation Area, or IOA) is located in a forest clearing, as shown in Figure 3.1.



**Figure 3.1:** Intensive Observation Area (IOA). The SodRad platform (red) and the area designated for slab extraction (blue) are shown. Photo taken from the IOA Camera.

### 3.3 SodRad Radiometers

#### 3.3.1 Technical Details

The radiometric portion of this field campaign involved analysing measurements made by the ground based radiometer system SodRad (Sodankylä Radiometer). The SodRad system is a commercially available radiometer system (RPG-8CH-DP) built by Radiometer Physics GmbH (Meckenheim, Germany). The SodRad system consists of six dual-polarized radiometers upon two separate platforms; SodRad1 (Figure 3.2a) houses radiometers measuring at 10.7, 18.7, 21.0, and 36.5 GHz, whilst SodRad2 (Figure 3.2b) houses radiometers measuring at 89.0 and 150.0 GHz. Both SodRad1 and SodRad2 are housed upon a 5m high metal scaffolding tower (Figure 3.2c). Five of the six frequencies (18.7, 21.0, 36.5, 89.0, and 150.0 GHz) were used throughout the ASMEx campaign.

Prior to the ASMEx campaign, preliminary tests of observation techniques showed that observations at 10.7 GHz proved to put the extracted snow slabs (detailed in Section 3.5.1) at an increased risk of cracking during the experimental set-up and radiometric observations, due to the position of the parabola reflector (shown in Figure 3.2a). Therefore, to reduce the risk of cracking the slab, observations at 10.7 GHz were omitted from this study.

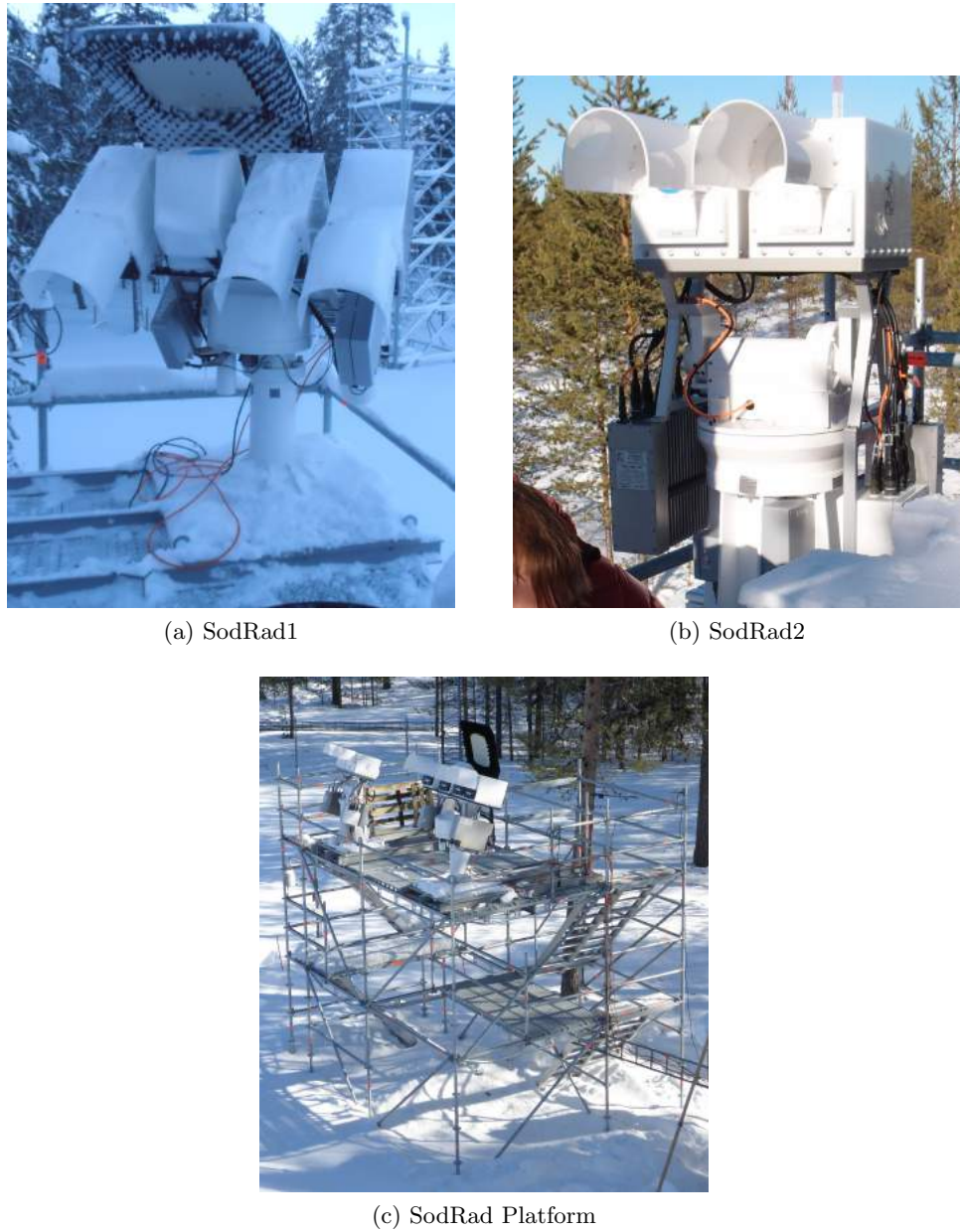


**Figure 3.2:** SodRad1 and SodRad2 platforms.

The SodRad system is capable of measuring brightness temperature of its surroundings by rotating on its elevation and azimuth axes. This allows the SodRad system to observe the brightness temperature of the snowpack, the sky, as well as objects placed in front of the radiometers. Figure 3.3a shows the orientation of the elevation angles for the

SodRad system. For data analysis purposes of the natural snowpack during ASMEEx, the SodRad radiometer platforms are oriented such that the snowpack is at  $180^\circ$ . The SodRad radiometers make use of an inbuilt corrugated feed horn antenna, which keeps the half power beam width (HPBW) at  $6^\circ$ . Other characteristics of the five SodRad radiometers ([Rose and Czekala \[2011\]](#)) used in this research are listed in Table 3.1.

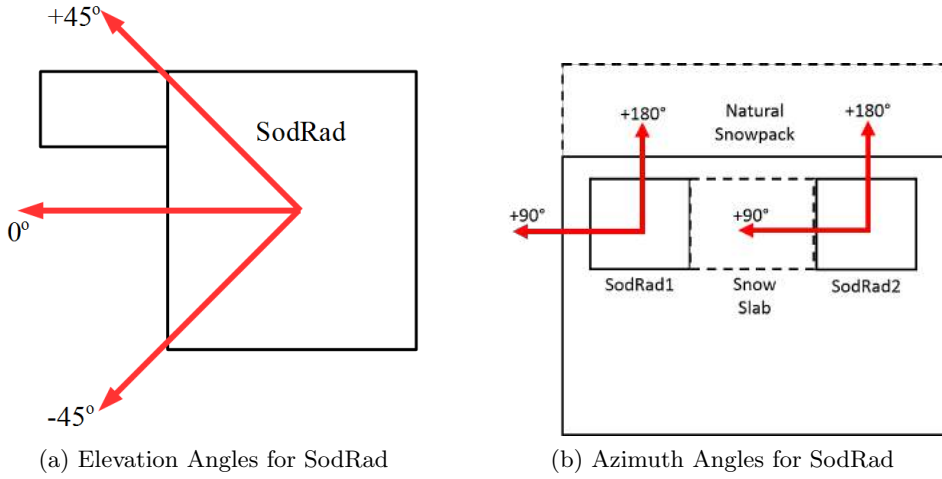


**Figure 3.3:** Elevation and Azimuth Angles for the SodRad system.

**Table 3.1:** Characteristics of the SodRad radiometer system

	SodRad				
Frequency (GHz)	18.7	21.0	36.5	89.0	150.0
Bandwidth (MHz)				400	
Receiver Noise Temperature (K)				<900	
Integration time (s)		Defined by the user, $\geq 1\text{s}$			
Sensitivity (K)				<0.05	
HPBW ( $^\circ$ )				6 $^\circ$	

### 3.3.2 SodRad Calibration

The major calibration of the SodRad system was completed using a two-point calibration method. A calibration barrel, made out of absorptive blackbody material at the ambient air temperature, was used to cover the entire aperture of the antennas, creating a warm calibration target. A cold calibration target was created using a second calibration barrel, cooled to 77 K via liquid nitrogen. By using the known physical temperatures (and therefore brightness temperature) of the two targets, as well as the outputted voltage from the SodRad system, a calibration curve was created. This two point method was completed prior to the first use of each SodRad system at the beginning of each ASMEEx winter season. At the beginning of each slab measurement, the warm calibration target was used to check that the SodRad calibration had not drifted since the last slab

measurements. After the SodRad radiometers have been calibrated with the warm calibration target, a zenith sky measurement was taken, in order to assess if any changes in downwelling sky radiation occurred during the slab observation period.

### 3.4 ASMEx Principle Set-up

An observable parameter belonging to radiometric properties is the brightness temperature  $T_B$  (see Section 2.1), at a measured fixed frequency, polarization, and angle of incidence  $\theta$ . The radiometric measurements of the ASMEx campaign were to observe the  $T_B$  of numerous homogeneous slab samples upon two bases of differing reflective properties; a blackbody base (reflectivity,  $r_0 = 0$ ) and a reflective metal base (reflectivity,  $r_0 = 1$ ). By observing the snow upon two bases of differing reflectivities, the individual slab flux coefficients could be calculated (based on the model originally described by [Wiesmann et al. \[1998\]](#)), as shown by the research in Chapter 5. Knowledge of the absorption and scattering coefficients of the individual slabs would allow for the derivation of a new extinction coefficient; the aim of the thesis.

The different radiometric observations made as part of ASMEx are shown in Figure 3.4. They are:

1. Snow slab on a reflective metal base at both horizontal and vertical polarizations ( $T_{BM}$ ),
2. Snow slab on a blackbody base, at both horizontal and vertical polarizations ( $T_{BA}$ ),
3. Empty Blackbody base, at both horizontal and vertical polarizations ( $T_{BE}$ ),
4. Clear sky brightness temperature ( $T_{SKY}$ ) at opposite incidence angles.

These radiometric observations took place on top of the SodRad tower (circled red in Figure 3.1, with additional experimental apparatus being needed, as shown in Figure 3.5. The basic premise of the ASMEx set-up was to place snow slabs on top of a setup with interchangeable bases; one of which being an assumed perfect reflector, and the other being an assumed reasonable blackbody absorber. As the reflective metal base was assumed to be perfect, any emission emanating from below will be reflected away. The reflecting metal base was placed above the absorbing base during the reflective base measurements, as this would allow for a stable platform for the snow slabs to rest. As the reflective metal base was to be placed on top of the absorbing material, the absorbing

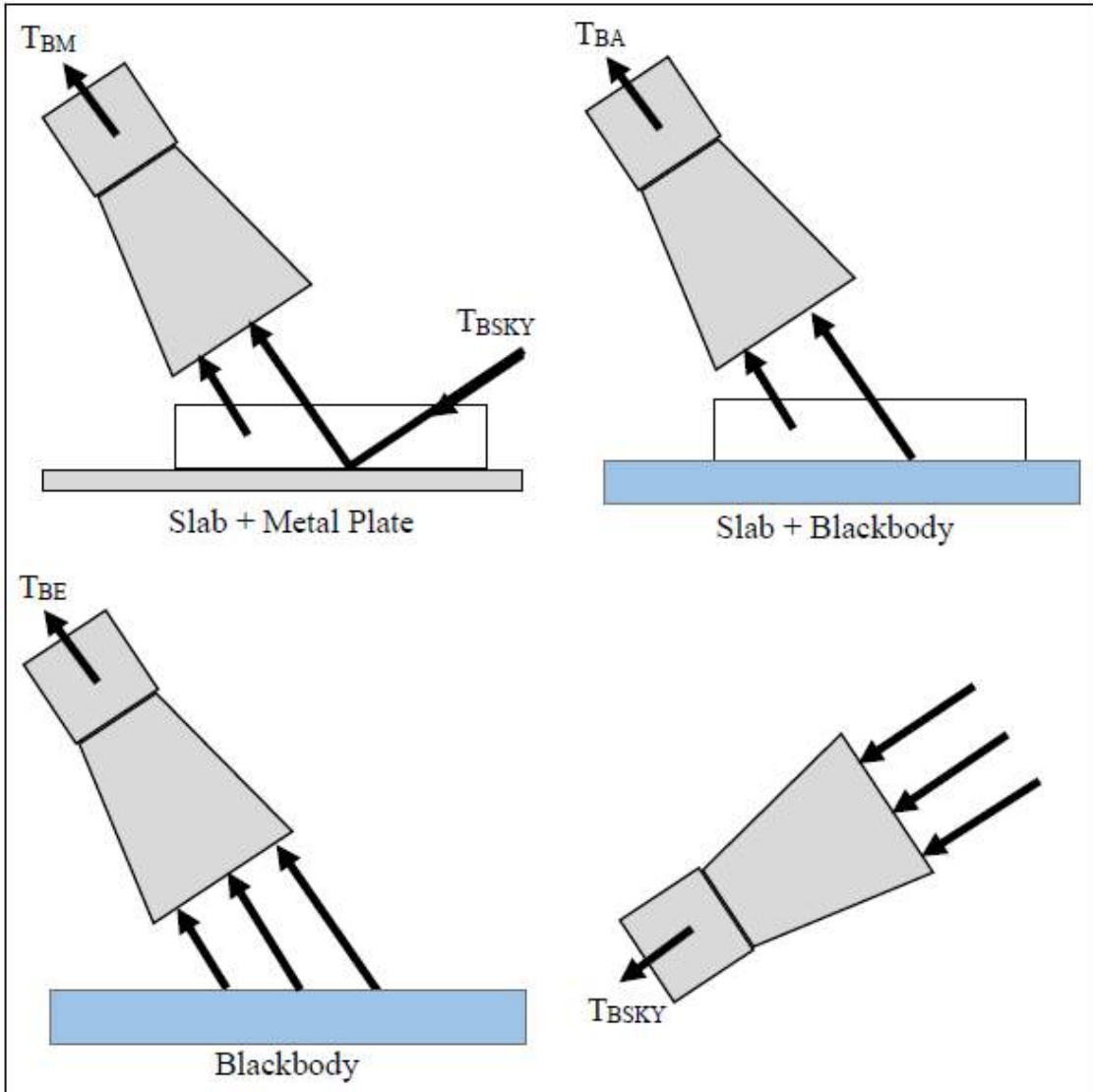


**Figure 3.4:** Top: Measurement of the brightness temperatures  $T_{BM}$  of snow on a metal plate (left) and  $T_{BA}$  of snow on a blackbody base (right). Bottom: Measurement of the brightness temperatures  $T_{BE}$  of the bare blackbody (left) and  $T_{SKY}$  of the sky.

material was designed to be part of the set up, and the reflecting metal plate would be removable, thus allowing for the snow slab to remain in place when the metal plate is removed.

The trolley set-up consisted of layers of absorbing material and Styrofoam sheeting, on top of a workmans trolley, that enabled the height to be adjusted. The height adjustment allowed the slab sample to be raised and lowered to the correct height, keeping the radiometer footprint equal in size. This is important, as SodRad1 and SodRad2 platforms are on positioner units with different heights. On top of the trolley sat a combination of Styrofoam sheets (5cm thick), and absorbing material. Styrofoam was chosen, due to its lightweight and structural properties, as well as being transparent at microwave frequen-

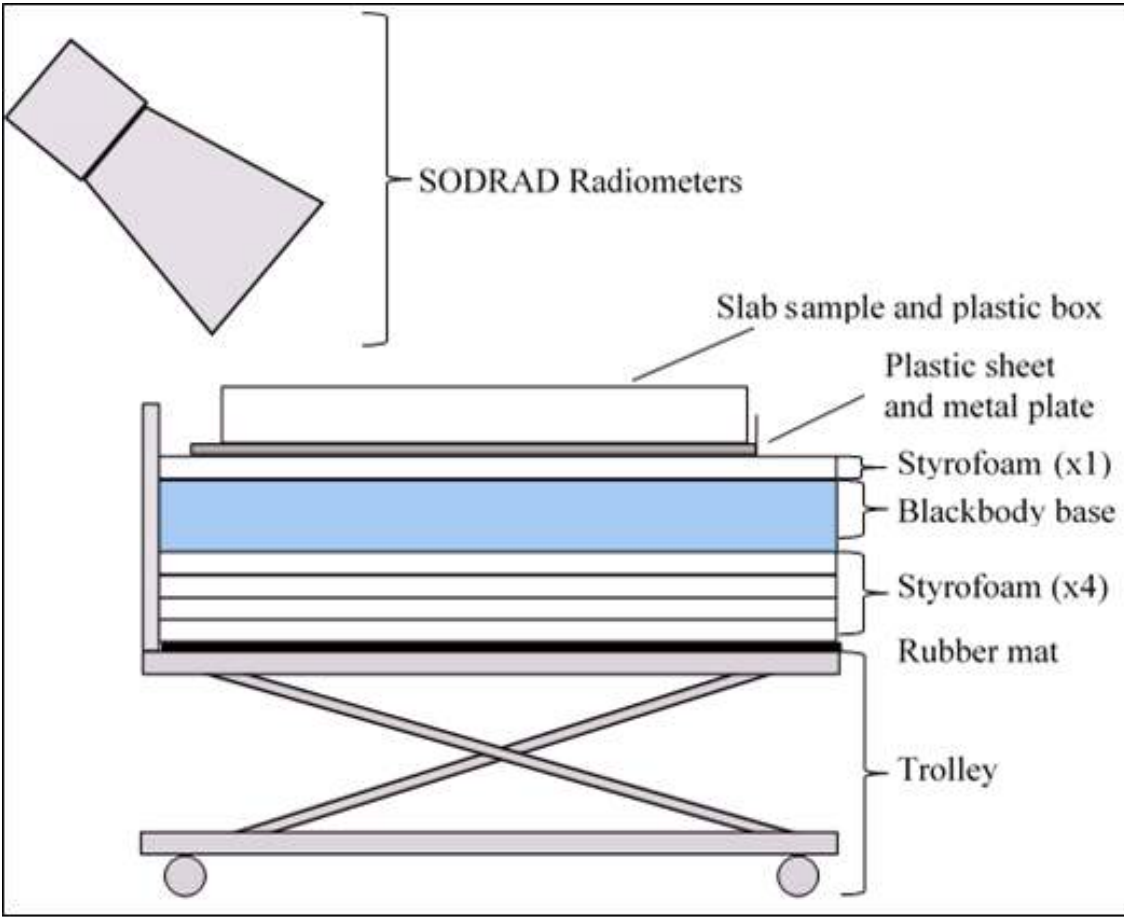


**Figure 3.5:** Sketch of the experimental apparatus which holds the slab sample.

cies. Between the bottom layer of Styrofoam and the trolley was a rubber mat, which helps secure the Styrofoam and absorbing material in place. Due to availability issues with the absorbing material, different designs of the set-up were trialled and used during the 2014 and 2015 ASMex periods, referred to as ASMex 2014 and 2015, although the overall function of the design did not change.

The first design (Figure 3.6a) was comprised of four pieces of absorbing material, sandwiched between numerous pieces of Styrofoam sheeting. The second design (Figure 3.6b) saw the inclusion of two newer, thinner pieces of absorbing material. This was to limit the effects of any reflections due to the flat surface of the absorbing material in design 1. Due to availability issues with the four large pieces of absorbing material, the third design (Figure 3.6c) featured the thin pieces of absorbing material (from design 2) as well as a thinner piece of absorbing material to replace the four large pieces. The rest of the missing height was made up of increased numbers of Styrofoam sheeting (not shown).

ASMex 2015 saw another change to the design; one which proved to be more perma-

ment. Figure 3.6d shows the design for ASMEx 2015. A Styrofoam box was built around two large pieces of absorbing material. The box was attached to two wooden planks, allowing the box to be securely attached to the trolley, vastly improving the stability. Above the box, sat a piece of Styrofoam, with snow slab positions marked. This piece of Styrofoam was used throughout ASMEx 2014, and allows the snow slab to be positioned in the same place every measurement. Unfortunately, the Styrofoam positioner had to be replaced during ASMEx 2015, due to its destruction during a storm. A replacement Styrofoam positioner was fashioned out of two smaller pieces of Styrofoam, taped together, thus resulting in a fifth design (not shown).

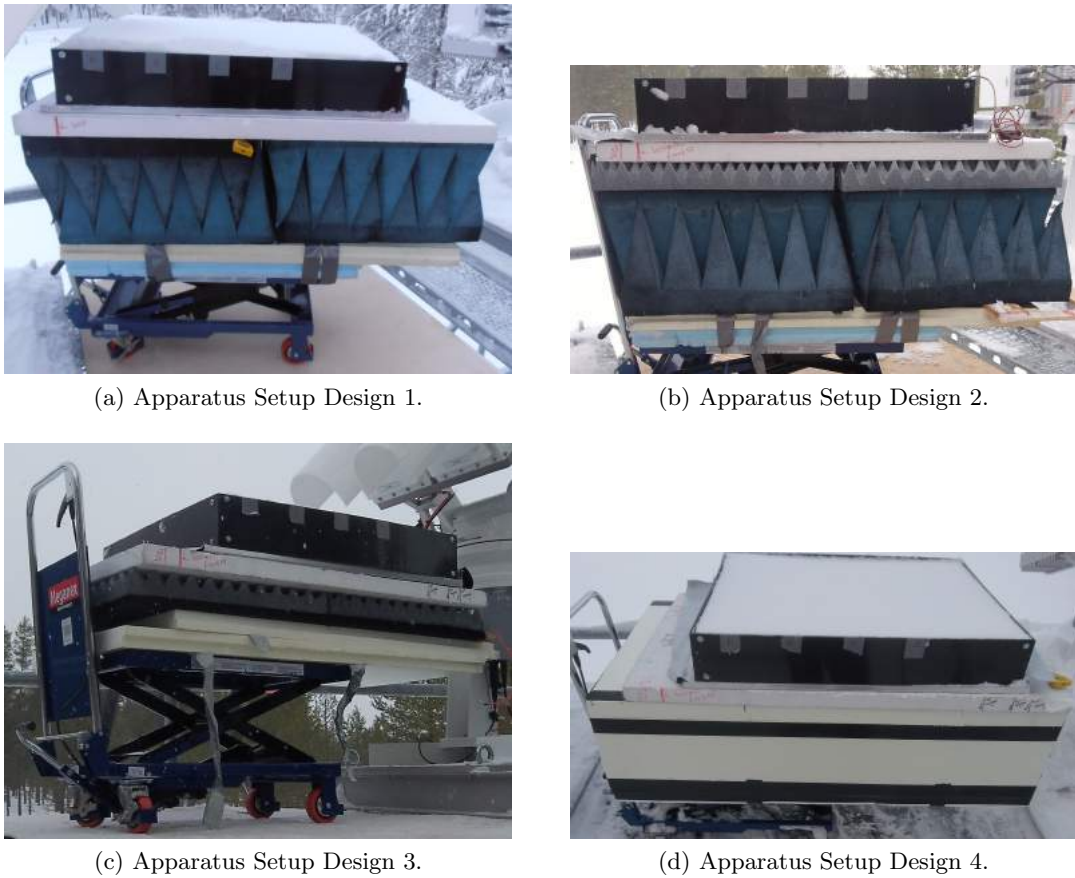


**Figure 3.6:** Various different experimental apparatus design.

The  $T_B$  of the empty set-up was measured at each frequency, at an incidence angle of  $50^\circ$ , after each slab measurement period. Using Eqn. 2.3, and physical temperature measurements of the absorbing material, the emissivity at each frequency can be calculated. Problems with the radiometer system during one measurement period (14/02/14 - slab A04) lead to the set-up not being measured, and the emissivity not being calculated. The fifth design of ASMEx setup (used for the last 5 slab measurements) created issues with regards to the radiometric measurements. The tape used to build the replacement

Styrofoam positioner contained metal strips. The metal strips caused a reflection of down-welling sky radiation, thus resulting in a reduction of observed brightness temperature (no reduction at 18.7 GHz, -1K at 21.0 GHz, -2K at 36.5 GHz, -8K at 89.0 GHz, and -15K at 150.0 GHz). This reduction was only observed at horizontal polarization. These reductions were corrected post-measurement, by calibrating the observed brightness temperatures of the affected slab measurements. Table 3.2 shows the corrected calculated emissivities of the empty slab.

**Table 3.2:** Emissivities measured of the different setup designs. Crosses denotes frequencies not available. Note that Slab A04, dated 14/02/14, is not present due to unreadable datafiles.

Slab	Freq Design	18.7 GHz		21.0 GHz		36.5 GHz		89.0 GHz		150.0 GHz	
		H	V	H	V	H	V	H	V	H	V
A01	1	0.97	0.99	0.97	0.99	0.99	0.99	x	x	x	x
A02	1	x	x	0.98	0.99	0.99	0.99	x	x	x	x
A03	2	1.00	1.00	1.00	1.00	x	x	x	x	x	x
A05	3	1.00	1.00	1.00	1.00	x	x	0.99	1.00	0.98	0.99
A06	3	0.97	0.99	0.98	0.98	x	x	0.98	0.99	0.95	0.97
A07	3	0.98	0.99	0.98	0.98	x	x	0.98	0.99	0.98	0.97
B01	4	0.99	0.99	0.99	0.99	0.98	0.99	x	x	x	x
B02	4	0.97	0.98	0.98	0.99	0.98	0.99	x	x	x	x
B03	5	0.97	1.00	1.00	1.00	0.99	1.00	x	x	x	x
B04	5	0.99	1.00	1.00	1.00	1.00	1.00	x	x	x	x
B05	5	0.98	0.99	1.00	0.99	0.98	0.99	1.00	1.00	0.99	0.99
B06	5	0.99	0.99	0.99	1.00	0.98	1.00	0.98	1.00	0.97	0.99
B07	5	0.99	1.00	1.00	1.00	0.99	1.00	0.99	0.99	0.98	0.99

It can be seen that, regardless of the set-up design, the emissivity of the set-up did not drop below 0.95. This suggests that the assumption of the absorbing material (as well as all set-up designs) being a reasonable blackbody absorber is valid, and can be used throughout ASMEx.

## 3.5 Experimental Proceedings

### 3.5.1 Slab Extraction and Transportation

The extraction, preparation, and transportation of the snow samples was one of the most difficult parts of the whole measurement campaign. The snow samples were required to be as undisturbed and natural as possible, whilst being removed from the natural snowpack, in order to preserve the natural microstructure within the snow slab. Preserving the microstructure would simplify the parameterization and simulation of the snow slabs with the n-HUT model. The snow sample, with dimensions of 80 x 60 x 15 cm<sup>3</sup>,

was extracted from the natural snow, allowing for the radiometric footprint to be large enough that numerous physical measurements can be completed within it, yet be small enough to be able to extract from the natural snowpack, and examine upon controlled conditions.



(a) Toothpick profile of the snow wall. (b) Layers highlighted via the toothpick profile.

**Figure 3.7:** Toothpick profile.

Initially, the stratigraphy of previously undisturbed snow was analysed, in order to locate a homogeneous layer of sufficient thickness. This was completed using traditional snow pit methods. A snow pit was dug, and the snow pit wall was smoothed. Next, a toothpick was lightly dragged down the trench wall. A sudden change in hardness (usually denoting a melt-freeze crust), density or grain size can be felt via a change in resistance with the toothpick. The toothpick was pushed into the snow at the level where

the change was felt, denoting the layer boundary, and the process was repeated until all layers were highlighted. Producing a toothpick profile allowed for homogeneous layers to be identified, and their thickness could be analysed for slab sample extraction. Figures 3.7a and 3.7b show one such toothpick profile. The stratigraphic layers were easy to identify from the toothpick profile, making selection of a homogeneous layer for sampling quick and efficient.

No physical measurement of the snow within the layer was completed at this time, as the physical observations of snow parameters were undertaken after the radiometric observations. This allows the radiometric measurements to be completed before the destructive techniques of snow characterization.

Once the toothpick profiles were complete, and a layer of homogeneous snow of sufficient thickness was found, the snow sample extraction could begin. Disturbed snow (hereby referred to as ruined snow) was used to construct a level platform, up to the base of the homogeneous layer. A metal plate ( $100 \times 65 \times 0.5 \text{ cm}^3$ ) was placed upon this ruined snow platform, and levelled using a spirit level. This metal plate had been left to cool to the ambient air temperature, thus keeping its temperature close to the snow temperature, and reducing the potential for the snow to melt-then-freeze to the plate. The metal plate was covered with a thin plastic sheet; in order to further reduce the potential for friction between the snow and the metal plate. The plastic sheeting also prevented the snow from freezing to the metal plate. Once the metal plate and plastic sheeting was level, it was pushed into the snowpack with a constant and sustained force, until it was completely embedded within the snowpack.

Next, a plastic frame (also virtually transparent to microwaves,  $t>0.999$ ) was placed onto the snowpack surface, directly above the embedded metal frame. This plastic frame has also been allowed to cool to the ambient air temperature, in order to reduce the snow melt-freeze problem. The plastic frame was orientated in such a way that predetermined markers were always in the same position, hence allowing for each individual slab sample to have the same shape and orientation. Cuts were made to the surface snow, using metal plates and saws, parallel to the sides of the plastic frame. This allowed the frame to sink to the level of the embedded metal frame. All cuts were made outside to the plastic frame, in order to limit the disruption to the potential sample. Figure 3.8 shows an example of the plastic frame being lowered into the snow. Note the metal plate and plastic sheeting below the plastic box. This denotes the bottom of the slab sample required.

Once the plastic frame was level with the metal plate, the entire sampling apparatus



**Figure 3.8:** Plastic frame being slide into the snowpack, prior to slab extraction. Metal plate and plastic sheet at the bottom of the picture.

(with enclosed snow slab) was pulled out of the snowpack onto the ruined snow platform. Any snow above the slab sample and plastic frame was carefully removed, using an additional metal plate cooled to the ambient temperature. This allowed the slab sample to be of uniform height. After a successful extraction, the slab sample was transported from the natural snowpack within the IOA, to the SodRad platform. Here, it was carefully carried to the top of the SodRad platform, and placed onto the top layer of Styrofoam of the experimental apparatus.

### 3.5.2 Radiometric Measurements

After the initial calibration of the SodRad radiometers, a set of zenith measurements were taken, to measure the downwelling brightness temperature from the sky. This zenith measurement was repeated throughout the measurement period; to try and capture any changes in the downwelling brightness temperatures, resulting from changing weather conditions.

Once the snow slab had been successfully transported to the SodRad platform (after the SodRad calibrations) the radiometric measurements began. During the radiometric measurements, the physical temperature of the snow, the air, and the absorbing base were measured. Thermometers placed inside the absorbing material allow the physical temperature to be measured. The reflective metal base, which had been left to reach the ambient temperature, was assumed to be equal to that of the air temperature. These

temperature measurements of the different bases were required for the modelling of the ground layer with the n-HUT model.

A thermometer was placed in the furthest corner of the snow slab (position  $T_R$  in Figure 3.9) to assess the thermal state of the sample. This snow temperature, along with measurements of air temperature, were used to monitor the state of the snow slab, and to avoid a wet slab measurement. The snow thermometer was removed during the radiometric measurements, to avoid influencing the  $T_B$  measurements. It was also placed outside of the footprint, so that that the disturbed snow did not affect the  $T_B$  measurement.

The position of the slab sample upon the experimental apparatus was kept as similar as possible, to remove any unwanted contributions to the measurements. This was done by locating the optimum position of the snow slab before the experiments took place, and marking the positions onto the top Styrofoam layer. This allowed for all slab samples to be swiftly aligned with the markings, for ease of use.

Table 3.3 shows the order of measurements for the reflective metal base measurements. It also shows the azimuth and elevation angle needed for each frequency. The differences in azimuth angle between the SodRad1 frequencies and SodRad2 frequencies are discussed in Section 3.3. 21.0 GHz had a different azimuth angle than the other two SodRad1 frequencies, due to the position of the safety rail at the top of the SodRad tower. It was for this reason that the 21.0 GHz frequency measurement is completed first, in order to limit the number of times the snow slab and trolley were moved.

The height of the base of snow slab (relative to the floor of the Radiometer Tower) for the SodRad1 measurements were different to those of SodRad2. This was due to the SodRad2 platform being shorter than that of SodRad1. Thus, to keep the radiometric footprint the same size for both platforms, the snow slab was lower in height for SodRad2.

During the SodRad1 measurements, the SodRad2 platform was rotated to an azimuth angle of  $90^\circ$ , and an elevation angle of  $-60^\circ$  (towards the ground). This was to minimize the influence of emissions from SodRad2, as there was potential for the emissions to influence the reflective plate observations. Testing prior to ASMEx found that SodRad2 was not seen by SodRad1 when in this position. Likewise, during the SodRad2 measurements, SodRad1 was rotated to an azimuth angle of  $270^\circ$ , and an elevation angle of  $-60^\circ$ .

After the reflecting plate observations were completed, observations of the down-welling sky radiation were made, to record the radiation being reflected by the reflecting bases (Figure 3.4). These equivalent-angle sky observations, or “equi-sky” observations, were made at an elevation angle of  $+40^\circ$  (towards the sky) and an azimuth angle of  $270^\circ$

**Table 3.3:** Reflective base measurement order, with associated set-up properties.

Metal Base				
Frequency (GHz)	Azimuth Angle	Elevation Angle (SodRad)	Incidence Angle	Snow Slab Height (cm)
21.0	290°	-40°	50 °	87
36.5	270°	-40°	50 °	87
18.7	270°	-40°	50 °	87
89.0	80°	-40°	50 °	74
150.0	80°	-40°	50°	74

and 80° for SodRad1 and SodRad2 respectively. A zenith measurement was made after the equi-sky measurements, to assess if the downwelling sky radiation had changed since the start of the radiometric observations.

After the equi-sky and zenith measurements, the reflective metal base was removed from the set-up, thus changing the base reflectivity to that of the absorbing base. The metal plate was slid out from under the snow slab quickly and smoothly, to try and avoid cracking the snow slab or introducing any other forms of structural damage. Once the metal plate had been removed from the set-up, the snow slab and trolley were re-aligned with the SodRad platform, ready for the absorber base measurements.

The order of frequencies was reversed for the absorber base measurements, to try and limit the number of times that the snow slab is moved. The order of frequencies for the absorber base measurements, like the reflective base measurements, are shown in Table 3.4.

**Table 3.4:** Absorber base measurement order, with associated set-up properties.

Absorbing Base				
Frequency (GHz)	Azimuth Angle	Elevation Angle (SodRad)	Incidence Angle	Snow Slab Height (cm)
150.0	80°	-40°	50°	74
89.0	80°	-40°	50°	74
18.7	270°	-40°	50°	87
36.5	270°	-40°	50°	87
21.0	290°	-40°	50°	87

After the absorber base measurements had been completed, a second set of equi-sky measurement were taken, to measure the downwelling emission of microwave radiation from the sky. A further zenith measurements was made, as a further check on the calibration. After the zenith measurement, SodRad1 and SodRad2 were rotated to give the most amount of room on the SodRad tower for the physical measurements to take place (azimuth angles of 180°, and an elevation angle of 0°).

After the physical measurements had been completed, the snow slab was removed from the set-up. The brightness temperature of the empty set up was then measured at each frequency, to calculate the emissivity of the set-up design (Table 3.2). After the empty set-up measurements, the SodRad radiometers were re-calibrated with the warm calibration target, to assess any  $T_B$  drift that may have occurred.

### 3.5.3 Snow Characteristic Measurements

In order for the snow characteristics and properties to be quantified, different observation techniques were used on the ASMEEx snow slabs. Some of the traditional snowpit techniques used, such as box cutter density measurements (discussed later in this section) are destructive sampling techniques; where part of the snow slab is destroyed after the observation is made. Therefore, the ordering of such observations were crucial, to allow for the maximum number of observations (both numerically and different types) to be made. The most destructive measurements ( $\mu$ CT sample collection) were completed last, in order to keep the snow slab intact for as long as possible. The order of slab characteristic measurements undertaken during ASMEEx are listed below, with the location of the measurements shown in Figure 3.9.

1. SnowMicroPen Profiles A1 – D3
2. Temperature Profiles
3. Box Cutter Density Profiles
4. SSA IceCube Observations
5. Traditional Grain size Macro-photographs
6.  $\mu$ CT Sample Extraction

Firstly, the internal stratigraphy of the snow slabs were recorded and examined using the SnowMicroPenetrometer (SMP, [Schneebeli and Johnson \[1998\]](#) and [Schneebeli et al. \[1999\]](#)). The SMP is a high resolution penetrometer, which is capable of measuring the penetrative resistance of snow quickly and with relative ease. By measuring the penetrative resistance of the snowpack, via forcing the penetrometer tip through the snowpack at a constant speed, stratigraphic data can be observed in a matter of minutes. The SMP measures the penetrative force in a range from 0.01 N (for soft snow) to 75 N (for very hard snow or ice) to a maximum depth of 1.7 m ([Proksch et al. \[2016\]](#)), with a

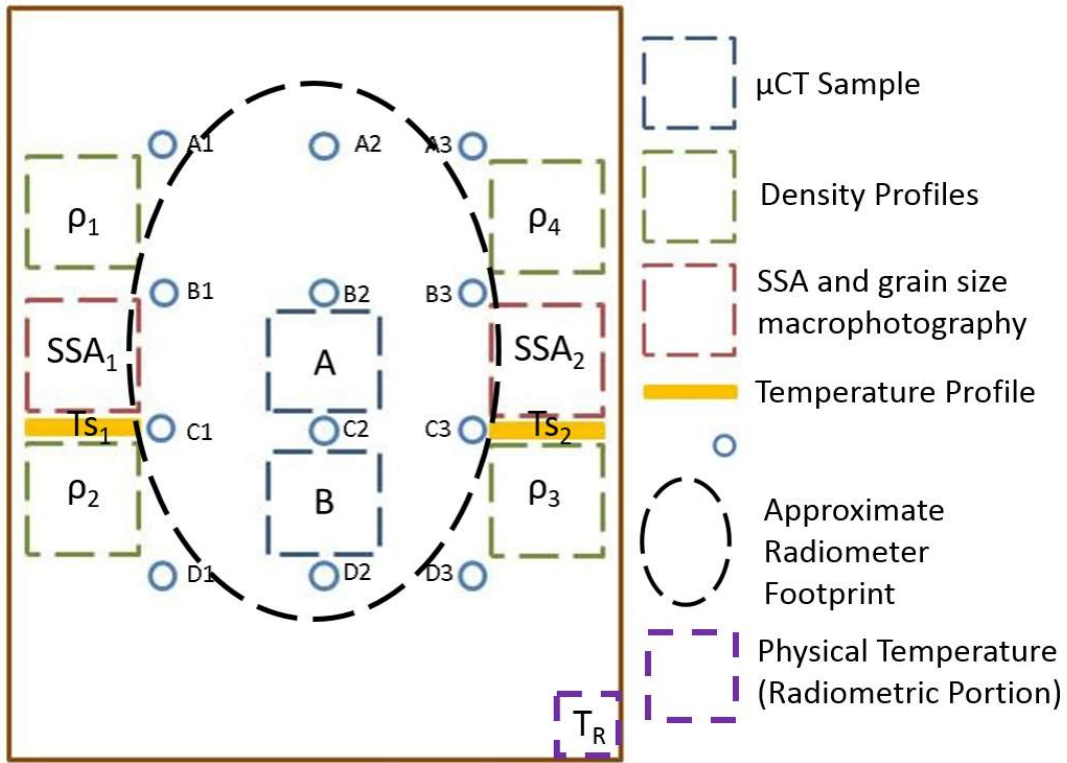


**Figure 3.9:** Approximate locations of the in situ measurements, including Temperature Profiles ( $T_{S1}$  and  $T_{S2}$ ), Density ( $\rho_1$ ,  $\rho_2$ ,  $\rho_3$ , and  $\rho_4$ ), Specific Surface Area ( $SSA_1$  and  $SSA_2$ ), SMP profiles (A1 - D3), and  $\mu$ CT samples (A and B). The approximate positioning of the radiometer footprint is also shown, along with the Temperature probe used during the radiometric measurements ( $T_R$ ).

constant speed of  $20 \text{ mm s}^{-1}$ . At this speed, snow slabs with depths of 15 cm (and 14 cm of air measured above the snow slab) can be recorded in under 20 seconds. The SMP instrument is composed of numerous components; the penetrometer, the motor unit, and the wired controller (Figure 3.10). The penetrometer sensor is a piezoelectric force sensor, fixed to the end of the displacement rod.

Löwe and van Herwijnen [2012] developed a stochastic approach with the penetrative resistance signal, which processed the penetrative resistance signal into three structural parameters; structural element size  $L$ , rupture force  $f$ , and deflection of rupture  $\delta$  (as shown in the schematic in Figure 3.11).

Proksch et al. [2015] used this stochastic model, through bilinear regression models, to develop a set of empirical relations between these structural parameters and snow characteristics parameters, such as density, and exponential correlation length.

Proksch et al. [2015] states that:

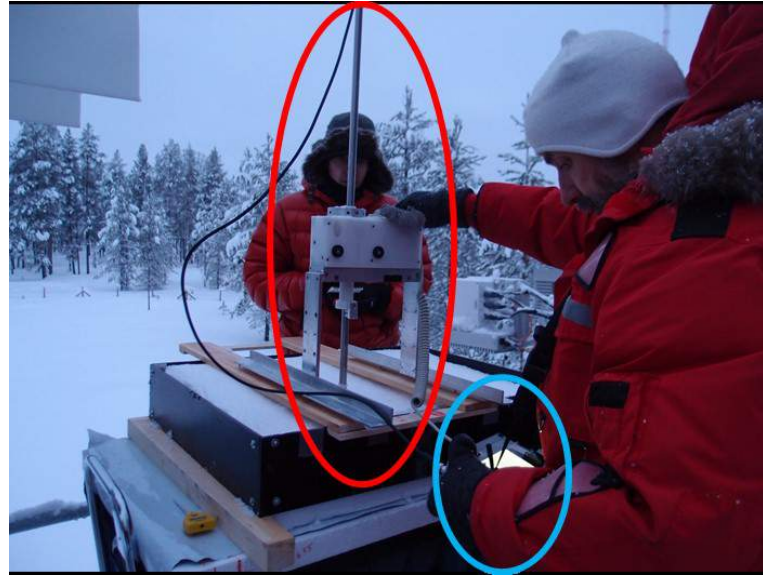


**Figure 3.10:** SMP measurements being taken from a slab sample. The penetrometer and motor unit (red) and the wired controller (blue) are highlighted.

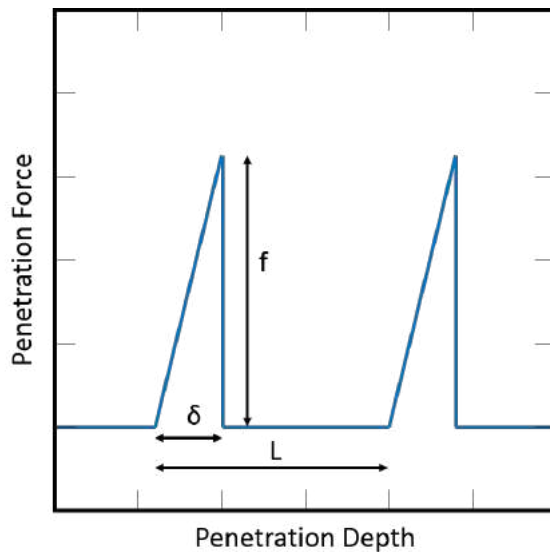


**Figure 3.11:** Schematic representation of the three basic structural parameters in SMP signals: structural element size L, rupture force f, and deflection at rupture  $\delta$ . Taken from Löwe and van Herwijnen [2012].

$$\rho_{SMP} = a_1 + a_2 \ln\left(\frac{\hat{F}}{F_0}\right) + a_3 \ln\left(\frac{\hat{F}}{F_0}\right)L + a_4 L \quad (3.1)$$

$$p_{ex,SMP} = b_1 + b_2 L + b_3 \ln\left(\frac{\hat{F}}{F_0}\right) \quad (3.2)$$

where  $\hat{F}$  is the median penetration force (N),  $F_0$  is 1 N, L is the structural element size (mm, both shown in Figure 3.11,  $a_1 = 420.747 \pm 8.31 \text{ kg m}^{-3}$ ,  $a_2 = 102.47 \pm 4.24 \text{ kg m}^{-3}$ ,  $a_3 = -121.15 \pm 10.65 \text{ mm}^{-1} \text{ kg m}^{-3}$ ,  $a_4 = -169.96 \pm 18.70 \text{ mm}^{-1} \text{ kg m}^{-3}$ ,  $b_1 = 0.0715 \pm$

0.0058 mm,  $b_2 = 0.299 \pm 0.011$  mm, and  $b_3 = 0.0149 \pm 0.0018$  mm. Unfortunately, due to calibration issues with the SMP (discussed later in Section 4.2.3), the regression models produced by Proksch et al. [2015] were not valid for the ASMEx observations. Individual ASMEx regression models were produced, as discussed in Section 4.2.3 (Martin Proksch, personnal correspondance).

To get an accurate representation of the stratigraphy and snow characteristics within the radiometer footprint, multiple profiles using the SMP were taken from each extracted snow slab. A total of 12 profiles were taken across each ASMEx snow slab, as shown in Figure 3.9. These profiles were labelled A1 – D3 for reference purposes. As the slab sample was to be kept as intact as possible, a wooden platform was built (seen in Figure 3.10), which rested upon the plastic box. The plastic box itself was lifted 5 cm in height, to allow the wooden platform to slide without disturbing the snow slab (also seen in Figure 3.10). The wooden platform and plastic box had predetermined markers, to allow for the SMP profiles to occur in the same location for all ASMEx snow slabs. The SMP profile file numbers were recorded to allow for analysis of the SMP profiles post-observation.

The 12 SMP profiles each left a hole with a radius of 1 cm; where the penetrometer had been inserted into the snow slab. These holes provided the perfect opportunity to measure the depth of the snow across the radiometer footprint. These 12 depth measurements (taking place in profile locations A1 – D3, as shown in Figure 3.9) were observed using a 2 m folding measuring stick (as shown in Figure 3.12), with 1 mm graduations. However, the slab depth was measured to the nearest 5 mm. Measurements of snow depth can also be taken from the SMP profiles, by looking for the snow-air and snow-ground interfaces in the penetrative resistance signals. The manual height measurements act as a second set of height measurements. Typical errors of 5 mm are present, as each SMP observation leaves a small pile of displaced snow (seen around the profile hole in Figure 3.12).

Upon completion of the SMP and manual slab height observations, the plastic box surrounding the snow slab was removed, exposing the external sides of the slab. This allows access for the remaining snow parameter measurements (with the exception of the  $\mu$ CT subsamples, which were removed from the centre of the slab (Figure 3.9).

Once the wooden platform and plastic box were removed from the snow slab, temperature profiles were completed in two locations in the snow slab (Figure 3.9). These measurements the first of the traditional snowpit observations completed at the slab edges, as they were the least destructive in nature. Physical temperatures were taken at 5 cm



**Figure 3.12:** Depth of slab B06 being recorded at profile A3.

intervals from the snow slab surface, using a TH310 Thermometer (Figure 3.13). The probe thermometer was pushed into the snow slab, and left to equalise to produce a stable physical temperature observation.

The density measurements using a box cutter (shown in Figure 3.14) were completed in four locations ( $\rho_1 - \rho_4$  in Figure 3.9), to allow for the variability of the slab to be measured. The density cutter was a self-made rectangular frame, open at both ended, as described by [Leppänen et al. \[2016b\]](#) and shown in Figure 3.14a. The dimensions of the box cutter were 5 cm x 10 cm x 10 cm (height x width x depth), giving a volume of 500 cm<sup>3</sup>. Density profiles were measured, starting with the closest 0.5 cm to the surface of



**Figure 3.13:** Physical temperature measurement at position Ts<sub>1</sub> for slab B06.

the slab. The sampler was inserted into the slab wall horizontally, and perpendicular to the vertical slab surface (as shown in Figure 3.14b). The sampler was then sealed, with a secondary rectangular frame that seals both ends (Figure 3.14a). The snow sampler was then extracted, and any snow on the outside of the sampler was removed. The snow within the sampler was then placed into a plastic bag, or small bucket, with known weight (Figure 3.14c). Finally, the snow inside the bucket/plastic bag was weighed, and the mass recorded. The density could then be calculated by dividing the mass of the snow within the bucket/plastic bag by its volume. The whole profile was observed in this manner. For snowpit observations, successive density measurements are not taken directly on top of one another, but in an alternate pattern. However, due to the limited amount of snow present in the snow slab, density profiles were completed with successive observations.

There are numerous potential error sources involved with the manual density measurements. If any snow remains on the outside of the sampler, then the recorded mass of the measured snow would be overestimated. By removing the snow from the external edges of the sampler, the potential for this source of error to occur was reduced. Another potential source of error occurs if snow were to get stuck to the inside of the sampler, such that the measured snow volume was smaller than  $500 \text{ cm}^3$ , thus giving an underestimation of density. If the snow sampled was made up of loose grains, such as depth hoar grains, then it is difficult to observe the density, as difficulties arise in trying to fill the box cutter, often leading to an underestimation. An additional error comes in the form of non-homogeneous layers within the density box cutter. If there are layers within the slab that have thicknesses of less than 5 cm (the height resolution of the box cutter), then the density measurement taken will act as a 5 cm bulk average measurement. A final potential error source comes in the form of potential compaction of the snow beneath the density sample.

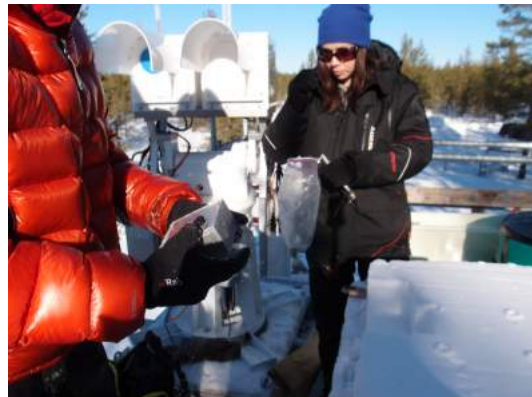
After completion of the four density profile measurements, the snow microstructure parameters were observed. This was completed through two separate techniques, using the IceCube instrument (Figure 3.15a) to observe values of Specific Surface Area (SSA), and through macro-photographs to observe values of traditional grain size (as described by [Fierz et al. \[2009\]](#)), in two locations across the ASMEx slab (Figure 3.9). The IceCube instrument (A2 Photonic Sensors, Grenoble, France, Figure 3.15a, [Zuanon \[2013\]](#)) is based on the DUFISSS (the DUal Frequency Integrating Sphere for Snow SSA measurements), laid out by [Gallet et al. \[2009\]](#), but only using a 1310 nm wavelength laser for reflective measurements. The schematic of the IceCube instrumentation is shown in Figure 3.15b.



(a) 500ml box cutter.



(b) Using the density cutter at position  $\rho_4$  for slab B04.



(c) Transporting the extracted density measurement for weighing.

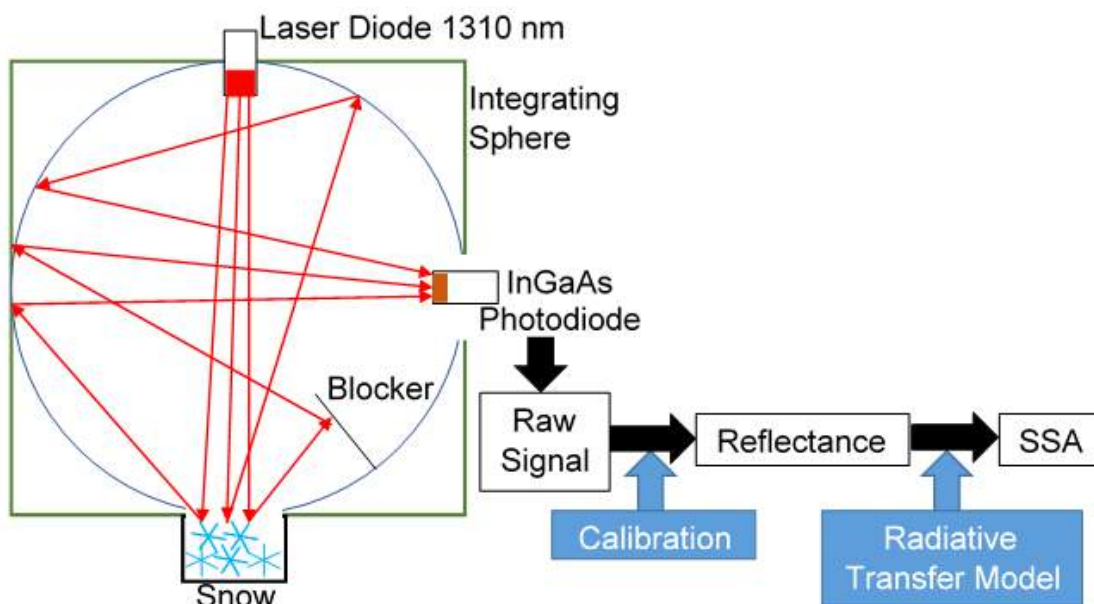
**Figure 3.14:** Density observations.

Before measurements of snow SSA began, the IceCube instrument was calibrated using six calibration standards of known reflectances. These calibration values are used in the software for post-processing, and to set the calibration curve.

Snow samples are extracted from the ASMEx slab with a vertical resolution of 3 cm, and placed under the monochromatic wavelength. The SSA snow sample is smoothed after extraction from the ASMEx slab, and broken grains are removed to reduce the amount of additional scattering. Light reflected by the snow is collected via a photodiode (as shown in Figure 3.15b), and is converted into a voltage. This voltage is recorded



(a) IceCube Instrumentation



(b) IceCube Schematic, adapted from [Zuanon \[2013\]](#).

**Figure 3.15:** IceCube Observations.

and converted to SSA using the post-processing software. The IceCube instrumentation determines SSA to a range of 10% in the range  $5 - 130 \text{ m}^2\text{kg}^{-1}$ . Measurement errors that occur with the IceCube instrument originate from the sample preparation (from packing the snow into the sample holder, and from the smoothing of the sample).

From each measurement of SSA, a calculation of the correlation length, and exponential correlation length can be made. Theory and description of correlation lengths of snow are discussed in Section 2.3.1. According to [Mätzler \[2002\]](#), the relation between correlation length, exponential correlation length, and SSA are as follows:

$$p_c = \frac{4(1-v)}{SSA} \quad (3.3)$$

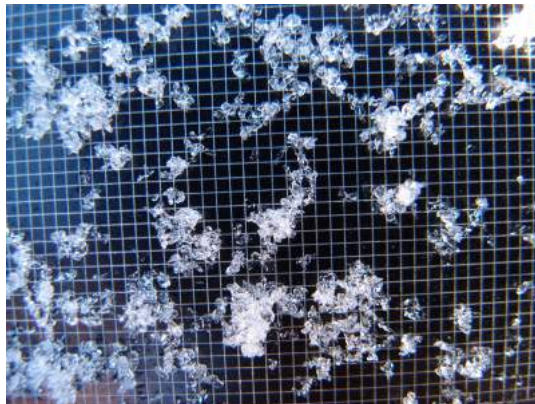
$$p_{ex} = 0.75 p_c = \frac{3(1-v)}{SSA} \quad (3.4)$$

where  $p_c$  = Correlation length,  $p_{ex}$  = Exponential correlation length, and  $v$  = is the volume fraction of ice ( $v = \frac{\rho_{snow}}{\rho_{ice}}$ ).

Upon the completion of each SSA measurement with the IceCube instrument, the snow within the IceCube sampler is assessed in terms of its traditional grain size. [Fierz et al. \[2009\]](#) defines the traditional grain size as “the average size of its grains”, and the grain size as “its greatest extension measured in millimetres”. Snow grains were taken from the SSA sampler and were placed upon a millimetre reference grid (manufactured by Sears, [Leppänen et al. \[2016b\]](#), Figure 3.16a), and macro-photographs were taken using a digital camera (Olympus XZ-1, resolution 3648 x 2736 pixels, with focal length of 28 mm), and a self-made stand (Figure 3.16b). Three photographs were taken from each SSA sample, to ensure a successful measurement of grain size. Post-processed grain sizes are visually estimated from the macro-photographs, to the nearest 0.25 mm. The main source of error are related to choosing the snow grains, and from the visual estimation of the snow grains. This may come from observer-related bias, or from clusters being formed during removal from the SSA sample.

With the completion of the snow characteristic observations, the micro-computer tomography ( $\mu$ CT) subsamples were extracted from the ASMEx slab, for  $\mu$ CT analysis.  $\mu$ CT is a powerful method of snow microstructure analysis, as it is able to record details of parameters, such as density, correlation length, exponential correlation length, and SSA, at a very fine resolution (10  $\mu$ m), by taking x-ray scans of the snow ([Schneebeli and Sokratov \[2004\]](#)). One of the main restrictions of taking  $\mu$ CT measurements tend to be co-located close to the  $\mu$ CT apparatus, due to the fragility of the snowpack, as well as the threat of changes to microstructure during long storage or transport ([Heggli et al. \[2009\]](#)). Samples taken from a remote location not co-located to the  $\mu$ CT scanners must be cast, otherwise the characteristics and properties of the snow samples would not be preserved.

The  $\mu$ CT subsamples container (17 cm x 5 cm x 5 cm, height x width x depth) were firmly pushed through the surface at positions  $\mu$ CT-A and  $\mu$ CT-B in Figure 3.9, fully encapsulating two snow profiles for  $\mu$ CT analysis. The two  $\mu$ CT subsamples were cut out of the ASMEx slab sample, carefully turned upside down (for storage) and placed into a deep freeze at -80°C, to hinder metamorphism. By placing the  $\mu$ CT subsamples into a deep freeze, the samples were able to be cast after the ASMEx campaign.



(a) Macro photography of snow grains on a millimetre grid.



(b) Camera unit for the macro photography.

**Figure 3.16:** Macro-photography of grain sizes for grain size observation.

The  $\mu$ CT subsamples were cast with Diethyl-Phthalate (DEP,  $C_{12}H_{14}O_4$ , [Schneebeli et al. \[2008\]](#)); a colourless, odourless compound. The  $\mu$ CT subsamples were removed from the deep freeze and were prepared to be cast. This consisted of cutting a small triangle out from one corner of the subsample. This allows a funnel (Figure 3.17a) to be inserted into the sample, without blocking the funnel or largely altering the microstructure properties. A metal frame is placed between the sample and the funnel, to hold the funnel in place (Figure 3.17a).

DEP (cooled to  $-7^\circ\text{C}$ ) was poured into the funnel (Figure 3.17b), allowing for the sample to be filled slowly from the bottom up. By pouring the DEP into the funnel slowly, the air pockets within the snow samples were filled. If filled correctly, the snow sample would be converted from an air-and-ice medium to an ice-and-DEP medium. Upon filling the air bubbles with DEP, the funnel and metal frame was removed. A small piece of solid DEP was placed into the liquid DEP within the ice-DEP medium. This acts as a local freezing nucleus, allowing the DEP to freeze when placed back into the deep freezer. Once fully frozen, all cast samples were transported to WSL SLF, in Davos, Switzerland;

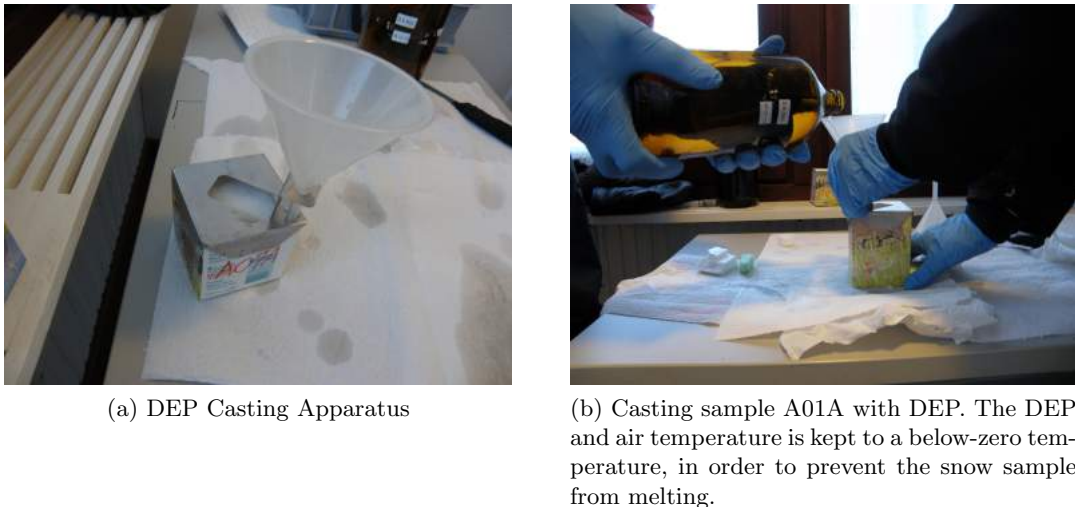
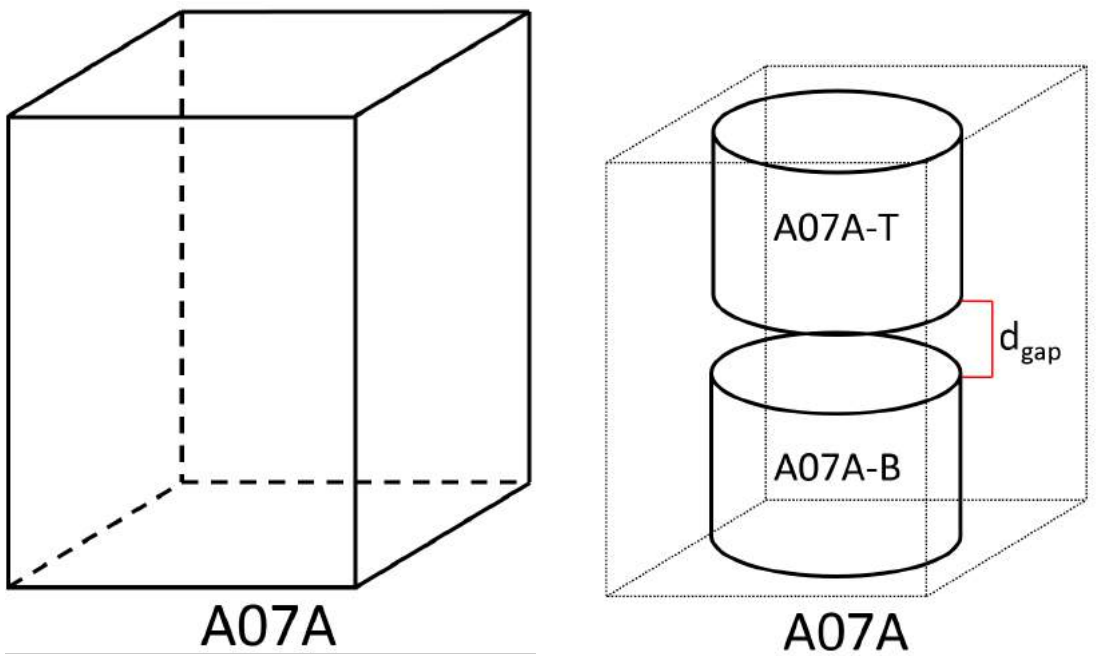


**Figure 3.17:** Casting samples for transportation to WSL Institute for Snow and Avalanche Research SLF, in Davos, Switzerland, for  $\mu$ CT analysis.

where the  $\mu$ CT apparatus is housed.

Upon arrival at WSL SLF, the ASMEx  $\mu$ CT samples were prepared for analysis. For the  $\mu$ CT analysis, the samples had to be processed, as shown in Figure 3.18. The casted profiles (Figure 3.18a) were cut into two halves (Figure 3.18b), designated XXXX-T and XXXX-B (for  $\mu$ CT subsample XXXX) respectively, to fit into the  $\mu$ CT sample holder. Profiles of slab B05 were not cut into two halves, as the slab thickness was approximately 5 cm (Section 4.16). Cutting the  $\mu$ CT samples in half implies that a small gap ( $d_{gap}$ ) is present, due to the physical presence of the saw. The analysis of  $\mu$ CT samples assumes that there is no gap; that  $d_{gap} = 0$ . The subsamples were scanned using a  $\mu$ CT80 bench top CT system (Scanco Medical AG, Brüttisellen, Switzerland), in a cold room at -20°C.

The x-ray attenuation coefficients of DEP and ice are very similar. This makes ice and DEP difficult to distinguish during the  $\mu$ CT analysis. However, DEP and air (and thus ice and air) have two very different x-ray attenuation coefficients, meaning that it is easy to differentiate between air and DEP/ice on the  $\mu$ CT scans. As the DEP had been set, and cannot be easily removed from the sample, the ice must be sublimated out of the samples. This leaves the DEP as a negative cast of the microstructure. In order to account for any air bubbles that were not filled by DEP, two scans are required; once before the sublimation of ice, and once after the sublimation of ice. The pre-sublimated scan will highlight the air bubbles within the sample, whilst the post-sublimated scans would highlight the air bubbles and the negative cast of the ice crystals. By comparing the two scans, the air bubbles can be removed from the scans, leaving just the ice microstructure information. The sublimation of ice is completed using a vacuum, capable of reducing the



(a)  $\mu$ CT subsample A07A schematic.

(b)  $\mu$ CT subsample A07A, split into two halves.

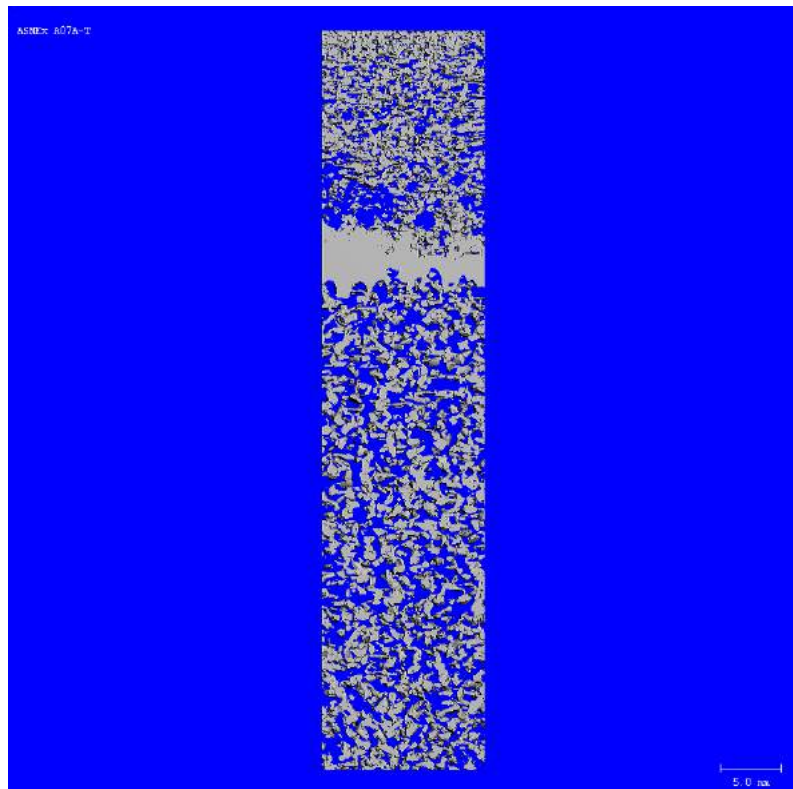
**Figure 3.18:** Schematic behind the cutting of the  $\mu$ CT subsamples.

pressure within the vacuum to 0.2 Pa, using a pump with a volume flow rate of  $5 \text{ m}^3\text{h}^{-1}$  (Heggli et al. [2009]).

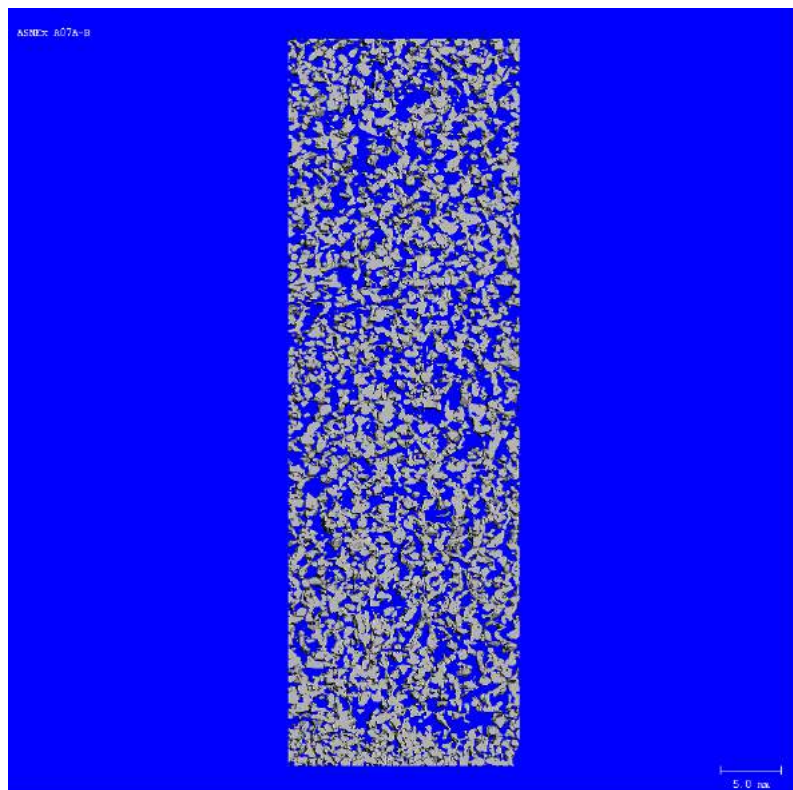
Upon completing scans both prior- and post-sublimation, any air pockets not filled with DEP during casting can be added to the porous nature of the snow subsamples. The imaging software supplied with the  $\mu$ CT instrument was then used to estimate the  $\mu$ CT scans, to produce observations of snow parameters and 3D images of the  $\mu$ CT samples. Figure 3.19 shows an example of 3D images of  $\mu$ CT sample A07A-T (Figure 3.19a) and A07A-B (Figure 3.19b). In Figure 3.19, a stratigraphic layer (an ice layer) can be seen, with a homogeneous layer of snow found beneath.

### 3.6 Problems faced during ASMEx

During the two campaign periods of ASMEx, two major problems hindered slab extraction and data collection; one being climatic in nature (as discussed in further in Section 3.6.1), and the other being due to equipment problems (as discussed in Section 3.6.2).



(a)  $\mu$ CT A07A-T



(b)  $\mu$ CT A07A-B

**Figure 3.19:**  $\mu$ CT imagery of  $\mu$ CT sample A07A. As described, the sample was split into two subsamples, A07A-T (a) being the top half of the subsample, and A07A-B (b) being the bottom half. Image courtesy of H. Löwe.

### 3.6.1 Climatic Problems

Across both campaign periods of ASMEx, the monthly average air temperature for February – April was warmer during 2014 and 2015 than the 1981 – 2010 climatic average. Table 3.5 shows the monthly average air temperature across the 2014 and 2015 ASMEx periods, as well as the 1981 – 2010 climatic average. The monthly temperature anomaly is shown in Figure 3.20. Each of the four months were ranked in order of air temperature from 1960 – 2016, with one being the warmest. The month’s ranks are also shown in Table 3.5. It can be seen that, whilst January had below average monthly temperatures for both 2014 and 2015, February – April all had above average temperatures. It can also be seen that February 2014 was the second warmest February (from between 1960 – 2016), and March 2015 was the warmest March across the same period.

**Table 3.5:** Average monthly air temperature during the ASMEx campaign periods, with the 1981-2010 average for comparison. Also shown are the monthly rank, when comparing the 1960 – 2016 period. Data: [en.ilmatieteenlaitos.fi/statistics-from-1961-onwards](http://en.ilmatieteenlaitos.fi/statistics-from-1961-onwards) (accessed 2017-02-02).

Month	1981-2010 Mean ( $^{\circ}\text{C}$ )	2014		2015	
		Mean ( $^{\circ}\text{C}$ )	Rank	Mean ( $^{\circ}\text{C}$ )	Rank
January	-13.5	-15.1	39	-14.1	33
February	-12.7	-4.0	2	-6.5	4
March	-7.5	-3.9	9	-2.3	1
April	-1.3	-0.2	15	0.9	8

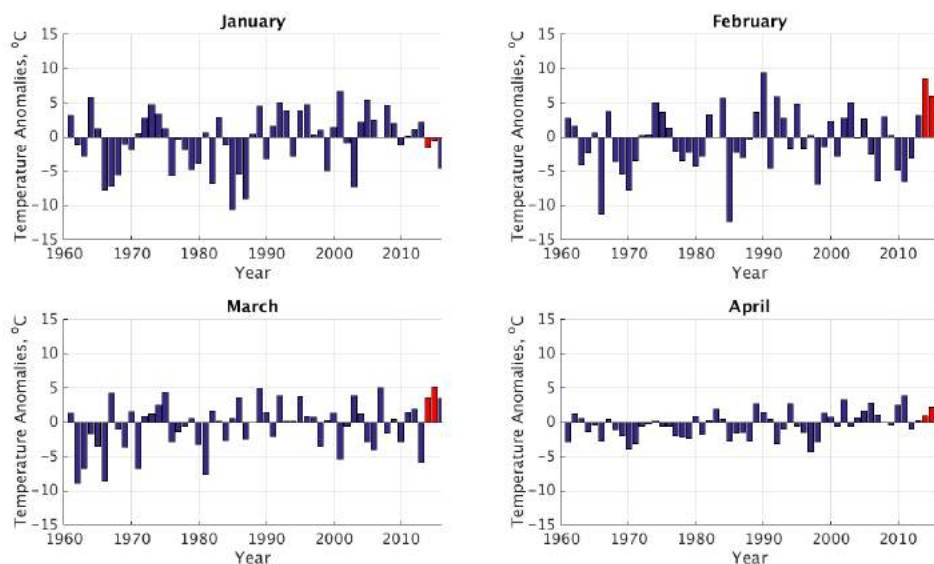


**Figure 3.20:** Monthly average temperature anomalies for January – April 1960 – 2016. 2014 and 2015 are highlighted with red bars. Data: [en.ilmatieteenlaitos.fi/statistics-from-1961-onwards](http://en.ilmatieteenlaitos.fi/statistics-from-1961-onwards) (accessed 2017-02-02).

The large positive temperature anomalies in February and March greatly increased

the chances of having positive temperatures occurring during the ASMEEx campaign. These positive temperature periods were avoided, to reduce the chance of having wet slab measurements. Figure 3.21 show the average daily temperatures recorded from the IOA automatic weather station between 1<sup>st</sup> January – 1<sup>st</sup> May 2014 and 2015 respectively. Plotted alongside the daily average air temperature is the minimum and maximum air temperatures recorded. From Figure 3.21, it is clear that, due to the seasonal change in air temperature, days with a maximum air temperature below 0°C were more frequent in the earlier months. ASMEEx slab measurements taking place on days where the maximum air temperature was forecast to be greater than 0°C took place earlier in the day, to best avoid the positive temperatures (as shown in Table 4.1). The exception to this (slab A03) resulted in a wet slab measurement.

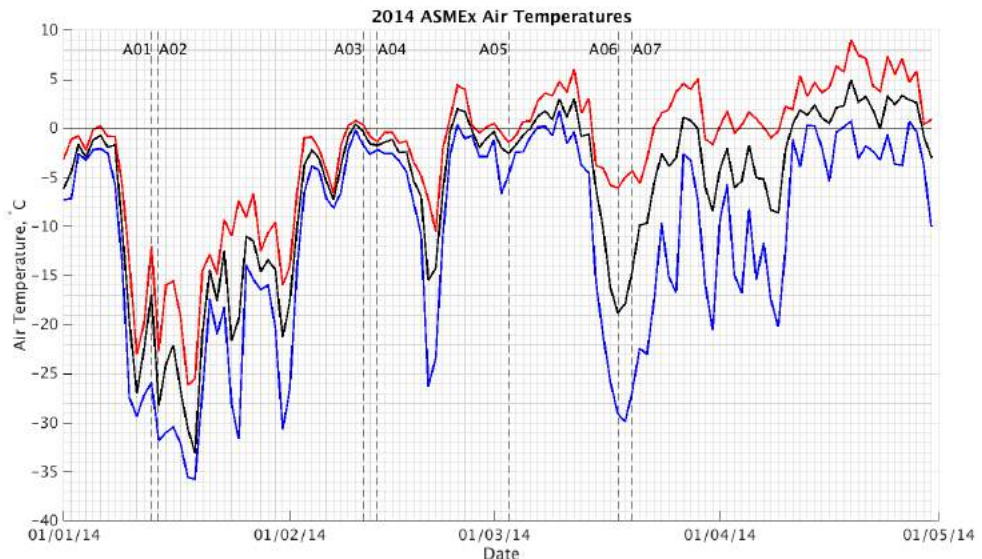
### 3.6.2 Equipment Problems

The second major problem experienced during ASMEEx occurred due to unavailable equipment. Unfortunately, not all ASMEEx slabs were observed with all available equipment, as shown in Table 3.6. Whilst all 14 slabs had observations at 21 GHz, not all slabs had observations with the other four radiometers. Figure 3.21a shows a very cold period (<-30°C) temperatures during January 2014, for a period of 2 weeks. During this time, the 18.7- and 36.5 GHz radiometers broke, due to the cold conditions. Whilst repairs to the 18.7 GHz radiometer were successful on site, the attempted repairs to the 36.5 GHz radiometer was unsuccessful. 36.5 GHz was removed from the SodRad tower at the beginning of February 2014, and returned to the manufacturers for repairs. It was returned to Sodankylä during the winter of 2014, and reattached to the SodRad tower at the end of January 2015.

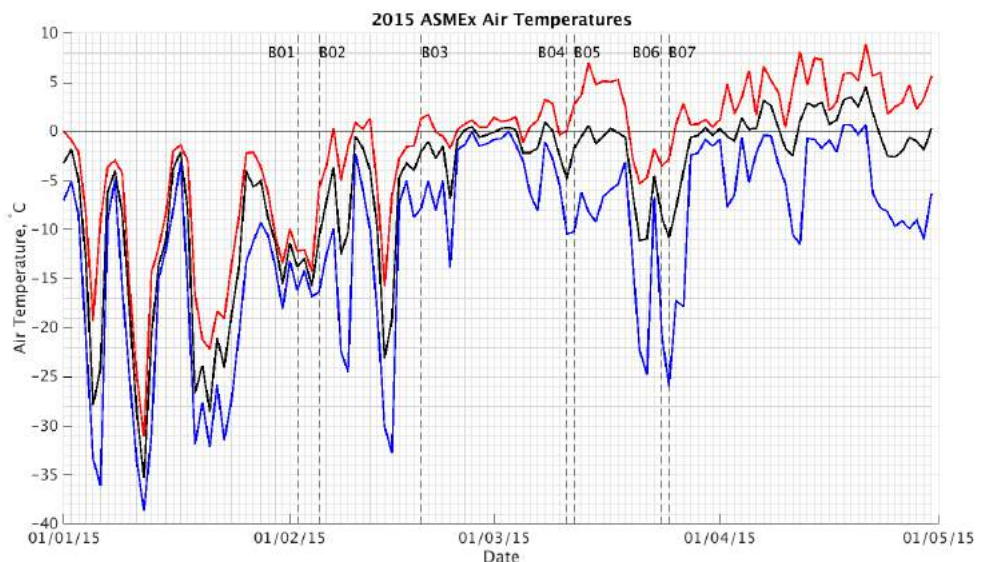
The unavailability of the SodRad2 platform for the first four slabs of each campaign year were due to non-responsive positioner units within the SodRad2 platform. The problem with the positioner did not allow the SodRad2 platform to change its elevation or azimuth angles, thus meaning that measurements could not take place until the problem was rectified.

During ASMEEx 2014, the IceCube instrument was not always available, as it was needed away from Sodankylä for a second fieldwork campaign. Unfortunately, this meant that the last 3 slabs in ASMEEx 2014 did not have SSA measurement profiles.

Table 3.6 shows the measurements completed on each slab sample. It shows the inconsistent number of frequencies throughout ASMEEx, and that (with the exception of



(a) January-May 2014



(b) January-May 2015

**Figure 3.21:** Maximum (red), minimum (blue), and mean (black) daily temperatures observed by the IOA Automatic Weather Station. Vertical dashed lines denote the dates of the ASMEx slab observations, denoted by the relevant slab reference.

**Table 3.6:** Frequencies measured during ASMEEx. Also lists slabs where the temperature ( $T_{snow}$ ), density ( $\rho_{snow}$ ), grain size (E), and specific surface area (SSA) measurements were taken. Also shows which slabs had SMP profiles and  $\mu$ CT ( $\mu$ CT) samples taken.

Slab	Radiometric Data (GHz)					Physical Data					
	18.7	21.0	36.5	89.0	150.0	$T_{phys}$	$\rho_{snow}$	E	SMP	SSA	$\mu$ CT
A01	X	X	X			X	X	X	X	X	X
A02		X	X			X	X	X	X	X	X
A03	X	X				X	X	X	X	X	X
A04	X	X				X	X	X	X	X	X
A05	X	X		X	X	X	X	X	X		X
A06	X	X		X	X	X	X	X	X		X
A07	X	X		X	X	X	X	X	X		X
B01	X	X	X			X	X	X	X	X	X
B02	X	X	X			X	X	X	X	X	X
B03	X	X	X			X	X	X	X	X	X
B04	X	X	X			X	X	X	X	X	X
B05	X	X	X	X	X	X	X	X	X	X	X
B06	X	X	X	X	X	X	X	X	X	X	X
B07	X	X	X	X	X	X	X	X	X	X	X

the IceCube measurements) the physical measurements were consistent.

### 3.7 Chapter Summary

Chapter 3 described the experimental proceedings behind the ASMEEx campaign; which aimed to produce a new dataset of radiometric, snow characteristic, and stratigraphic parameters of extracted snow slabs upon two bases with differing reflective properties. In doing so, the first of the two goals for the completion of the first thesis aim was met.

**Aim 1, Goal 1: Complete the Arctic Snow Microstructure Experiment (ASMEEx); in which radiometric and snow characteristic properties of snow slabs upon two bases of differing reflectivities.**

As previously described in Section 3.4, snow slabs were extracted from the natural snowpack, and were radiometrically observed upon two separate bases with differing reflecting properties; one acting as a perfect reflector and another assumed to be acting as a reasonable blackbody absorber. Although the absorbing base apparatus went through several different iterations (Figures 3.6a – 3.6d), the emissivity of the apparatus was high enough to validate the assumption of a reasonable absorber (Table 3.2).

As Chapter 3 focuses upon the experimental proceedings of the ASMEEx campaign,

details were given about the way in which the snow slabs were selected and extracted from the natural snowpack, with the aims of selecting from homogeneous layers within the snowpack. Upon extraction, the snow slabs were radiometrically observed at five different frequencies (18.7, 21.0, 36.5, 89.0, and 150.0 GHz) upon the two different bases with the SodRad1 and SodRad2 radiometer platforms. The downwelling microwave radiation was also observed at each of these frequencies, for future use within the extinction coefficient calculation (shown in Chapter 5).

After completion of the radiometric observations, each snow slab was characterised in terms of its physical parameters; such as physical temperature, thickness, bulk density, traditional grain size, and specific surface area. These observations were made using traditional snowpit observation techniques, as well as through modern observation techniques (the IceCube instrumentation, the SMP, and through  $\mu$ CT analysis).

Different observation techniques were used during the ASMEEx snow slab observations, as it allowed for new modern techniques (SMP and  $\mu$ CT analysis) to be compared to those of the traditional snowpit observations. The different types of observation techniques can also be compared in terms of their influence upon the simulated brightness temperature via multiple simulations of the HUT snow emission model. The comparisons of observation data in Section 4.2.3.2 and the simulated brightness temperature comparison in Section 4.3 shows a comparison of the influence of each type of instrumentation upon the ASMEEx data.

The experimental proceedings presented in this chapter details the way in which the ASMEEx dataset was collected, thus completing the first goal of the first research aim. Chapter 4 shows the analysis of the ASMEEx dataset, completing the second goal, fully achieving the first research aim.

## Chapter 4:

# ASMEEx results and single layer HUT model simulations

### 4.1 Chapter Introduction

Chapter 4 is split into numerous sections. The ASMEEx campaign field data is found throughout Section 4.2. The radiometric data (observed brightness temperatures) of the extracted snow slabs upon the two bases with differing reflectivity properties are detailed in Section 4.2.2. The snow characteristic data is displayed in Section 4.2.3. The snow characteristic data includes the location of the extracted snow slab within the snowpack, as well as bulk values of physical temperature, traditional grain size (as defined by Fierz et al. [2009]), density, SSA, calculated exponential correlation length, and calculated optical diameter. The bulk values of density, SSA, calculated exponential correlation length and calculated optical diameter as measured with traditional snowpit techniques and the two modern observation techniques (the SnowMicroPen and X-ray computer tomography) are also compared and contrasted within Section 4.2.3. The traditional and modern snow characteristic observation techniques were also used to perform a simple stratigraphy analysis of each individual slab sample; to test the homogeneity of the slabs. The homogeneity of the slabs, as well as discussion of the different observation techniques, are found as part of Section 4.2.4. The single layer HUT snow emission model is utilized in Section 4.3 to complete simulated brightness temperatures of the extracted ASMEEx snow slabs, using the observed snow characteristics as input parameters. Two sets of simulations were completed; one containing all snow slab data, and another containing those deemed homogeneous in the homogeneity analysis in Section 4.2.4.

As previously stated in Chapter 3, the ASMEEx campaign was the focus of work

completed by [Maslanka et al. \[2016\]](#). In this chapter, the data collected as part of the ASMEEx campaign, as well as the comparison between the observed and simulated brightness temperatures (using the single layer HUT model), will be analysed and discussed further.

## 4.2 Fieldwork Data

During both winters of the ASMEEx campaign, many different observations were made as part of the data retrieval from the slabs. The following subsections will describe the data that have been collected; radiometric measurements, snow characteristic measurements, as well as the stratigraphic observations using the SnowMicroPen (SMP) and X-ray computer tomography ( $\mu$ CT) analysis. Full data tables can be found in the Appendix (specific locations will be referenced in the relevant subsections). Metadata is also described within the following subsections.

### 4.2.1 Slab Metadata

Table 4.1 shows the metadata of the ASMEEx slab campaign. Each slab measurement began in the morning; with initial calibration of the radiometers (as described in Section 3.3.2) beginning as soon as possible. The physical measurements took place after the radiometric measurements, as described in Section 3.5.3.

**Table 4.1:** Metadata from the ASMEEx campaign. The radiometric observation and snow characteristic measurement start times are shown, in Local Time.

Ref.	Date [ddmmyy]	Radiometric Start Time	Snow Characteristic Start Time	Depth of slab in snowpack from surface
A01	130114	09:00	14:00	00 - 15 cm
A02	140114	09:00	15:00	33 - 48 cm
A03	110214	08:30	17:00	10 - 25 cm
A04	130214	08:30	15:30	48 - 63 cm
A05	030314	08:30	15:00	25 - 40 cm
A06	180314	08:30	15:00	18 - 33 cm
A07	200314	08:00	13:15	20 - 35 cm
B01	020215	08:15	14:00	00 - 15 cm
B02	050215	08:30	14:00	00 - 15 cm
B03	190215	08:30	13:00	30 - 45 cm
B04	110315	07:15	10:30	29 - 44 cm
B05	120315	06:45	10:30	74 - 79 cm
B06	240315	08:45	12:00	35 - 50 cm
B07	250315	08:30	12:00	64 - 79 cm

## 4.2.2 Radiometric Results

### 4.2.2.1 Radiometric Data

As previously described in Section 3.4, four unique radiometric observations (shown in Figure 3.4) were repeated many times over the course of ASMEEx. These four unique observations were:

1. Snow slab on a reflective metal base at both horizontal and vertical polarizations ( $T_{BM}$ ),
2. Snow slab on a blackbody base, at both horizontal and vertical polarizations ( $T_{BA}$ ),
3. Empty Blackbody base, at both horizontal and vertical polarizations ( $T_{BE}$ ),
4. Clear sky brightness temperature ( $T_{BSKY}$ ) at opposite incidence angles.

Each one of the four observations was repeated for each available frequency, at both horizontal and vertical polarizations, for each individual slab sample. This has resulted in a large collection of brightness temperature data, whose numerical values can be found in Appendix A, and is displayed graphically in Figures 4.1 - 4.14. These radiometric data form the basis of the initial comparisons with the HUT snow emission model simulations, found in Chapter 4, as these radiometric data form the observations against which the simulated data will be contrasted.

### 4.2.2.2 Radiometric Comparisons

While the radiometric properties of each slab are dependent on the snow characteristics, it is possible to comment upon some of the similarities shown across Figures 4.1 - 4.14. Figures 4.1 - 4.7 show the radiometric data for slabs A01 - A07 respectively, while Figures 4.8 - 4.14 show the radiometric data for slabs B01 - B07 respectively. They show the  $T_B$  values of the snow slab upon the absorbing (-Abs) and reflecting (-Ref) bases, at horizontal (H-) and vertical (V-) polarizations, as well as the respective sky  $T_B$  values ( $Sky_A$  for the absorbing bases,  $Sky_R$  for the reflective bases) for the measured frequencies.

It can be seen across Figures 4.1 - 4.14 that, for the lower frequencies, the reflective base  $T_B$  values differ greatly from the absorbing base  $T_B$  values. At the lower frequencies, the absorbing base  $T_B$  values are much greater than those of the reflective base  $T_B$  values. However, as the frequencies increase to the higher frequency values measured, the difference between the reflective base and absorbing base  $T_B$  values is much smaller; and

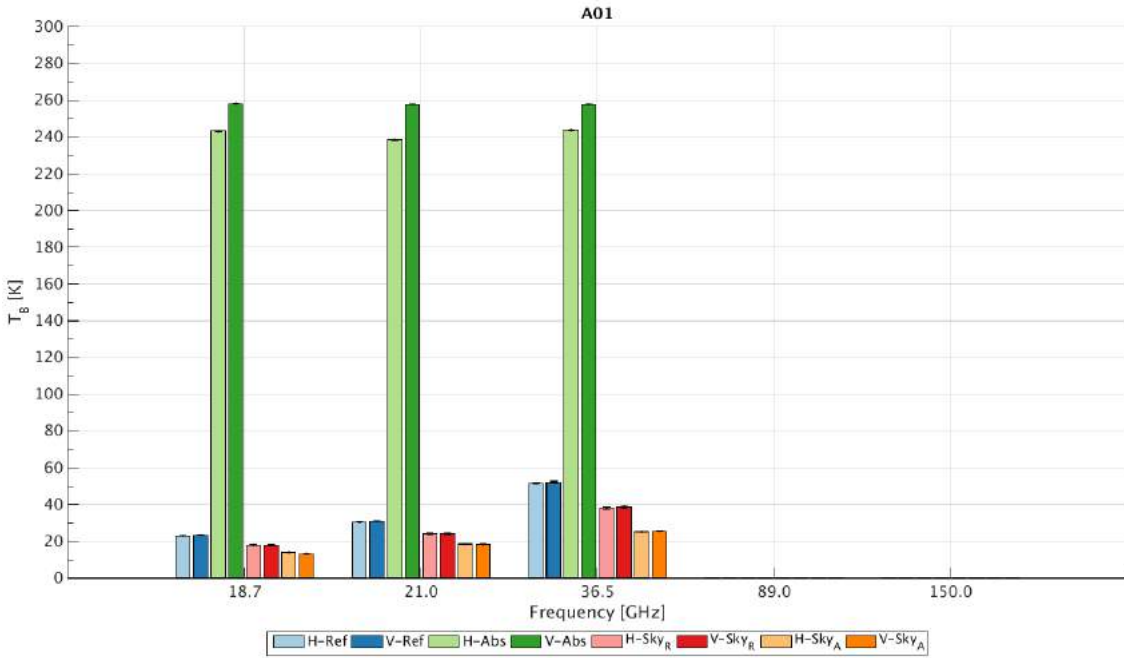


**Figure 4.1:**  $T_B$  values at horizontal ( $H-$ , pale colours) and vertical ( $V-$ , dark colours) polarizations for snow slab A01 at all measured frequencies. Measurements include  $T_B$  values upon the reflective base ( $-Ref$ , blue), upon the absorbing base ( $-Abs$ , green), downwelling sky  $T_B$  values associated with the reflective base ( $Sky_R$ , red) and absorbing base ( $Sky_A$ , orange) measurements.

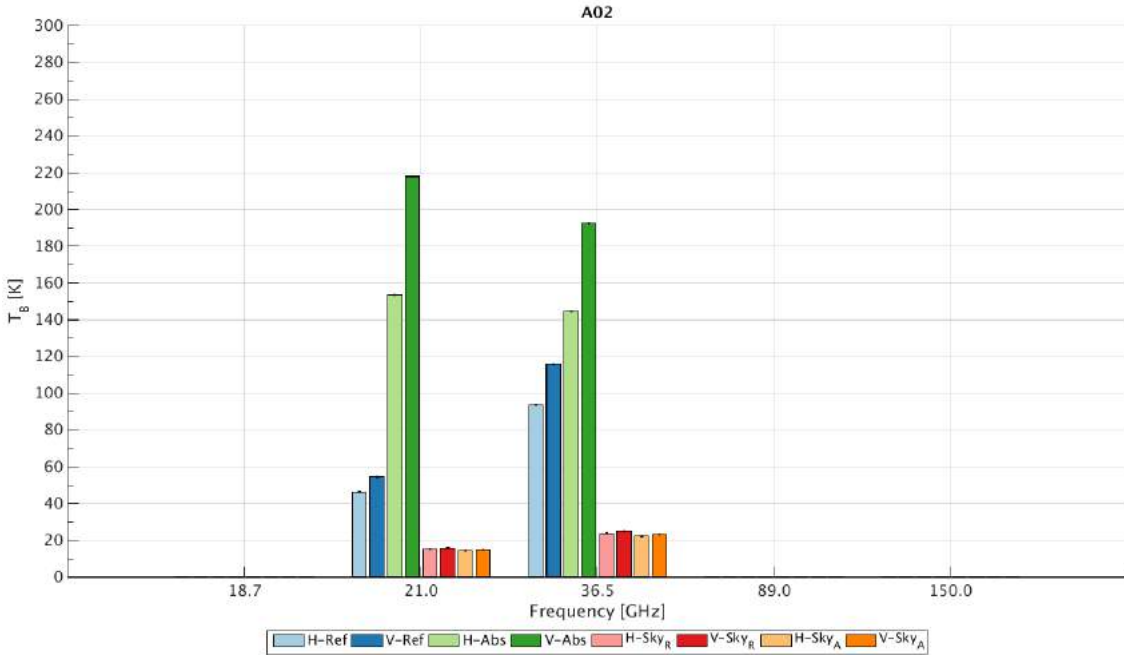


**Figure 4.2:**  $T_B$  values at horizontal ( $H-$ , pale colours) and vertical ( $V-$ , dark colours) polarizations for snow slab A02 at all measured frequencies. Measurements include  $T_B$  values upon the reflective base ( $-Ref$ , blue), upon the absorbing base ( $-Abs$ , green), downwelling sky  $T_B$  values associated with the reflective base ( $Sky_R$ , red) and absorbing base ( $Sky_A$ , orange) measurements.

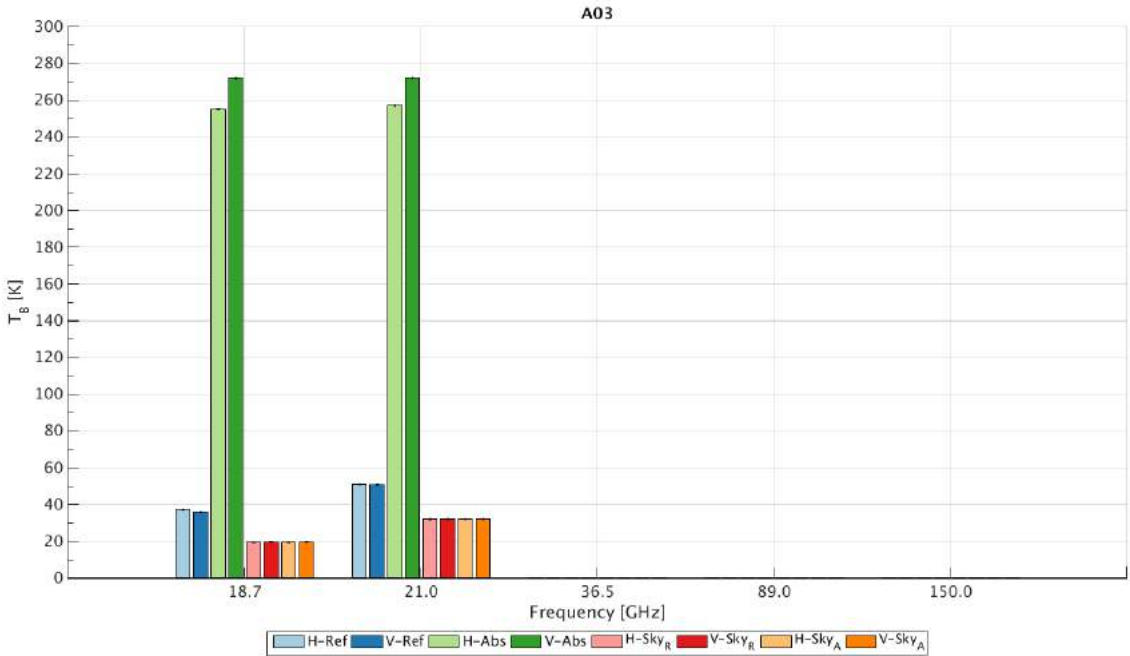


**Figure 4.3:**  $T_B$  values at horizontal ( $H-$ , pale colours) and vertical ( $V-$ , dark colours) polarizations for snow slab A03 at all measured frequencies. Measurements include  $T_B$  values upon the reflective base ( $-Ref$ , blue), upon the absorbing base ( $-Abs$ , green), downwelling sky  $T_B$  values associated with the reflective base ( $Sky_R$ , red) and absorbing base ( $Sky_A$ , orange) measurements.

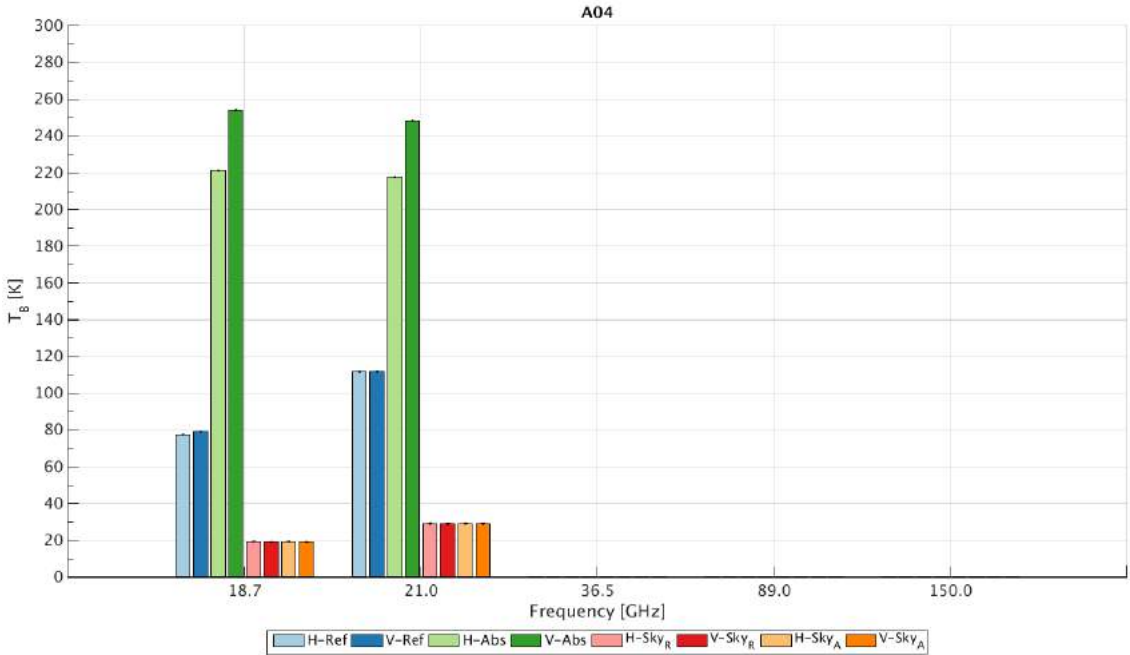


**Figure 4.4:**  $T_B$  values at horizontal ( $H-$ , pale colours) and vertical ( $V-$ , dark colours) polarizations for snow slab A04 at all measured frequencies. Measurements include  $T_B$  values upon the reflective base ( $-Ref$ , blue), upon the absorbing base ( $-Abs$ , green), downwelling sky  $T_B$  values associated with the reflective base ( $Sky_R$ , red) and absorbing base ( $Sky_A$ , orange) measurements.

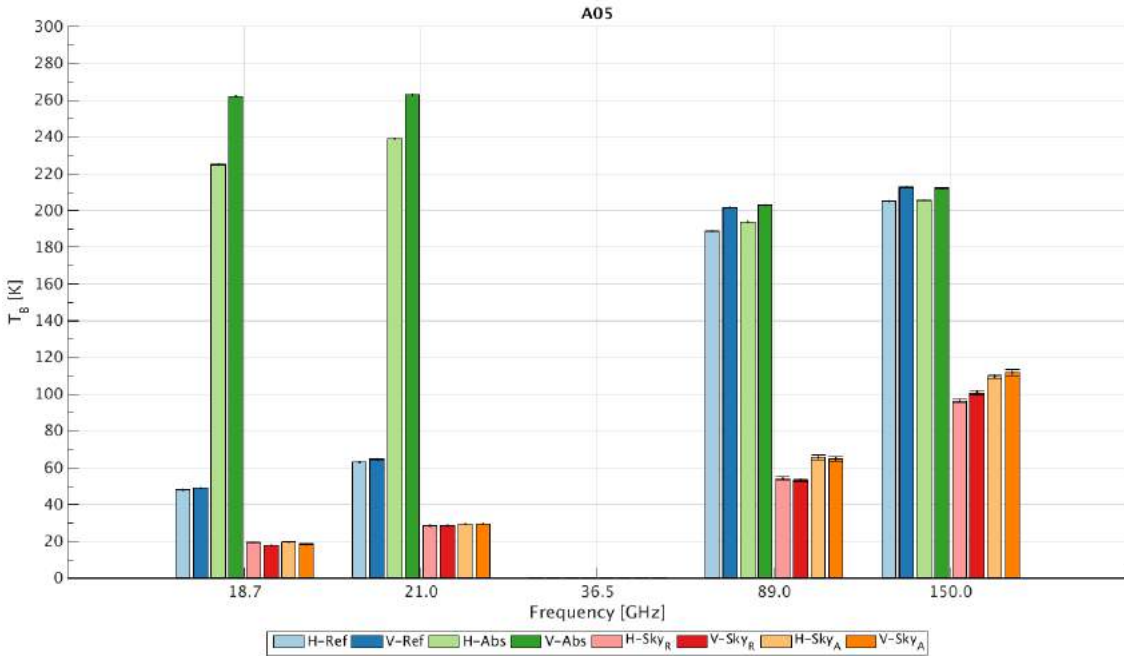


**Figure 4.5:**  $T_B$  values at horizontal ( $H-$ , pale colours) and vertical ( $V-$ , dark colours) polarizations for snow slab A05 at all measured frequencies. Measurements include  $T_B$  values upon the reflective base ( $-Ref$ , blue), upon the absorbing base ( $-Abs$ , green), downwelling sky  $T_B$  values associated with the reflective base ( $Sky_R$ , red) and absorbing base ( $Sky_A$ , orange) measurements.

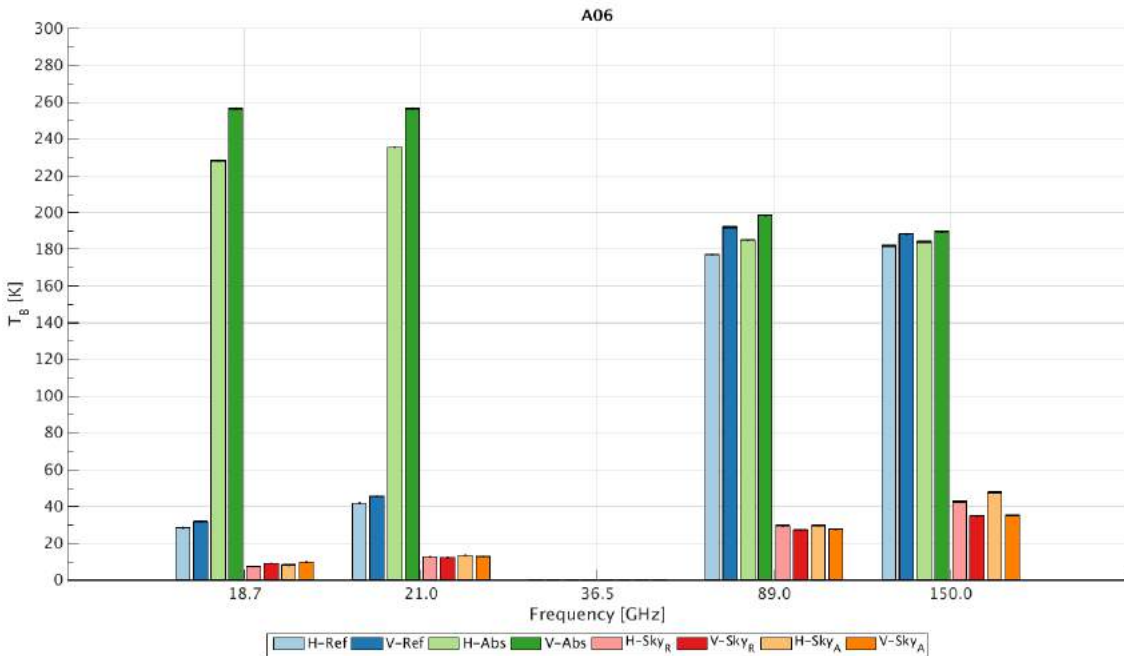


**Figure 4.6:**  $T_B$  values at horizontal ( $H-$ , pale colours) and vertical ( $V-$ , dark colours) polarizations for snow slab A06 at all measured frequencies. Measurements include  $T_B$  values upon the reflective base ( $-Ref$ , blue), upon the absorbing base ( $-Abs$ , green), downwelling sky  $T_B$  values associated with the reflective base ( $Sky_R$ , red) and absorbing base ( $Sky_A$ , orange) measurements.

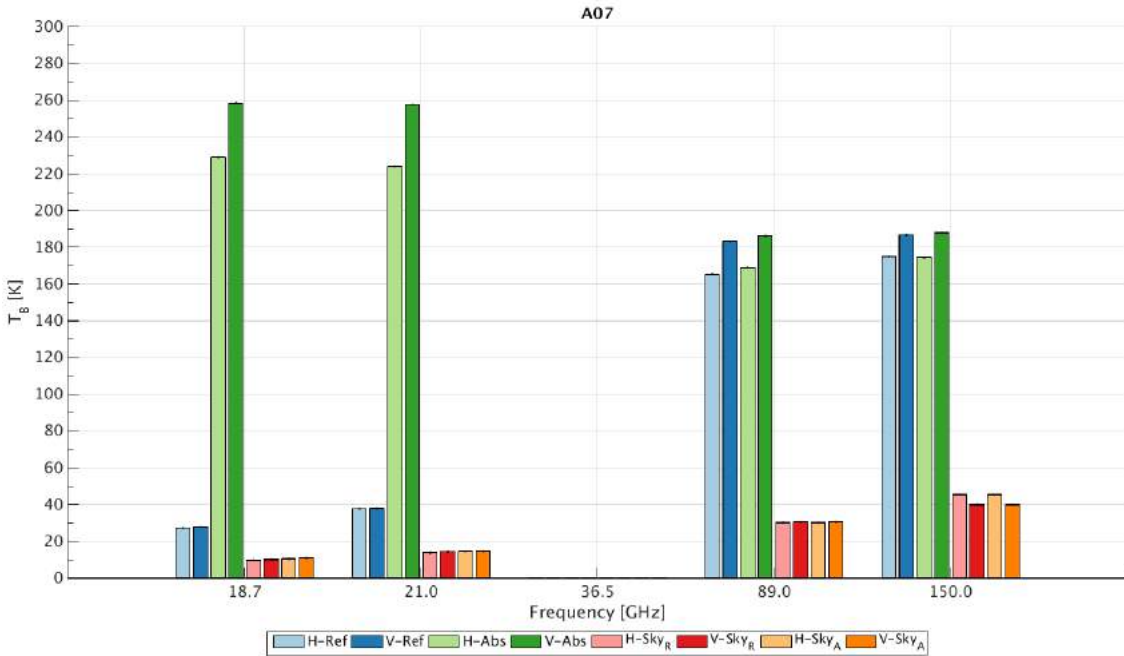


**Figure 4.7:**  $T_B$  values at horizontal ( $H-$ , pale colours) and vertical ( $V-$ , dark colours) polarizations for snow slab A07 at all measured frequencies. Measurements include  $T_B$  values upon the reflective base ( $-Ref$ , blue), upon the absorbing base ( $-Abs$ , green), downwelling sky  $T_B$  values associated with the reflective base ( $Sky_R$ , red) and absorbing base ( $Sky_A$ , orange) measurements.

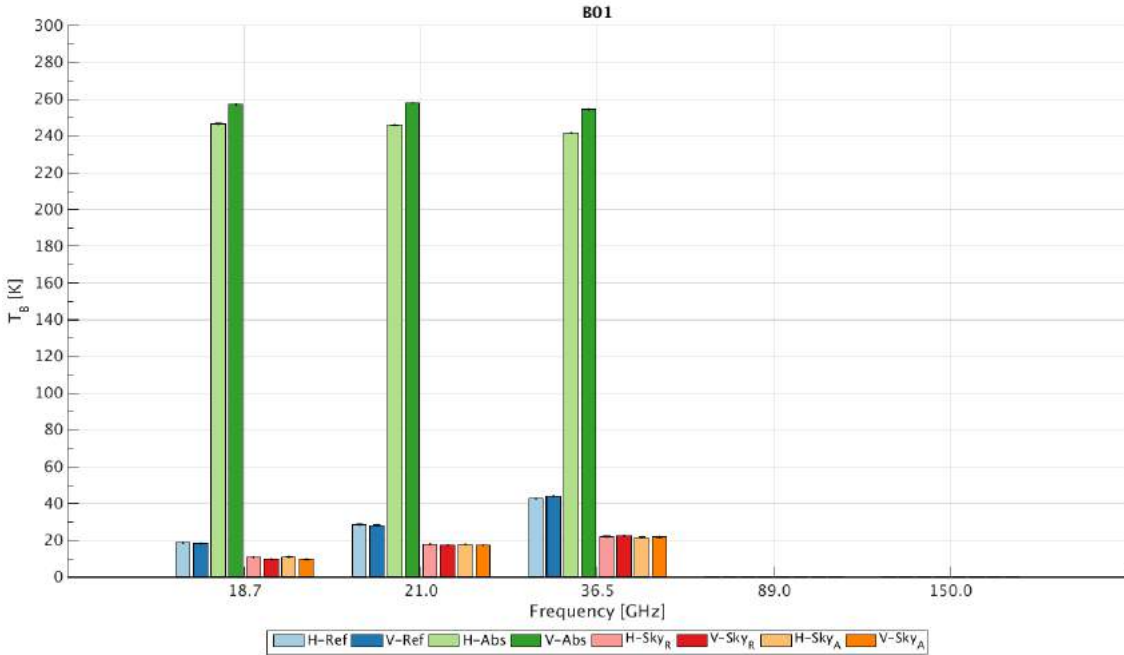


**Figure 4.8:**  $T_B$  values at horizontal ( $H-$ , pale colours) and vertical ( $V-$ , dark colours) polarizations for snow slab B01 at all measured frequencies. Measurements include  $T_B$  values upon the reflective base ( $-Ref$ , blue), upon the absorbing base ( $-Abs$ , green), downwelling sky  $T_B$  values associated with the reflective base ( $Sky_R$ , red) and absorbing base ( $Sky_A$ , orange) measurements.

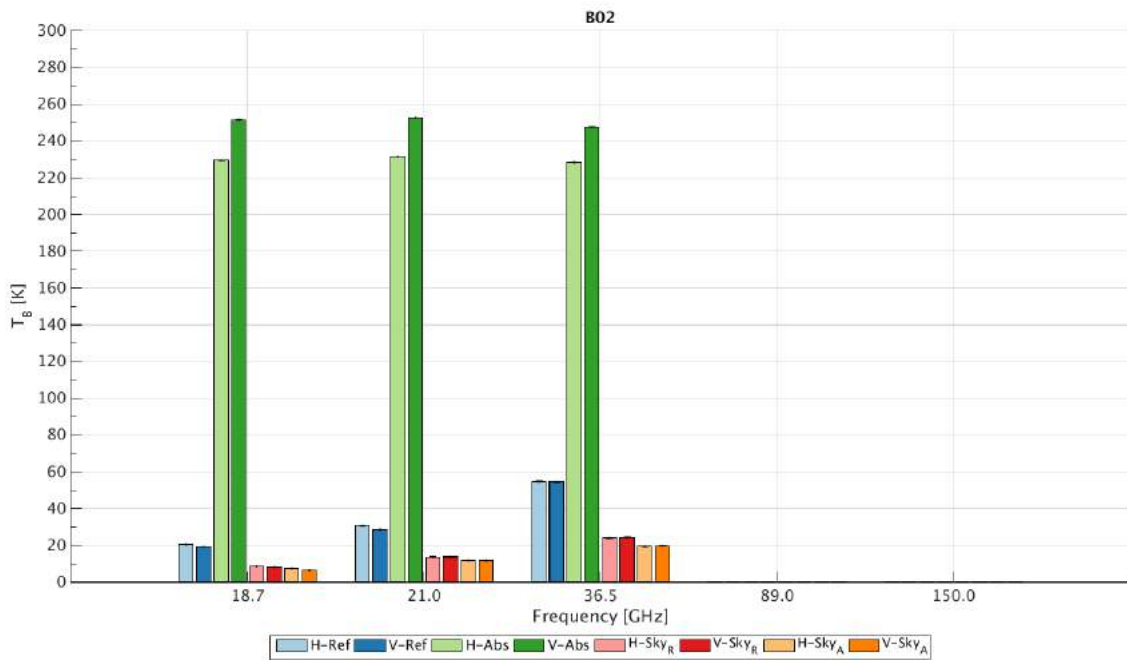


**Figure 4.9:**  $T_B$  values at horizontal ( $H-$ , pale colours) and vertical ( $V-$ , dark colours) polarizations for snow slab B02 at all measured frequencies. Measurements include  $T_B$  values upon the reflective base ( $-Ref$ , blue), upon the absorbing base ( $-Abs$ , green), downwelling sky  $T_B$  values associated with the reflective base ( $Sky_R$ , red) and absorbing base ( $Sky_A$ , orange) measurements.

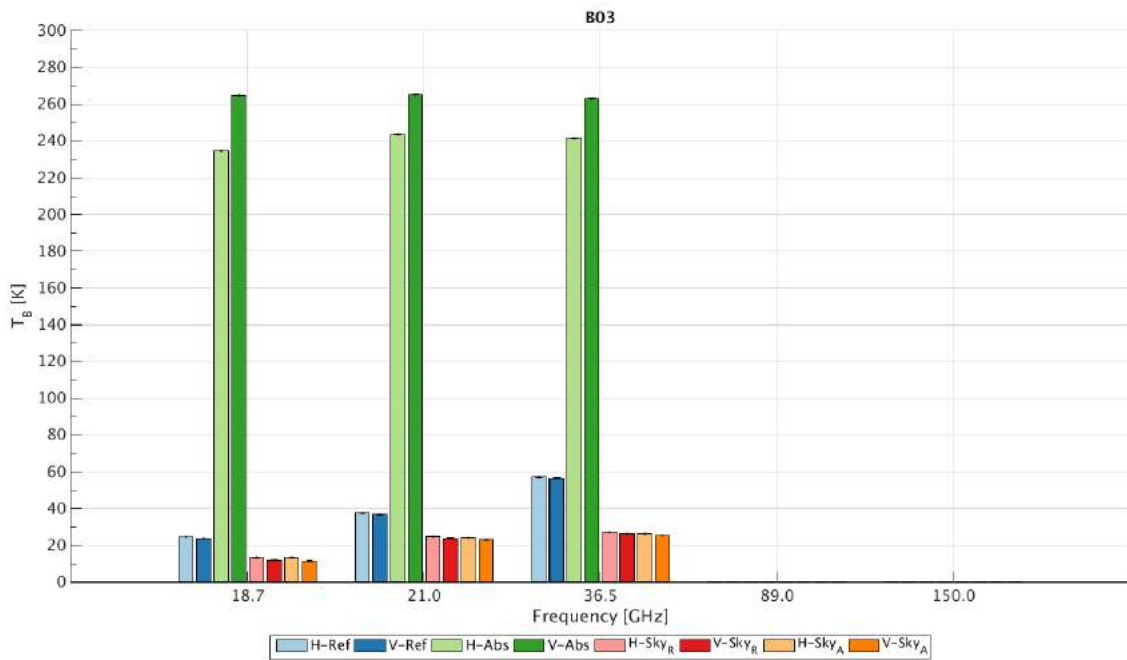


**Figure 4.10:**  $T_B$  values at horizontal ( $H-$ , pale colours) and vertical ( $V-$ , dark colours) polarizations for snow slab B03 at all measured frequencies. Measurements include  $T_B$  values upon the reflective base ( $-Ref$ , blue), upon the absorbing base ( $-Abs$ , green), downwelling sky  $T_B$  values associated with the reflective base ( $Sky_R$ , red) and absorbing base ( $Sky_A$ , orange) measurements.

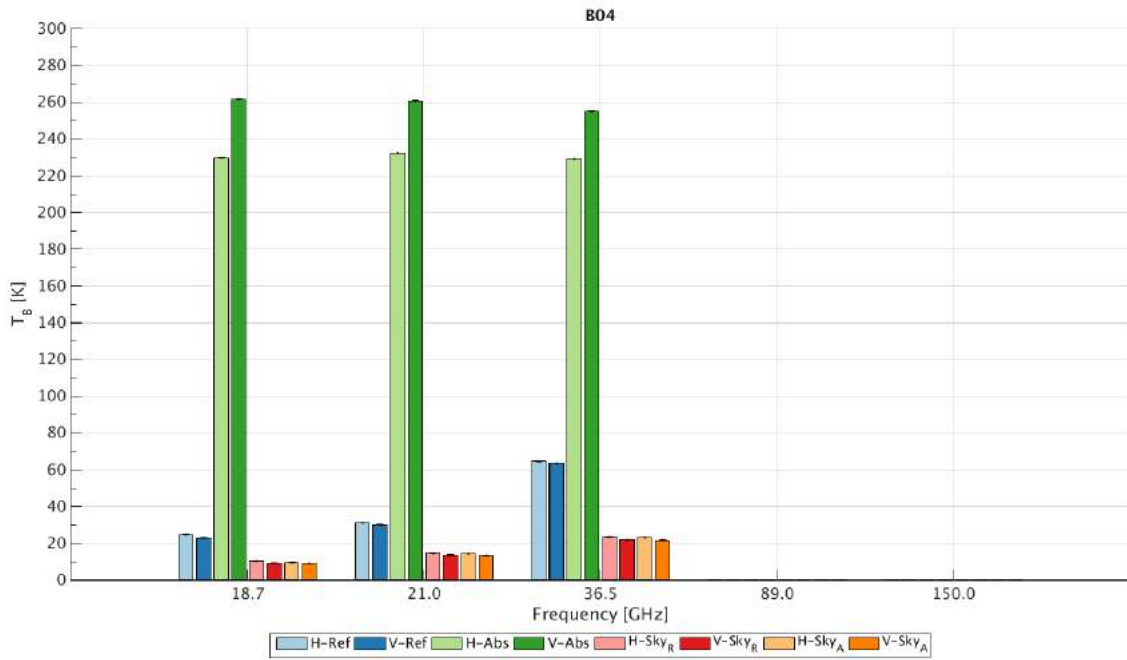


**Figure 4.11:**  $T_B$  values at horizontal ( $H-$ , pale colours) and vertical ( $V-$ , dark colours) polarizations for snow slab B04 at all measured frequencies. Measurements include  $T_B$  values upon the reflective base ( $-Ref$ , blue), upon the absorbing base ( $-Abs$ , green), downwelling sky  $T_B$  values associated with the reflective base ( $Sky_R$ , red) and absorbing base ( $Sky_A$ , orange) measurements.

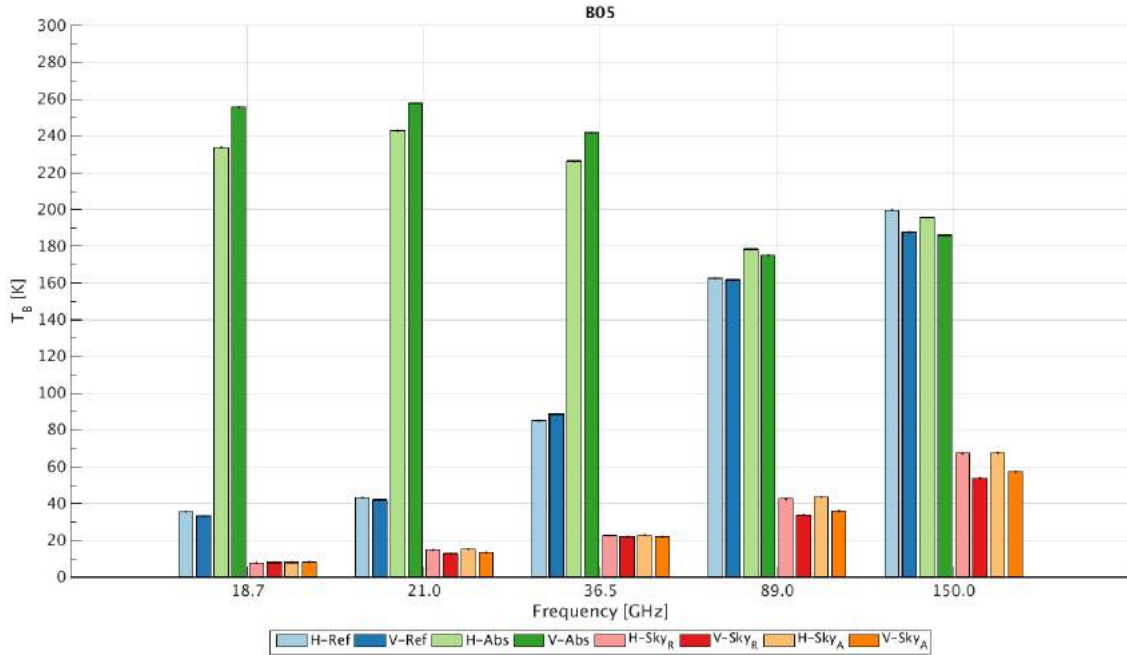


**Figure 4.12:**  $T_B$  values at horizontal ( $H-$ , pale colours) and vertical ( $V-$ , dark colours) polarizations for snow slab B05 at all measured frequencies. Measurements include  $T_B$  values upon the reflective base ( $-Ref$ , blue), upon the absorbing base ( $-Abs$ , green), downwelling sky  $T_B$  values associated with the reflective base ( $Sky_R$ , red) and absorbing base ( $Sky_A$ , orange) measurements.

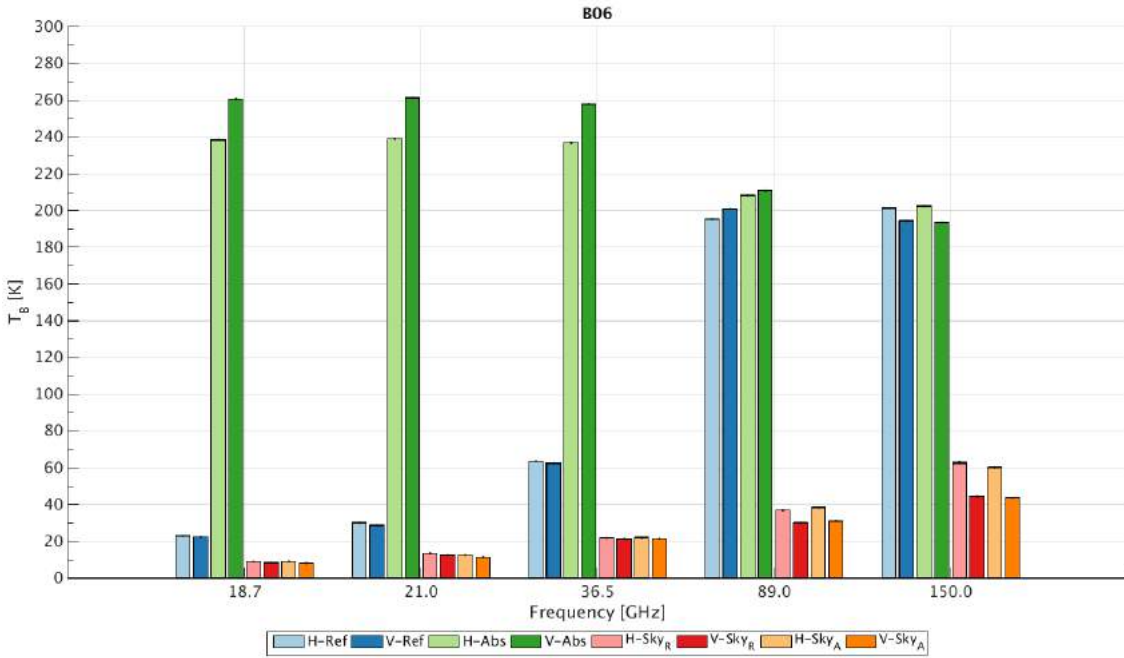


**Figure 4.13:**  $T_B$  values at horizontal ( $H-$ , pale colours) and vertical ( $V-$ , dark colours) polarizations for snow slab B06 at all measured frequencies. Measurements include  $T_B$  values upon the reflective base ( $-Ref$ , blue), upon the absorbing base ( $-Abs$ , green), downwelling sky  $T_B$  values associated with the reflective base ( $Sky_R$ , red) and absorbing base ( $Sky_A$ , orange) measurements.

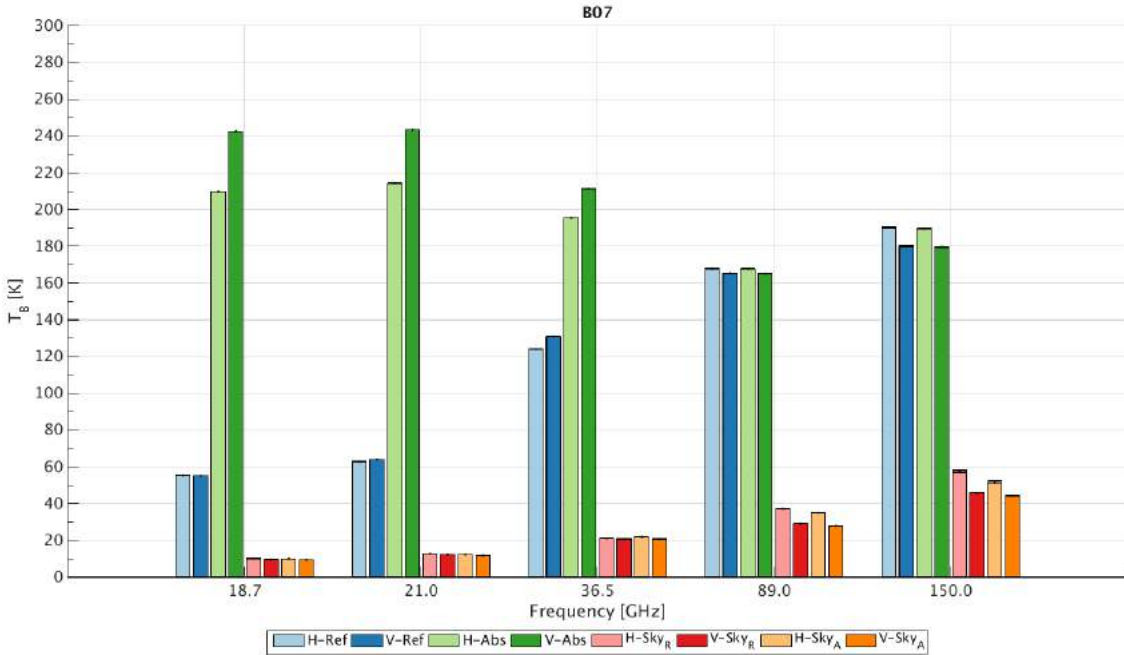


**Figure 4.14:**  $T_B$  values at horizontal ( $H-$ , pale colours) and vertical ( $V-$ , dark colours) polarizations for snow slab B07 at all measured frequencies. Measurements include  $T_B$  values upon the reflective base ( $-Ref$ , blue), upon the absorbing base ( $-Abs$ , green), downwelling sky  $T_B$  values associated with the reflective base ( $Sky_R$ , red) and absorbing base ( $Sky_A$ , orange) measurements.

at 150.0 GHz, they are close to zero. This is due to the differing penetration depth at different frequencies (Section 2.3.2). At 18.7 GHz, the penetration depth is much greater than at 150 GHz. This means that radiation at 18.7 GHz is able to (for the reflective base cases) pass through the surface of the snow slab, transmit through the snowpack to the reflective base plate, be reflected and transmit back through the snow slab without being scattered by a large amount. Therefore, the observed  $T_B$  values at 18.7 GHz can be likened to the contribution of microwave emission from the underlying ground (for the reflective base cases, the source of this emission is the downwelling sky  $T_B$ , while for the absorbing base cases, the source of this emission is from the underlying blackbody absorber). Figuratively, this contribution comes from contribution 2 in Figure 2.9.

At 150.0 GHz, the penetrative depth is much smaller (using Eqn. 2.23 at 150.0 GHz for slab B07 gives a penetration depth of 0.16 m) than at lower frequencies (at 18.7 GHz,  $\delta_p$  for slab B07 is 1.30 m). This is to be expected, as the snow crystals will much readily scatter the higher frequency radiation, due to the much smaller wavelengths being the similar order of magnitude to the size of the snow crystal (150 GHz has a wavelength of 0.002 m, while 18.7 GHz has a wavelength of 0.016 m). This much smaller wavelength, and smaller penetration depth, results in an increased amount of scattering, limiting the path length of the microwave radiation. The emission of microwaves from the absorbing base, and the reflected downwelling radiation from the reflective base, appear to have an increasingly reduced effect as the frequency increases; as the brightness temperature difference between the snow upon the absorbing and reflective bases decreases as the frequency increases. The increased scattering and reduced penetration depth have reduced the influence from the underlying surfaces of the slabs.

When comparing the  $T_B$  values of the snow slabs between the two polarizations on both the absorbing and reflective bases, it is often the case that the values at horizontal polarization are smaller than those at vertical polarizations. This is expected, as horizontal polarization  $T_B$  values are very dependent upon the internal layering within the slab, while the vertical polarization  $T_B$  values are dependent upon the slab depth (Colbeck [1991] and Rees et al. [2010]). As the slab depths varied very little across all the slabs (with the exception of slab B05), the small differences in density and other internal parameters may be the reason for the difference between the horizontal and vertical polarization slab  $T_B$  values. The internal stratigraphy of the slabs will be discussed further in Section 4.2.4.

The brightness temperature values of the sky measurements also vary with frequency.

It can be seen that the magnitude of the downwelling sky  $T_B$  values increase with increasing frequency. If the sky and overall weather conditions (such as cloud cover, precipitation, etc) did not change over the course of the slab measurements, then there is no difference between the  $T_B$  values of downwelling sky measurements associated with the absorbing and reflective bases. At lower frequencies, there is very little difference between the horizontal and vertical polarization  $T_B$  values. At higher frequencies (89.0 and 150.0 GHz), the horizontal  $T_B$  values are larger than the vertical  $T_B$  values.

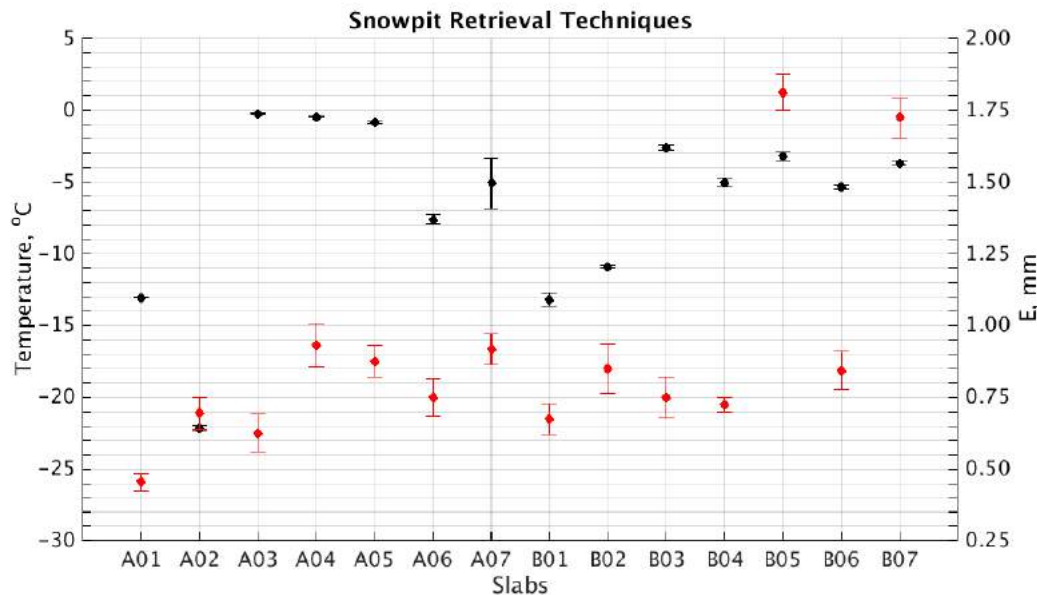
### 4.2.3 Snow Characteristics Results

#### 4.2.3.1 Snow Characteristics Data

As previously described in Section 3.5.3, many different snow parameters were observed once the radiometric section of ASMEEx was complete. This subsection highlights the data collected using Snowpit techniques (density cutters and IceCube measurements), the  $\mu$ CT retrieval techniques, and the SMP retrieval techniques, as well as observations of bulk average physical temperatures and traditional grain size (as defined by Fierz et al. [2009]). Comparisons of commonly measured and calculated parameters will be made between the snowpit,  $\mu$ CT, and SMP techniques. Tables B.1 – B.6 in the appendix show the data in its numerical form, with graphical representation of the data being presented in this subsection.

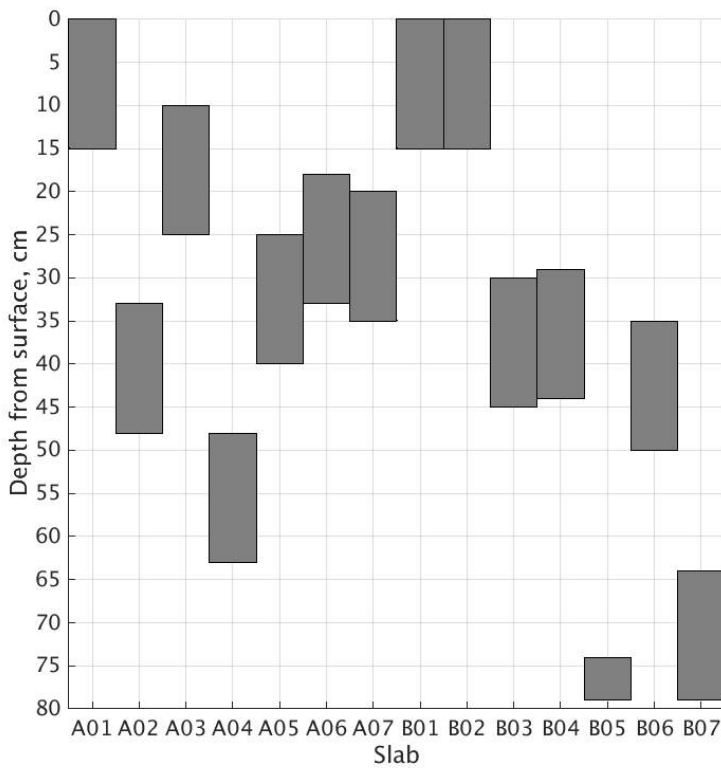
Whilst the physical temperature ( $T_{phys}$ ) and traditional grain size (E, Fierz et al. [2009]) were determined by probe thermometer and macrophotography respectively, the snow density ( $\rho_{snow}$ ) and Specific Surface Area (SSA) were measured using three separate techniques.  $\rho_{snow}$  and SSA were measured using techniques commonly found in snowpit observations completed at the FMI ARC. This consisted of box cutter density measurements ( $\rho_s$ ) and IceCube SSA measurements ( $SSA_s$ ). Snow density and SSA were also calculated using measured profiles of penetrative resistance, using the SMP across the slab sample( $\rho_{SMP}$  and  $SSA_{SMP}$  respectively). Snow density and SSA were also measured from subsamples within the snow slab, using a  $\mu$ CT measurement technique ( $\rho_\mu$  and  $SSA_\mu$  respectively). From measurements of snow density and SSA, calculations of exponential correlation length ( $P_{ex}$ ) and optical diameter ( $D_{opt}$ ) can be made. The snowpit, SMP, and  $\mu$ CT measurements were made, so that measurements of snow density and SSA could be completed from the same snow sample, using each of the techniques in turn. By testing the same snow with the three sets of measurements, a direct comparison between the three methods was made.

Figure 4.15 shows the bulk average values of  $T_{phys}$  and E across all 14 slab samples. Standard error of the mean (SEM) values are displayed as error bars around the bulk average values. It can be seen that a range of bulk average  $T_{phys}$  values were recorded ( $-22^{\circ}\text{C} - 0^{\circ}\text{C}$ ) for the duration of ASMEEx, with 13 of the 14 slabs having an SEM of less than  $0.3^{\circ}\text{C}$ . The large SEM of  $1.8^{\circ}\text{C}$ , associated with slab A07, was a result of the positioning of the slab with respect to the sun. One side of the slab was more exposed to the sun, leading to one side being heated more than the other, post-extraction.



**Figure 4.15:** Bulk average  $T_{phys}$  (black) and traditional grain size E (red) values for the ASMEEx slabs.

The bulk average values of E recorded varies from  $0.45 - 1.81$  mm. This large variation in value of E is due to slab samples being extracted from different depths within the natural snowpack, allowing for slab samples to be extracted from different “ages” of natural snow. The smaller values of E were found in slabs at the beginning of each years measurement campaign (Table 4.1), as well as from depths close to the natural snowpack surface; when the natural snowpack has not experienced a large change in characteristics due to the metamorphism of the snow. The larger values of E, such as slabs B05 and B07, were found from “old snow” regions; i.e. depths where the snow has been present for long periods of time, and where large changes under metamorphism has taken place. As homogeneous slabs were wanted for radiometric observation, more slabs were extracted from the top or middle of the natural snowpack (Figure 4.16), to try and maximise the chances of obtaining homogeneous slabs. The SEM values of E are similar for the majority of the slab samples, with a SEM in the region of  $\pm 0.06$  mm. Slabs A01 and B04, however, have a much smaller value of SEM, in the region of  $\pm 0.02$  mm.

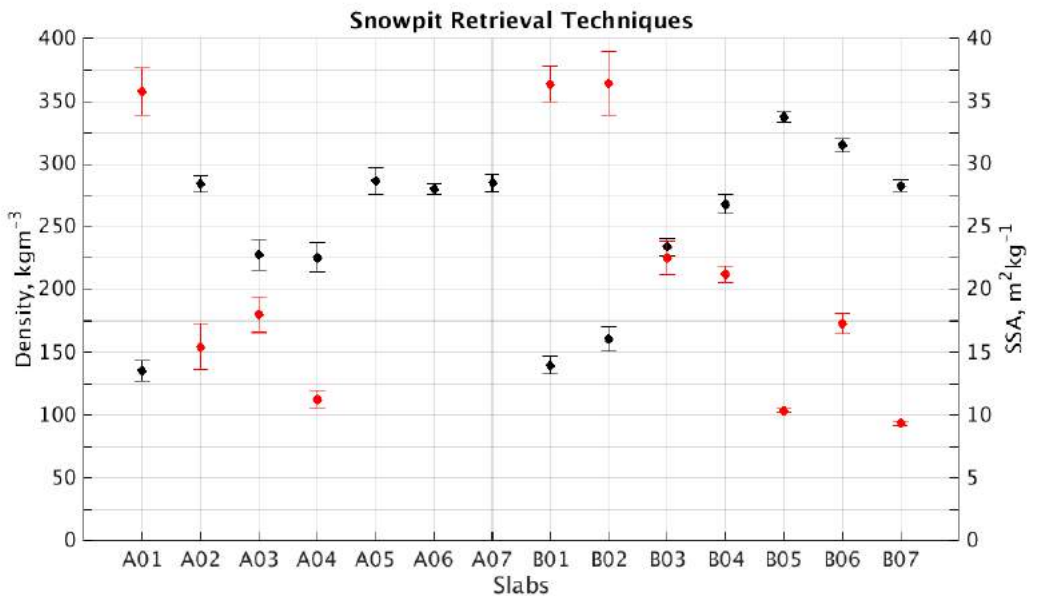


**Figure 4.16:** Location of ASMEEx snow slabs within the natural snowpack. Slab depths were measured from the surface.

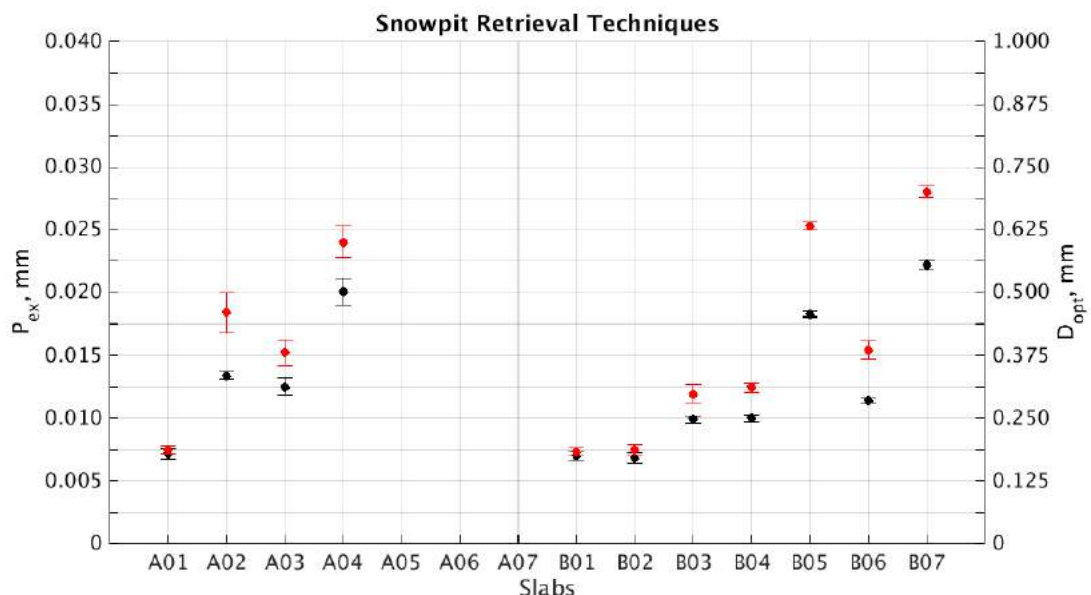
Figure 4.17 shows the bulk average values of density ( $\rho_s$ ) and SSA ( $SSA_s$ ) as measured by snowpit techniques (box cutter and IceCube, Figure 4.17a), as well as calculated values of exponential correlation length ( $P_{exs}$ ) and optical diameter ( $D_{opts}$ ), using data from the snowpit techniques (Figure 4.17b). It should be noted that as slabs A05, A06, and A07 did not have an IceCube machine present, no IceCube  $SSA_s$  measurements took place. Therefore, slabs A05, A06, and A07 have no exponential correlation length or optical diameter calculations, using IceCube SSA data. Comparisons of these three slabs are not possible with  $\mu$ CT or SMP retrieved data.

It can be seen that the bulk average values of  $\rho_s$  vary from  $135.5 - 337.5 \text{ kgm}^{-3}$ . The SEM values range from  $4.2 - 12.1 \text{ kgm}^{-3}$ , with no apparent relationship between the magnitude of the SEM value and the slab associated with it, with the exception of slab B05; the smaller slab thickness only allowed for four box cutter measurements, compared to 12 box cutter measurements for the other 13 slabs.

The values of  $SSA_s$  vary from  $9.4 - 36.4 \text{ m}^2\text{kg}^{-1}$ , showing the range of bulk average values of fresh snow and coarse grains. The SEM values for the deeper slabs (B05 and B07) are smaller than those slabs taken from the top and middle of the snowpack. Slab



(a) Density (black) and SSA (red) measurements, using the box cutter (density) and IceCube (SSA) instrumentation.

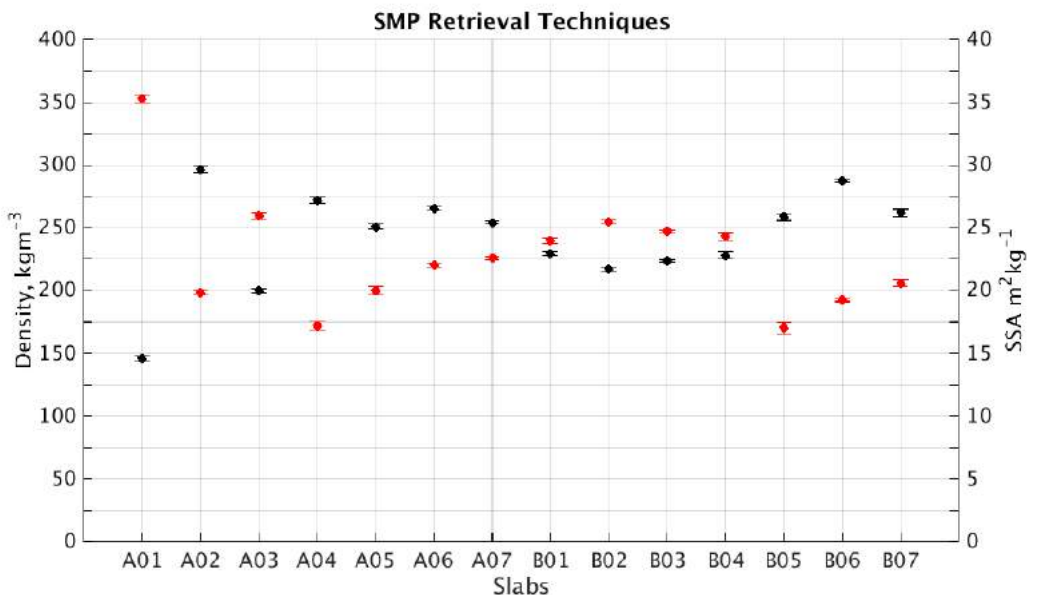


(b) Calculated values of  $p_{ex}$  (black) and  $D_{opt}$  (red), using the box cutter (density) and IceCube (SSA) instrumentation

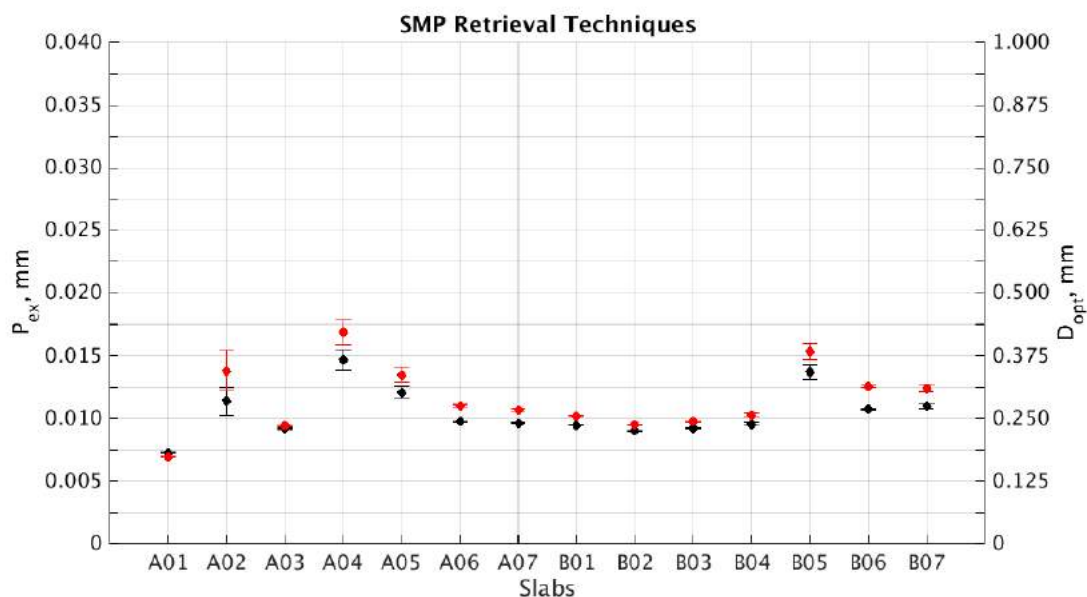
Figure 4.17: ASMEx snow characteristics data, recorded using snowpit techniques.

B05, due to its shorter thickness, only allowed for four IceCube measurements, compared to the 12 – 15 of the other 13 slabs.

Figure 4.17b shows the calculated values of  $P_{exs}$  and  $D_{opts}$  for the ASMEEx slabs, using Eqns. 3.4 and 2.19 respectively.  $P_{exs}$  and  $D_{opts}$  are inversely proportional to the values of  $SSA_s$ . The values of  $P_{exs}$  SEM range from 0.018 – 0.108 mm, and values of  $D_{opts}$  SEM vary from 0.008 – 0.041 mm. The large value of  $D_{opts}$  SEM from slab A02 come from the large variation in  $SSA_s$  values, due to the stratigraphic layers present (Section 4.2.4).



(a) Density (black) and SSA (red) measurements from the SMP measurements.



(b) Calculated values of  $p_{ex}$  (black) and  $D_{opt}$  (red), using SMP data.

**Figure 4.18:** ASMEEx snow characteristics data, recorded using the SMP.

Figure 4.18 shows the bulk average values of density ( $\rho_{SMP}$ ) and SSA ( $SSA_{SMP}$ ) as measured using the SMP (Figure 4.18a), as well as the calculated values of exponential correlation length ( $P_{exSMP}$ ) and optical diameter ( $D_{optSMP}$ ), using data from the SMP (Figure 4.18b). The SMP bulk values are calculated using SMP profiles B2 and C2 (Figure 3.9). The values of bulk average  $\rho_{SMP}$  is calculated using a similar model to that in Proksch et al. [2015]. However, the regression models used in the ASMEEx campaign are calibrated using the box cutter density measurements, and thus use different coefficients within the regression model. The ASMEEx  $\rho_{SMP}$  regression model is:

$$\rho_{SMP} = a_1 + a_2 \ln\left(\frac{\hat{F}}{F_0}\right) + a_3 \ln\left(\frac{\hat{F}}{F_0}\right)L + a_4 L \quad (4.1)$$

where  $\hat{F}$  is the median penetration force as measured by the SMP, L is the typical distance between elements (snow crystals),  $a_1 = 322.57 \pm 33.361 \text{ kg m}^{-3}$ ,  $a_2 = 35.943 \pm 11.289 \text{ kg m}^{-3}$ ,  $a_3 = -3.5225 \pm 10.892 \text{ kg m}^{-3} \text{ mm}^{-1}$ , and  $a_4 = 20.155 \pm 40.621 \text{ kg m}^{-3} \text{ mm}^{-1}$ . Likewise,  $SSA_{SMP}$  is also calculated using a regression model, similar to that by Proksch et al. [2015]. However, the regression model used by ASMEEx has been calibrated using IceCube measurements of the slab samples. Thus,  $SSA_{SMP}$  is calculated using:

$$SSA_{SMP} = b_1 + b_2 \ln\left(\frac{\hat{F}}{F_0}\right) + b_3 \ln\left(\frac{\hat{F}}{F_0}\right)\delta + b_4 \delta \quad (4.2)$$

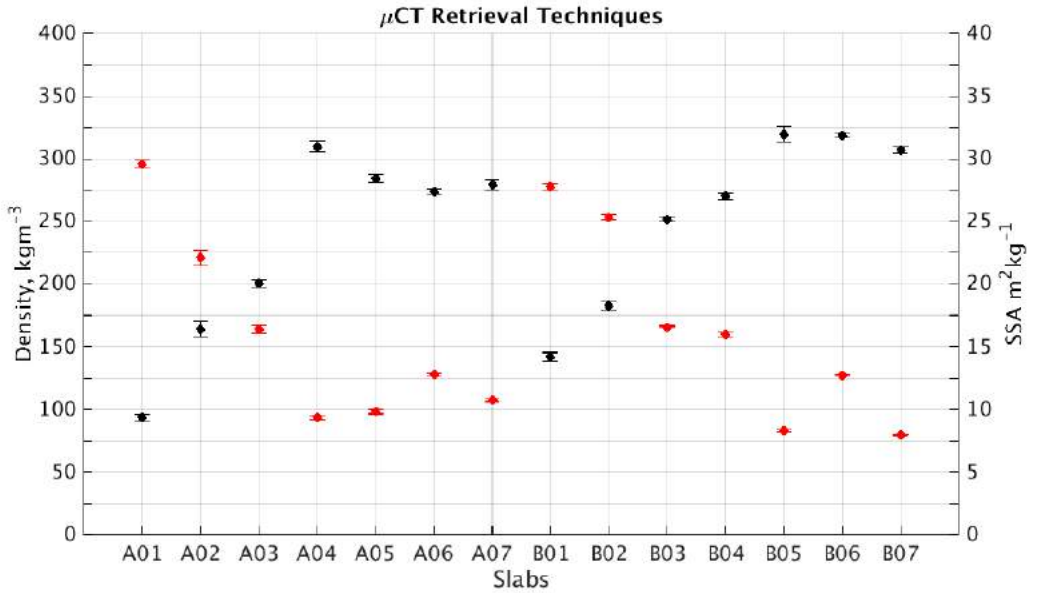
where  $\delta$  is the elastic deflection length,  $b_1 = 17.038 \pm 2.8121 \text{ m}^2 \text{ kg}^{-1}$ ,  $b_2 = -3.3379 \pm 0.83986 \text{ m}^2 \text{ kg}^{-1}$ ,  $b_3 = 15.606 \pm 8.4328 \text{ m}^2 \text{ kg}^{-1} \text{ mm}^{-1}$ , and  $b_4 = -0.32609 \pm 17.869 \text{ m}^2 \text{ kg}^{-1} \text{ mm}^{-1}$ .

Like with  $\rho_s$ , the bulk values of  $\rho_{SMP}$  varied across all 14 ASMEEx slabs. However, unlike the values of  $\rho_s$ , the range of  $\rho_{SMP}$  values is much smaller; from 145.7 – 287.5  $\text{kg m}^{-3}$ . The values of  $SSA_{SMP}$  also cover a smaller range than that of  $SSA_s$ ; from 17.0 – 35.3  $\text{m}^2 \text{ kg}^{-1}$ . The calculated values of  $P_{exSMP}$  and  $D_{optSMP}$  also span a much smaller range than that of their snowpit counterparts, with a range of 0.0726 – 0.1468 mm and 0.19 – 0.46 mm respectively. A comparison of the measurements observed with snowpit and SMP techniques are shown in Section 4.2.3.2.

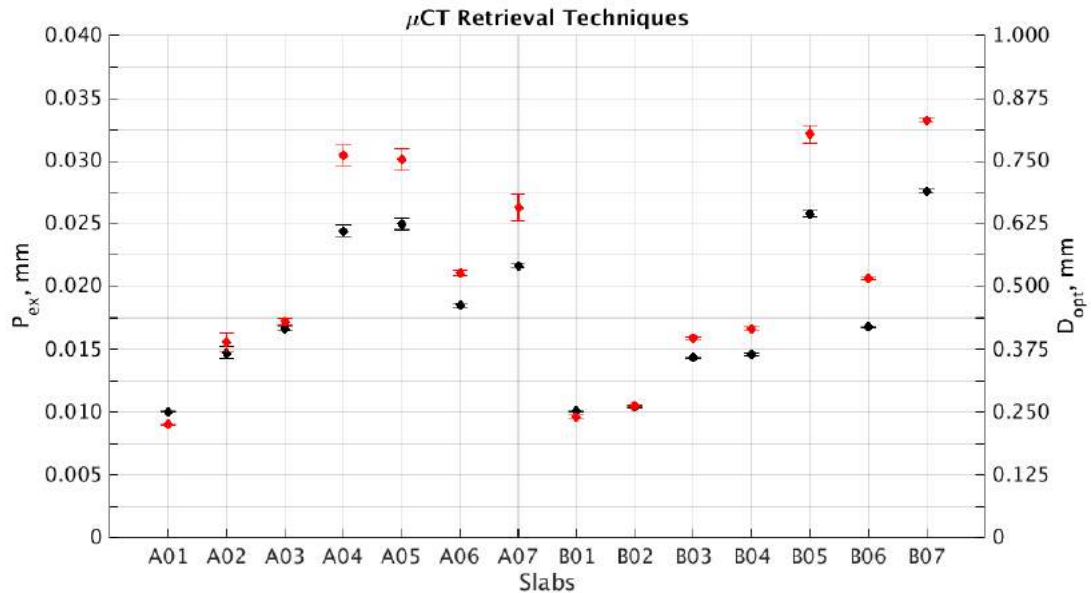
Due to the much higher resolutions (1.25 mm) of the SMP data, the values of  $\rho_{SMP}$  SEM and  $SSA_{SMP}$  SEM are much smaller than the values of  $\rho_s$  SEM and  $SSA_s$  SEM respectively.

Figure 4.18b show the calculated values of  $P_{exSMP}$  and  $D_{optSMP}$ , using the bulk average values of  $\rho_{SMP}$  and  $SSA_{SMP}$ . Like with the  $\rho_{SMP}$  SEM and  $SSA_{SMP}$  SEM

values, the values of  $P_{exSMP}$  and  $D_{optSMP}$  SEM are very small with respect to the values of  $\rho_s$  SEM and  $SSA_s$  SEM, due to the much higher resolution.



(a) Density (black) and SSA (red) measurements from the  $\mu\text{CT}$  measurements.



(b) Calculated values of  $p_{ex}$  (black) and  $D_{opt}$  (red), using  $\mu\text{CT}$  data.

**Figure 4.19:** ASMEEx snow characteristics data, recorded using the  $\mu\text{CT}$  retrieval technique.

Figure 4.19 shows the bulk average values of density ( $\rho_\mu$ ) and SSA ( $SSA_\mu$ ) as measured using the  $\mu\text{CT}$  retrieval methods (as described by [Schneebeli and Sokratov \[2004\]](#) and [Proksch et al. \[2016\]](#)) for the ASMEEx snow slabs (Figure 4.19a), as well as the calculated values of exponential correlation length ( $P_{ex\mu}$ ) and optical diameter ( $D_{opt\mu}$ ), using data from the  $\mu\text{CT}$  retrieval (Figure 4.19b). Like with the SMP bulk average values, the

$\mu$ CT bulk average values make use of the two  $\mu$ CT profiles in the centre of the radiometric footprint.

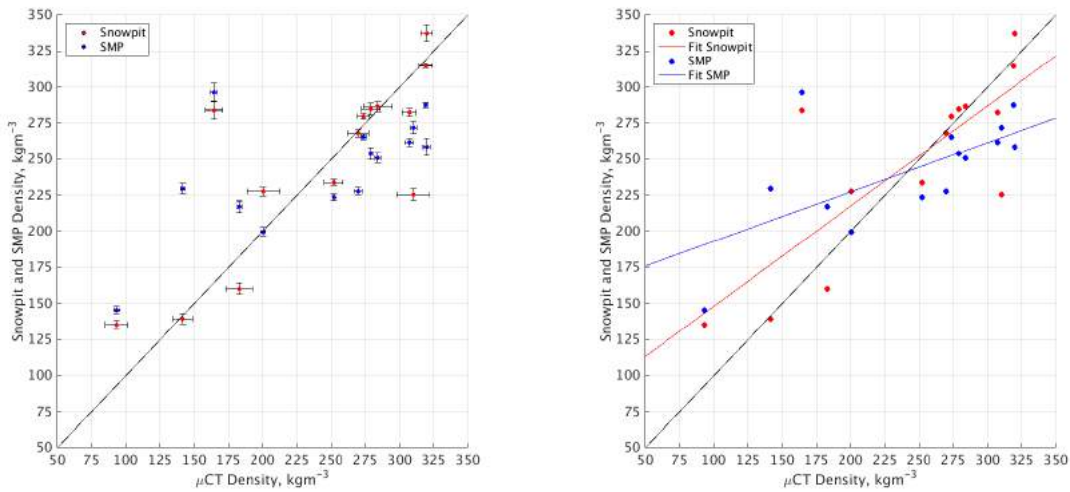
The bulk values of  $\rho_\mu$  range from 93.5 – 319.8  $\text{kgm}^{-3}$ , with bulk values of  $\text{SSA}_\mu$  ranging from 7.3 – 27.1  $\text{m}^2\text{kg}^{-1}$ . The corresponding values of  $P_{ex\mu}$  and  $D_{opt\mu}$  range from 0.1006 – 0.2760 mm and 0.25 – 0.91 mm respectively. The parameters measured via  $\mu$ CT analysis are compared to both the snowpit technique and SMP measurements in Section 4.2.3.2.

The values of  $\rho_\mu$  SEM, like  $\rho_{SMP}$  SEM, are smaller than those of  $\rho_s$  SEM; due to a much larger resolution (60 voxels, 1.08 mm) than that of the box cutter (50 mm). Similarly, the values of  $\text{SSA}_\mu$  SEM, although the stratigraphically complex slab A02 does have the larger values of  $\rho_\mu$  SEM and  $\text{SSA}_\mu$  SEM. The values of  $P_{ex\mu}$  SEM and  $D_{opt\mu}$  SEM do show a similar level of variation to that of  $P_{exSMP}$  SEM and  $D_{optSMP}$  SEM.

#### 4.2.3.2 Snow Characteristic Comparison

While  $T_{phys}$  and E were measured using traditional snowpit techniques (Fierz et al. [2009]),  $\rho$ , SSA,  $P_{ex}$ , and  $D_{opt}$  were measured (and calculated for  $P_{ex}$  and  $D_{opt}$ ) using three sets of techniques; snowpit (box cutter and IceCube), SMP, and  $\mu$ CT retrievals. Proksch et al. [2016] discusses the advantages and disadvantages of each retrieval, with respect to density. The traditional box cutter technique is more robust, more portable, cheaper, and easier to use, as well as having a technical simplicity lacking by the SMP and  $\mu$ CT techniques. However, the box cutter technique can suffer from compaction and loss of snow within the sample, providing an overestimation and underestimation of the recorded density measurement respectively. The box cutter also suffers from a much larger resolution than that of the SMP or  $\mu$ CT techniques. In terms of measurement time, the SMP is more time efficient, as a snowpit is not needed for SMP measurements to take place. Vertical profiles of density (as well as SSA and other snow characteristics) can be recorded through repeated measurements, allowing for spatial variability to be investigated (Proksch et al. [2016]). However,  $\mu$ CT measurements provide a higher resolution of recorded data, and can produce a binary image, containing the full microstructure of the snow sample. The main uncertainty of the  $\mu$ CT measurements come from the binary image generation (Proksch et al. [2016]). In this comparison section, the  $\mu$ CT recorded snow characteristics will be treated as “truth”, and be used as the control dataset to which the snowpit and SMP measurements will be compared.

Figure 4.20 shows a comparison of box cutter and SMP measured density values,

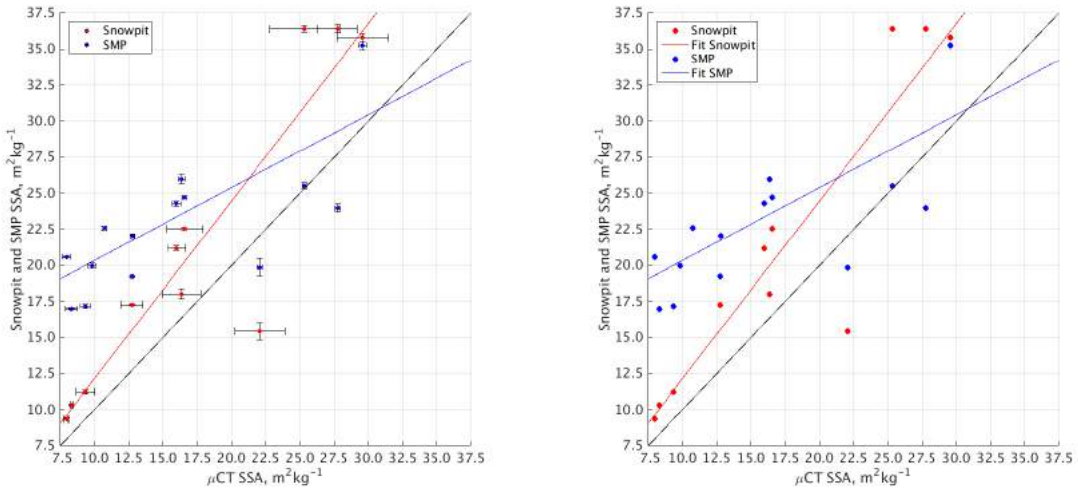


(a) Comparison of  $\rho_s$  (red) and  $\rho_{SMP}$  (blue) with  $\rho_\mu$ . SEM values are plotted as error bars.  
 (b) Linear fits of  $\rho_s$  (red) and  $\rho_{SMP}$  (blue) with  $\rho_\mu$ .

**Figure 4.20:** Comparison of density values measured with snowpit, SMP, and  $\mu\text{CT}$  techniques.

compared to  $\mu\text{CT}$  density values. Figure 4.20a shows the associated SEM values, while Figure 4.20b shows a linear fit for each of the comparison, with a 1:1 line plotted to represent the  $\mu\text{CT}$  retrieval method. It can be seen that the box cutter and SMP both underestimate (overestimate) the value of  $\rho$  above (below) the value of  $\rho_\mu = 255 \text{ kgm}^{-3}$  for the box cutter, and  $\rho_\mu = 242 \text{ kgm}^{-3}$  for the SMP. These threshold values are both smaller than the threshold values calculated by Proksch et al. [2016] ( $\rho_{threshold} = 296 - 350 \text{ kgm}^{-3}$  depending on cutter shape). Two slabs stand out for the box cutter  $\rho$  values; one overestimation (Slab A02:  $\rho_s = 284.2 \pm 6.23 \text{ kgm}^{-3}$ ) and one underestimation (Slab A04:  $\rho_s = 225.7 \pm 12.10 \text{ kgm}^{-3}$ ). Two overestimations stand out for the  $\rho_{SMP}$  values: Slab A02 ( $\rho_{SMP} = 296.4 \pm 2.46 \text{ kgm}^{-3}$ ) and slab B01 ( $\rho_{SMP} = 229.5 \pm 1.74 \text{ kgm}^{-3}$ ). Slab A02 was very stratigraphically complex, as shown in Section 4.2.4. The  $\mu\text{CT}$  retrieval was better at identifying ice layers. The smaller resolution of  $\rho_s$  hindered the retrieval of the bulk averages of slabs with non-homogeneous layers smaller than the box cutter resolution. Proksch et al. [2016] discusses how the SMP data had to be discarded in their investigation, due to calibration issues (from the calculation of regression model coefficients). These calibration issues may be present, due to the larger spread of  $\rho_{SMP}$  measurements. This spread can be seen in Figure 4.20b, where the linear fits are shown. The box cutter linear fit has an  $R^2$  value of 0.6285, with respect to the  $\mu\text{CT}$  data. The SMP linear fit is much weaker, with an  $R^2$  value of 0.3991. This smaller  $R^2$  value associated with  $\rho_{SMP}$  suggests that the SMP instrumentation may be suffering from

calibration issues.

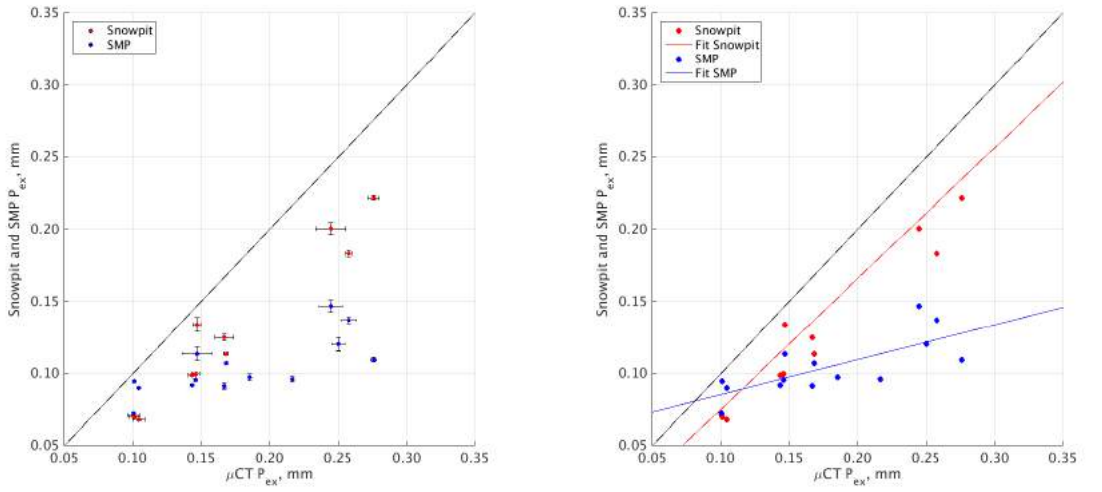


(a) Comparison of SSA<sub>s</sub> (red) and SSA<sub>SMP</sub> (blue) with SSA<sub>μ</sub>. SEM values are plotted as error bars.  
 (b) Linear fits of SSA<sub>s</sub> (red) and SSA<sub>SMP</sub> (blue) with SSA<sub>μ</sub>.

**Figure 4.21:** Comparison of SSA values measured with snowpit, SMP, and  $\mu$ CT techniques.

Figure 4.21 shows a comparison of IceCube and SMP measured SSA values, compared to  $\mu$ CT measured SSA values. Like Figure 4.20, Figure 4.21a show the associated SEM values, while Figure 4.21b show a linear fit for each comparison, with a 1:1 line plotted to represent the  $\mu$ CT data. In Figure 4.21a, more SSA<sub>SMP</sub> values are present, due to the IceCube availability issues. While no individual SSA<sub>s</sub> values stand out as a large overestimate or underestimate, there is a tendency for the IceCube to slightly overestimate SSA, with respect to the  $\mu$ CT technique. This can be seen by the IceCube linear fit in Figure 4.21b. However, the same cannot be said for the values of SSA<sub>SMP</sub>, which largely overestimate the values of SSA with respect to the  $\mu$ CT data. The level of overestimation can be seen in Figure 4.21b. The IceCube linear fit has an R<sup>2</sup> value of 0.6517, and the SMP linear fit has an R<sup>2</sup> value of 0.2814, both with respect to the  $\mu$ CT data. This small R<sup>2</sup> value, and general overestimation of SSA by the SMP instrumentation, further suggests that the SMP instrumentation may be suffering from calibration issues.

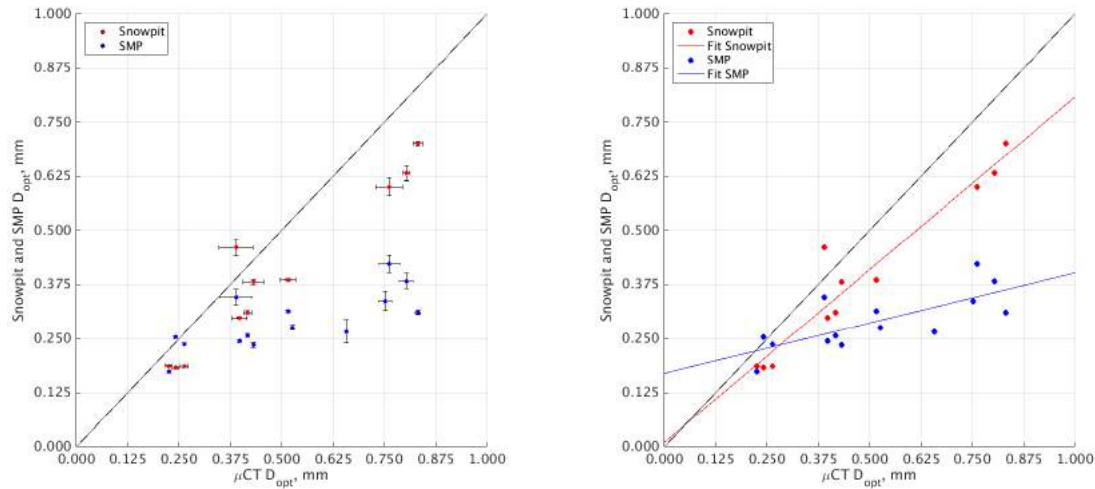
Figure 4.22 shows the comparison of  $P_{exs}$  and  $P_{exSMP}$  values, compared to  $P_{ex\mu}$  values. Figure 4.22a show the associated SEM values to each calculated value, while Figure 4.22b show the resulting linear fits. As  $P_{ex}$  is a product of both  $\rho$  and SSA (from Eqn. 3.4), the resulting overestimations and underestimations from the snowpit and SMP linear fits are present here. A near constant underestimation is present in the  $P_{exs}$  linear fit; a product of the slight overestimation of SSA<sub>s</sub> and mixture of over- and underestimation of  $\rho_s$ .  $P_{exSMP}$  has a large underestimation, due to the large overestimation of SSA<sub>SMP</sub>.



(a) Comparison of  $P_{exs}$  (red) and  $P_{exSMP}$  (blue) with  $P_{ex\mu}$ . SEM values are plotted as error bars.  
 (b) Linear fits of  $P_{exs}$  (red) and  $P_{exSMP}$  (blue) with  $P_{ex\mu}$ .

**Figure 4.22:** Comparison of  $P_{ex}$  values calculated from data collected via the snowpit, SMP, and  $\mu$ CT techniques.

The linear fit of  $P_{exs}$  and  $P_{exSMP}$  have  $R^2$  values of 0.7416 and 0.1433 respectively.



(a) Comparison of  $D_{opts}$  (red) and  $D_{optSMP}$  (blue) with  $P_{ex\mu}$ . SEM values are plotted as error bars.  
 (b) Linear fits of  $D_{opts}$  (red) and  $D_{optSMP}$  (blue) with  $P_{ex\mu}$ .

**Figure 4.23:** Comparison of  $D_{opt}$  values calculated from data collected via the snowpit, SMP, and  $\mu$ CT techniques.

Figure 4.23 shows a similar pattern of underestimation as Figure 4.22. Figure 4.23 shows the comparison of  $D_{opts}$  and  $D_{optSMP}$ , with respect to  $D_{opt\mu}$ . Figure 4.23a show the associated SEM errors, while Figure 4.23b show the resulting linear fits. Similar to those with  $P_{ex}$ ,  $D_{opts}$  suffers from a slight underestimation, while  $D_{optSMP}$  suffers from a

large underestimation with respect to  $D_{opt\mu}$ . The values of  $R^2$  for  $D_{opts}$  and  $D_{optSMP}$  is 0.8384 and 0.1666 respectively.

Table 4.2 shows the RMSE, bias, and  $R^2$  values calculated for the snowpit and SMP observation techniques, compared to the  $\mu$ CT analysis. It's clear that, from the values in Table 4.2 coupled with Figure 4.20, the density observations produced with the box cutter technique do provide a much closer observed bulk value of density than with the SMP instrumentation, when compared to the bulk values of  $\mu$ CT observed density. The IceCube instrumentation also produces more accurate values of bulk SSA than the SMP instrumentation (shown by Figure 4.21), with smaller RMSE and bias values, as well as the much larger  $R^2$  values. Whilst the measurements from the SMP are at a much higher resolution than the coarse snowpit measurements, the current regression models, unfortunately, used by the SMP instrument for ASMEEx campaign did not produce accurate measurements of snow characteristics. Therefore, the snowpit and SMP data will not be used in the single layer HUT simulation shown in Section 4.3, or in the calculation of a new extinction coefficient, shown in Chapter 5.

**Table 4.2:** Snow characteristic retrieval statistics for the snowpit and SMP techniques. RMSE and bias values of density ( $\text{kgm}^{-3}$ ), SSA ( $\text{m}^2\text{kg}^{-1}$ ),  $P_{ex}$  and  $D_{opt}$  (mm) are shown.

Parameter	Snowpit			SMP		
	RMSE	Bias	$R^2$	RMSE	Bias	$R^2$
$\rho$	42.93	4.53	0.6285	54.49	-0.50	0.3991
SSA	5.84	3.81	0.6517	8.23	6.63	0.2814
$P_{ex}$	0.0453	-0.0426	0.7416	0.0876	-0.0744	0.1433
$D_{opt}$	0.1083	-0.0865	0.8384	0.2785	-0.2256	0.1666

## 4.2.4 Stratigraphic Results

### 4.2.4.1 Stratigraphic Data

This section highlights the ASMEEx data collected in its profile form, in order to assess its homogeneity. Figures 4.24 – 4.37 show the profiles of density,  $\rho$  (far left), SSA (middle left), exponential correlation length  $P_{ex}$  (middle right), and optical diameter  $D_{opt}$  (far right), for all 14 ASMEEx slab samples. Each snow characteristic profile shows the observations from all available box cutter and IceCube measurements, as well as from both  $\mu$ CT samples, and two SMP profiles from the centre of the slab. It should be noted that slab A02 only had one  $\mu$ CT sample taken from it, in the  $\mu$ CT samples B location (Figure 3.9). Only SMP profiles from positions B2 and C2 are shown on Figures 4.24 – 4.37, as these two profiles are located closest to the  $\mu$ CT samples, in the centre of the

radiometric footprint. The profiles of  $P_{ex}$  and  $D_{opt}$  are calculated, using Eqns.3.4 and 2.19 respectively, from measured values of  $\rho$  and SSA for their respective techniques.

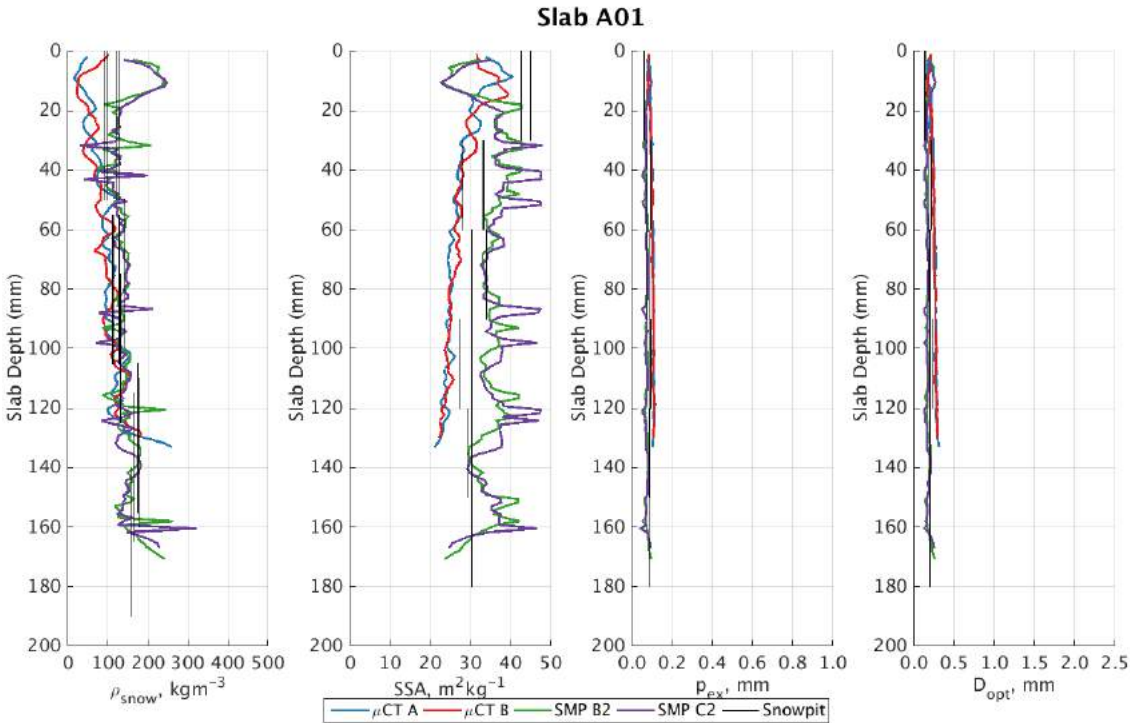


**Figure 4.24:** Profiles of density (far left), SSA (middle left), exponential correlation length (middle right), and optical diameter (far right), for the three different observation techniques for Slab A01.

#### 4.2.4.2 Stratigraphic Comparison

When looking at all profiles, it can clearly be seen that the snowpit techniques (box cutter and IceCube) do not capture the structural and vertical variability of the slab, in any of the four snow characteristic parameters shown. Any internal layers are too finely scaled to be effectively measured by the coarse resolution of the snowpit techniques. This makes stratigraphy analysis of the ASMEEx slabs with snowpit techniques very difficult, and thus stratigraphy analysis will focus on the SMP and  $\mu$ CT profiles. The snowpit techniques, however, are useful for the calculation of bulk average values, as each box cutter or IceCube measurement is effectively measuring multiple bulk averages.

The stratigraphic profiles shown in Figures 4.24 – 4.37 reinforce the findings in Section 4.2.3.2; with observations using snowpit techniques and  $\mu$ CT analysis being in agreement with one another, while those using the SMP (especially  $SSA_{SMP}$ ) being inaccurate. The calculated values of  $P_{ex}$  and  $D_{opt}$ , using observed values of  $\rho$  and SSA, have under- and overestimations associated with the dependent variables. The underestimation of  $SSA_s$

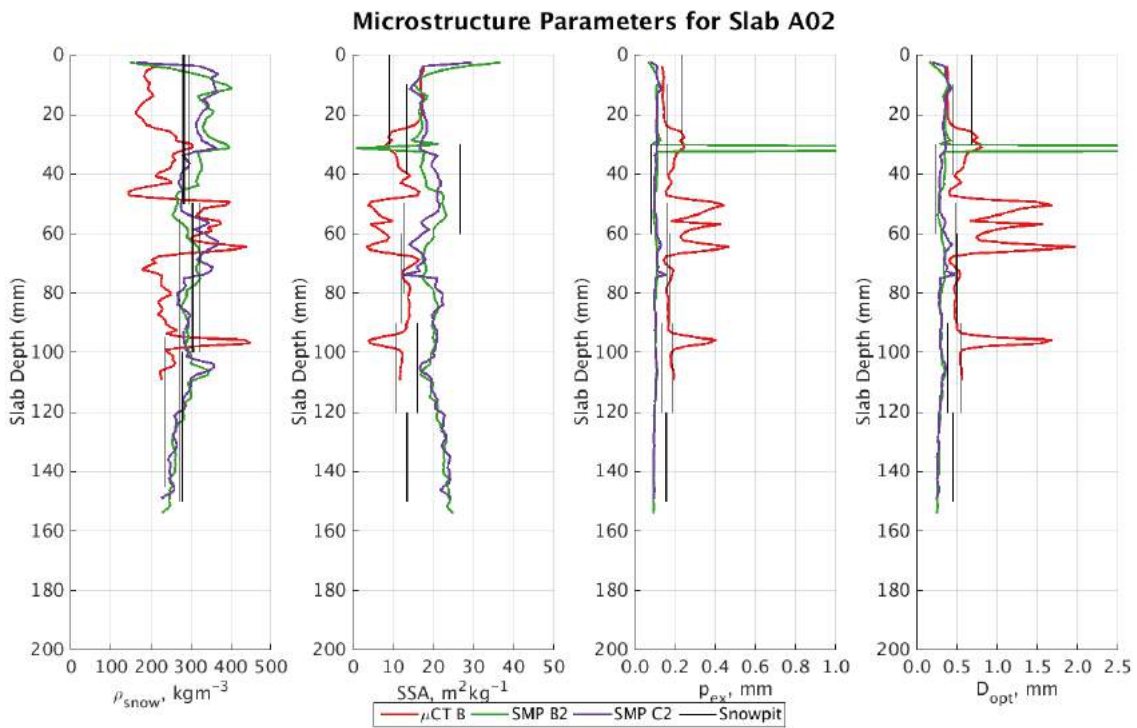


**Figure 4.25:** Profiles of density (far left), SSA (middle left), exponential correlation length (middle right), and optical diameter (far right), for the three different observation techniques for Slab A02. Note: only one  $\mu\text{CT}$  sample was analysed for A02.

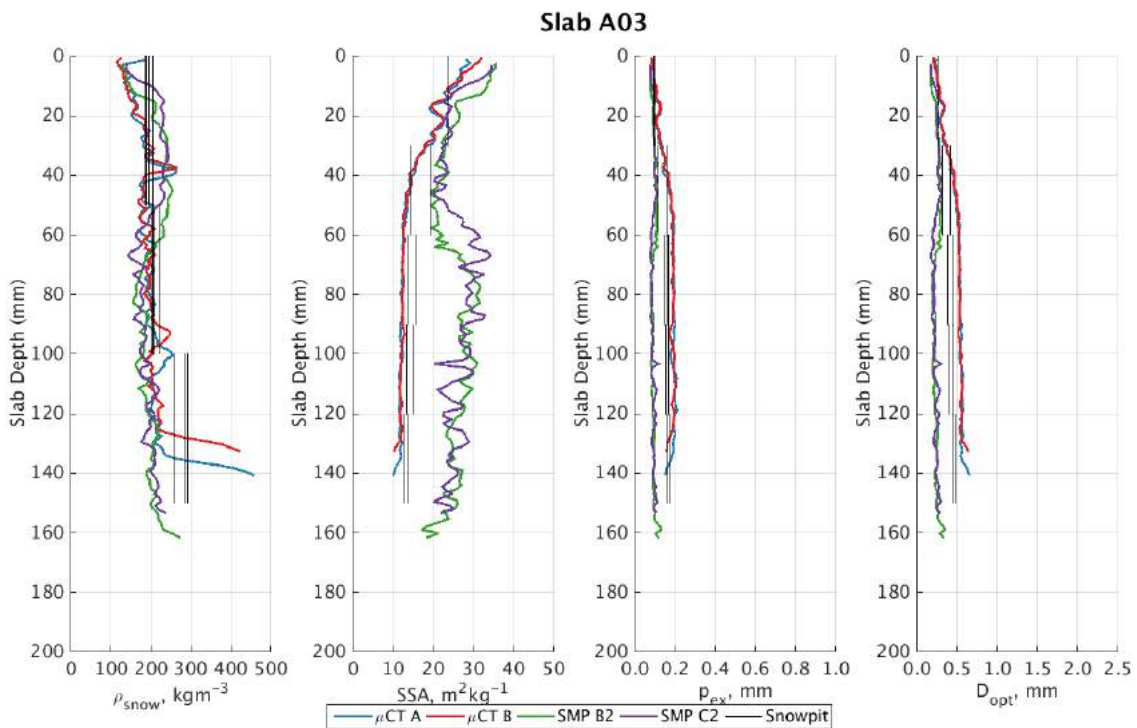


**Figure 4.26:** Profiles of density (far left), SSA (middle left), exponential correlation length (middle right), and optical diameter (far right), for the three different observation techniques for Slab A03.

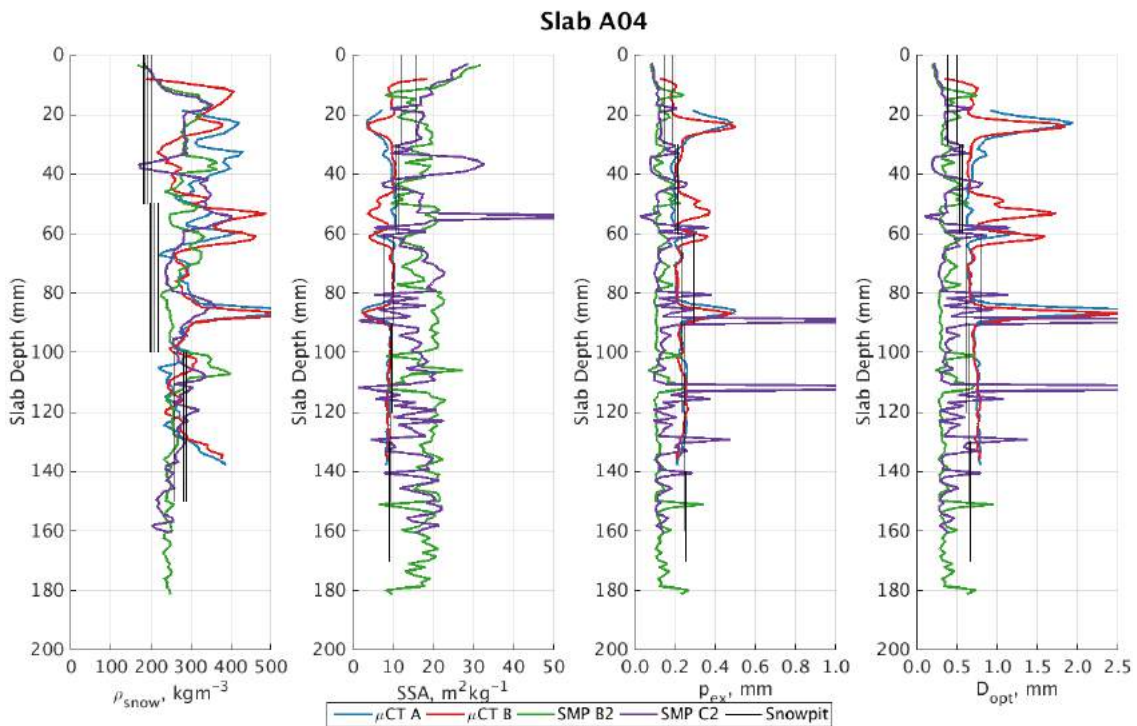


**Figure 4.27:** Profiles of density (far left), SSA (middle left), exponential correlation length (middle right), and optical diameter (far right), for the three different observation techniques for Slab A04.

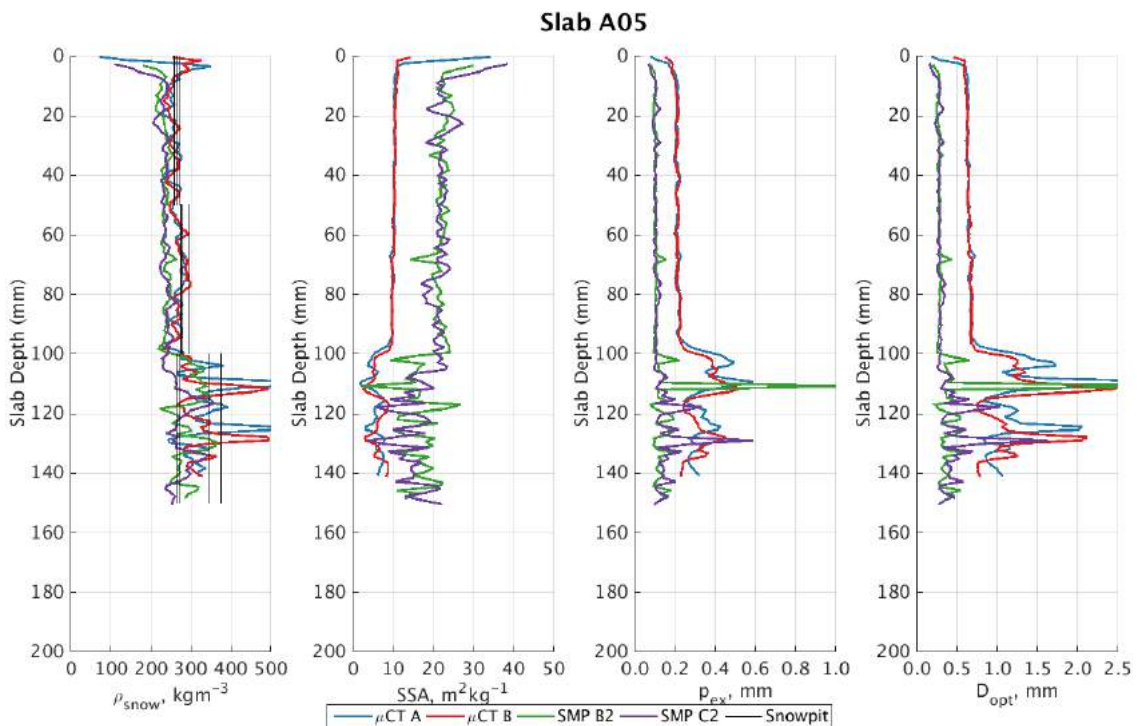


**Figure 4.28:** Profiles of density (far left), SSA (middle left), exponential correlation length (middle right), and optical diameter (far right), for the three different observation techniques for Slab A05. Note: the IceCube machine was not present for slab A05, so no SSA profiles were measured traditionally.

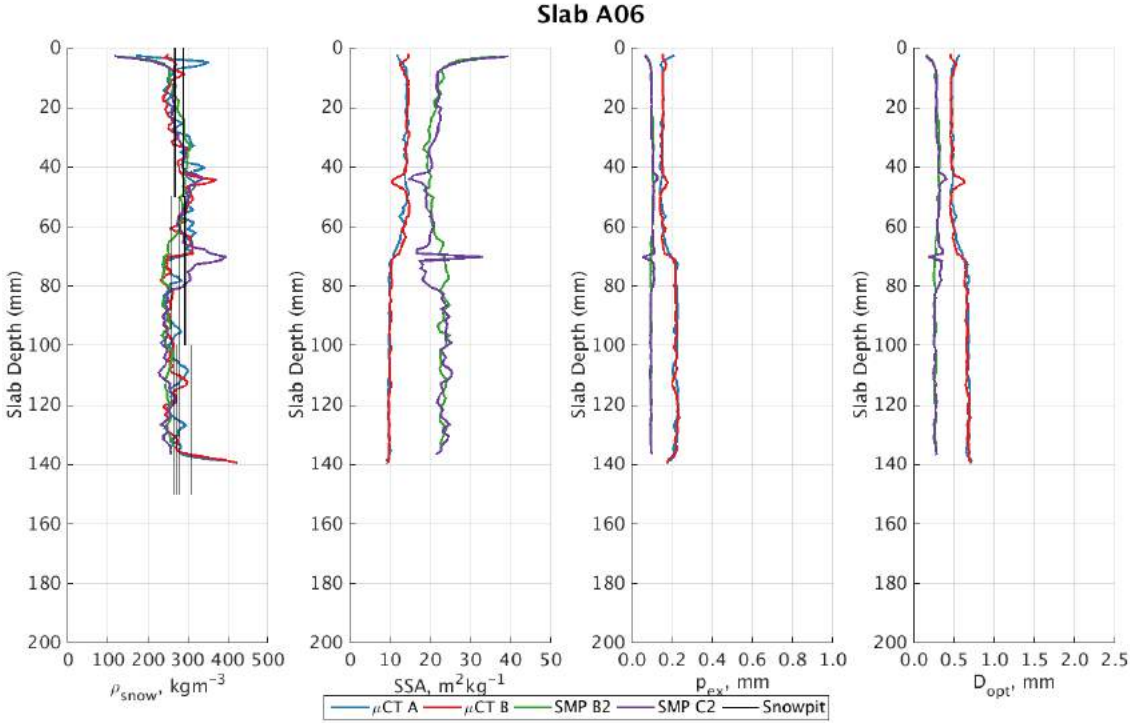


**Figure 4.29:** Profiles of density (far left), SSA (middle left), exponential correlation length (middle right), and optical diameter (far right), for the three different observation techniques for Slab A06. Note: the IceCube machine was not present for slab A06, so no SSA profiles were measured traditionally.

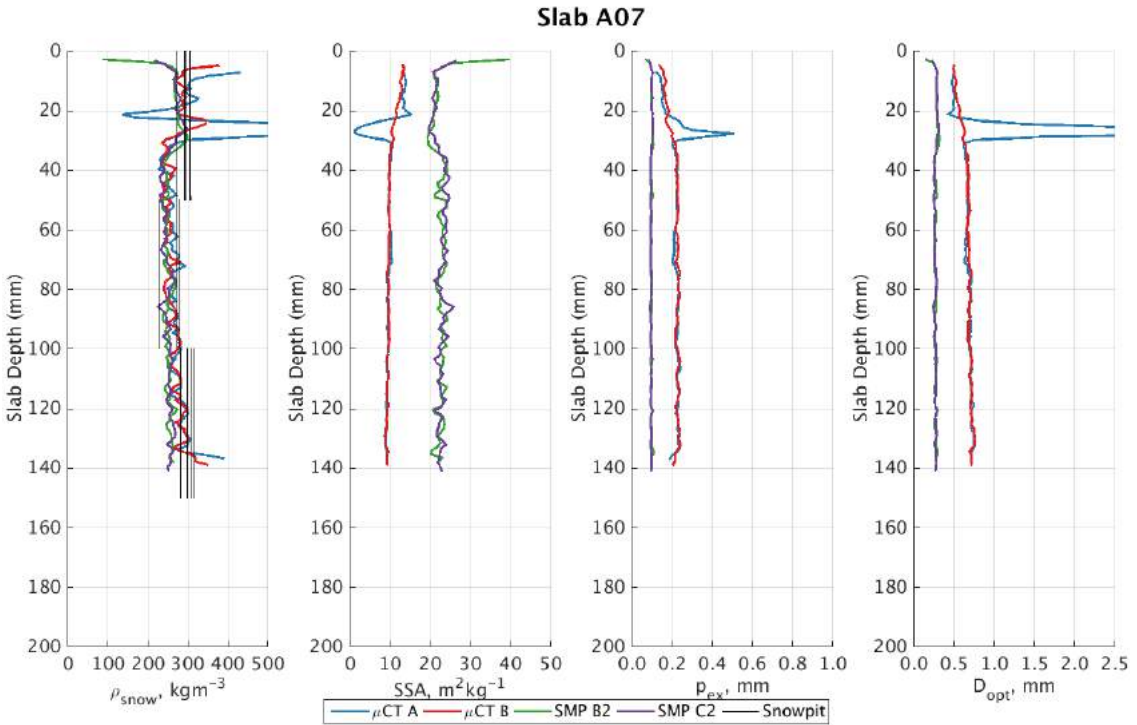


**Figure 4.30:** Profiles of density (far left), SSA (middle left), exponential correlation length (middle right), and optical diameter (far right), for the three different observation techniques for Slab A07. Note: the IceCube machine was not present for slab A07, so no SSA profiles were measured traditionally.

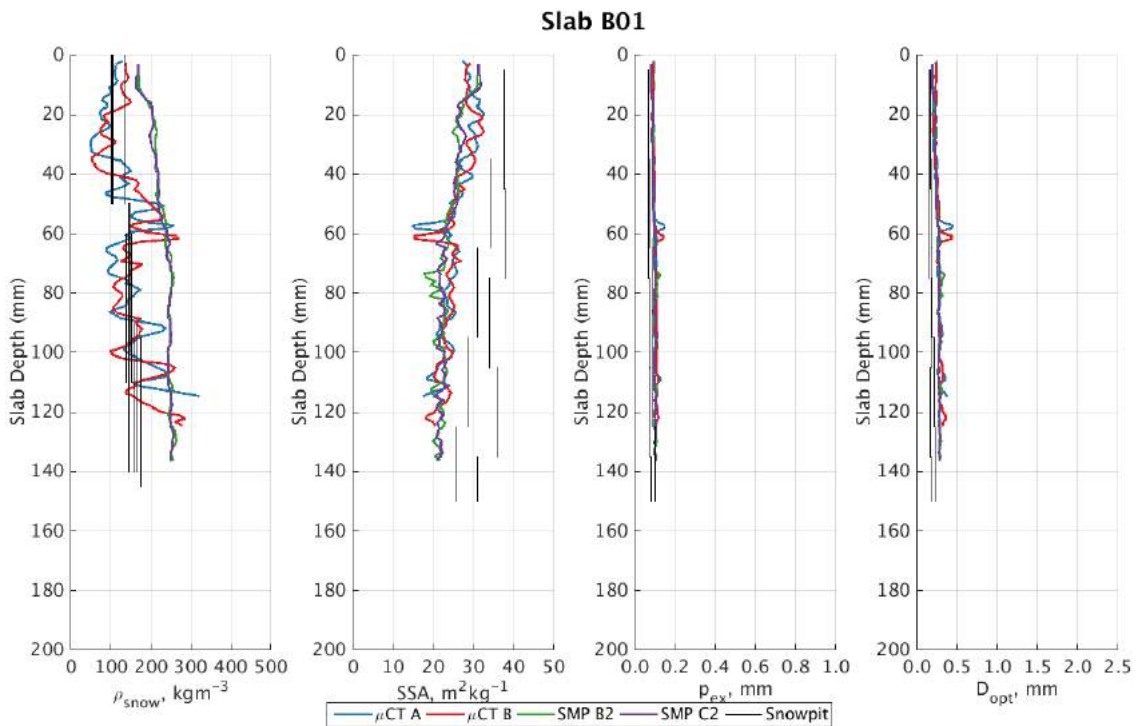


**Figure 4.31:** Profiles of density (far left), SSA (middle left), exponential correlation length (middle right), and optical diameter (far right), for the three different observation techniques for Slab B01.

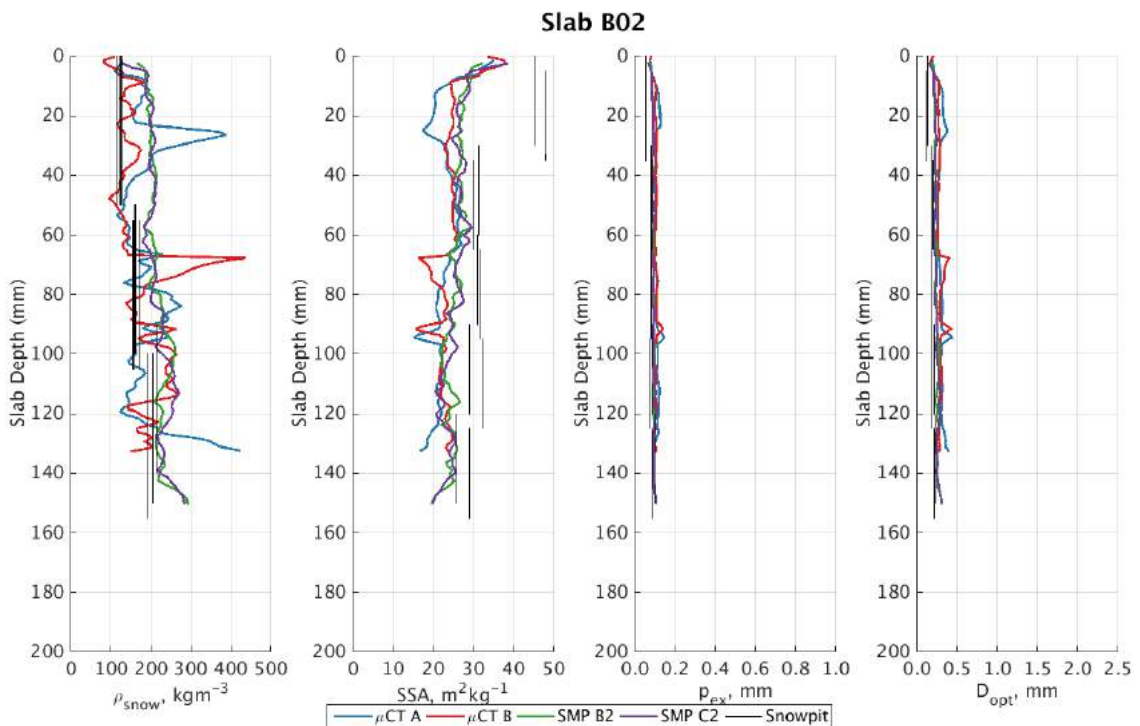


**Figure 4.32:** Profiles of density (far left), SSA (middle left), exponential correlation length (middle right), and optical diameter (far right), for the three different observation techniques for Slab B02.

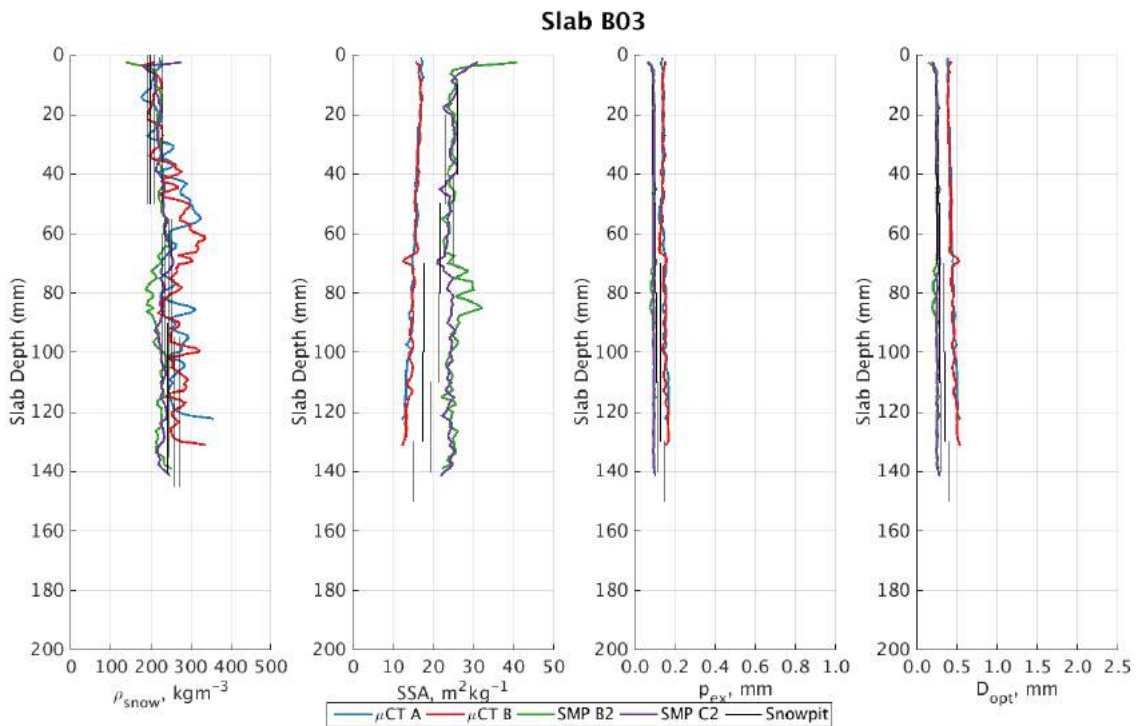


**Figure 4.33:** Profiles of density (far left), SSA (middle left), exponential correlation length (middle right), and optical diameter (far right), for the three different observation techniques for Slab B03.

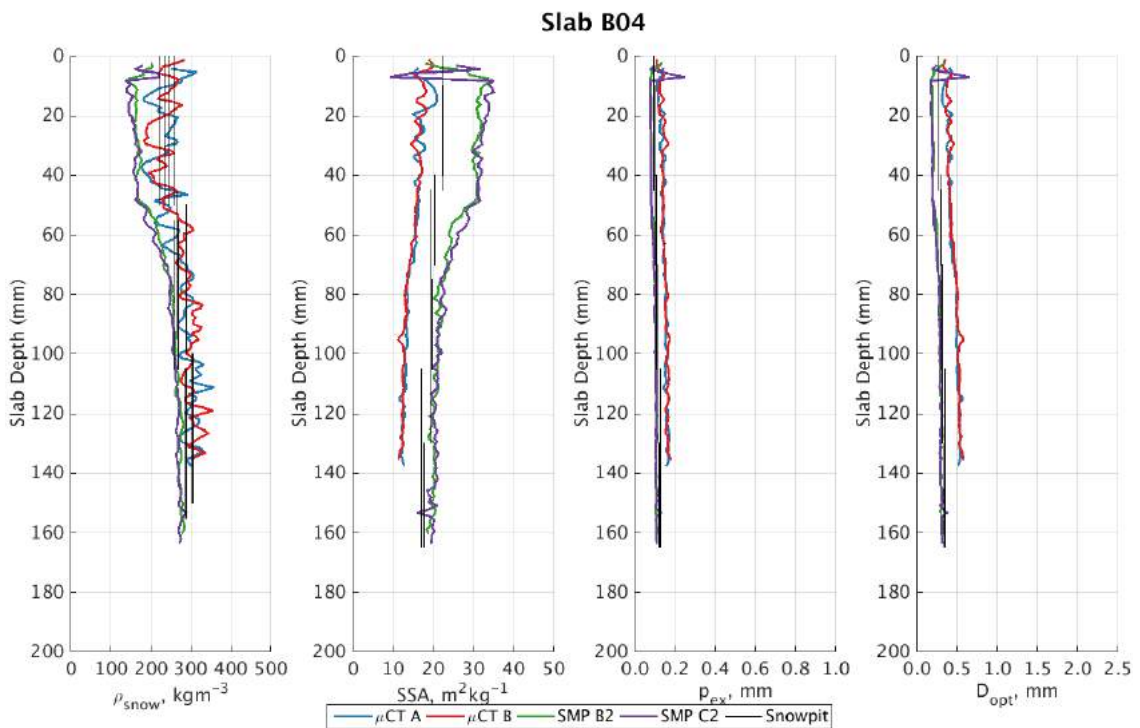


**Figure 4.34:** Profiles of density (far left), SSA (middle left), exponential correlation length (middle right), and optical diameter (far right), for the three different observation techniques for Slab B04.

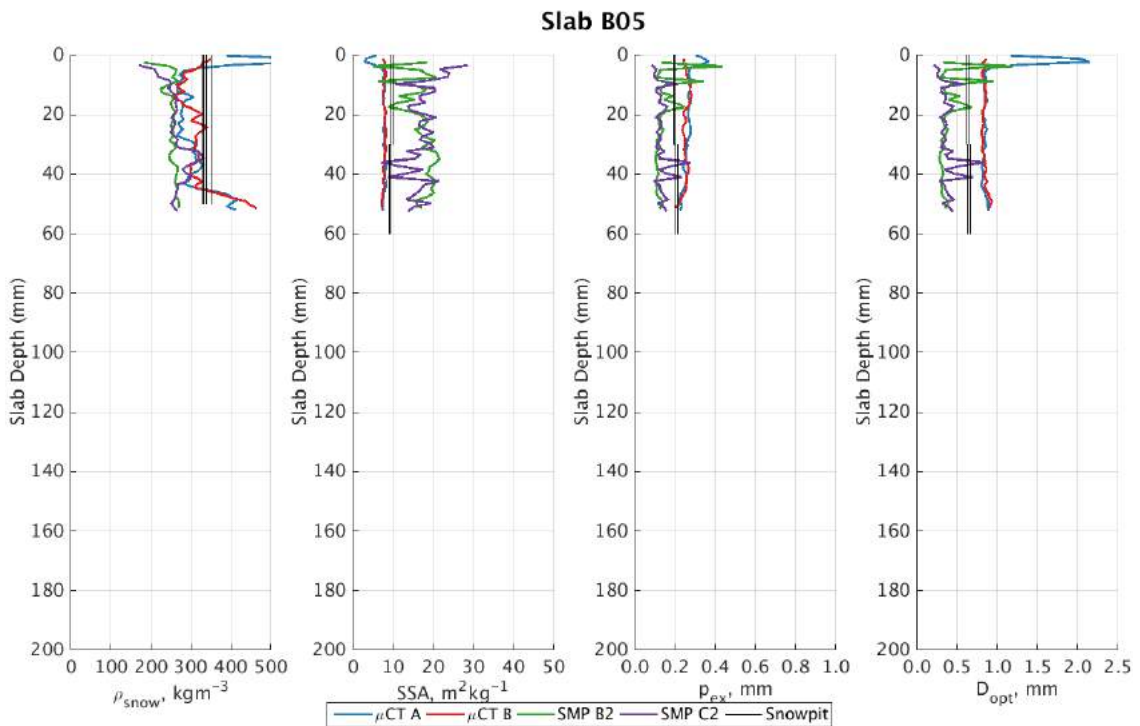


**Figure 4.35:** Profiles of density (far left), SSA (middle left), exponential correlation length (middle right), and optical diameter (far right), for the three different observation techniques for Slab B05.

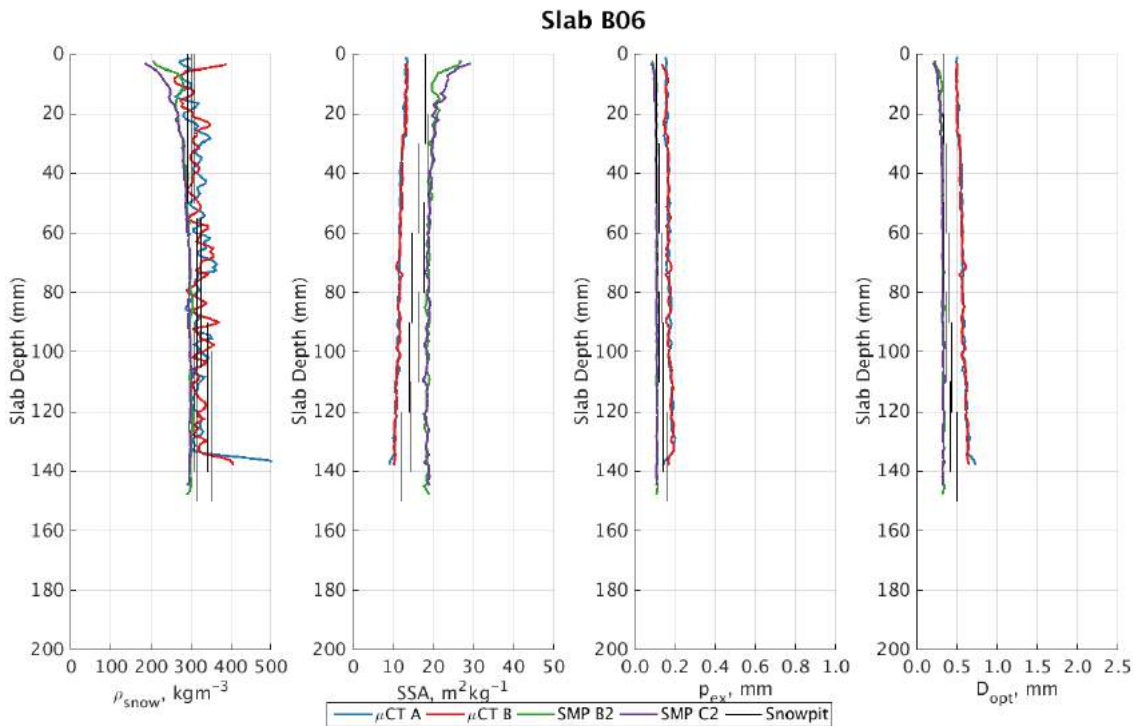


**Figure 4.36:** Profiles of density (far left), SSA (middle left), exponential correlation length (middle right), and optical diameter (far right), for the three different observation techniques for Slab B06.

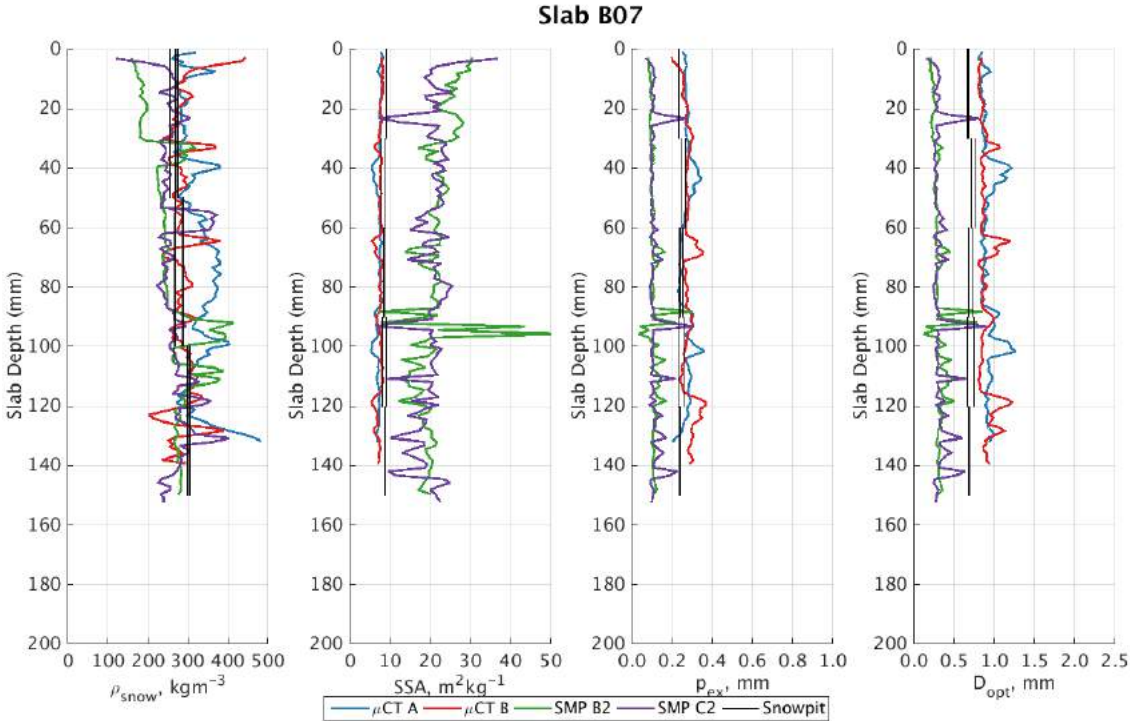


**Figure 4.37:** Profiles of density (far left), SSA (middle left), exponential correlation length (middle right), and optical diameter (far right), for the three different observation techniques for Slab B07.

for fresh snow, coupled with the overestimation of  $\rho_s$  from the box cutter method, results in a near uniform underestimation of  $P_{\text{exs}}$  (Figure 4.22b). The large overestimation of  $\text{SSA}_{\text{SMP}}$ , however, masks any contribution from the over- and underestimation of  $\rho_{\text{SMP}}$ . This leads to the large underestimation of  $P_{\text{exSMP}}$  present across all values of  $P_{\text{ex}\mu}$  larger than 0.1 mm; representing all but fresh snow types. Similarly, the profiles of  $D_{\text{opt}}$  also suffers from a slight underestimation for the more coarse grains, while profiles of  $D_{\text{opt}\mu}$  largely underestimate the values of  $D_{\text{opt}}$ .

#### 4.2.4.3 Homogeneity Analysis

Due to the accuracy issues surrounding the SMP measured and calculated snow characteristics, the SMP technique will not be used for stratigraphy analysis of the slabs. Stratigraphy analysis of the slabs will therefore be focused around the  $\mu\text{CT}$  technique and snow characteristics. The stratigraphy of the slabs can be easily seen in the  $\mu\text{CT}$  profiles. Homogeneous slabs would have uniform values of snow characteristics, such as  $\rho$ , SSA,  $P_{\text{ex}}$ , and  $D_{\text{opt}}$ . Sudden changes of any of these parameters would suggest a layer being present within the slab (Fierz et al. [2009]). Such sudden changes can be seen in various ASMEEx slabs, such as slab A05 (Figure 4.28). In slab A05. the top 100 mm were found to

be homogeneous, as shown by the uniform profiles. However, ice layers were found in the lower 50 mm, signified by the sudden increase and variability of  $\rho$ ,  $P_{ex}$ , and  $D_{opt}$ , and the sudden decrease in SSA, in the  $\mu$ CT profiles. By using the  $\mu$ CT profiles, and assessing the level of variability present, it is possible to categorise the slabs as either homogeneous or non-homogeneous. The  $\mu$ CT instrumentation are the only set instrumentation in the ASMEx campaign to complete this analysis, as the snowpit techniques suffer from a too coarse resolution, and the SMP technique suffers from calibration issues.

The  $\mu$ CT snow characteristic profiles can be assessed, using standard deviation threshold values, in terms of its stratigraphy. Slabs can be categorised as homogeneous or non-homogeneous depending on if the standard deviation values fall below or above the threshold values. Figure 4.38 show the standard deviation values of each  $\mu$ CT sample for density (Figure 4.38a), SSA (Figure 4.38b),  $P_{ex}$  (Figure 4.38c), and  $D_{opt}$  (Figure 4.38d).

The horizontal line depicted on Figures 4.38c and 4.38d show the threshold values designated homogeneous and non-homogeneous slabs. No threshold value of homogeneity was applied to the density standard deviation values, as the standard deviation values of density of slab A02 (a slab known to contain ice layers) were similar to those calculated for A01 (a slab taken from fresh surface snow); a slab known to be homogeneous. Thus, it was decided that density standard deviation values were not included in the assessment of internal stratigraphy. The standard deviation values of SSA also were not used in the assessment of internal stratigraphy. This too is due to the standard deviation values of slab A02 being equal to that of slab A01, while slab A03 (a wet homogeneous slab) has a larger calculated standard deviation value.

The two calculated snow characteristics profiles,  $P_{ex}$  and  $D_{opt}$ , do show a clear distinction between homogeneous and non-homogeneous profiles. Larger standard deviation values in both of these parameters are linked to the stratigraphy of the slabs. Threshold values of 0.035 mm and 0.15 mm for  $P_{ex}$  and  $D_{opt}$ , respectively, were chosen to define the homogeneous and non-homogeneous categories. These values were chosen by comparing values of standard deviation of known homogeneous slabs (such as slab A01 and B06) with those known to be non-homogeneous (such as slabs A02 and A05). The homogeneity of certain slabs were made very clear during the extraction of the slab from the natural snowpack, as ice layers within the snowpack were visually inspected and cut through, when cutting the slab out of the snowpack (Section 3.5.1). Using these visually derived threshold values, 8  $\mu$ CT  $P_{ex}$  profiles, and 7  $\mu$ CT  $D_{opt}$  profiles, were defined as non-homogeneous. Table 4.3 shows a comparison of all  $\mu$ CT profiles of  $P_{ex}$  and  $D_{opt}$ , with

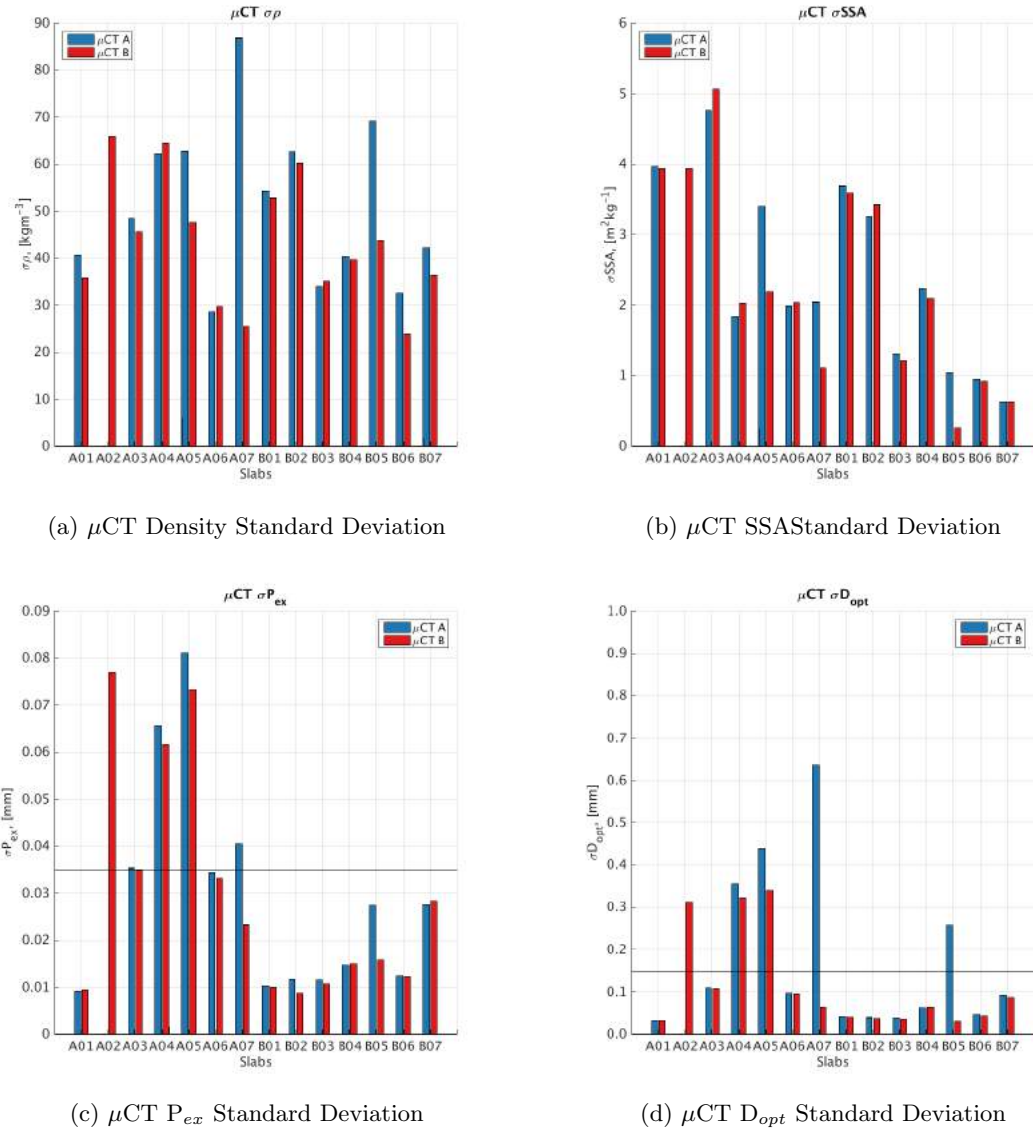


**Figure 4.38:** Standard deviation of snow characteristics from  $\mu\text{CT}$  profiles. Horizontal lines show threshold values for the stratigraphy analysis.

respect to the threshold values, and the category of stratigraphy analysis.

It can be seen that slabs deemed non-homogeneous by one snow characteristic was often deemed non-homogeneous by the other profile. The main exception to this are the profiles measured in slab A03, whose  $P_{ex}$  profiles have standard deviation values above the 0.035 mm threshold, but have  $D_{opt}$  profiles with standard deviation values below the threshold. By looking at the profiles of slab A03 (Figure 4.26), the profiles of SSA clearly show a profile on decreasing SSA in the uppermost 60 mm, with the lowermost 80 mm having a uniform profile. This pattern in the SSA profile is shown inversely in the  $P_{ex}$  and  $D_{opt}$  profiles; that the uppermost 60 mm have an increasing snow characteristic, with the lowermost 80 mm being uniform. While the discussion on the nature of the homogeneity

**Table 4.3:** Profiles that have a  $\sigma$  value higher than the designated threshold value. As slab A02 does not have a  $\mu$ CT A profile, it is denoted with N/A.

Slab	$P_{ex}$		$D_{opt}$		Homogeneity
	$\mu$ CT A	$\mu$ CT B	$\mu$ CT A	$\mu$ CT B	
A01					Homogeneous
A02	N/A	X	N/A	X	Non-homogeneous
A03	X	X			Wet
A04	X	X	X	X	Non-homogeneous
A05	X	X	X	X	Non-homogeneous
A06					Homogeneous
A07	X		X		Non-homogeneous
B01					Homogeneous
B02					Homogeneous
B03					Homogeneous
B04					Homogeneous
B05			X		Homogeneous
B06					Homogeneous
B07					Homogeneous

of slab A03 is complex, slab A03 will not be used in simulating the brightness temperature through the HUT snow emission model (Section 4.3). This is due not to its stratification (as all other slabs will be initially simulated), but is due to the slab being classified as “wet” (Section 2.3.2.2). Slab A03 has been classified as wet, due to the above-melting air temperature experienced during the extraction and observation of the slab, as well as the near-melting temperature of the slab during the snow characteristic observation (Figure 4.15).

#### 4.2.5 Fieldwork Data Discussion

As shown in Section 4.2, ASMEEx campaign data were collected from extracted snow slabs upon two different radiometric bases. The radiometric data, collected first, gave observed brightness temperatures of the snow slabs. From the radiometric data alone, interesting patterns could be discussed. The difference between the brightness temperature of snow upon the absorbing base and snow upon the reflective base was found to decrease as the frequency increased; a pattern which is indicative of the decreased penetrative depth of microwave radiation with decreasing wavelength. The pattern also suggests that there is an increasing amount of scattering of microwave radiation taking place within the slab as the frequency increases; a fact that has been widely discussed in the literature (Hallikainen et al. [1987], Roy et al. [2004], Kontu and Pulliainen [2010], Chang et al. [1987], Rees [2006], and Grody [2008]). The large difference in brightness temperatures of snow upon the two radiometric bases comes from the way in which the ground emission of

microwave radiation occurs. As the absorbing base is a near-perfect blackbody absorber (Table 3.2), the absorbing base emits a brightness temperature close to its physical temperature. This large brightness temperature is propagated through the snow slab, and observed by the SodRad platform. The reflective plate is not treated as a near-perfect absorber, but as a near-perfect reflector. This means that the ground emission of microwaves in fact comes from downwelling sky radiation propagating downwards through the snowpack. This downwelling radiation is present for the absorbing base observations, but it is readily absorbed by the near-perfect absorber, so is neglected from the analysis.

Snow characteristic data was collected in three different ways; through snowpit techniques (probe thermometers, macrophotography, box cutter, and IceCube measurements), through SMP techniques (from regression models using measured penetrative resistance), and through  $\mu$ CT techniques (from scans of subsamples using  $\mu$ CT methods). The purpose of this comparison is to test the three different techniques for their suitability and accuracy of measuring snow characteristic parameters. Whilst physical temperatures and traditional grain size were measured using only the snowpit techniques, snow density and SSA were measured using all three techniques, allowing for a comparison of measurements and accuracy. It was found that the snowpit measurements of density and SSA were close to those of the  $\mu$ CT techniques, whilst the measurements of density and SSA using the SMP techniques were not as close. This lack of accuracy has been accredited to problems with calibration coefficients within the regression model used with the SMP raw data. The closeness of the snowpit techniques measurements, and subsequent lack of accuracy with the SMP data, to the  $\mu$ CT data is mirrored in the stratigraphy analysis, when comparing profiles of data.

The single layer HUT snow emission model does not require high resolution profiles of data, but bulk averages of snowpacks, as the model assumes the snowpack is homogeneous. In this instance, either the box cutter density measurements or the  $\mu$ CT profile data would be sufficient, as bulk averages of box cutter and  $\mu$ CT density measurements agree with an  $R^2$  of 0.63 (Table 4.2). However, when higher resolution measurements are needed (such as the stratigraphy analysis in Section 4.2.4.3, or analysis of slab anisotropy in Section 5.3.2.1), the coarse resolution of the box cutter and IceCube measurements is not sufficient.

### 4.3 Comparison of HUT Simulations: ASMEEx

Through the radiometer and snow characteristic observations, the radiometric, snow characteristic, and stratigraphic properties of all 14 snow slabs are known. Using this data, the microwave emission of the snow slabs were simulated, using the single layer HUT snow emission model. Two separate sets of simulations were produced; brightness temperature simulations using snowpit instrumentation data (box cutter density and, through Eqn. 2.17, SWE), and brightness temperature simulations using  $\mu$ CT instrumentation data ( $\mu$ CT density and, through Eqn. 2.17, SWE). The slabs were modelled as controlled single layer snowpacks, upon a ground layer. The ground layer, for the ASMEEx slab samples, are the two different bases used in the radiometric observation, as described in Section 3.4. The radiometric properties of the ground layer can be altered within the HUT snow emission model; this alters the reflective properties of the ground-snow boundary. For the reflective base, the snow-ground boundary was treated as a perfect reflector, such that the reflective properties of the ground were set to one ( $r_{ground} = 1$ ).. For the absorbing base, the snow-ground boundary was treated as a perfect absorber, therefore the snow-ground boundary had zero reflective properties ( $r_{ground} = 0$ ).

For the reflective base, the physical air temperature was used as the physical temperature of the metal reflective plate. The physical temperature of the air was used, as the metal plate was left exposed to the air, during the night prior to the campaign measurement. This allowed for the metal plate to equalise to the air temperature, and thus keep the metal plate below freezing. The absorbing bases were also left to cool in the sub-zero air, and had its physical temperature measured using a probe thermometer throughout the radiometric measurements, in order to observe and record any sudden changes in physical temperature.

After the correct ground properties had been inputted into the HUT snow emission model, the snow slabs were inputted into the HUT snow emission model. As discussed by Pulliainen et al. [1999] and Lemmetyinen et al. [2010], the HUT snow emission model requires the snowpack (or snow slabs in the ASMEEx campaign) to be described by its depth, density, traditional grain size, physical temperature, snow moisture content and snow/ice salinity (as described in Fierz et al. [2009]). For the ASMEEx slabs, both the salinity and the snow moisture content were assumed to be zero. As the dry slabs were simulated with the HUT snow emission model, slab A03 was not be modelled, due to the warmer than freezing air temperature during observations (as described in Section 4.2.4.2).

For this initial simulation of brightness temperature using the HUT snow emission model, two separate extinction coefficients could be used (as described in depth in Section 2.5.4.3). For this study, the extinction model produced by Hallikainen et al. [1987] was used. This extinction coefficient was chosen, as the range of traditional grain sizes used to build the Hallikainen et al. [1987] extinction coefficient (0.2 – 1.6 mm) is similar to the traditional grain size range observed in the ASMEEx campaign (0.45 – 1.81 mm). The Roy et al. [2004] extinction coefficient was not used, as the range of traditional grain sizes (1.3 – 4.0 mm) used to develop the model does not encompass the grain sizes observed in the ASMEEx campaign.

The input files for the single layer HUT simulation runs were created using observations of snowpack parameters via snowpit observation techniques and  $\mu$ CT observation techniques (Section 3.5.3), thus producing two sets of brightness temperature simulations.

Figures 4.39 – 4.43 show the two different set of HUT simulation runs, using the snowpit and  $\mu$ CT techniques, at 18.7, 21.0, 36.5, 89.0, and 150.0 GHz respectively. Subplots (a) and (b) shows the snowpit HUT brightness temperature simulations, while subplots (c) and (d) show the HUT brightness temperature simulations using the  $\mu$ CT snow characteristic data. Using the stratigraphy analysis performed in Section 4.2.4, homogeneous and non-homogeneous slabs were determined, allowing for a revised set of simulations to take place. Therefore, by defining homogeneous slabs as those in Table 4.3, another set of HUT simulation runs were completed. Within Figures 4.39 – 4.43, subplots (a) and (c) show simulations completed using all dry slabs (all slabs excluding A03), and subplots (b) and (d) show the HUT brightness temperatures using only the homogeneous dry slabs.

From Figures 4.39 – 4.43, RMSE and bias statistics were calculated, in order to assess the modelled brightness temperature accuracy. Tables 4.4 and 4.5 show the values of RMSE and bias for each set of HUT simulations, at each frequency. Some common RMSE and bias patterns can be seen in Tables 4.4 and 4.5 across the four simulation runs. Simulations of brightness temperature at 18.7, 21.0, and 36.5 GHz have smaller RMSE values than those at 89.0 and 150.0 GHz. This is to be expected at 150.0 GHz, as the HUT snow emission model is not applicable at such a high frequency (Pulliainen et al. [1999] and Hallikainen et al. [1987]). However, 89.0 GHz is within the operational frequency of the HUT snow emission model.

The large RMSE values associated with the 89.0 GHz simulations are associated with the smaller penetration depths experienced with that frequency. Using Eqn. 2.23, the penetration depth at 89.0 GHz (assuming a complex permittivity of  $\epsilon = 1.5 + 0.01i$ )

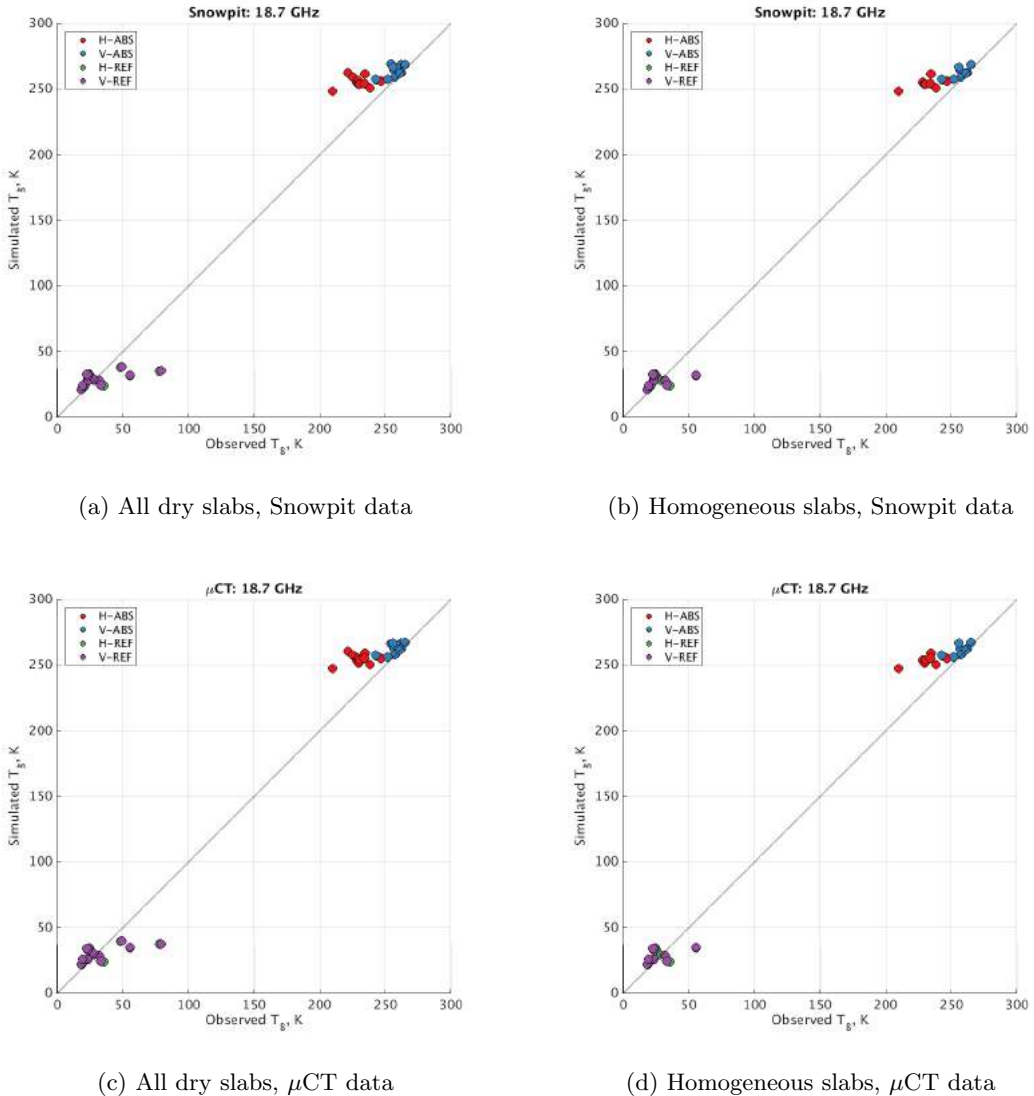


**Figure 4.39:** HUT Simulations compared to SodRad observations for the absorbing base (H-Pol: Red / V-Pol: Blue) and reflective base (H-Pol: Purple / V-Pol: Orange) at 18.7 GHz. Simulations use the traditional observations ((a) and (b)), and  $\mu$ CT observations ((c) and (d)) of snow slab parameters. Simulations are defined by using all dry slabs ((a) and (c)) and homogeneous slabs ((b) and (d)).

is 0.0657 m (using Eqn. 2.23), meaning that the power of the microwave emission has been reduced by a factor of  $e$  in 6.57 cm of snow. As the snow slabs have a thickness of approximately 15 cm (with the exception of slab B05, whose slab has a thickness of approximately 5 cm), large amounts of radiation have been scattered away at this high frequency. As a significant proportion of the radiation has been scattered away in such a small depth, the emission from the underlying surface (emitted by the blackbody absorber or the reflected sky radiation from the reflective plate) has little effect in the observed brightness temperature. This can be seen in both Figure 4.42 and 4.43 respectively, as the range of all observed brightness temperatures are much smaller (35 K at 150.0

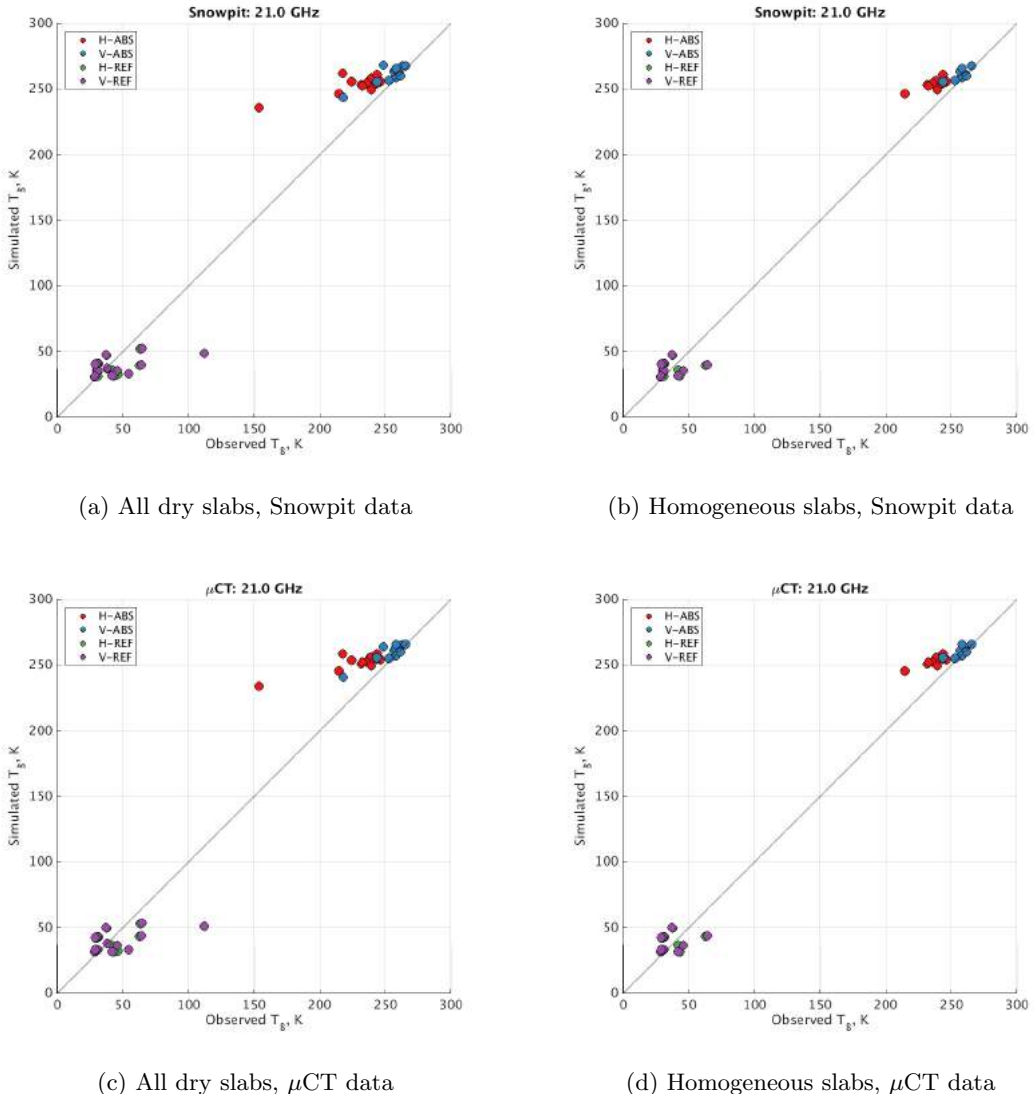


**Figure 4.40:** HUT Simulations compared to SodRad observations for the absorbing base (H-Pol: Red / V-Pol: Blue) and reflective base (H-Pol: Purple / V-Pol: Orange) at 21.0 GHz. Simulations use the traditional observations ((a) and (b)), and  $\mu$ CT observations ((c) and (d)) of snow slab parameters. Simulations are defined by using all dry slabs ((a) and (c)) and homogeneous slabs ((b) and (d)).

GHz and 50 K at 89.0 GHz), than at the lower three frequencies. It can also be seen in Figures 4.42 and 4.43 that the HUT simulated brightness temperatures are generally underestimated at 89.0 GHz (as shown by the negative bias values in Table 4.5) and largely overestimated at 150.0 GHz. The simulated brightness temperatures for the absorbing base simulations (H-Abs and V-Abs) at 89.0 GHz are more accurate than the simulated brightness temperatures for the reflective base simulations (H-Ref and V-Ref), as the magnitude of the 89.0 GHz RMSE and bias values are smaller. The larger RMSE and bias values for the reflecting plate simulations is due to the problems the single layer HUT snow emission model has in simulating the reflecting plate at higher frequencies, due to

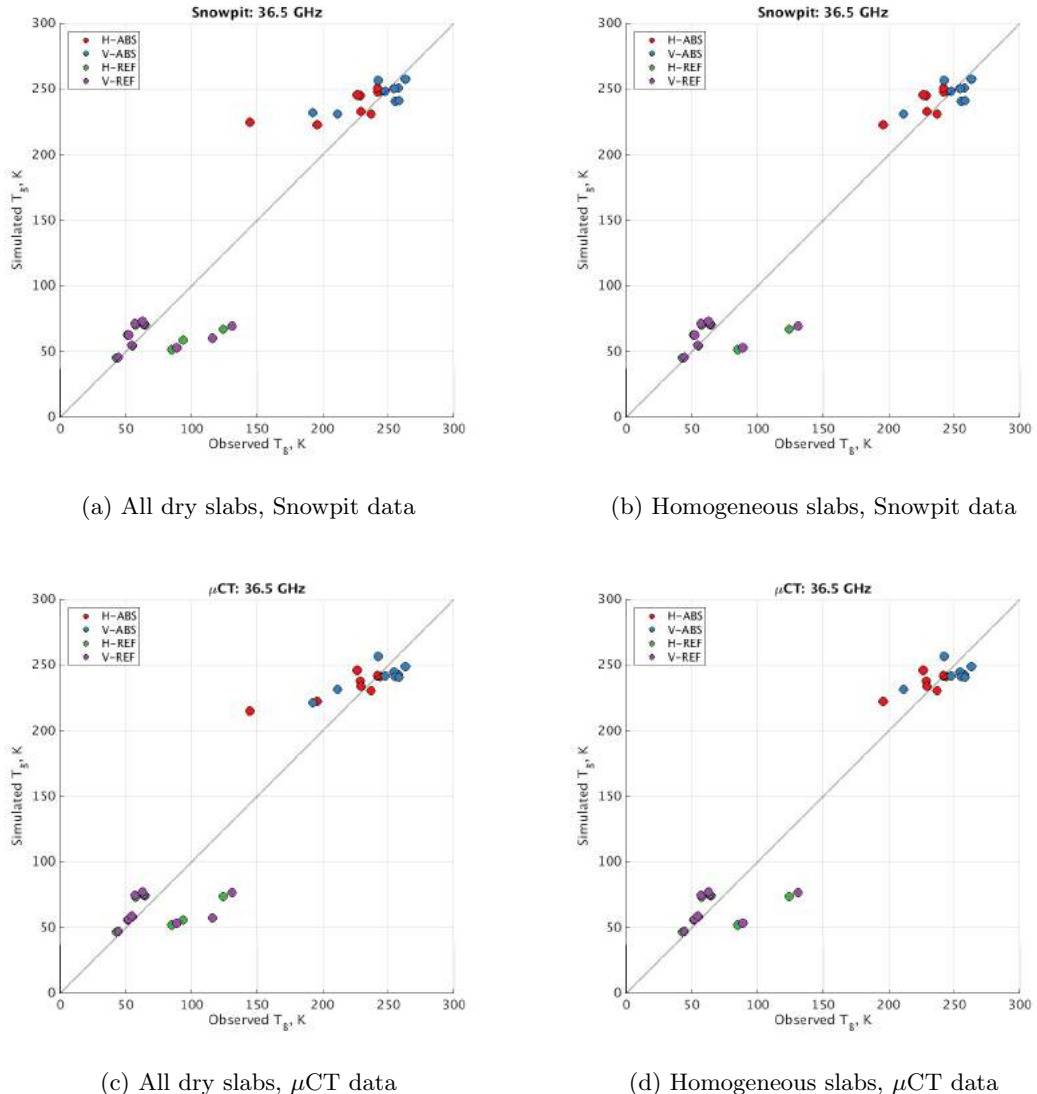


**Figure 4.41:** HUT Simulations compared to SodRad observations for the absorbing base (H-Pol: Red / V-Pol: Blue) and reflective base (H-Pol: Purple / V-Pol: Orange) at 36.5 GHz. Simulations use the traditional observations ((a) and (b)), and  $\mu$ CT observations ((c) and (d)) of snow slab parameters. Simulations are defined by using all dry slabs ((a) and (c)) and homogeneous slabs ((b) and (d)).

the properties of the reflective plate. The microwave emission from the reflective plate comes from the downwelling sky radiation, after it has propagated through the slab. This propagation through the slab at 89.0 GHz is not modelled correctly, and thus produce the incorrect values of brightness temperature for the reflective plates.

For the lower three frequencies, the simulations of the snow upon the absorbing base at horizontal polarizations have the largest magnitude of RMSE and bias. This is true for both the dry slab simulations and homogeneous simulations, and for both the snowpit and  $\mu$ CT data inputs. This suggests that the larger error values are a result of problems within the simulation, rather than measurement technique or slab homogeneity. There

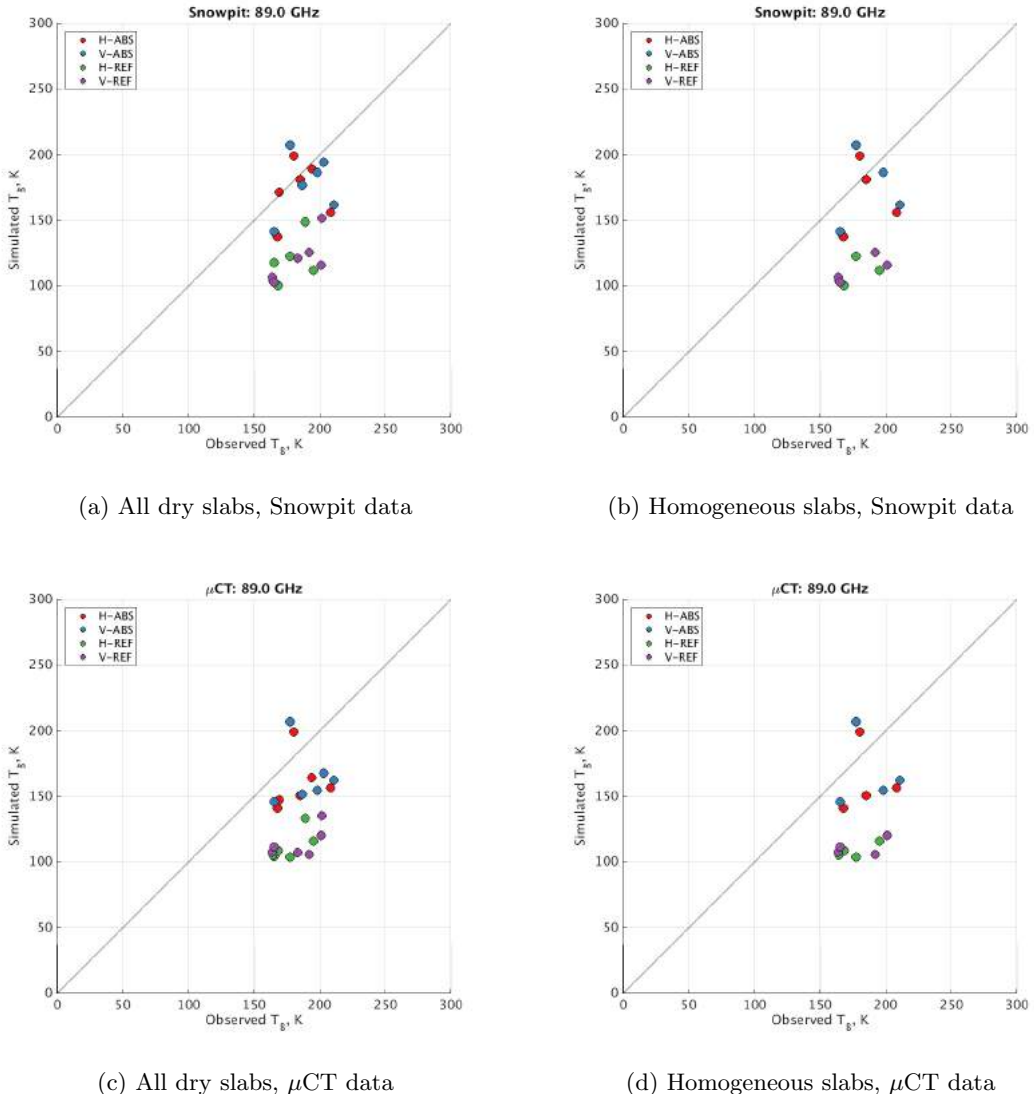


**Figure 4.42:** HUT Simulations compared to SodRad observations for the absorbing base (H-Pol: Red / V-Pol: Blue) and reflective base (H-Pol: Purple / V-Pol: Orange) at 89.0 GHz. Simulations use the traditional observations ((a) and (b)), and  $\mu$ CT observations ((c) and (d)) of snow slab parameters. Simulations are defined by using all dry slabs ((a) and (c)) and homogeneous slabs ((b) and (d)).

is a reduction in magnitude in the RMSE and bias values when comparing the two homogeneity simulations, which is a result of removing the non-homogeneous slabs. The larger magnitude of RMSE and bias is not present for the horizontal reflective base simulations, which suggests that the large error values are only associated with the horizontal polarization absorbing base simulations.

The smallest values of RMSE are found with the simulations of the snow upon the absorbing base at vertical polarizations, for both the dry and homogeneous slab simulations. The values of RMSE are improved when using only the homogeneous slabs instead of the dry slabs; although it should be noted that this improvement is not as large as those

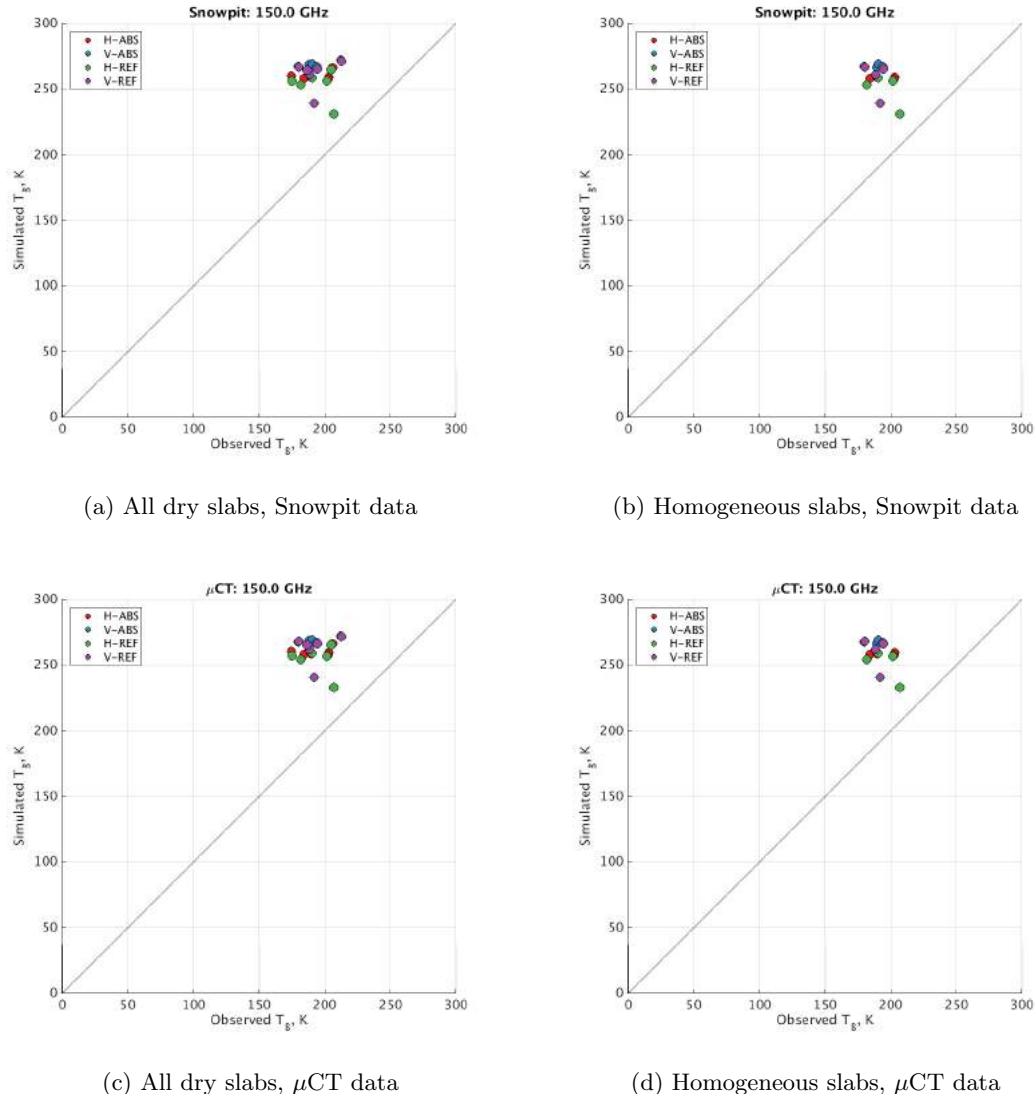


**Figure 4.43:** HUT Simulations compared to SodRad observations for the absorbing base (H-Pol: Red / V-Pol: Blue) and reflective base (H-Pol: Purple / V-Pol: Orange) at 150.0 GHz. Simulations use the traditional observations ((a) and (b)), and  $\mu$ CT observations ((c) and (d)) of snow slab parameters. Simulations are defined by using all dry slabs ((a) and (c)) and homogeneous slabs ((b) and (d)).

involving the other polarization or the reflective base. This suggests that the simulations of snow on the absorbing base at vertical polarizations are less sensitive to the stratigraphy than at horizontal polarizations. This link with stratigraphy sensitivity with the natural snowpack is mirrored by [Rees et al. \[2010\]](#), who states that horizontally polarized channels are more sensitive to stratigraphy.

When comparing the dry slab simulations to those completed with those using only homogeneous slabs, it can be seen that the homogeneous slabs produce simulations with lower magnitude RMSE and bias values. This is expected, as the non-homogeneous slabs have been assumed to be homogeneous for the all dry slab simulations. This introduces

**Table 4.4:** RMSE values for the simulated brightness temperatures (K). Simulation runs include all dry slabs and all dry homogeneous slabs. RMSE values are categorised by the instrumentation technique used (snowpit techniques defined by “Pit”, and  $\mu$ CT techniques defined by “ $\mu$ CT”).

Freq (GHz)	All Dry Slabs						All Homogeneous Slabs					
	H-Abs	V-Abs	H-Ref	V-Ref	H-Abs	V-Abs	H-Ref	V-Ref	H-Abs	V-Abs	H-Ref	V-Ref
Pit	$\mu$ CT	Pit	$\mu$ CT	Pit	$\mu$ CT	Pit	$\mu$ CT	Pit	$\mu$ CT	Pit	$\mu$ CT	
18.7	26.8	25.6	8.2	7.2	15.3	14.6	15.7	15.1	20.4	19.6	6.2	8.8
21.0	32.0	30.6	10.4	9.0	20.3	19.6	21.1	20.5	15.8	14.9	4.7	4.35
36.5	29.9	26.3	17.6	16.7	25.8	24.8	31.1	30.5	13.3	11.9	11.5	13.6
89.0	22.5	28.1	22.8	31.6	52.5	56.5	61.3	61.3	22.4	24.9	22.3	26.3
150.0	58.6	58.7	66.6	66.6	54.1	54.9	60.7	61.6	45.4	45.4	56.2	56.3
									39.7	40.8	41.4	50.1
												51.0

**Table 4.5:** Bias values for the simulated brightness temperatures (K). Simulation runs include all dry slabs and all dry homogeneous slabs. Bias values are categorised by the instrumentation technique used (snowpit techniques defined by “Pit”, and  $\mu$ CT techniques defined by “ $\mu$ CT”).

Freq (GHz)	All Dry Slabs						All Homogeneous Slabs					
	H-Abs	V-Abs	H-Ref	V-Ref	H-Abs	V-Abs	H-Ref	V-Ref	H-Abs	V-Abs	H-Ref	V-Ref
Pit	$\mu$ CT	Pit	$\mu$ CT	Pit	$\mu$ CT	Pit	$\mu$ CT	Pit	$\mu$ CT	Pit	$\mu$ CT	
18.7	25.0	24.0	6.6	5.5	-4.2	-3.1	-4.1	-2.9	16.4	15.8	4.1	3.5
21.0	25.9	24.5	7.1	5.5	-7.1	-5.9	-7.6	-6.4	12.3	11.5	2.7	2.0
36.5	18.0	13.6	3.1	-1.4	-9.7	-8.1	-11.9	-10.3	9.1	5.8	-1.4	-4.6
89.0	-8.7	-18.2	-9.1	-19.0	-44.2	-48.5	-47.9	-52.3	-8.4	-11.8	-6.8	-10.3
150.0	50.1	50.2	57.3	57.4	44.9	45.6	51.7	52.5	31.8	31.9	39.7	39.7
									27.27	27.27	27.8	34.7
												35.3

errors when the non-homogeneous slabs are simulated, as the internal stratigraphy causes reflections of the emitted microwave radiation that is not modelled. When the non-homogeneous slabs are excluded from the simulations, the single layer HUT snow emission model is only simulating single layer snow slabs, and thus produces simulations with lower RMSE and bias values.

When comparing the HUT simulations involving the snowpit measurements with those using the  $\mu$ CT measurements, it can be seen that the values of RMSE are very similar. Whilst using the  $\mu$ CT values of density (and calculated values of SWE) produce a slightly lower RMSE values than those using snowpit values of density, modelling the slabs as single layers produces similar values of bulk average density (as shown in Figure 4.20). This means that the box cutter values of density are comparable to those measured by  $\mu$ CT techniques, for use within the single layer HUT snow emission model. There also is a slight improvement with the  $\mu$ CT HUT snow emission simulations in terms of values of bias, with the exception of the homogeneous reflective base and absorbing base at 89.0 GHz simulations. The homogeneous reflective base simulations have a slightly larger bias when compared to the snowpit data input simulations. The absorbing base simulations at 89.0 GHz using the  $\mu$ CT data input files have bias values with magnitudes approximately 10 K larger for all dry slab simulations, and 3 K larger for the homogeneous simulations. This shows that, for single layer HUT model simulations, observations using traditional box cutter density measurements are sufficient for snowpack parameterisation, when  $\mu$ CT observations are not available.

## 4.4 Chapter Summary

Previously, in Chapter 3, the experimental proceedings of the ASMEEx campaign were described, focusing on the differing radiometric observations, as well as differences in physical parameter observation techniques. Chapter 4 displayed all data that were collected during the ASMEEx campaign, with the data being categorised into three main sections: radiometric, snow characteristic, and stratigraphic. In doing so, the second goal of the first thesis aim was reached.

**Aim 1, Goal 2:** Analyse the ASMEEx dataset; comparing the different instrumentation techniques used, as well as their affect upon the simulated brightness temperatures, using the single layer HUT snow emission model.

During the ASMEEx campaign, 14 snow slabs were extracted and examined in the manner described in Chapter 3. Of those 14 slabs, 13 were considered dry, with slab A03 being designated as a wet slab due to the above-freezing air temperatures present during observation. The 14 slab samples were extracted from various depths within the natural snowpack, with the aim of capturing all manner of snow crystal types and sizes. 13 of the 14 snow slabs were of a similar approximate thickness of 15 cm, with slab B05 being approximately 5 cm thick.

Across all ASMEEx slabs, the snow slabs upon the absorbing base exhibited larger brightness temperatures than when upon the reflecting bases; an expected observation as the emission from the absorbing bases were much larger than that being reflected from the sky (downwelling sky radiation was the emission source for the reflecting plate). The difference in observed brightness temperatures between snow upon the absorbing and reflective bases decreased with increasing frequency; another expected result, due to the increased amount of scattering present when wavelengths approach scatterer size.

The ASMEEx snow slabs exhibited a range of observed physical parameters, due to the selection of slabs over the two winter periods. Bulk physical temperature values ranged from  $-22.2 - -0.25$  °C. The bulk traditional grain size ranged from 0.45 – 1.81 mm, showing fresh snow and depth hoar samples respectively.

The traditional snowpit techniques (density box cutter and IceCube instrumentation) were compared against both the SnowMicroPen and the  $\mu$ CT analysis techniques. It was clear from the data collected that the SMP instrumentation did not accurately sample the snow parameters, as the values of bulk density and SSA were inaccurate when compared to those from the traditional and  $\mu$ CT techniques. It was for this reason that the data collected with the SMP instrumentation were not used for the extinction coefficient calculation within Chapter 5.

The stratigraphy of individual slabs were displayed, using profiles of observed density and SSA from all three measurement techniques, as well as calculated profiles of exponential correlation length and optical diameter (using Eqns. 2.22 and 2.19 respectively). Whilst displayed, the SMP profiles were not used to determine the nature of the slab homogeneity, due to the problems discussed with the observed values. As the resolution

of the traditional observations were too coarse (5 cm for box cutter observations, 3 cm for IceCube observations), the  $\mu$ CT profile were used to determine slab homogeneity. Nine of the 13 dry slabs were deemed homogeneous, using threshold values of parameter standard deviation to determine homogeneous slabs.

It was shown that both the RMSE and bias values were lower when restricting the slabs from all dry slabs to all dry homogeneous slabs. Across both sets of simulations, the RMSE and bias values of horizontal polarization simulations on the absorbing base were greater than those at the vertical polarizations, whilst the reflective plate simulations were similar regardless of polarization. The magnitude of the RMSE and bias values shown in Tables 4.4 and 4.5 were similar, suggesting that a significant portion of the RMSE errors were due to a persistent bias that was present.

The research presented in this chapter, along with that of Chapter 3, details the completion of the ASMEEx campaign, and thus the completion of the first thesis aim. Chapter 5 builds upon the work presented here, by using the ASMEEx dataset to derive a new extinction coefficient model for use with the n-HUT model.

## **Chapter 5:**

# **Extinction Coefficient Calculation**

### **5.1 Chapter Introduction**

Chapters 3 and 4 showed the methodology and the results of the ASMEx campaign, as well as the results of the comparisons between the observed brightness temperatures and the simulated brightness temperatures using the single layer HUT model. In doing so, the three goals associated with the first research aim were met.

By using the data collected in Chapters 3 and 4, Chapter 5 will show the derivation of a new extinction coefficient model for the use with the n-HUT model, using a methodology similar to that laid out by [Wiesmann et al. \[1998\]](#). Unlike the research by [Wiesmann et al. \[1998\]](#), the newly derived extinction model uses both frequency and optical grain size as model parameters. Aim 2 states:

#### **Aim 2**

Derivation of a new extinction coefficient model, using the ASMEx dataset.

#### **Goals**

1. Calculate individual absorption and scattering coefficients of the ASMEx snow slab dataset, using a flux coefficient model.
2. Derive an empirical extinction coefficient model, using ASMEx absorption and scattering coefficients.
3. Implement the newly derived extinction coefficient model in the HUT snow emission model.

In order for the ASMEEx extinction coefficient model to be derived, the radiometric properties of each slab sample was calculated. Section 5.2 shows the methodology behind calculating the individual flux coefficients of each ASMEEx slabs. Section 5.3 details the implementation of the ASMEEx data through the FCM, and retrieving flux coefficients for each ASMEEx slab. An analysis of the absorption and scattering coefficients can also be found in Section 5.3. The scattering coefficients (at vertical polarizations) were used to create a single empirical extinction coefficient model, with both frequency and optical diameter as input parameters. Implementation of the extinction coefficient model in the n-HUT model is found in Section 5.4.

## 5.2 Flux Coefficient Model

### 5.2.1 Snow Slab Reflectivities

The flux coefficient model (FCM) described in [Wiesmann et al. \[1998\]](#) builds upon the work of [Weise \[1996\]](#); where the microwave properties of snow slabs upon different bases (resulting in the snow-ground boundary having different reflective properties) were measured, with the emissivity, transmissivity, and reflective properties calculated. [Wiesmann et al. \[1998\]](#) then used the reflective, transmissive, and emissive properties of the snow slabs with a simple sandwich model, to calculate the internal scattering and absorption coefficients. This study follows on from the work by [Wiesmann et al. \[1998\]](#), by using the same simplified sandwich model to retrieve the scattering and absorption coefficients of the ASMEEx snow slabs. From the retrieved six-flux coefficients, an extinction coefficient model was developed, to be used with the n-HUT model.

As part of the ASMEEx campaign, three different microwave emissions (Figure 3.4) were measured:

- Brightness temperature of the snow slab upon a reflector ( $T_{BM}$ ),
- Brightness temperature of the snow slab upon an absorber ( $T_{BA}$ ),
- Brightness temperature of the sky ( $T_{BSKY}$ ).

As explained in Section 2.4.2, the brightness temperature of the snow slab upon the reflecting base,  $T_{BM}$ , is comprised of radiation from two separate sources. One contribution comes from the emitted radiation of the snow, due to the physical snow temperature  $T_{phys}$ . The second contribution comes from the downwelling sky brightness temperature

$T_{BSKY}$ , after it has propagated through the snow slab. The total reflectivity of the slab (including the interface and internal reflections) upon the reflective plate can be defined as  $r_{met}$ , such that:

$$T_{BM} = (1 - r_{met})T_{phys} + r_{met}T_{BSKY} \Rightarrow r_{met} = \frac{T_{BM} - T_{Phys}}{T_{BSKY} - T_{Phys}} \quad (5.1)$$

$r_{met}$  is related to the internal reflectivities ( $r$ ), transmissivities ( $t$ ), and interface reflectivities ( $r_i$ ), by:

$$r_{met} = r_i + (1 - r_i)^2 R_{met} \quad (5.2)$$

where:

$$R_{met} = \frac{r + \frac{t^2}{1-r}}{1 - rr_i - \frac{r_i t^2}{1-r}} \quad (5.3)$$

The brightness temperature of the snow slab upon the absorbing base,  $T_{BA}$ , is also comprised from two separate sources, similar to that of  $T_{BM}$ . The first contribution, the emission from the snow slab itself, is the same as the first contribution for the snow upon the reflective base observations, as  $T_{phys}$  is uniform for both observations. The second contribution, however, comes solely from the absorbing blackbody base (as it is assumed that the reflectivity is zero). This much smaller value of base reflectivity results in downwelling sky radiation to be absorbed. Similar to Eqn. 5.1,  $T_{BA}$  and  $r_{abs}$  can be expressed as:

$$T_{BA} = (1 - r_{abs})T_{phys} + r_{abs}T_{BSKY} \Rightarrow r_{abs} = \frac{T_{BA} - T_{Phys}}{T_{BSKY} - T_{Phys}} \quad (5.4)$$

It is assumed that the absorber temperature and the snow physical temperature are equal, and that, similar to  $r_{met}$ ,  $r_{abs}$  is the total reflectivity of the slab upon the absorbing base, including the interface and internal reflections.  $r_{abs}$  can also be written as:

$$r_{abs} = r_i + (1 - r_i)^2 R_{abs} \quad (5.5)$$

where  $R_{abs}$  is described, similarly to  $R_{met}$ , by:

$$R_{abs} = \frac{r + \frac{r_i t^2}{1-rr_i}}{1 - rr_i - \frac{(r_i t)^2}{1-rr_i}} \quad (5.6)$$

The values of the internal reflectivities ( $r$ ), the interface reflectivities ( $r_i$ ) and transmissivities ( $t$ ) have been calculated, from the measured brightness temperatures  $T_{BA}$ ,  $T_{BM}$ , and  $T_{BSKY}$ , while  $r_i$ , is known. [Toure et al. \[2008\]](#), who has also used the methodology laid out by [Wiesmann et al. \[1998\]](#), states that if the air-snow interface is considered to be flat, then  $r_i$  can be computed using the Fresnel reflectivity formula at the given incidence angle, polarization and dielectric slab permittivity. Then, to obtain the values of  $r$  and  $t$ , Eqns. 5.1 – 5.6 must be solved.

To calculate the internal reflectivities and transmissivities of the individual slabs, the slab permittivities and interface reflectivities must be calculated; in order to correctly calculate the propagation of radiation through the individual slabs. The complex permittivities and Fresnel reflectivities of snow layers are calculated using the HUT model (Eqns. 2.28 – 2.38).

## 5.2.2 Calculating the absorption and scattering flux coefficients

After the calculation of the dielectric constants of snow and interface reflectivities, the FCM can be used to determine the absorption and scattering slab coefficients. The framework of the FCM is described below.

### 5.2.2.1 Description of FCM for internal reflectivity and transmissivity of snow slabs

Consider a snow slab, lying parallel to the base, with internal emissivity  $e$ , reflectivity  $r$ , and transmissivity  $t$ , physical temperature  $T_{phys}$ , density  $\rho_{snow}$ , and dielectric constant  $\epsilon_{snow}$ , as shown in Figure 5.1. The slab has a surface reflectivity  $r_i$ , while the reflectivity of the base  $r_{GND}$  is well defined (assumed  $r_{GND} = 0$  for the absorbing base, and  $r_{GND} = 1$  for the reflective plate). The radiation travelling through the slab can be defined in the two vertical ( $T_1$  and  $T_2$ ) and four horizontal directions ( $T_3$  to  $T_6$  respectively).

The horizontal fluxes suffer total internal reflection when reaching the slab boundary, if the internal incidence angle  $\theta$  is larger than that of the critical angle  $\theta_c = \arcsin(\frac{1}{n})$ , where  $n$  is the refractive index of the slab. On the contrary, radiation at an incidence angle smaller than  $\theta_c$  can be transmitted through the slab. This radiation belongs to  $T_1$  for downwelling radiation or  $T_2$  for upwelling radiation. The transfer equations for the six directional radiation fluxes can be written as:

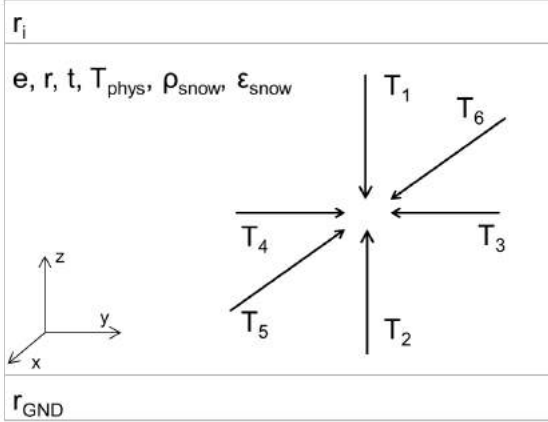


**Figure 5.1:** The six fluxes of radiation inside the snow slab.

$$-\frac{dT_{01}}{dz} |\cos \theta| = -\gamma_a(T_{01} - T_{phys}) - \gamma_b(T_{01} - T_{02}) - \gamma_c(4T_{01} - T_{03} - T_{04} - T_{05} - T_{06}) \quad (5.7)$$

$$\frac{dT_{02}}{dz} |\cos \theta| = -\gamma_a(T_{02} - T_{phys}) - \gamma_b(T_{02} - T_{01}) - \gamma_c(4T_{02} - T_{03} - T_{04} - T_{05} - T_{06}) \quad (5.8)$$

$$-\frac{dT_{03}}{dx} |\cos \theta| = -\gamma_a(T_{03} - T_{phys}) - \gamma_b(T_{03} - T_{04}) - \gamma_c(4T_{03} - T_{01} - T_{02} - T_{05} - T_{06}) \quad (5.9)$$

$$\frac{dT_{04}}{dx} |\cos \theta| = -\gamma_a(T_{04} - T_{phys}) - \gamma_b(T_{04} - T_{03}) - \gamma_c(4T_{04} - T_{01} - T_{02} - T_{05} - T_{06}) \quad (5.10)$$

$$-\frac{dT_{05}}{dy} |\cos \theta| = -\gamma_a(T_{05} - T_{phys}) - \gamma_b(T_{05} - T_{06}) - \gamma_c(4T_{05} - T_{01} - T_{02} - T_{03} - T_{04}) \quad (5.11)$$

$$\frac{dT_{06}}{dy} |\cos \theta| = -\gamma_a(T_{06} - T_{phys}) - \gamma_b(T_{06} - T_{05}) - \gamma_c(4T_{06} - T_{01} - T_{02} - T_{03} - T_{04}) \quad (5.12)$$

where  $\gamma_a$  is the six-flux absorption coefficient,  $\gamma_b$  is the six-flux backwards scattering coefficient (scattering in the backwards direction), and  $\gamma_c$  is the six-flux scattering coeffi-

cient around  $90^\circ$  (scattering perpendicular to the direction of travel). If the snow slab is plane-parallel (where there is no variation around the x or y axis), then Eqns. 5.9 - 5.12 are equal to zero.

If the snow slab is isotropic around the z axis, then all horizontal fluxes are the same, thus:

$$T_{03} = T_{04} = T_{05} = T_{06} = \frac{\gamma_a T_{phys} + \gamma_c(T_1 + T_2)}{\gamma_a + 2\gamma_c} \quad (5.13)$$

By substituting Eqn. 5.13 into Eqns. 5.7 and 5.8, we get the two directional radiation flux equations, with modified absorption ( $\gamma'_a$  is the two-flux absorption coefficient) and scattering ( $\gamma'_b$  is the two-flux scattering coefficient) coefficients:

$$-\frac{dT_{01}}{dz} |\cos \theta| = -\gamma'_a(T_{01} - T_{phys}) - \gamma'_b(T_{01} - T_{02}) \quad (5.14)$$

$$\frac{dT_{02}}{dz} |\cos \theta| = -\gamma'_a(T_{02} - T_{phys}) - \gamma'_b(T_{02} - T_{01}) \quad (5.15)$$

where

$$\gamma'_a = \gamma_a \left( 1 + \frac{4\gamma_c}{(\gamma_a + 2\gamma_c)} \right) \quad (5.16)$$

$$\gamma'_b = \gamma_b + \frac{4\gamma_c^2}{\gamma_a + 2\gamma_c} \quad (5.17)$$

For a constant value of  $T_{phys}$ ,  $T_{01}$  and  $T_{02}$  can be written as:

$$T_{01} = T_{phys} + A \exp(\gamma z') + B \exp(-\gamma z') \quad (5.18)$$

$$T_{02} = T_{phys} + r_0 A \exp(\gamma z') + \frac{B \exp(-\gamma z')}{r_0} \quad (5.19)$$

where  $z' = \frac{z}{|\cos \theta|}$  is the path length through the slab. The coefficients A and B are found at the boundary conditions  $z=0$  and  $z=d$ . The term  $r_0$  is the reflectivity at infinite thickness, given by:

$$r_0 = \frac{\gamma'_b}{\gamma'_a + \gamma'_b + \gamma} \quad (5.20)$$

and the damping (attenuation) coefficient  $\gamma_d$  is given by:

$$\gamma_d = \sqrt{\gamma'_a(\gamma'_a + 2\gamma'_b)} \quad (5.21)$$

### 5.2.2.2 Inverting the six-flux model

As shown in Eqns. 5.1 and 5.4, the total reflectivity of the snow upon the reflective and absorptive bases can be calculated by manipulating the values of observed brightness temperature of the slab, sky, and the physical temperature of the snow. Using the values of  $r_{met}$  and  $r_{abs}$ , the values of  $R_{met}$  and  $R_{abs}$  can be calculated using Eqns. 5.2 and 5.5 respectively, if the value of  $r_i$  is known.  $r_i$  is assumed to be the Fresnel reflectivity, as calculated by Eqns. 2.40 and 2.41.

Rearranging Eqns. 5.3 and 5.6 gives the following non-linear equations:

$$r = R_{abs} \left( 1 - rr_i - \frac{(r_i t)^2}{(1 - rr_i)} \right) - \frac{r_i t^2}{1 - rr_i} \quad (5.22)$$

$$t^2 = R_{met}((1 - rr_i)(1 - r) - r_i t^2) - r(1 - r) \quad (5.23)$$

where the values of  $R_{met}$ ,  $R_{abs}$  and  $r_i$  are known. Wiesmann et al. [1998] proposed an iterative procedure to solving these non-linear equations; by using  $r_i = 0$  to find an initial solution to Eqns. 5.22 and 5.23, giving:

$$r = R_{abs}; t^2 = (R_{met} - R_{abs})(1 - R_{abs}) \quad (5.24)$$

These first guesses were then inserted into the right hand side of Eqns. 5.22 and 5.23, as well as the correct value of  $r_i$ , calculated from Eqns. 2.40 and 2.41. This leads to new values of  $r$  and  $t^2$ , which are then iteratively inserted into Eqns. 5.22 and 5.23 to produce improved values of  $r$  and  $t^2$ . This process is repeated until the difference between the old and new values is below 0.0005 (where  $|r_{old} - r_{new}| < 0.0005$ ).

For a snow slab of thickness  $d$ , the values of the internal reflectivity and transmissivity of the slab, considering all multiple reflections, can also be calculated by:

$$r = r_0 \frac{1 - t_0^2}{1 - r_0^2 t_0^2} \quad (5.25)$$

$$t = t_0 \frac{1 - r_0^2}{1 - r_0^2 t_0^2} \quad (5.26)$$

where  $r_0$  is the reflectivity of infinite slab thickness, and by:

$$t_0 = \exp\left(\frac{-\gamma_d d}{|\cos \theta|}\right) \quad (5.27)$$

where  $t_0$  is the one-way transmissivity through the slab, and  $\gamma_d$  is the damping coefficient. Wiesmann et al. [1998] proposed that a second iteration procedure could be used to calculate the values of  $r_0$  and  $t_0$ . Firstly, Eqns. 5.25 and 5.26 are manipulated such that;

$$r_0 = \frac{-1 + \sqrt{1 + 4G^2}}{2G}; G \equiv \frac{r_0}{1 - r_0^2} = \frac{r}{t} \frac{t_0}{1 - t_0^2} \quad (5.28)$$

$$t_0 = t \left(1 + r_0^2 \frac{1 - t_0^2}{1 - r_0^2}\right) \quad (5.29)$$

By, using a first solution of  $t_0 = t$ , new values of  $r_0$ , and therefore,  $t_0$  can be calculated. Inserting these values into the right hand side of Eqns. 5.28 and 5.29 will lead to improved values of  $r_0$  and  $t_0$ . This iterative process leads to a rapid convergence around  $r_0$  and  $t_0$ .

Once convergence around  $r_0$  and  $t_0$  occurs, the two-flux absorption and scattering coefficients ( $\gamma'_a$  and  $\gamma'_b$  respectively) can be calculated using Eqns. 5.27, 5.30 and 5.31 respectively. The two-flux absorption only considers radiation fluxes travelling in the vertical directions (where  $T_3 = T_4 = T_5 = T_6 = 0$ ).

$$\gamma'_a = \gamma \frac{1 - r_0}{1 + r_0} \quad (5.30)$$

$$\gamma'_b = (\gamma + \gamma'_a) \frac{r_0}{1 - r_0} \quad (5.31)$$

To transform the two-flux coefficients into six-flux coefficients (taking horizontal direction fluxes into account), the solid body angles of the upwelling and downwelling radiative fluxes must be considered. For the upwelling and downwelling radiation (beams  $T_{01}$  and  $T_{02}$ ), the solid angle of radiation can be written as:

$$\Omega_1 = 2\pi \left(1 - \sqrt{\frac{\epsilon - 1}{\epsilon}}\right) \quad (5.32)$$

The solid angle of trapped radiation is equal to:

$$\Omega_2 = 2\pi - \Omega_1 = 2\pi \sqrt{\frac{\epsilon_{snow} - 1}{\epsilon_{snow}}} \quad (5.33)$$

Using the two solid angles for upwelling and trapped radiation, it is possible to calculate the ratio between the backscattering and the scattering around  $90^\circ$ . As the six-flux scattering coefficient can be calculated by the sum:

$$\gamma_s = 2\gamma_b + 4\gamma_c \quad (5.34)$$

As the backscattering coefficient is linked to the value of  $\Omega_1$ , and the trapped radiation is linked to the value of  $\Omega_2$ , it is possible to calculate the ratio between the two scattering coefficient terms via:

$$F = \frac{2\gamma_c}{\gamma_b} = \frac{\Omega_2}{\Omega_1} = \frac{\left(\sqrt{\frac{\epsilon-1}{\epsilon}}\right)}{\left(1 - \sqrt{\frac{\epsilon-1}{\epsilon}}\right)} \quad (5.35)$$

Eqn. 5.35 can be rearranged such that  $\gamma_c = \frac{F\gamma_b}{2}$ . The six-flux coefficients can be calculated from the snow permittivity  $\epsilon'_{snow}$  and the two-flux coefficients, using Eqns. 5.30 and 5.31. The six-flux absorption coefficient ( $\gamma_a$ ) is calculated during the calculation of  $\gamma_b$ . Full proof of these equations, and calculation of all two- and six-flux coefficients can be found in Appendix C.

## 5.3 Applying ASMEEx data to Wiesmann et al. (1998) Methodology

Using the FCM described in Section 5.2, the two- and six-flux coefficients, along with other key parameters, have been calculated, using the ASMEEx slab data, observed using  $\mu$ CT analysis where applicable. Tables 5.1 and 5.2 show the evaluated slab emissivities and two- and six-flux coefficients, for vertical and horizontal polarizations respectively.

**Table 5.1:** Vertical Polarization: Radiometric Properties and Flux Coefficients of the ASMEEx slabs.

Sample	f	$e_{abs}$	$e_{met}$	$r_0$	$t_0$	$\gamma'_a$	$\gamma'_b$	$\gamma_a$	$\gamma_s$
	GHz					$m^{-1}$	$m^{-1}$	$m^{-1}$	$m^{-1}$
1v	18.7	0.993	0.023	0.318	0.978	0.047	0.064	0.021	0.153

Sample	f	$e_{abs}$	$e_{met}$	$r_0$	$t_0$	$\gamma'_a$ $m^{-1}$	$\gamma'_b$ $m^{-1}$	$\gamma_a$ $m^{-1}$	$\gamma_s$ $m^{-1}$
	GHz								
1v	21.0	0.991	0.029	0.256	0.975	0.060	0.055	0.030	0.140
1v	36.5	0.991	0.061	0.151	0.958	0.128	0.054	0.081	0.154
2v	21.0	0.861	0.165	0.292	0.847	0.397	0.461	0.172	1.147
2v	36.5	0.744	0.402	0.325	0.574	1.228	1.757	0.512	4.229
3v	18.7	0.997	0.064	0.342	0.935	0.151	0.238	0.063	0.565
3v	21.0	0.998	0.078	0.309	0.926	0.186	0.240	0.080	0.586
4v	18.7	0.926	0.237	0.107	0.844	0.576	0.155	0.379	0.507
4v	21.0	0.900	0.340	0.143	0.753	0.899	0.349	0.532	1.065
5v	18.7	0.961	0.122	0.175	0.911	0.329	0.169	0.173	0.496
5v	21.0	0.962	0.148	0.156	0.895	0.404	0.177	0.221	0.537
5v	89.0	0.666	0.678	0.318	0.102	5.910	8.097	2.469	19.635
5v	150.0	0.625	0.653	0.366	0.158	4.289	7.797	1.709	18.173
6v	18.7	0.965	0.089	0.217	0.930	0.244	0.173	0.118	0.470
6v	21.0	0.965	0.132	0.159	0.906	0.373	0.168	0.205	0.505
6v	89.0	0.718	0.692	0.268	0.155	5.640	5.645	2.524	14.405
6v	150.0	0.670	0.665	0.314	0.066	7.416	9.909	3.128	24.105
7v	18.7	0.963	0.069	0.274	0.939	0.189	0.196	0.084	0.499
7v	21.0	0.959	0.093	0.207	0.928	0.260	0.171	0.128	0.475
7v	89.0	0.656	0.644	0.329	0.108	5.949	8.711	2.457	20.913
7v	150.0	0.649	0.644	0.335	0.067	7.113	10.784	2.921	25.761
8v	18.7	0.983	0.034	0.172	0.976	0.090	0.045	0.053	0.127
8v	21.0	0.986	0.044	0.172	0.968	0.118	0.059	0.070	0.167
8v	36.5	0.971	0.090	0.049	0.949	0.247	0.027	0.211	0.089
9v	18.7	0.959	0.044	0.129	0.971	0.111	0.038	0.071	0.115
9v	21.0	0.963	0.060	0.054	0.966	0.153	0.019	0.126	0.065
9v	36.5	0.940	0.127	0.165	0.909	0.339	0.160	0.198	0.461
10v	18.7	0.979	0.046	0.360	0.951	0.130	0.230	0.053	0.537
10v	21.0	0.979	0.053	0.339	0.946	0.151	0.234	0.062	0.557
10v	36.5	0.970	0.124	0.164	0.911	0.368	0.172	0.202	0.510
11v	18.7	0.977	0.054	0.358	0.943	0.132	0.230	0.053	0.538
11v	21.0	0.974	0.065	0.309	0.938	0.161	0.208	0.068	0.509
11v	36.5	0.949	0.170	0.063	0.899	0.449	0.064	0.335	0.242

Sample	f	$e_{abs}$	$e_{met}$	$r_0$	$t_0$	$\gamma'_a$	$\gamma'_b$	$\gamma_a$	$\gamma_s$
	GHz					$m^{-1}$	$m^{-1}$	$m^{-1}$	$m^{-1}$
12v	18.7	0.946	0.096	0.201	0.926	0.751	0.472	0.368	1.327
12v	21.0	0.954	0.114	0.207	0.912	0.894	0.590	0.432	1.641
12v	36.5	0.888	0.269	0.126	0.813	2.358	0.780	1.374	2.543
12v	89.0	0.595	0.542	0.403	0.224	9.372	21.142	3.603	48.053
12v	150.0	0.606	0.619	0.379	0.109	14.664	28.884	5.738	66.694
13v	18.7	0.974	0.054	0.409	0.936	0.151	0.353	0.058	0.798
13v	21.0	0.976	0.064	0.385	0.928	0.181	0.368	0.071	0.847
13v	36.5	0.961	0.167	0.175	0.876	0.505	0.260	0.261	0.764
13v	89.0	0.760	0.719	0.218	0.199	5.653	4.035	2.683	11.040
13v	150.0	0.669	0.672	0.309	0.049	8.672	11.234	3.626	27.513
14v	18.7	0.897	0.176	0.161	0.874	0.501	0.230	0.271	0.690
14v	21.0	0.900	0.202	0.140	0.860	0.586	0.222	0.334	0.696
14v	36.5	0.767	0.444	0.281	0.562	1.661	1.807	0.725	4.550
14v	89.0	0.569	0.567	0.418	0.040	6.792	16.785	2.595	37.766
14v	150.0	0.601	0.600	0.384	0.032	7.876	15.924	3.089	36.634

**Table 5.2:** Horizontal Polarization: Radiometric Properties and Flux Coefficients of the ASMEx slabs.

Sample	f	$e_{abs}$	$e_{met}$	$r_0$	$t_0$	$\gamma'_a$	$\gamma'_b$	$\gamma_a$	$\gamma_s$
	GHz					$m^{-1}$	$m^{-1}$	$m^{-1}$	$m^{-1}$
1h	18.7	0.932	0.020	0.594	0.961	0.041	0.297	0.015	0.621
1h	21.0	0.911	0.027	0.595	0.948	0.055	0.400	0.020	0.836
1h	36.5	0.931	0.061	0.415	0.927	0.127	0.309	0.051	0.693
2h	21.0	0.588	0.132	0.649	0.707	0.322	3.389	0.111	6.989
2h	36.5	0.535	0.308	0.556	0.471	0.937	5.276	0.334	11.155
3h	18.7	0.931	0.070	0.393	0.920	0.166	0.354	0.066	0.808
3h	21.0	0.935	0.079	0.361	0.916	0.187	0.331	0.076	0.774
4h	18.7	0.797	0.229	0.400	0.732	0.565	1.257	0.222	2.857
4h	21.0	0.774	0.339	0.357	0.631	0.924	1.591	0.378	3.727
5h	18.7	0.814	0.113	0.502	0.833	0.303	1.228	0.110	2.649
5h	21.0	0.864	0.142	0.400	0.835	0.386	0.858	0.150	1.953

Sample	f	$e_{abs}$	$e_{met}$	$r_0$	$t_0$	$\gamma'_a$ $m^{-1}$	$\gamma'_b$ $m^{-1}$	$\gamma_a$ $m^{-1}$	$\gamma_s$ $m^{-1}$
	GHz								
5h	89.0	0.621	0.618	0.380	0.050	6.757	13.369	2.660	30.836
5h	150.0	0.591	0.619	0.418	0.157	3.814	9.403	1.459	21.163
6h	18.7	0.855	0.082	0.505	0.877	0.225	0.929	0.082	2.000
6h	21.0	0.882	0.116	0.407	0.863	0.325	0.752	0.125	1.703
6h	89.0	0.659	0.626	0.349	0.168	4.504	7.431	1.830	17.535
6h	150.0	0.627	0.625	0.373	0.041	7.636	14.515	3.035	33.631
7h	18.7	0.849	0.068	0.544	0.887	0.187	0.978	0.067	2.077
7h	21.0	0.827	0.095	0.516	0.855	0.265	1.170	0.096	2.509
7h	89.0	0.584	0.569	0.421	0.113	4.708	11.791	1.798	26.493
7h	150.0	0.580	0.583	0.421	0.048	6.538	16.383	2.496	36.807
8h	18.7	0.941	0.031	0.499	0.953	0.083	0.332	0.031	0.717
8h	21.0	0.936	0.044	0.455	0.941	0.118	0.363	0.046	0.798
8h	36.5	0.918	0.087	0.388	0.902	0.237	0.490	0.097	1.119
9h	18.7	0.872	0.047	0.571	0.915	0.120	0.746	0.043	1.569
9h	21.0	0.878	0.068	0.503	0.899	0.175	0.715	0.065	1.540
9h	36.5	0.861	0.129	0.419	0.843	0.346	0.860	0.136	1.930
10h	18.7	0.861	0.044	0.596	0.914	0.125	0.916	0.044	1.912
10h	21.0	0.891	0.053	0.524	0.917	0.150	0.693	0.054	1.481
10h	36.5	0.882	0.124	0.395	0.857	0.368	0.796	0.144	1.815
11h	18.7	0.854	0.056	0.568	0.900	0.139	0.845	0.049	1.780
11h	21.0	0.862	0.065	0.534	0.894	0.162	0.798	0.058	1.701
11h	36.5	0.843	0.169	0.399	0.804	0.448	0.990	0.174	2.254
12h	18.7	0.862	0.106	0.452	0.861	0.832	2.500	0.310	5.522
12h	21.0	0.895	0.112	0.390	0.873	0.878	1.844	0.340	4.226
12h	36.5	0.824	0.253	0.353	0.731	2.202	3.712	0.881	8.744
12h	89.0	0.597	0.528	0.424	0.244	8.398	21.486	3.180	48.189
12h	150.0	0.633	0.654	0.372	0.131	13.668	25.790	5.380	59.868
13h	18.7	0.887	0.054	0.528	0.914	0.151	0.715	0.054	1.527
13h	21.0	0.888	0.065	0.494	0.905	0.185	0.713	0.067	1.545
13h	36.5	0.875	0.170	0.352	0.821	0.514	0.864	0.206	2.036
13h	89.0	0.741	0.687	0.271	0.215	4.811	4.895	2.108	12.492
13h	150.0	0.686	0.677	0.316	0.088	6.879	9.304	2.855	22.633

Sample	f	$e_{abs}$	$e_{met}$	$r_0$	$t_0$	$\gamma'_a$	$\gamma'_b$	$\gamma_a$	$\gamma_s$
						$m^{-1}$	$m^{-1}$	$m^{-1}$	$m^{-1}$
GHz									
14h	18.7	0.770	0.174	0.473	0.760	0.503	1.718	0.186	3.754
14h	21.0	0.786	0.195	0.438	0.752	0.571	1.586	0.215	3.527
14h	36.5	0.702	0.415	0.386	0.508	1.542	3.156	0.604	7.250
14h	89.0	0.567	0.563	0.434	0.058	5.782	15.674	2.186	34.945
14h	150.0	0.634	0.627	0.368	0.074	6.158	11.355	2.448	26.421

Both the two- and six-flux absorption and scattering coefficients calculated from the FCM will be analysed separately. In Section 5.3.1, the absorption coefficients will be analysed, and compared to the theoretical absorption coefficient used by the n-HUT model,  $k_{a,HUT}$ . In Section 5.3.2, the scattering coefficients will be discussed and analysed.

### 5.3.1 Flux Coefficient Model: Absorption Coefficient

Values of  $\gamma_a$  at both horizontal and vertical polarizations for all 14 ASMEx slabs were calculated, compared and contrasted with the theoretical absorption coefficient used by the n-HUT model (Eqn. 2.42). Figure 5.2 shows the absorption coefficients for Slabs A01 - A07, while Figure 5.3 shows those calculated for Slabs B01 - B07. The physical temperature, bulk density, and permittivity of each slab are displayed within each slabs figure.

Across all 14 slabs, it can be seen that the values of  $\gamma_a$  suffer from a slight polarization difference; with  $\gamma_{av}$  being slightly larger than that of  $\gamma_{ah}$ . The absorption coefficients are seen to increase with increasing frequency. At 150 GHz, this increase in absorption is less prominent, due to the reduced penetration depth (Eqn. 2.23), resulting in a failure of the retrieval method at these frequencies. The values of  $\gamma_{ah}$  and  $\gamma_{av}$  across all 14 slabs are comparable with the theoretical absorption coefficient  $k_{a,HUT}$ , with the exception of those calculated at 150 GHz. Although slab A03 shows comparable values of  $\gamma_{ah}$  and  $\gamma_{av}$ , the slab was categorised as wet, and thus was not used for derivation of the extinction coefficient later in the chapter.

As  $k_{a,HUT}$  was found to be comparable to both  $\gamma_{ah}$  and  $\gamma_{av}$ , within an order of magnitude, at the lower three frequencies (where internal processes are more dominant than those at the surface), the effect of using either  $\gamma_{ah}$ ,  $\gamma_{av}$ , or  $k_{a,HUT}$  within the n-HUT

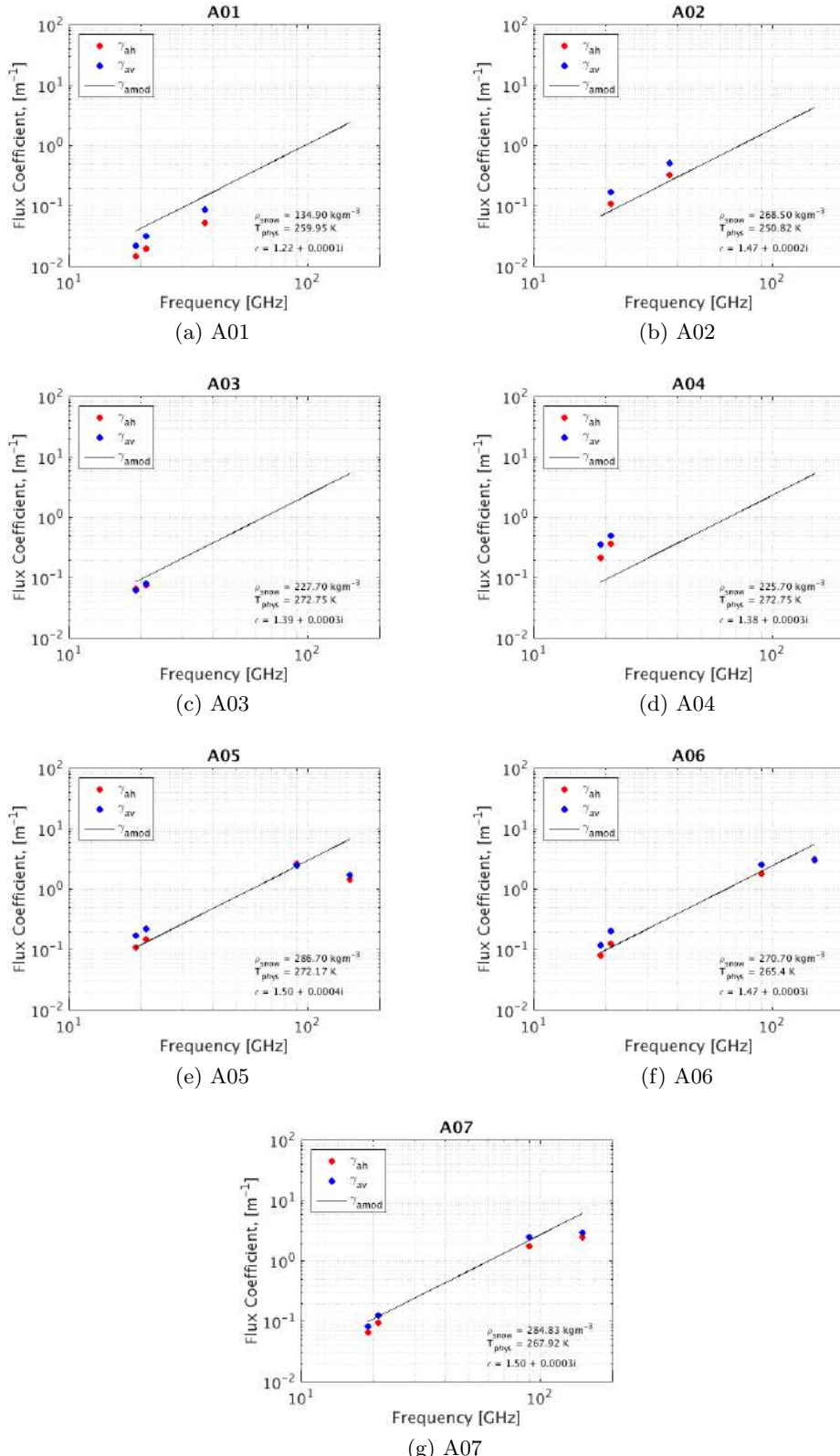


**Figure 5.2:** Six-flux absorption coefficients, at H-Pol (Red) and V-Pol (blue), alongside the theoretical absorption coefficient used by the n-HUT model (black), at all measured frequencies, for the 2014 slab samples. Each subplot shows the physical temperature, average density, and dielectric constant of the slab; calculated using the permittivity model described in Section 2.5.4.1.

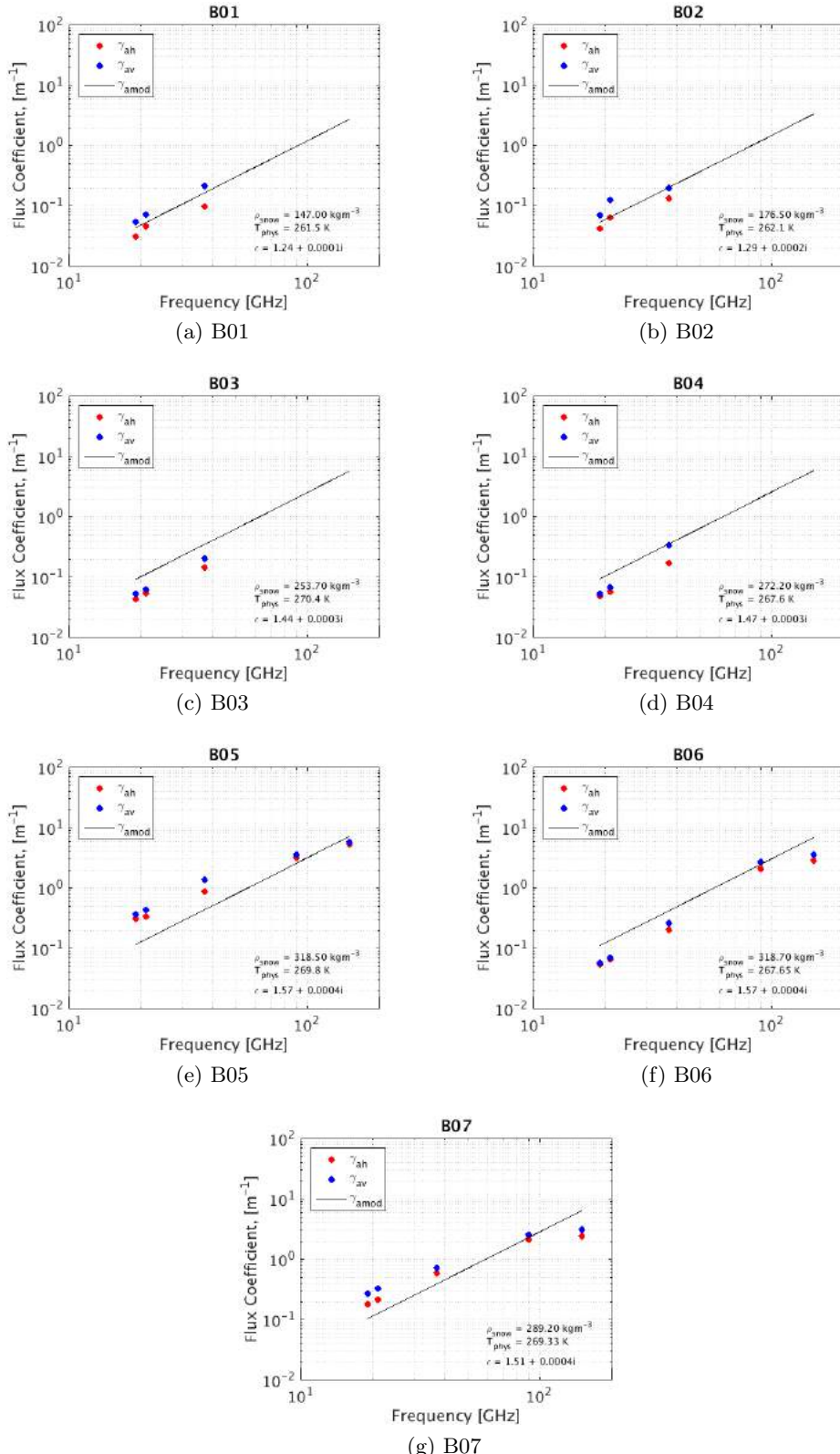


**Figure 5.3:** Six-flux absorption coefficients, at H-Pol (Red) and V-Pol (blue), alongside the theoretical absorption coefficient used by the n-HUT model (black), at all measured frequencies, for the 2015 slab samples. Each subplot shows the physical temperature, average density, and dielectric constant of the slab; calculated using the permittivity model described in Section 2.5.4.1.

model can be considered negligible. The theoretical absorption coefficient is therefore robust, and was used in the calculation of the extinction coefficient.

### 5.3.2 Flux Coefficient Model: Scattering Coefficient

Figure 5.4 shows the scattering coefficients for Slabs A01 - A07, while Figure 5.5 shows the scattering coefficients for Slabs B01 - B07.

Across all 14 slabs, it can be seen that, generally, the values of both the horizontal polarization six-flux scattering coefficients ( $\gamma_{sh}$ ) and the vertical polarization six-flux scattering coefficient ( $\gamma_{sv}$ ) increase with increasing frequency. This is to be expected, as the wavelength decreases with increasing frequency. As the wavelength approaches that of the scatterer size (in this instance, the snow crystal size), the amount of scattering would increase (Chang et al. [1976], Mätzler [1994], and Tait [1998]). However, it can be seen that some slabs do not follow this relationship, as slabs A01, B01, and B04 do not experience increasing scattering with increasing frequency. All three slabs have only three frequency observations (due to the unavailability of the SodRad2 platform, Section 3.6.2), thus not providing information at higher frequencies. As the scattering coefficients at 18.7 and 21.0 GHz are of similar orders of magnitudes, the scattering coefficients at 36.5 GHz appear to be where the problem lies. The flux coefficient model appears to have an issue with calculating the scattering coefficients of slabs made up of surface snow.

It can also be seen across all 14 slabs that there is a polarization difference present, unlike with the absorption coefficients.  $\gamma_{sh}$  is larger than  $\gamma_{sv}$  for all slab samples. This difference in scattering coefficient magnitude with respect to polarization was commented upon in the original literature (Wiesmann et al. [1998]), however no reason was given for the difference, and further analysis completed within the literature (Wiesmann et al. [1998] and Toure et al. [2008]) neglected slab samples with a large difference present. Toure et al. [2008] also undertook a similar experiment to both Wiesmann et al. [1998] and to the ASMEx campaign with a study that looked at changing microstructure and its effect upon  $\gamma_s$ . Toure et al. [2008] measured the SSA through a process using near-infrared digital photography (Matzl and Schneebeli [2006] and Toure et al. [2008]). Toure et al. [2008] has a polarization difference present in their results, but further analysis only focuses on the  $\gamma_{sv}$ .

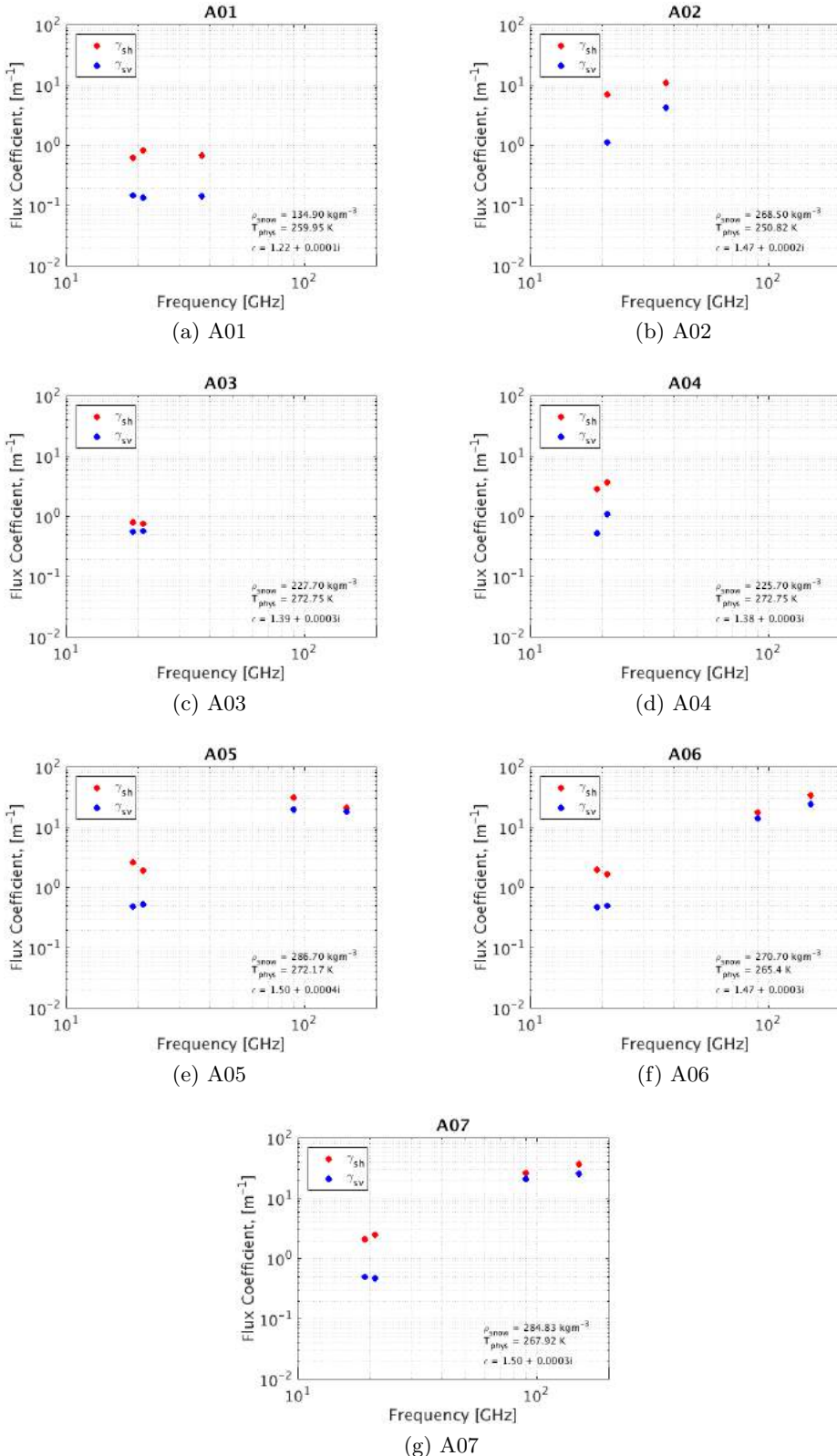


**Figure 5.4:** Six-flux scattering coefficients, at both H-Pol (Red) and V-Pol (Blue), at all measured frequencies, for the 2014 slab samples. Each subplot shows the physical temperature, average density, and dielectric constant of the slab, calculated with the permittivity model described in Section 2.5.4.1.

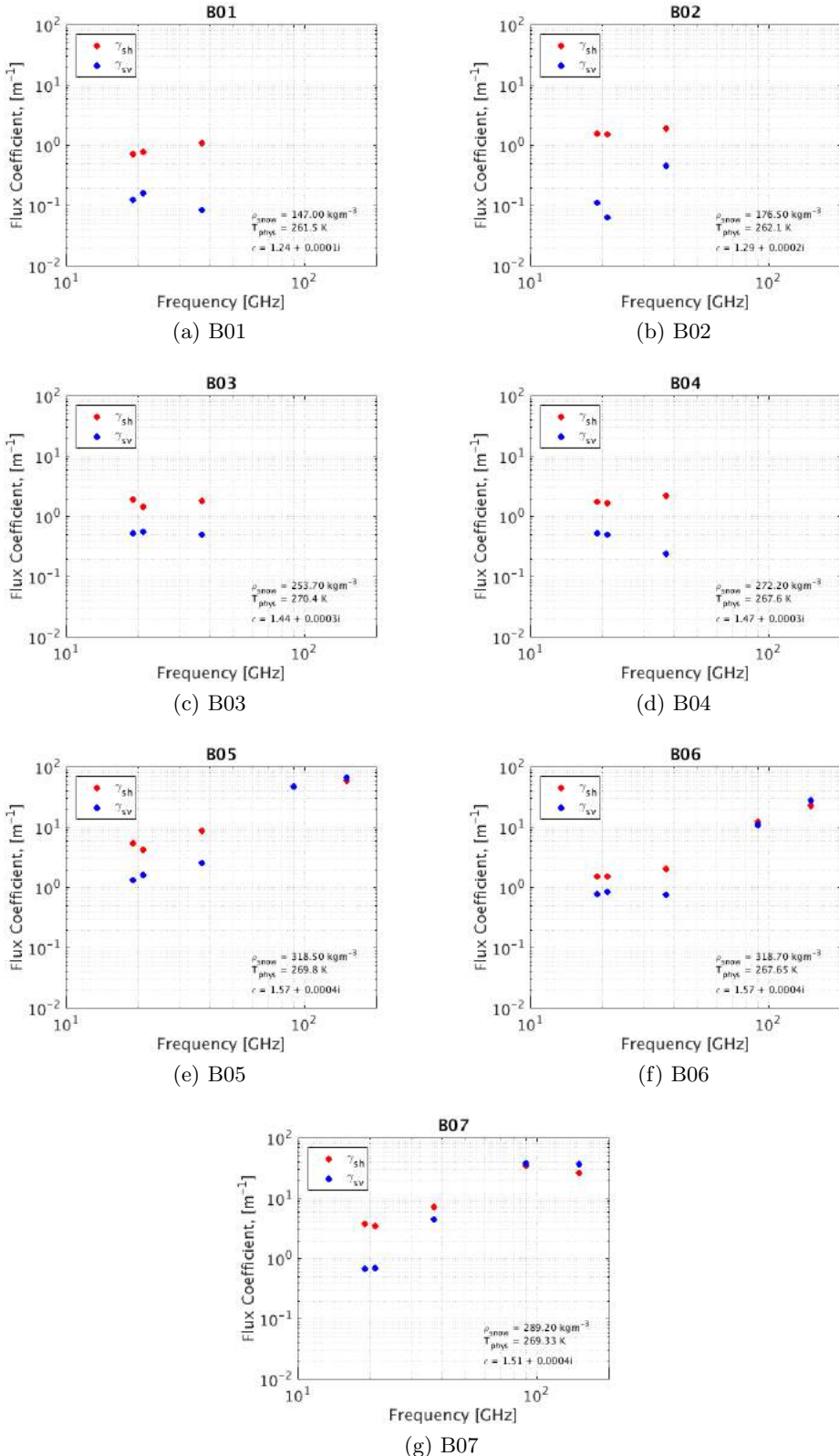


**Figure 5.5:** Six-flux scattering coefficients, at both H-Pol (Red) and V-Pol (Blue), at all measured frequencies, for the 2015 slab samples. Each subplot shows the physical temperature, average density, and dielectric constant of the slab, calculated with the permittivity model described in Section 2.5.4.1.

### 5.3.2.1 ASMEx Anisotropy Studies

The ASMEx campaign contained observations of snow parameters using both traditional snowpit observations and high-resolution  $\mu$ CT analysis (Section 4.2.3); with the aim of characterising the snow slabs. The high resolution  $\mu$ CT data was used to test the anisotropy of the slab samples, in order to assess if the anisotropy of the snow slabs was the reason behind the polarization difference in scattering coefficients.

As snow settles under gravity, and is subject to continuous vertical temperature gradient, snow crystals are, over time, orientated in such a way that the snow cannot be treated as isotropic; that snow crystal orientation is independent of direction. Therefore, it cannot be assumed to be isotropic in a thermal, mechanical, or electromagnetic sense ([Leinss et al. \[2016\]](#)). This electromagnetic anisotropic nature was suspected to be the reason behind the polarization difference experienced between  $\gamma_{sh}$  and  $\gamma_{sv}$ , as the two perpendicular polarizations would view the snow crystals in different orientations.

The anisotropy of the  $\mu$ CT snow samples were assessed and described in terms of correlation length ([Mätzler \[2002\]](#)) in the x, y, and z directions ( $P_{ci}$  in  $i \in (x,y,z)$ ). In this study, the vertical-to-horizontal correlation length ratio is defined as  $\varepsilon = \frac{p_z}{p_{xy}}$ .

[Leinss et al. \[2016\]](#) discusses the concept of linking the anisotropy of the snow with the effective permittivity  $\epsilon_{eff,i}$  for  $i \in (x,y,z)$ . [Leinss et al. \[2016\]](#) uses an extension to the classic Maxwell-Garnett mixing formula for ice in an air medium ([Polder and Van Santen \[1946\]](#) and [Sihvola \[2000\]](#)). The original Maxwell-Garnett formula states that:

$$\epsilon_{eff} = \epsilon_{air} + 3\phi\epsilon_{air} \frac{\epsilon_{ice} - \epsilon_{air}}{\epsilon_{ice} + 2\epsilon_{air} - \phi(\epsilon_{ice} - \epsilon_{air})} \quad (5.36)$$

where  $\phi$  is the ice volume fraction,  $\epsilon_{air}$  is the permittivity of air ( $\epsilon_{air} = 1$ ), and  $\epsilon_{ice}$  is the permittivity of ice ( $\epsilon_{ice} \approx 3.17$  ([Mätzler \[1998\]](#))). [Leinss et al. \[2016\]](#) found that a more accurate way to calculate the effective permittivity was to use a weighted average involving the Maxwell-Garnett formula, and the “Inverse” Maxwell-Garnett formula (modelling air in a medium of ice), such that:

$$\epsilon_{eff} = \frac{\epsilon_{eff,MG} + \epsilon_{eff,MGI}\phi\epsilon_{ice}}{1 + \phi\epsilon_{ice}} \quad (5.37)$$

For isotropic snow, where the vertical and horizontal length scales are equal,  $\epsilon_{eff,MG}$  should agree with measurements of permittivity, however using the Maxwell-Garnett formula alone produces an underestimation ([Mätzler \[1996\]](#) and [Leinss et al. \[2016\]](#)). Equa-

tion 5.37 assumes that the snow is isotropic, and that the ice crystals are spherical in nature. In these cases, Eqn 5.37 gives values of permittivity within  $\pm 0.7\%$  of the permittivity model stated in Section 2.5.4.1 (Leinss et al. [2016]).

However, for non-spherical assumptions (anisotropic snow) the effective permittivity in the spatial directions could change dramatically enough to effect the polarization difference in the six-flux scattering coefficients. By assuming that the horizontal and vertical polarizations align perfectly with the perpendicular spatial directions, effective permittivities in the different spatial directions (and thus different polarizations), were calculated.

For non-spherical crystals (anisotropic, where the vertical-to-horizontal length scale ratio  $\neq 1$ ) an adaptation to the Maxwell-Garnett and inverse Maxwell-Garnett equations, to include a “depolarization” factor for aligned ellipsoidal inclusions,  $N_i$  (Sihvola [2000] and Leinss et al. [2016]) was used. Using this inclusion, the Maxwell-Garnett and inverse Maxwell-Garnett equations for anisotropic medium (in this instance, snow) are:

$$\epsilon_{eff,MG,i} = \epsilon_{air} + \phi \epsilon_{air} \frac{\epsilon_{ice} - \epsilon_{air}}{\epsilon_{air} + (1 - \phi) N_i (\epsilon_{ice} - \epsilon_{air})} \quad (5.38)$$

$$\epsilon_{eff,MGI,i} = \epsilon_{ice} + \phi \epsilon_{ice} \frac{\epsilon_{air} - \epsilon_{ice}}{\epsilon_{ice} + \phi N_i (\epsilon_{air} - \epsilon_{ice})} \quad (5.39)$$

Equation 5.37 is then used to combine the mixing formulae to get the permittivity in each spatial direction for  $i \in (x,y,z)$ .

The polarization factors satisfy  $N_x + N_y + N_z = 1$  for any ellipsoid (Polder and Van Santen [1946]). For spherical grains,  $N_x = N_y = N_z = \frac{1}{3}$ , and Eqn 5.38 becomes Eqn 5.36 (Löwe et al. [2013]). Leinss et al. [2016] showed that the depolarization factor  $N_i$  could be expressed in terms of an anisotropy parameter  $Q$ , such that  $N_i = Q$  for  $i = x$  and  $y$ , and  $Q = 1 - 2N_i$  for  $i = z$ , where  $Q$  is expressed as:

$$Q = \begin{cases} \frac{1}{2} \left\{ 1 + \frac{1}{\varepsilon^2 - 1} \left[ 1 - \frac{1}{2\chi_b(\varepsilon)} \ln \left( \frac{1 + \chi_b(\varepsilon)}{1 - \chi_b(\varepsilon)} \right) \right] \right\}, & \text{for } \varepsilon > 1 \\ \frac{1}{2} \left\{ 1 + \frac{1}{\varepsilon^2 - 1} \left[ 1 - \frac{1}{\chi_a(\varepsilon)} \tan(\chi_a(\varepsilon)) \right] \right\}, & \text{for } \varepsilon < 1 \end{cases} \quad (5.40)$$

where  $\varepsilon$  is the vertical-to-horizontal correlation length ratio ( $\frac{p_z}{p_{xy}}$ ), and  $\chi_a(\varepsilon)^2 = -\chi_b(\varepsilon)^2 = \frac{1}{\varepsilon^2} - 1$ . When  $\varepsilon = 1$ , both forms of Eqn 5.40 give  $Q \rightarrow \frac{1}{3}$ .

As the  $\mu$ CT profile data includes correlation length data in all three spatial dimensions, it is possible to produce anisotropy parameter profiles for each  $\mu$ CT profile. From

these profiles, measurements of effective permittivity in all three spatial directions can be produced.

Figure 5.6 shows the variation in correlation length (Figure 5.6a and Figure 5.6b), the anisotropy factor Q (Figure 5.6c and Figure 5.6d), and the effective permittivity profile in the three spatial directions (Figure 5.6e and Figure 5.6f) for the two  $\mu$ CT samples taken from Slab A06. The dashed lines in the anisotropy factor and the effective permittivity plots show the anisotropic factor for isotropic snow (0.33) and the permittivity (calculated by the permittivity model in Section 2.5.4.1) respectively. It can be seen that, for this slab, the horizontal correlation length was larger than the vertical correlation length ( $\epsilon < 1$ ), and thus the crystals were horizontal ellipsoid in nature. The effective permittivity in the different spatial directions were different, with  $\epsilon_{eff,x}$  and  $\epsilon_{eff,y}$  being larger than  $\epsilon_{eff,z}$ .

However, it can be seen in Table 5.3 that the calculated values of  $\epsilon_{eff}$  (using the  $\mu$ CT samples) were similar to that of the bulk value of  $\epsilon$ , as calculated by the permittivity model used by the n-HUT model (Section 2.5.4.1).

Slab	$\epsilon$	$\epsilon_{eff,x}$	$\epsilon_{eff,y}$	$\epsilon_{eff,z}$
A01	1.2203	1.1462	1.1462	1.1381
A02	1.4655	1.4284	1.4282	1.4104
A03	1.3862	1.3430	1.3429	1.3228
A04	1.3824	1.5468	1.5468	1.5484
A05	1.5024	1.5058	1.5057	1.4965
A06	1.4699	1.4838	1.4844	1.4556
A07	1.4986	1.4929	1.4930	1.4751
B01	1.2410	1.2259	1.2257	1.2115
B02	1.2925	1.3124	1.3126	1.2944
B03	1.4362	1.4417	1.4419	1.4139
B04	1.4729	1.4823	1.4821	1.4496
B05	1.5696	1.5553	1.5550	1.5594
B06	1.5700	1.5770	1.5763	1.5452
B07	1.5076	1.5394	1.5390	1.5397

**Table 5.3:** Values of  $\epsilon$  from the permittivity model and from anisotropy analysis.

These bulk values of  $\epsilon_{eff,x}$  and  $\epsilon_{eff,y}$ , when used as an alternative value for the snow permittivity, produce new values of the six-flux scattering coefficients, shown in Figures 5.7 and 5.8, with  $\epsilon_{eff,x}$  being used for the horizontal polarization scattering coefficient calculations, and  $\epsilon_{eff,y}$  being used for the vertical polarization scattering coefficient calculations. It should be noted that the horizontal and vertical polarizations were not oriented such that they aligned with the x and y directions, as the snow slabs were observed at an incidence angle of  $50^\circ$  (Section 3.5.2). Bulk values of  $\epsilon_{eff,x}$  and  $\epsilon_{eff,y}$  place bounds on the expected retrieved six-flux scattering coefficients, if the anisotropic nature of snow

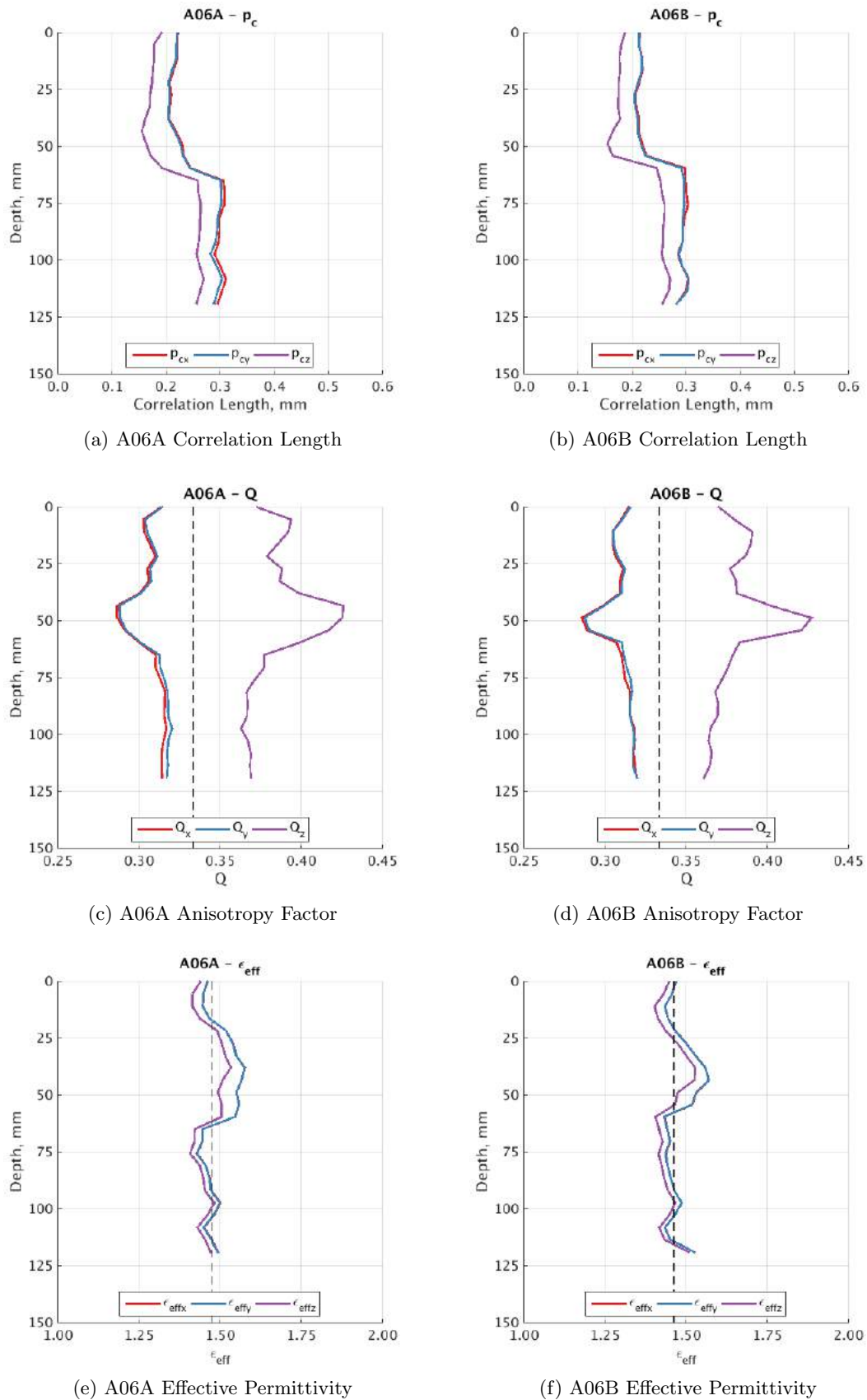
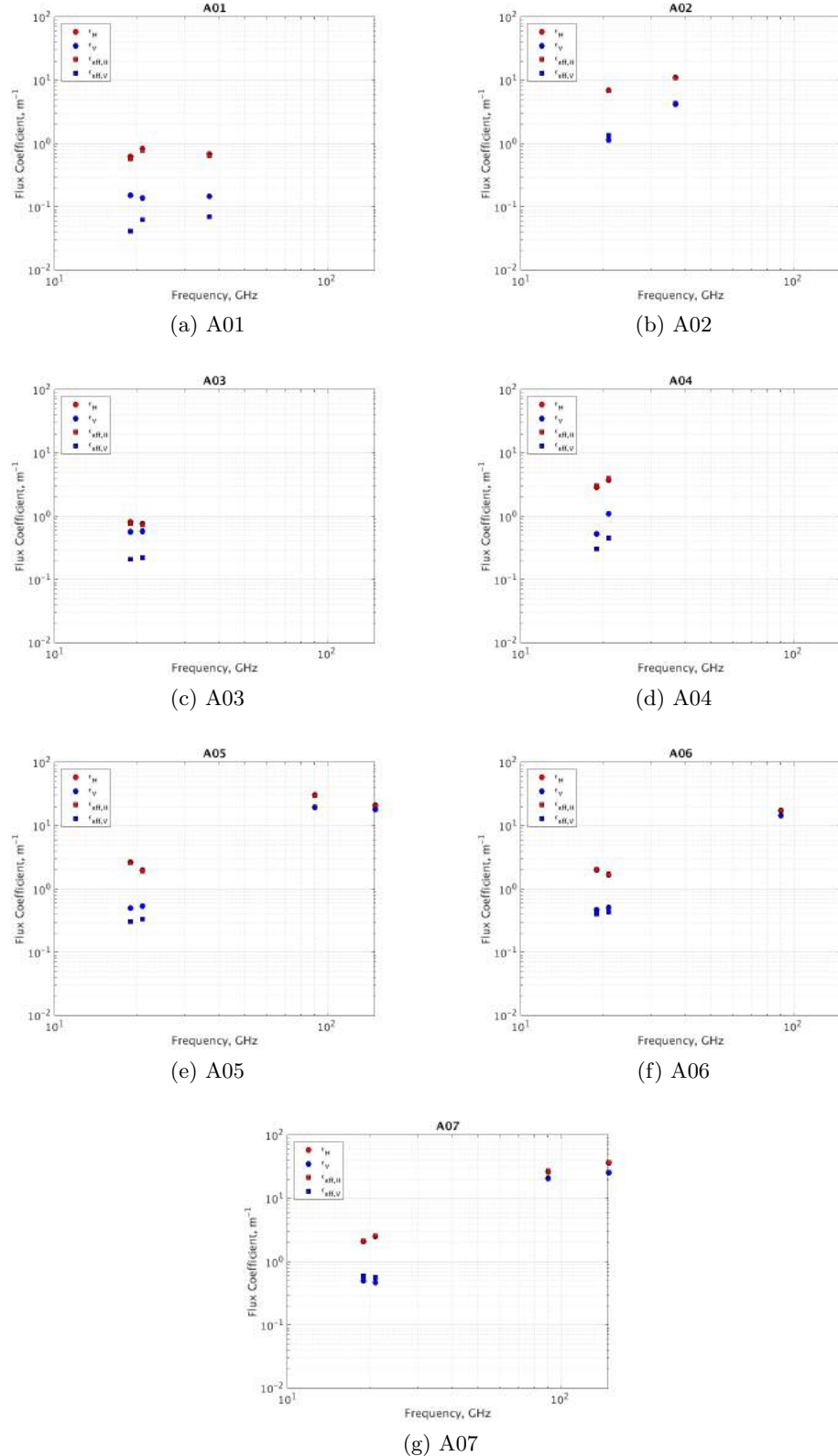
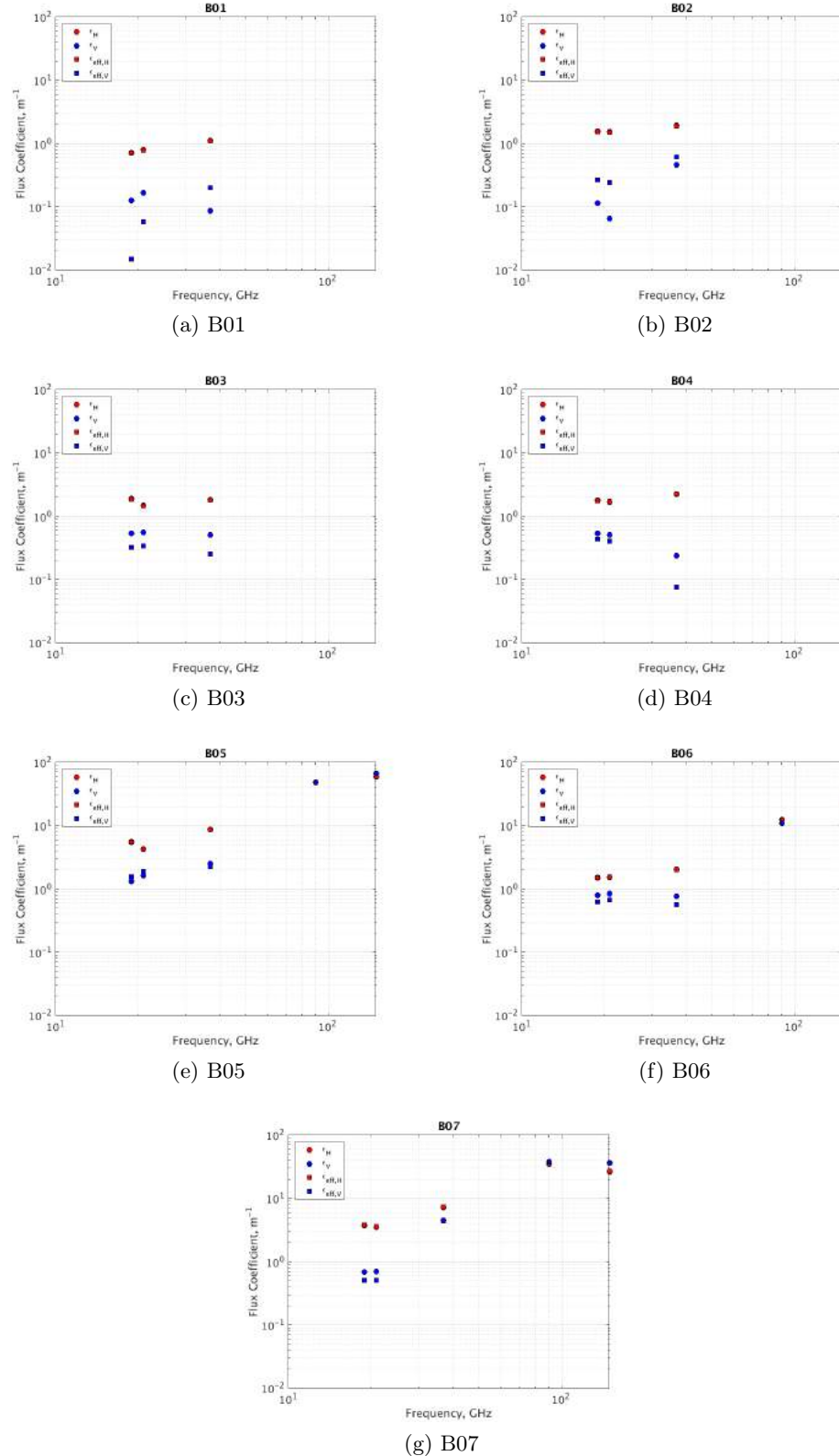


Figure 5.6:  $\mu$ CT anisotropy studies of Slab A06.



**Figure 5.7:** Six-flux scattering coefficients for the 2014 slab samples, calculated with the Flux Coefficient Model, using the permittivity model in Section 2.5.4.1 (circles) and the effective permittivities through the anisotropy calculations (squares), at both horizontal (red) and vertical (blue) polarizations.



**Figure 5.8:** Six-flux scattering coefficients for the 2015 slab samples, calculated with the Flux Coefficient Model, using the permittivity model in Section 2.5.4.1 (circles) and the effective permittivities through the anisotropy calculations (squares), at both horizontal (red) and vertical (blue) polarizations.

was the reason behind the scattering coefficient polarization difference. The variations in six-flux scattering coefficient were present due to different calculated values of  $r_{ih}$  and  $r_{iv}$ , as well as the value of  $\Omega_1$  and  $\Omega_2$  in Eqns. 5.32 and Eqns. 5.33 respectively. It was speculated that, by changing the values of the bulk  $\epsilon$  to that of  $\epsilon_{eff,x}$  and  $\epsilon_{eff,y}$ , the Fresnel reflectivities and two- to six-flux conversion would result in altered six-flux scattering coefficients, thus removing the polarization difference from the six-flux scattering coefficients.

Looking at Figures 5.7 and 5.8, it was shown that the effective permittivity did not have a large effect upon  $\gamma_{sh}$ . However, the values of  $\gamma_{sv}$  using the effective permittivities were lower than those using the permittivity model. This decrease in scattering coefficients at vertical polarizations shows that the polarization difference was not reduced by using the anisotropy analysis. Thus, the anisotropic effective permittivity does not improve the retrieval of scattering coefficients, and was not used further.

## 5.4 Extinction Coefficient Model

Using the retrieved coefficients from the [Wiesmann et al. \[1998\]](#) methodology, it was possible to reproduce a simple empirical extinction coefficient model, adding together the contribution from the theoretical absorption coefficient used within the n-HUT model (from Eqn. 2.42) with the retrieved six-flux scattering coefficient. Rather than use the flux coefficient model (stated in Section 5.2) to attempt to calculate the individual flux coefficients of individual layers within a multiple layer snowpack, an empirical scattering coefficient model was developed, using both frequency and optical grain size as variables. Optical grain size ( $D_{opt}$ ), calculated from observations of SSA, was used for the empirical scattering coefficient model, as observations of SSA (and thus calculated values of  $D_{opt}$ ) do not suffer from the problems of observer-subjectivity that observations of traditional grain size are subject to. Measurements of traditional grain size are influenced by the skill and expertise of the observer. The traditional grain size observations are that of the average value of the largest extent of the grains ([Fierz et al. \[2009\]](#)). Thus, as snow crystals are not spherical in nature (as shown by the anisotropy studies in Section 5.3.2.1), the mean value of largest extent of the grains will produce an overestimation of the amount of scattering, as grains are not orientated in such a way that the largest extent is perpendicular to the beam of radiation. Observations of SSA, through  $\mu$ CT analysis ([Heggli et al. \[2009\]](#)), hemispheric reflectances with DUFISS or IceCube instruments ([Gallet et al. \[2009\]](#) and [Zuanon \[2013\]](#)), from NIR photography ([Matzl and Schneebeli \[2006\]](#)), or from

gas-absorption techniques ([Legagneux et al. \[2002\]](#)) take this into account, as SSA is a function of both surface area and volume of the snow (Eqn. [2.18](#)). It also allows for direct comparison between SSA and correlation length (which are theoretically related, Eqn. [2.22](#)).

For the derived scattering coefficient model, the vertical scattering coefficient ( $\gamma_{sv}$ ) was used. The empirical scattering coefficient model used the following equation:

$$k_s = \alpha(D_o)^{c_1}(F)^{c_2} \quad (5.41)$$

where  $\gamma_s$  is the scattering coefficient (in this study,  $\gamma_{sv}$ ),  $D_o$  is optical diameter (mm), F is the frequency (GHz),  $c_1$  and  $c_2$  are the exponent dependencies of the optical diameter and frequency respectively, and  $\alpha$  is a multiplication coefficient. While Eqn. [5.41](#) has three unknown coefficients, each unknown term was calculated independently.

#### 5.4.1 Frequency Dependency

To calculate the frequency dependency, the first two terms of Eqn. [5.41](#) were combined, such that:

$$\beta = \alpha D_o^{c_1} \quad (5.42)$$

Therefore:

$$k_s = \beta F^{c_2} \quad (5.43)$$

By plotting all values of  $\gamma_{sv}$  against frequency upon a loglog plot for each individual slab sample, any regression line (calculated from Eqn. [5.43](#)) plotted has a gradient equal to the frequency exponent. Figure [5.9a](#) shows the  $\gamma_{sv}$  regression lines from all 14 slabs plotted with respect to frequency. While each regression line carried its own equation, in the form shown in Eqn. [5.43](#),  $c_2$  was independent of  $\beta$ . Table [5.4](#) shows the values of  $\beta$  and  $c_2$  for each slab for the  $\gamma_{sv}$  regression lines. As  $\beta$  was independent of  $c_2$ , the values of  $\beta$  were normalised to determine  $c_2$ . By setting the value of  $\beta$  to 1 for all slabs, the exponents were compared, to find a common exponent as shown in Figure [5.9b](#). From Figure [5.9b](#), it is clear that a common frequency exponent band was present.

The reasoning being the common band was thought to be from one of two separate sources; slab homogeneity or number of measurements. As the plots in Figure [5.9](#) used all

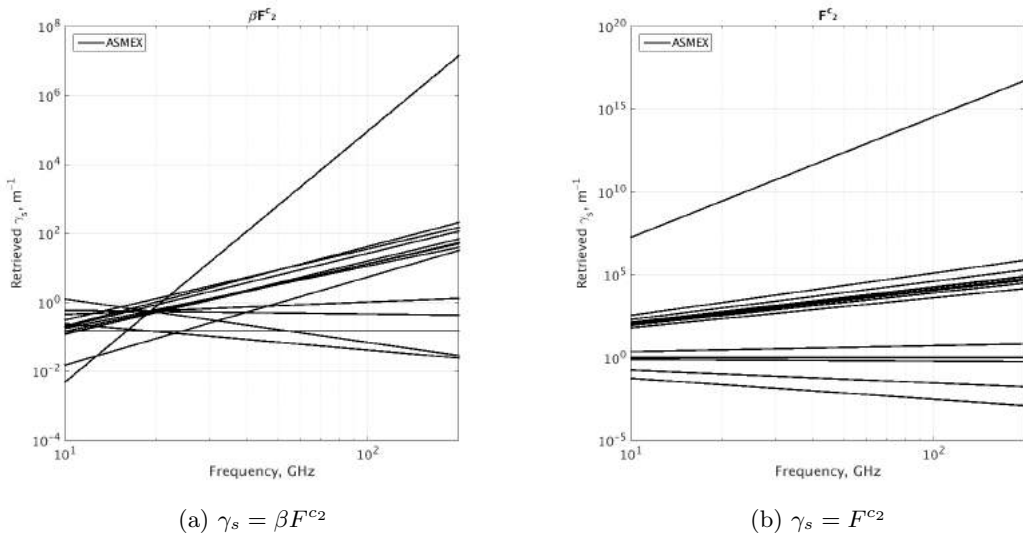


**Figure 5.9:** Regression lines of  $\gamma_s$  for the 14 ASMEEx slab samples, with respect to Frequency.

Slab	$\beta$	$c_2$	Number of points	Homogeneity
A01	0.1441	0.0027	3	Homogeneous
A02	0.0010	2.3045	2	Non-Homogeneous
A03	0.1959	0.3589	2	Homogeneous but wet
A04	0.0000	7.2697	2	Non-Homogeneous
A05	0.0016	1.9547	4	Non-Homogeneous
A06	0.0012	2.0252	4	Homogeneous
A07	0.0009	2.1194	4	Non-Homogeneous
B01	1.4063	-0.7651	3	Homogeneous
B02	0.0000	2.5535	3	Homogeneous
B03	0.7530	-0.1075	3	Homogeneous
B04	22.4420	-1.2562	3	Homogeneous
B05	0.0027	2.0621	5	Homogeneous
B06	0.0027	1.8080	5	Homogeneous
B07	0.0014	2.1339	5	Homogeneous

**Table 5.4:** Individual slab values for the unknown terms in Eqn. 5.43.

14 slabs, a mixture of both homogeneous and non-homogeneous slabs (as shown in Table 5.4), a hypothesis is that the homogeneity of the slabs may cause the common band of frequency exponents. Non-homogeneous slabs have numerous discrete permittivity and density changes through different periods of snowfall, and for melt-freeze events, resulting in numerous different volume scattering, while the homogeneous slabs (with no additional internal layers) would have a single scattering coefficient. An alternative hypothesis is that the spread may be related to the number of frequency measurements. Slabs measured with four or more frequencies may have regression lines that are very different to those with two or three.

Both potential reasons were tested, as shown in Figure 5.10. Figure 5.10a shows the homogeneity theory (with stratigraphy highlighted into one of two groups), and Figure 5.10b illustrates the test of the frequency theory (with the number of points, highlighted accordingly). It can be seen that, from Figure 5.10a, homogeneity does not appear to have a large influence; as four of the eight values of  $c_2$  that fall in the common band were homogeneous. With four homogeneous slabs outside the common band, it appears that homogeneity does not affect the frequency dependency. It can be seen in Figure 5.10b that the slabs with more frequency measurements fall within the common band. The common band of frequency exponents were made up with regression lines with four or more frequencies. The homogeneous slabs tended to be found at the beginning of each campaign period; when large fresh snowfall was more likely, and melt-freeze periods were much less likely due to the much colder air temperatures and diurnal cycle. Unfortunately, these periods were periods when the SodRad2 platform were not available. This means that the slabs that were measured with all radiometers were more likely to be non-homogeneous.

From Figures 5.10a and 5.10b, it was clear that the number of frequency measurements was a stronger determiner of the frequency exponent band, rather than the homogeneity of the slabs. To calculate a common frequency exponent, a mean exponent was calculated from within a threshold region. The threshold values used were  $1 < c_2 < 3$ , giving a mean  $c_2$  value of 2.1202.

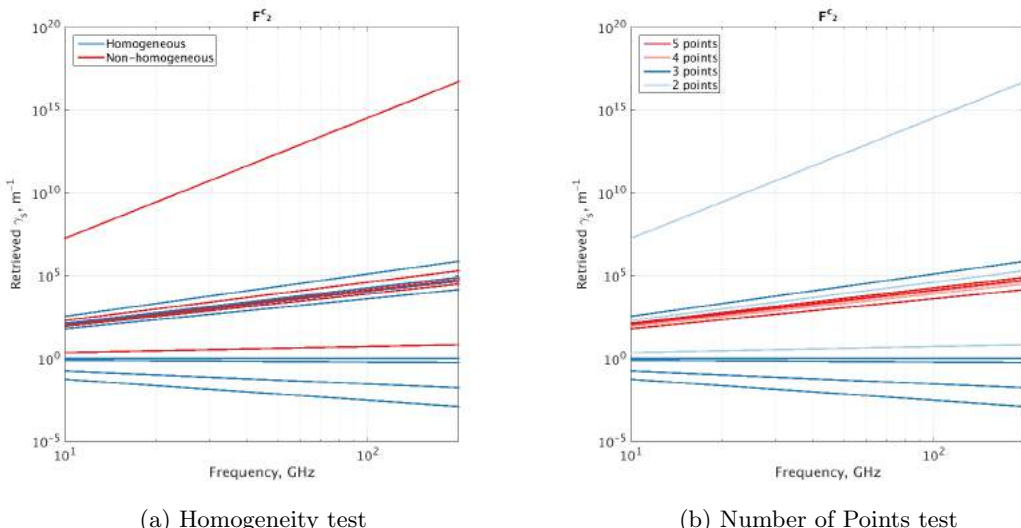


**Figure 5.10:** Frequency common band test.

### 5.4.2 Optical Diameter Dependency

To calculate the optical diameter dependency, a similar form of analysis to that of the frequency dependency was used. By combining  $\alpha$  and the frequency term:

$$\Phi = \alpha F^{c_2} \quad (5.44)$$

Eqn. 5.41 was transformed to:

$$k_s = \Phi D_o^{c_1} \quad (5.45)$$

Similar to the frequency dependency studies, by plotting  $\gamma_s$  against values of  $D_o$  on the same axis, all five frequencies were compared. The regression lines in Figure 5.11a were plotted in such a way that the gradient was equal to the value of  $c_1$ . Table 5.5 shows the values of  $\Phi$ ,  $c_1$ , and the number of slabs measured at each individual frequency.

Frequency (GHz)	$\Phi$	$c_1$	Number of points
18.7	1.7671	1.4793	13
21.0	2.6041	1.7717	14
36.5	10.3767	2.6029	9
89.0	114.7299	2.6246	6
150.0	65.6039	1.2384	6

Table 5.5: Individual frequency values for the unknown terms in Eqn. 5.45.

As  $\Phi$  was independent of  $c_1$ , it was set to be equal to 1, in order to analyse the values

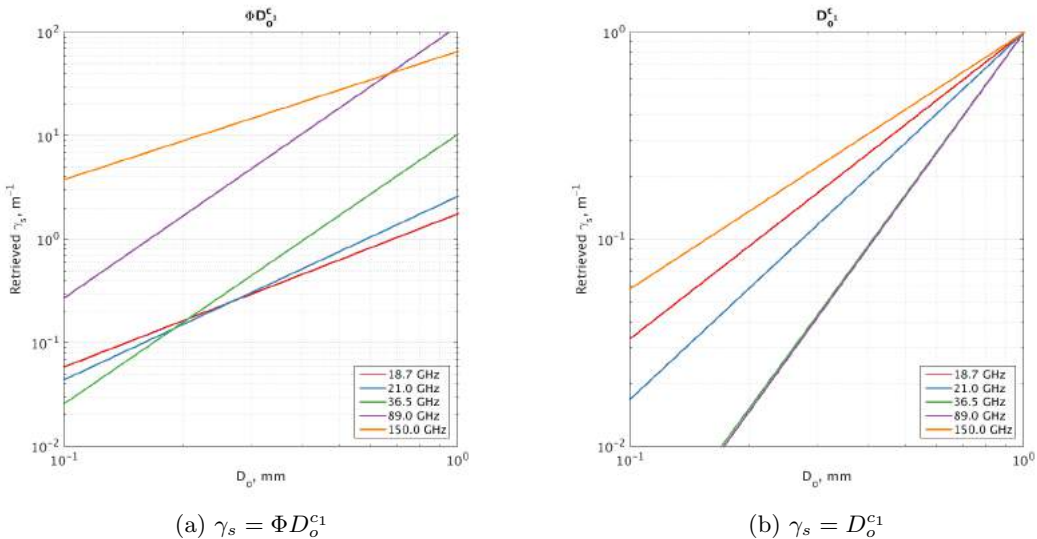


Figure 5.11: Regression lines of  $\gamma_s$  for the 5 ASME frequencies, with respect to optical diameter.

of  $c_1$ . Figure 5.11b shows the values of  $c_1$  plotted upon the same axis, which allowed for direct comparison.

It was seen that, unlike the frequency exponents analysis, there were no real common band of exponents. This did not allow for an easy calculation of the optical diameter exponent. Analysis of the number of points (Figure 5.12) did not give a clear indication of a potential mean optical diameter calculation, as the two frequencies with the most measurements (18.7 and 21.0 GHz) were not close to those with fewer measurements. For this analysis, the regression law (calculated by Eqn. 5.45) at 150.0 GHz were not important. Due to the much smaller penetration depths at 150.0 GHz, scattering at this frequency is focused higher in the pack, and is not representative of the scattering within the snowpack. Neglecting the exponent law of 150 GHz allowed the mean optical diameter exponent to be determined as 2.1196.

### 5.4.3 $\alpha$ Calculation

$\alpha$  was calculated by substitution of  $c_1$  and  $c_2$  with their respective values; the gradient of the retrieved scattering coefficient against  $D_o^{c_1} F^{c_2}$ . Figure 5.13 shows the derived scattering coefficients plotted against the derived exponent terms. Each individual frequency was highlighted, showing the problems 150.0 GHz had in comparison to the other frequencies. The solid lines show a regression line of the lower four frequencies, through the origin, as an optical diameter of zero would exhibit no scattering. From Figure 5.13, the value of the gradient, and hence  $\alpha$ , was equal to  $0.0065 \text{ m mm}^{-2.12} \text{ GHz}^{-2.12}$ , with an  $r^2$  value of 0.94 across 18.7 – 89.0 GHz.

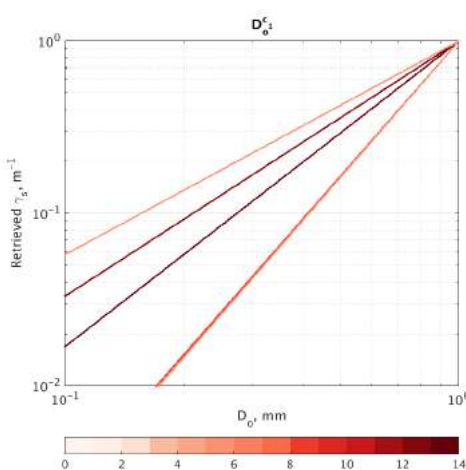
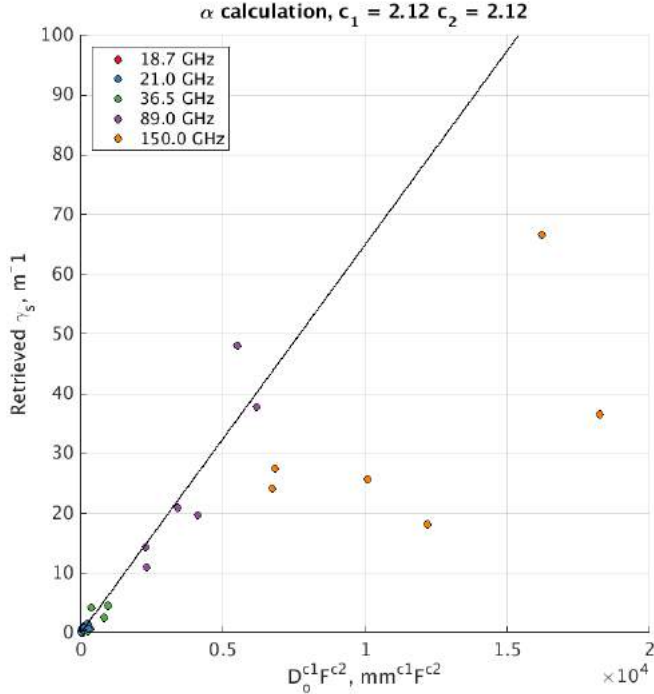


Figure 5.12: Number of points analysis.

Figure 5.13: Calculation of  $\alpha$ .

#### 5.4.4 Development of the Scattering Coefficient Model

With the calculation of the values of  $c_1$ ,  $c_2$ , and  $\alpha$ , the empirical scattering coefficient model was written as:

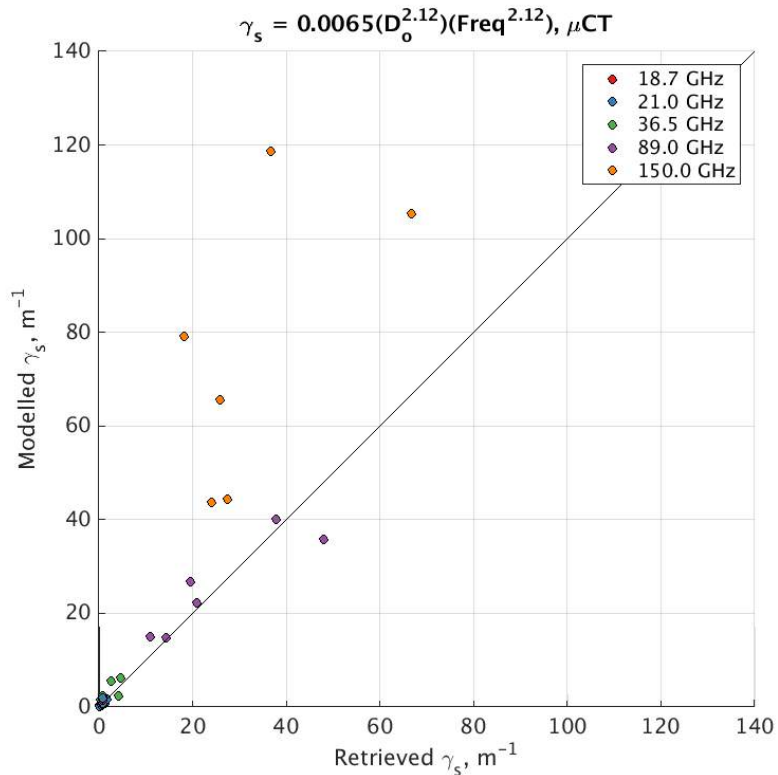
$$k_s = 0.0065(D_o)^{2.12}(F^{2.12}) \quad (5.46)$$

Figure 5.14 shows the retrieved scattering coefficients from the [Wiesmann et al. \[1998\]](#) methodology plotted against the modelled scattering coefficients from the above analysis, at all frequencies. The retrieved scattering coefficients were plotted against the respective modelled scattering coefficient. A 1:1 line was plotted alongside, allowing for direct comparison. It can be seen that the modelled scattering coefficient was a good representation of the retrieved coefficients for the lower four frequencies. This was to be expected, as the scattering coefficients modelled was built using data from these frequencies, excluding 150.0 GHz. Due to the small amount of higher frequency data collected (six slabs measured at both 89.0 and 150.0 GHz), statistics on each frequency were not meaningful. However, by comparing all frequencies (42 points), statistics upon the modelled scattering coefficients is more significant. Individual frequencies were analysed, and the effects inferred by neglecting them in turn, and comparing the resulting  $r^2$  value are shown below. Table 5.6 shows the  $r^2$  values of the modelled scattering coefficient compared to the

retrieved scattering coefficient for all frequencies combined; as well as by neglecting each frequency in turn. It can clearly be seen that, when the 150.0 GHz data were neglected, the  $r^2$  value increased dramatically from 0.637 (when no frequencies were neglected) to 0.933. This suggests that 150.0 GHz does not fit well with the scattering coefficient model. When 150.0 GHz remains, and each of the other four frequencies were neglected in turn, the  $r^2$  value remained in the range 0.55 – 0.58; a lower value than that of no neglected frequency (and a value much lower than that when 150.0 GHz was neglected).

Frequency Neglected (GHz)	$r^2$
None	0.637
150.0	0.933
89.0	0.580
36.5	0.576
21.0	0.552
18.7	0.555

**Table 5.6:** Values of  $r^2$  for neglected frequencies.



**Figure 5.14:** Retrieved vs modelled  $k_s$  values.

### 5.4.5 Extinction Coefficient Model

Thus, using the theoretical absorption coefficient from Section 5.3.1 and the empirical scattering coefficient model derived above, the empirical extinction coefficient model, derived from the ASMEx campaign is:

$$k_{e,ASMEx} = k_{a,theo} + k_{s,Mas} \quad (5.47)$$

$$\Rightarrow k_{e,ASMEx} = (4\pi F \times 10^9) (\sqrt{\mu_0 \epsilon_0 \epsilon'_{snow}}) \left( \sqrt{0.5 \left( \sqrt{1 + \left( \frac{\epsilon''_{snow}}{\epsilon'_{snow}} \right)^2} \right)} - 1 \right) + 0.0065(D_o)^{2.12}(F^{2.12}) \quad (5.48)$$

where  $k_{e,ASMEx}$  is the extinction coefficient from the ASMEx campaign ( $m^{-1}$ ),  $k_{a,theo}$  is the theoretical absorption coefficient,  $k_{s,Mas}$  is the newly derived empirical scattering coefficient model,  $\lambda$  is the wavelength of radiation measured, and  $\epsilon'_{snow}$  and  $\epsilon''_{snow}$  are the real and imaginary parts of the dielectric constant of snow respectively.

### 5.4.6 Implementation of the Derived Extinction Coefficient Model into the n-HUT Model

With the completion of the derived extinction coefficient model of Eqn. 5.48, it was implemented into the multiple layer HUT snow emission model, similar to those calculated by Hallikainen et al. [1987], Roy et al. [2004], and Beser [2011] in Section 2.5.4.3. The above derived extinction coefficient was easy to implement, as shown in Figure 5.15. The original Hallikainen et al. [1987] extinction coefficient calculated the extinction in units decibels per meter ( $dB/m$ ), whilst the derived extinction coefficient calculated the extinction in units of per meter ( $m^{-1}$ ). In order to properly implement the new extinction coefficient into the n-HUT model, the derived extinction coefficient was divided by  $\frac{10}{ln(10)} \approx 4.343$  (Rees [2012]). Figure 5.15 shows an adapted schematic of processes within the multiple layer HUT snow emission model, similar to the original schematic shown in Section 2.5.4 (Figure 2.10). The adapted inputs and calculations, shown in green, show the differences between the original and the adapted multiple layer HUT snow emission model. As the extinction coefficient calculation depends of the optical diameter rather than the traditional grain size, the multi-layered snowpack must be described by its optical diameter. Thus, the input parameters, along with the parameter designation values, must be altered accordingly.

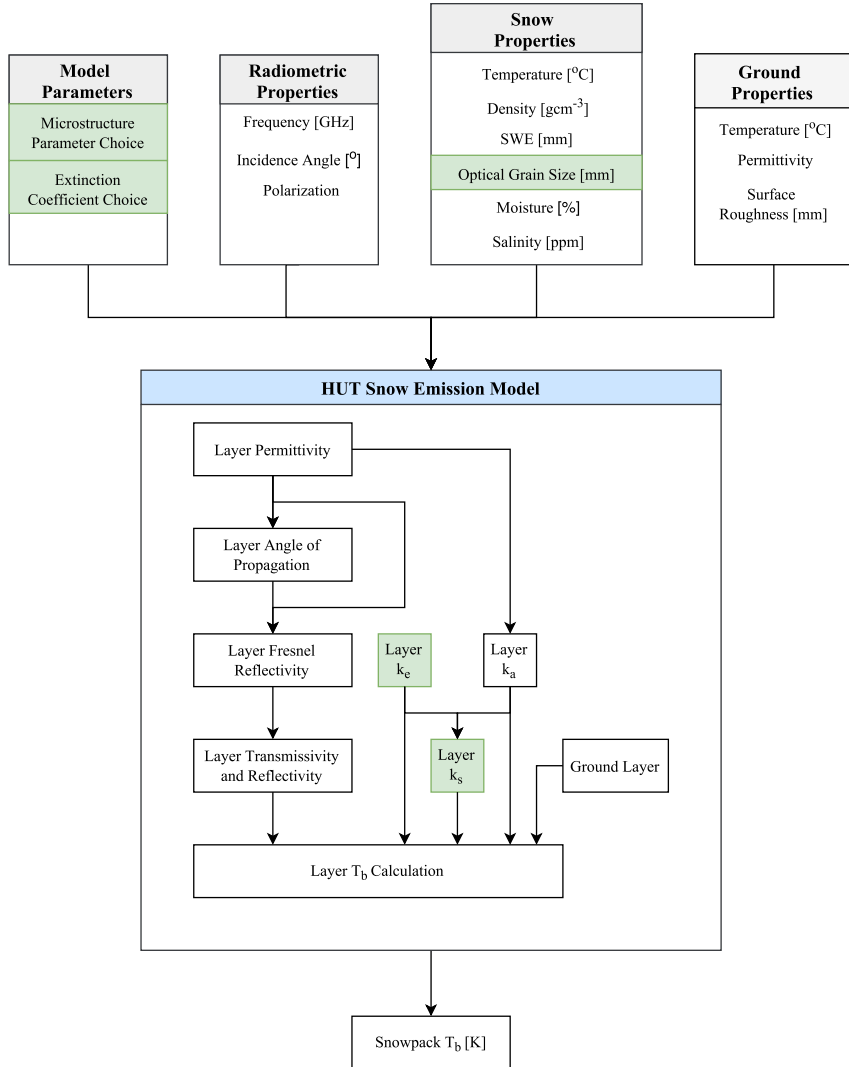


**Figure 5.15:** Schematic diagram of the HUT snow emission model, adapted for use with the derived extinction coefficient. Model Inputs (grey boxes) are grouped within the four categories. The internal running of the HUT snow emission model is shown within the blue box. Adaptations from the original schematic (Figure 2.10) are shown in green.

By producing and implementing a new extinction coefficient that utilizes  $D_{opt}$  (through observed values of SSA) into the n-HUT model, the operational capability has been greatly increased. As the SSA is observed through objective observation techniques (through observations with the IceCube instrument ([Zuanon \[2013\]](#)),  $\mu$ CT analysis ([Heggli et al. \[2009\]](#))), and correct SMP observations ([Proksch et al. \[2015\]](#))), the n-HUT model does not require subjective observations of traditional grain size for simulations of brightness temperature to be obtained. This allows for a reduction in the number of potential sources of error during snowpit observations, as the snowpack parameters are observed through objective techniques, removing the subjectivity from the observations.

## 5.5 Chapter Summary

Previously in Chapter 4, the observed radiometric, snow characteristic, and stratigraphic data collected as part of the ASMEEx campaign was shown. In this chapter, the ASMEEx dataset is utilized to produce a new extinction coefficient model. To produce a new model, the three individual goals of the second thesis aim were met.

### Aim 2, Goal 1: Calculate individual absorption and scattering coefficients of the ASMEEx snow slab dataset, using a flux coefficient model.

Initially, the individual absorption and scattering flux coefficients of the ASMEEx slabs were calculated, using the raw radiometric data in conjunction with a flux coefficient model. The flux coefficient model is made of two separate models; an initial sandwich layer model that calculates the two-way flux (upwards and downwards) coefficients, and a model to convert the two flux coefficients into six-way flux (upwards, downwards, and four internally trapped horizontal directions) coefficients, using simulated values of the complex dielectric constant. The simulated complex dielectric constant was calculated using a model listed within the n-HUT model (Eqns. 2.28 – 2.38). Both the sandwich layer model and the two- to six-flux conversion model were originally described by [Wiesmann et al. \[1998\]](#).

The calculated two- and six-flux absorption coefficients were compared to the theoretical absorption coefficient used within the n-HUT model, and it was shown that the six-flux absorption coefficient were small than the two flux equivalent. It was also shown that both the two- and six-flux absorption coefficients were comparable to that of the theoretical absorption coefficient. Thus, the theoretical absorption coefficient used within the n-HUT model would continue to be used, and would make the absorption part of the newly derived extinction coefficient.

The calculated two- and six-flux scattering coefficients were contrasted against each other. It was found that, unlike the absorptive coefficient calculation, the six-flux scattering coefficients were larger than the corresponding two flux coefficient. This mirrored the finding of [Wiesmann et al. \[1998\]](#) and [Toure et al. \[2008\]](#), who also used a flux coefficient model in their studies. The studies of both [Wiesmann et al. \[1998\]](#) and [Toure et al. \[2008\]](#) also found a polarization difference within their calculated scattering coefficients, with the vertical polarization being smaller than those in the horizontal polarization; this difference was also present in the ASMEEx flux coefficient calculation. While it was initially

thought that the anisotropic nature of the snow was causing the polarization difference, it was shown that, by using an extension of the classic Maxwell-Garnett mixing formula ([Leinss et al. \[2016\]](#)) to calculate corrected effective permittivities, the anisotropic medium did not appear to reduce the polarization difference.

**Aim 2, Goal 2: Derive an empirical extinction coefficient model, using ASMEx absorption and scattering coefficients.**

Due to the persistent polarization difference, it was decided that the vertical polarization scattering coefficient would be the area of focus for the derived extinction coefficient; as vertical polarization was the focus of research by both [Wiesmann et al. \[1998\]](#) and [Toure et al. \[2008\]](#). An empirical formulae for calculating the vertical scattering coefficient, using the frequency and optical diameter (calculated from SSA) was derived, similar in fashion to the work by [Toure et al. \[2008\]](#). Optical diameter was chosen over traditional grain size, due to the more objective method in which the optical diameter was derived. Observations of traditional grain size are subjective to observer experience, through analysis in the field or through macro-photography post-observation. The frequency and optical diameter dependencies were calculated in turn, each with their own set of limitations and assumptions. It was assumed that the frequency dependency would be found within a common exponent threshold, shown in Figure 5.10 by assessing the frequency dependency with respect to the number of frequency observations made. As detailed in Section 3.6.2, not all slabs were observed at all frequencies, due to equipment issues. Slabs measured at four or more frequencies tended to show similar patterns of frequency dependency. There did not appear to be a link between frequency dependencies and homogeneity of the slab, as the influence by the number of observations overpowered the response.

The optical diameter dependency was calculated in a similar fashion to that of the frequency dependency. However, the number of observations did not provide a clear indication of a common band, as there were too few frequencies to draw a sufficient dependency from. However, observations at 150 GHz would be predominately from the upper layer of the snow, due to its small depth. Therefore, the 150 GHz observations within the optical diameter dependency studies were neglected, thus the dependency was calculated from the 18.7 – 89.0 GHz observations and flux coefficients.

After calculating both dependencies and an empirical scaling factor, the derivation the ASMEx extinction coefficient was complete, finishing the second of three goals towards the second thesis aim. The ASMEx extinction coefficient was calculated to be:

$$k_{e,ASMEx} = (4\pi f)(\sqrt{\mu_0 \epsilon_0 \epsilon'_{snow}}) \left( \sqrt{0.5 \left( \sqrt{1 + \left( \frac{\epsilon''_{snow}}{\epsilon'_{snow}} \right)^2} \right) - 1} + 0.0065 D_o^{2.12} F^{2.12} \right) \quad (5.49)$$

**Aim 2, Goal 3: Implement the newly derived extinction coefficient model in the HUT snow emission model.**

Upon the completion of the extinction coefficient, it was implemented into the n-HUT model, to produce the adapted n-HUT model. The new extinction coefficient model was implemented as an extension to the pre-existing extinction coefficient sub-function, which allowed for the selection of different extinction coefficients. A full schematic of the adapted n-HUT model, with changes from the original n-HUT model highlighted, was shown in Figure 5.15.

The research presented in this chapter details the completion of the second thesis aim; as a new extinction coefficient was derived from the ASMEx dataset for use with the n-HUT model. Chapter 6 will evaluate this, by testing the original n-HUT model against the adapted n-HUT model, with both the original and the newly derived extinction coefficients.

## Chapter 6:

# Sodankylä Radiometer Experiment (SoRaX)

## 6.1 Chapter Introduction

Chapter 5 detailed the methodology behind the creation of the derived extinction coefficient model (Eqn. 5.48), from calculated values of the dielectric constant, as well as radiometric and physical properties of the ASMEx snow slabs. In Section 5.4.6, the newly derived extinction coefficient model was input into the n-HUT model (detailed by the schematic in Figure 5.15), completing the three goals of the second thesis aim; to calculate the individual flux coefficients of the ASMEx snow slabs, to create a single extinction coefficient model using these flux coefficients, and to implement the derived extinction coefficient into the n-HUT model.

Throughout this chapter, the *adapted* n-HUT model refers to the n-HUT model, with the derived extinction coefficient in Section 5.4.5. The *original* n-HUT model refers to the n-HUT model with the extinction coefficient model from Hallikainen et al. [1987].

The intent of this chapter is to test the adapted multiple layer HUT snow emission model against the original multiple layer HUT snow emission model. In doing so, the goals set out to complete the third and final research aim in Section 1.3 would be met. Aim 3 states:

### Aim 3

Validate the new extinction coefficient with independent natural snowpack data.

## Goals

1. Analyse data collected as part of the Sodankylä Radiometer Experiment (SoRaX), to assess the usability of the SoRaX snowpit observations.
2. Simulate the brightness temperature, using both the original and the newly derived extinction coefficients.
3. Compare and contrast the brightness temperature errors from both extinction coefficient models.

In order for the adapted n-HUT model to be tested, radiometric and physical snow parameters must be collected, allowing for simulated brightness temperatures to be produced and compared to observed brightness temperatures of the snowpack. This chapter presents the research which is focused upon completing the above three goals; by introducing the SoRaX campaign, detailing the observations made, and showing comparisons of simulated brightness temperatures using both the original and the adapted n-HUT models. The SoRaX field campaign was initially designed to examine the influence of small scale spatial variability of snow cover on observed microwave signatures. Physical snow parameters were observed through numerous individual snowpits, connected via a number of snow trenches. Section 6.2 details the SoRaX field campaign, with information on its location being shown in Section 6.2.1. Adaptations to the SodRad platform for the SoRaX campaign are detailed in Section 6.2.2, with full experimental proceedings discussed in Section 6.2.3. The primary data collected from snow pit observations are shown in Section 6.3. The data visualisation are split into two sections; one detailing the radiometric data (Section 6.3.1), and one detailing the snow pit observations (Section 6.3.2). Finally, the simulated brightness temperatures (using both the original and adapted n-HUT models) are compared and contrasted to the observed brightness temperatures in Section 6.4.

## 6.2 Sodankylä Radiometer Experiment

In this Section, information about the SoRaX campaign is discussed. As previously mentioned, SoRaX was designed to examine the influence of small scale spatial variability of snow cover on observed microwave signatures ([Leppänen et al. \[2016a\]](#)). To examine this variability in microwave signatures over an extended timeframe, SoRaX took place from August 2015 – March 2016, and can be split into two separate experiments. The

first experiment involved near-continuous observations of brightness temperature of the natural snowpack. The brightness temperature measurements involved three different radiometer platforms; SodRad1 (observations at 10.6, 18.7, 21.0, and 36.5 GHz), SodRad2 (observations at 89.0 and 150.0 GHz), and ELBARA-II (the ETH L-Band Radiometer for soil moisture research ([Schwank et al. \[2010\]](#))), producing observations at 1.4 GHz). These radiometer observations were coupled with weekly snow pit observations, which allowed for manual determination of the snowpack properties and characteristics throughout the near-continuous brightness temperature observation. In order to not disturb the snowpack observed by the radiometers, the weekly snow pit observations took place outside the radiometer field of view, as shown in Figure 6.1.

The second experiment involved methodically cataloguing the properties and characteristics of the snowpack underneath the radiometer footprints. This was completed via a number of snow trenches situated within the radiometer footprints. Observations of snow parameters, such as density and SSA, required undisturbed snow in order to be representative of the surrounding snowpack, as the observation techniques are destructive in nature (Section 3.5.3). The snow parameter observations took place in a number of snow pits. All snow pits located at similar radiometer elevation angles were connected via a snow trench, in order to assess the horizontal variability of the snowpack through NIR photography (Section 6.3.2). Therefore, each trench was located parallel to an elevation angle measured during the first experiment, allowing for a direct comparison to be made. Each trench encompasses the azimuth angle range, to allow for numerous comparisons to be made.

This second experiment (hereby referred to as the SoRaX snow removal experiment) was conducted by members of the FMI, the University of Northumbria, and the University of Waterloo, in order to manually quantify the snowpack parameters. The SoRaX snow removal experiment provided the ideal framework and observations to allow for evaluation of the adapted n-HUT model, as it provided an independent set of snowpit and radiometric observations needed for model evaluation. Observations of the snow parameters during the snowpit observations, such as density, SSA, and traditional grain size, were used with both the original and adapted n-HUT models, in order to assess the differing extinction coefficients used, through changes in simulated brightness temperature. These simulated brightness temperatures would be compared to the observed brightness temperatures, using the SodRad1 platform.

### 6.2.1 SoRaX: Location

As previously mentioned, the full SoRaX campaign took place between August 2015 – March 2016, with the SoRaX snow removal experiment occurring between 29th February and 4th March 2016. Similar to the ASMEEx campaign, SoRaX took place at the FMI ARC (previously discussed in Section 3.2). The SoRaX observations took place at the IOA site, using the SodRad (Section 3.3) and ELBARA-II radiometer platforms for brightness temperature observations. Figure 6.1 shows the IOA, with the radiometer platforms, automatic weather stations, and natural snowpack locations highlighted. It should be noted that, whilst both ASMEEx and SoRaX took place within the IOA, different areas within the IOA were used (3.1).



**Figure 6.1:** FMI ARC Intensive Observation Area (IOA). The SodRad and ELBARA-II platforms (red) and automatic weather station instrumentation (black) are shown. The location of the FMI weekly snow pit measurement (purple) and the SoRaX trench locations (blue) are also highlighted. Photo taken from the IOA Camera.

### 6.2.2 SoRaX: Radiometers

As this study focuses on the assessment of the extinction coefficient within the original and adapted n-HUT models, observed brightness temperatures were required for a comparison with the different sets of simulated brightness temperatures to be made. Thus, the brightness temperatures of the snowpack recorded at 18.7, 21.0, and 36.5 GHz (all found on the SodRad1 platform) were used. These frequencies were chosen, as the extinction coefficient was derived between 18.7 – 89.0 GHz (Section 5.4.2). When testing

the adapted n-HUT model, 1.4, 10.7, 89.0, and 150.0 GHz were excluded; 89.0 and 150.0 due to the small penetration depths (Eqn. 2.23), and 1.4 and 10.7 GHz due to being outside the range of operational frequencies of the extinction coefficient.

The technical details of the SodRad1 platform can be found in Section 3.3, such as the integration time (1 second), sensitivity ( $< 0.05$  K), and Half Power Beam Width ( $6^\circ$ ) of the SodRad radiometers (Table 3.1), as well as the method of liquid nitrogen calibration technique. Figure 6.2 shows the elevation and azimuth angles applicable to the SoRaX campaign.

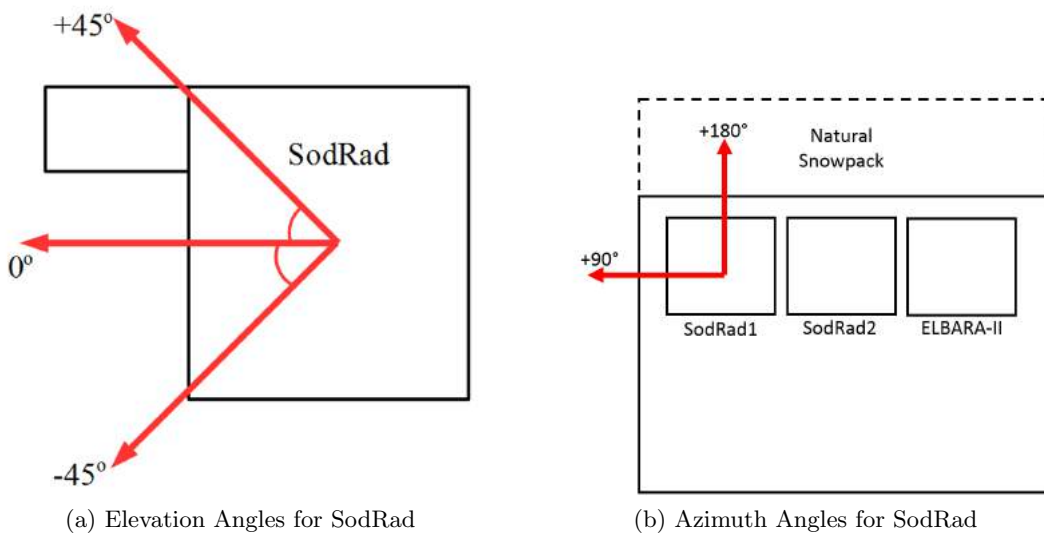


**Figure 6.2:** Elevation and Azimuth Angles for the SoRaX radiometer platforms.

### 6.2.3 SoRaX: Experimental Proceedings

This subsection details the procedures followed during the SoRaX snow removal experiment. As many observation techniques were used in both the ASMEx and SoRaX campaigns, the techniques will be briefly discussed here, with details of error sources being discussed in Section 3.5.2 (for radiometric measurements) and Section 3.5.3 (for snow characteristic measurement techniques). Where a new measurement technique is introduced for the SoRaX snow removal campaign, it will be discussed in full.

Throughout the entirety of the SoRaX campaign, radiometric observations of the natural snowpack were completed hourly, at 1.4, 10.7, 18.7, 21.0, 36.5, 89.0, and 150.0 GHz, at both horizontal and vertical polarizations. The radiometric observations were completed with the three tower-based radiometer platforms mentioned in Section 6.2.2; SodRad1, SodRad2, and ELBARA-II. As this study focuses on the observations at 18.7 – 36.5 GHz, future references of radiometric observations refer to observations at these

three frequencies.

The hourly radiometric observations of the IOA snowpack consisted of observations of overlapping radiometric footprints, with their centres being orientated in a grid-like pattern across numerous azimuth and elevation angles (as shown in Figure 6.3). Observations were made between azimuth angles of  $170^\circ$  and  $190^\circ$ , at  $2^\circ$  increments, and between elevation angles of  $-30^\circ$  and  $-60^\circ$ , at  $10^\circ$  increments. In addition to the natural snowpack observations, the SodRad1 platform observed zenith ( $90^\circ$  elevation,  $360^\circ$  azimuth) brightness temperatures, to record the down welling sky brightness temperatures. Each zenith observation was completed immediately after the completion of the hourly IOA snowpack scan.

Upon the completion of the radiometric measurements of the snowpack (and subsequent re-calibration of the radiometers), the SoRaX snow removal experiment began. Initially, the snow trench locations were marked out, marking out the position of the  $-60^\circ$ ,  $-50^\circ$ ,  $-40^\circ$ , and  $-30^\circ$  trenches (relative to the elevation angle of the SodRad platform). Figure 6.4a shows the locations of the proposed SoRaX snow removal experiment trenches,

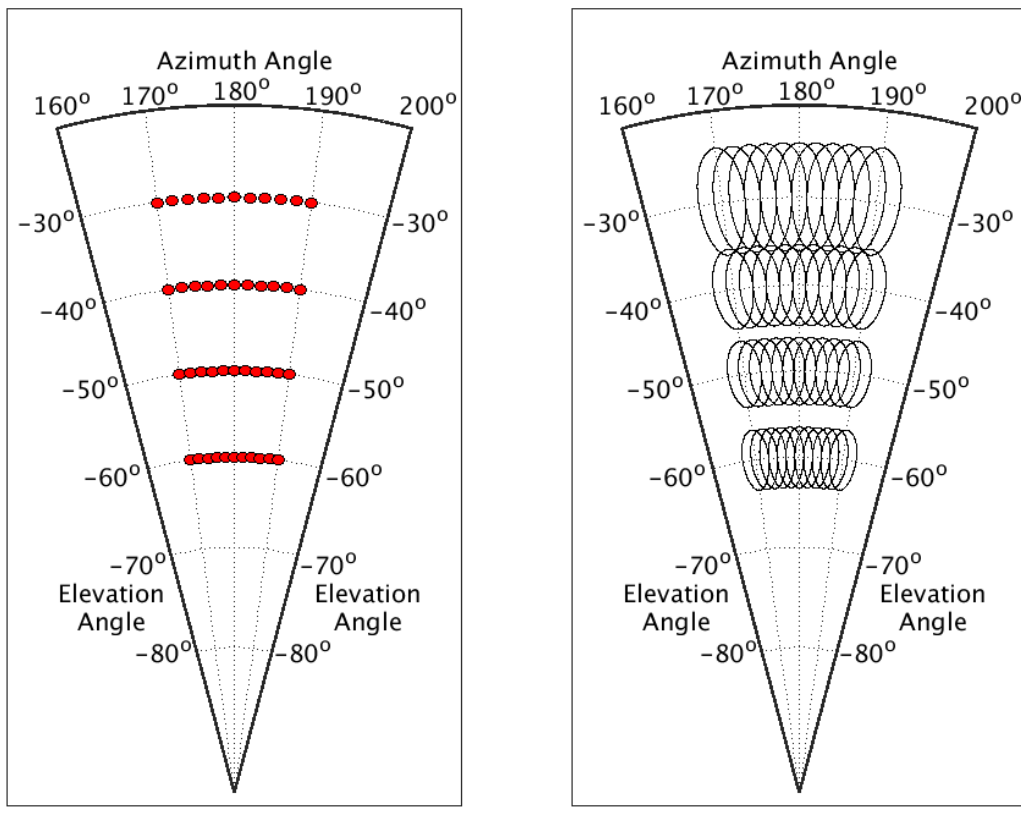


**Figure 6.3:** SoRaX SodRad1 observations. Individual azimuth and elevation scans (red) and HPBW footprints (black) are shown.

whilst Figures 6.4b – 6.4e shows photos of the individual trenches being observed.

As the snowpits aimed to allow for the observation of undisturbed snow, the snow trenches were ordered so that the -30° trench was completed first. The snowpit observations took place along the trench. Upon completion of all snowpit observations along the -30° trench, a new trench was dug parallel to the -40° elevation scan. This process was repeated, until the snowpit observations in the -60° trench were completed. All snow that was removed was placed either behind or to the side of the trenches (as seen in Figures 6.4b – 6.4e), in order to limit the mechanical destruction to the snow trench wall, and the remaining snowpack.

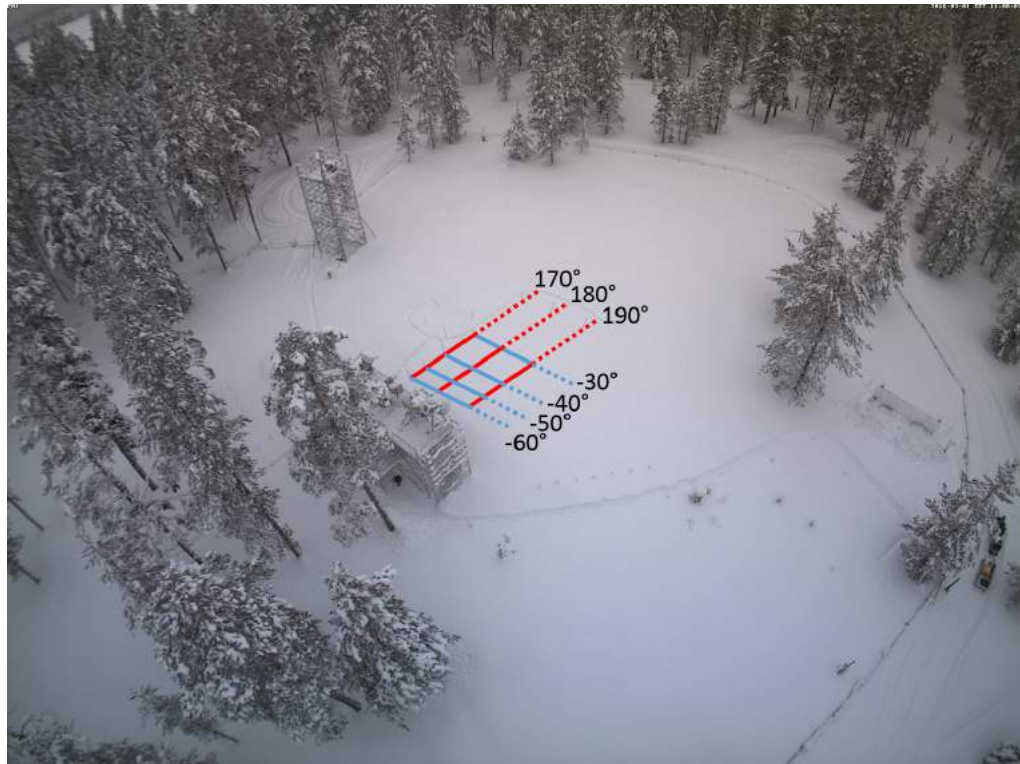
After digging the snow trench to the sufficient width, the wall of the snow trench was smoothed with a large metal sheet (as shown in Figure 6.5), which has been left to cool to the ambient temperature; in a similar fashion to that of the snow pits dug for slab extraction during ASMEx (Section 3.5.1). The trench wall required smoothing with a thin metal sheet, in order for accurate stratigraphy analysis via near-infrared photography (NIR photography, Matzl and Schneebeli [2006], Toure et al. [2008], and Tape et al. [2010]) to take place.

Through photographs of the smooth trench wall at NIR wavelengths ( $\approx$  850 nm), the snowpack stratigraphy can be assessed. This is due to the relationship between the reflectance of the snow crystals at NIR wavelengths, and the snow's SSA properties. The NIR photography technique works on a similar principle to that of the IceCube instrumentation (Section 3.5.3, Zuanon [2013]). By observing the reflectance of the snowpack at known NIR wavelengths, the stratigraphy of the snowpack can be assessed.

After smoothing the trench wall, an extended measuring rod with half-centimetre markings (shown in Figures 6.6a – 6.6c) was used to measure the width of the trench, and provide a reference point for the remainder of the SoRaX trench observations.

An aluminium rail with adjustable tripods at either end was positioned parallel to the trench wall at an approximate distance of 1 m from the trench wall (Figures 6.6a and 6.6b). A digital SLR camera, adapted to capture photographs at 850 nm was attached to the metal rail (Figure 6.6b). A series of photographs were taken (approximately at 50 cm intervals) along the aluminium rail, to capture the structural variability of the trench wall. An example of the NIR photographs taken is shown in Figure 6.6c, which was taken 50 cm from the start of the -60° trench.

The series of photographs were aligned so that the photographs could produce a single long NIR graphic, from which the layer boundaries could be estimated.



(a) Schematic of SoRaX radiometer scans of the natural snowpack. Snow trenches are aligned along each  $10^\circ$  variation of elevation, and are 5m in length, to encompass the range of azimuth angles measured.



(b) SoRaX Trench at  $-30^\circ$  of elevation.



(c) SoRaX Trench at  $-40^\circ$  of elevation.



(d) SoRaX Trench at  $-50^\circ$  of elevation.

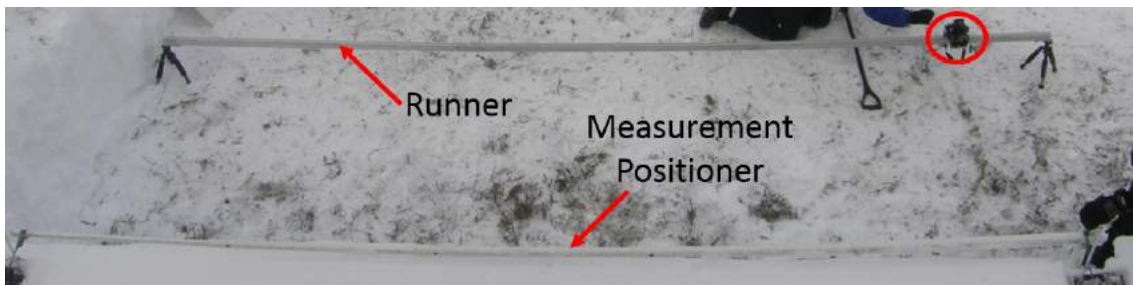


(e) SoRaX Trench at  $-60^\circ$  of elevation.

**Figure 6.4:** Images of the SoRaX snow removal experiment in the IOA. Images were taken from 1st March – 3rd March 2016. Photos taken from the IOA Camera.



**Figure 6.5:** Smoothing the SoRaX trench walls. Photo courtesy of A. Kontu.



(a) NIR photography equipment. The NIR camera (circled in red) is located upon a 5 m runner, facing the trench wall. The horizontal positioner is always in the cameras field of view.



(b) NIR photography being used in the SoRaX trench. A vertical positioner is used to allow for stratigraphy to be vertically located during processing.



(c) NIR photo, from the  $-60^\circ$  trench, at 0.5 m.

**Figure 6.6:** NIR photography used in the SoRaX snow removal experiment. Photos courtesy of R. Kelly and T. Watts.

After the completion of the trench NIR photography, the NIR apparatus was removed, allowing for additional snow pit observations to take place throughout the trench. The trench wall was then considered as a series of connected snow pits, with a total length of 5 m. Typical snow pit observations then took place at 6 locations across the snow trench, allowing for snow pit observations to have a horizontal resolution of 1 m (with the exception of traditional grain size measurements, which happened at 3 m only). By taking multiple observations of snow properties across the 5 m trench, the spatial and small-scale variability of the snowpack was observed.

The stratigraphy of the individual snowpits were manually recorded, similar to how the homogeneous layers were detected prior to slab extraction in the ASMEx campaign (Section 3.5.1). The layers were manually detected through changes in visual appearance and differences in hardness, wetness, and grain size and type, as described by [Leppänen et al. \[2016b\]](#) and [Fierz et al. \[2009\]](#), by using a soft brush (for soft snow layer detection) and a toothpick (for hard layer detection).

Physical temperature profiles were observed, similar to the physical temperature measurements completed in the snow characteristic section of the ASMEx observations (Section 3.5.3), with a vertical resolution of 10 cm. The physical temperature measurements, like the ASMEx slab physical temperature measurements, were recorded with a TH310 probe thermometers (Milwaukee Electronics Kft., Szeged, Hungary, [Leppänen et al. \[2016b\]](#)). Prior to the snowpack profile measurements, the thermometer was cooled in air to the ambient temperature, and the air temperature was recorded.

After completing the physical temperature profile, profiles of SSA were recorded, using the IceCube instrument (A2 Photonic Sensors, Grenoble, France, [Zuanon \[2013\]](#)), similar to those taken from the ASMEx slabs samples (Section 3.5.3). IceCube measurements of SSA were taken with a vertical resolution of 3 cm, from the snowpack surface, until the vegetation layer at the bottom of the snowpack. Observations of SSA using the IceCube machine are not possible in the vegetation layer, as the vegetation made filling the IceCube sampler difficult.

In addition to the SSA observations, measurements of traditional grain size (as defined as E by [Fierz et al. \[2009\]](#)) was recorded from snow within the IceCube sampler, similar to that in the ASMEx campaign. Snow crystals were extracted from the IceCube sampler, onto a 1 mm reference plate (manufactured by Sear, [Leppänen et al. \[2016b\]](#)) and macrophotographs were taken, using a digital camera and self-made illuminated stand (as discussed in Section 3.5.3). The grain size and type were estimated visually upon the

completion of the SoRaX snow removal experiment, to a resolution of 0.25 mm. By using the snow within the IceCube sampler, the traditional grain size macrophotography also had a vertical resolution of 3 cm, and could allow for direct comparison between the measurements of SSA and traditional grain size.

Vertical profiles of density were also observed at each snowpit, using box cutter instrumentation (Figure 6.7a– 6.7b). However, unlike the IceCube profiles, the vertical resolution of the density measurements were not uniform, as individual profiles varied between a vertical resolution of 5 cm (Figure 6.7a) and 3 cm (Figure 6.7a) across the SoRaX snow removal experiment. This variation in vertical resolution is due to two different styles of density box cutter instrumentation being present. Profiles with a resolution of 5 cm used a box cutter with dimensions 5 cm x 10 cm x 10 cm (height by width by depth), identical to those used in the ASMEx campaign (Section 3.5.3, Figure 6.7a). Profiles with a resolution of 3 cm used a box cutter with dimensions 3 cm x 5.5 cm x 6 cm (height by width by depth), as shown in Figure 6.7b. Thus, due to its shorter height dimension, a higher resolution density profile is able to be observed. Like the IceCube measurement procedure, density profiles were taken in an alternate pattern (Figure 6.7c), to reduce the impact of compaction and mechanical metamorphism upon the density measurements. As shown in Section 3.5.3 and by Proksch et al. [2016], box cutter profiles accurately sample the bulk density measurements, when compared to  $\mu$ CT techniques, despite the much coarser resolution (Section 4.2.4). Any layers with a thickness less than the resolution of the box cutters, however, will be sampled incorrectly.

After the completion of the above mentioned techniques in each of the elevation angle snowpits (for example, all -30° snowpits), the next SoRaX trench was dug. This was done by extending the already dug trench to the next elevation angle marker (Figure 6.4a). The trench observations were then repeated for each measured elevation angle, as shown by Figures 6.4b – 6.4e, until the snowpack properties and characteristics were quantified and observed.

### 6.3 SoRaX Observations

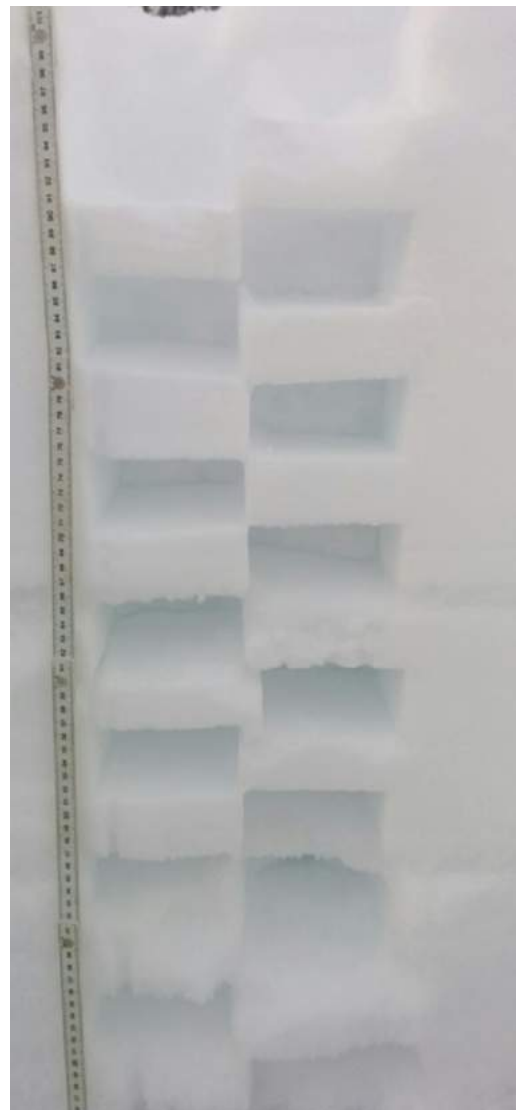
In this section, the observations made during the SoRaX snow removal experiment are shown. The observations are split into two separate sections; a radiometric observation section (Section 6.2.2) and a snow characteristic observation section (Section 6.3.2).



(a) 500 ml box cutter. The tape surrounding parts of the box cutter allows for additional grip.



(b) 100 ml box cutter being cooled in the natural snowpack.

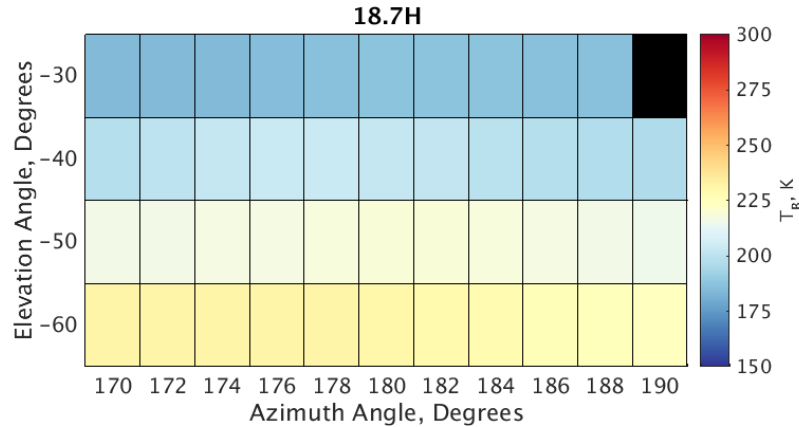


(c) Density profile in the natural snowpack.

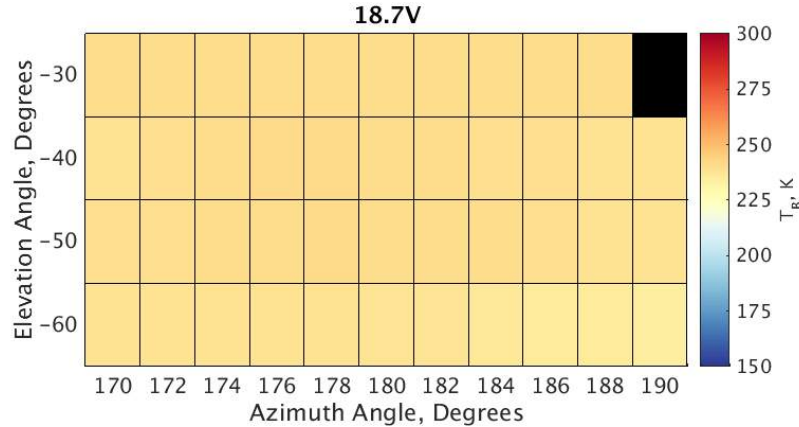
**Figure 6.7:** Density box cutters used in the SoRaX snow removal experiment. Photos courtesy of R. Kelly.

### 6.3.1 Radiometric Observations

Figures 6.8 – 6.10 show the radiometric observations at 18.7, 21.0, and 36.5 GHz respectively, at both (a) horizontal and (b) vertical polarizations. Due to issues regarding the observation at -30° elevation, 190° azimuth, this brightness temperature observation has been neglected from this study. It can be seen that across all three frequencies, numerous patterns can be seen and explained.



(a) Observed Brightness Temperatures at horizontal polarization at 18.7 GHz.



(b) Observed Brightness Temperatures at vertical polarization at 18.7 GHz.

**Figure 6.8:** Observed Brightness Temperatures at 18.7 GHz, at the range of elevation and azimuth angles.

It can be seen that, for all three frequencies, the brightness temperatures observed at horizontal polarization brightness temperatures are lower than those observed at vertical polarizations. This is not an unexpected result. A polarization difference is consistent within the literature ([Mätzler \[1987\]](#), [Rott et al. \[1993\]](#), [Mätzler \[1994\]](#), [Tedesco and Kim \[2006\]](#), [Lemmettyinen et al. \[2010\]](#)). The difference in polarization is present due to the internal stratigraphy of the natural snowpack. It is well documented that a deeper snowpack is more likely to contain numerous internal layers, making the snowpack non-homogeneous. These internal layer boundaries introduce the polarization difference,

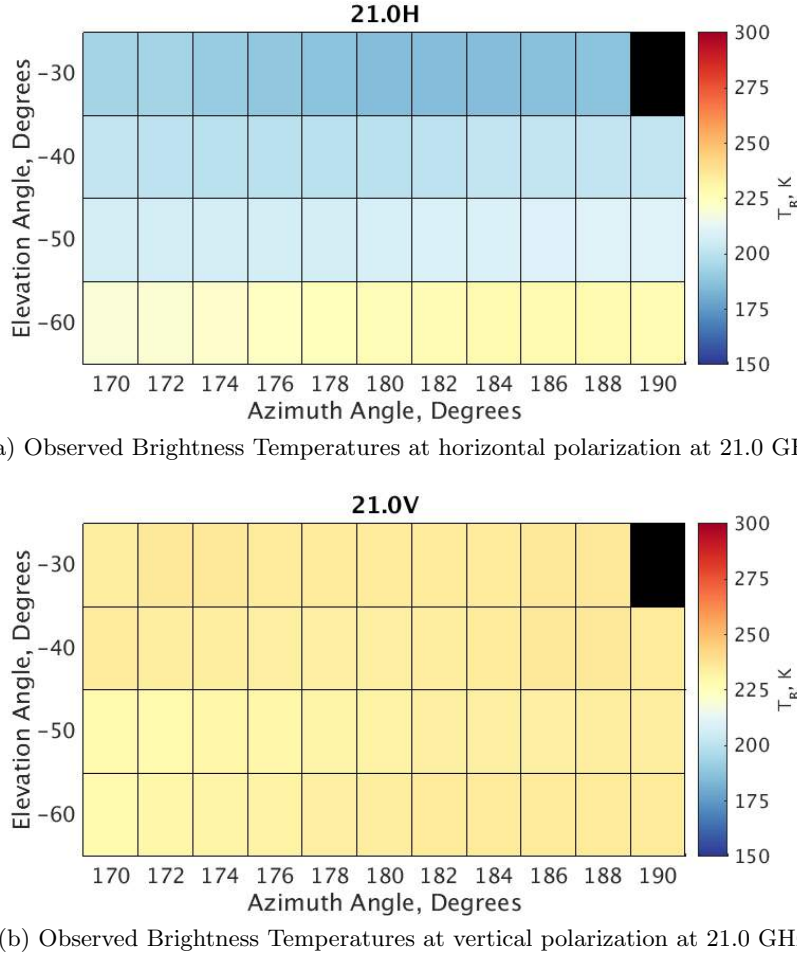


**Figure 6.9:** Observed Brightness Temperatures at 21.0 GHz, at the range of elevation and azimuth angles.

and increase said polarization difference with each subsequent layer (Mätzler [1994]), as described by the Fresnel interface reflectivity equations (Eqns. 2.40 and 2.41 for the horizontal and vertical polarizations respectively). As the Fresnel equations produce differing reflectivity values for the separate polarizations, this results in a polarization difference.

It can also be seen that, as the frequency increases, the observed brightness temperatures decreases, for both polarizations. This too is to be expected, as it is also consistent with findings within literature (Hallikainen et al. [1987], Roy et al. [2004], Kontu and Pulliainen [2010], Chang et al. [1987], Rees [2006], and Grody [2008]). This decrease in observed brightness temperature comes from the relationship with the scattering properties of the snowpack with the properties of the microwave radiation that is being observed. It has been previously stated, in Section 2.4.1, that the amount of scattering is dependent on both frequency and grain size. As the traditional grain size across the individual trench has been assumed to be horizontally uniform, the variation in scattering must come from the differing frequencies observed.

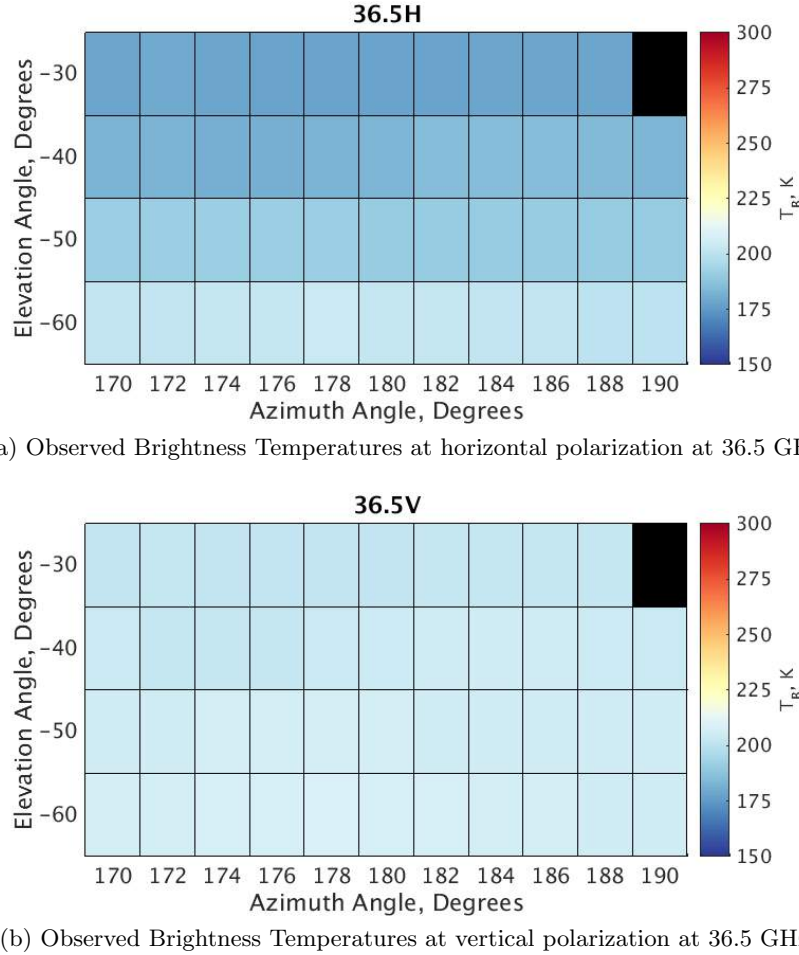


**Figure 6.10:** Observed Brightness Temperatures at 36.5 GHz, at the range of elevation and azimuth angles.

As the frequency of observation increases, the wavelength decreases. The wavelength of microwave radiation at 18.7 and 21.0 GHz is 1.6 and 1.4 cm respectively. These wavelengths are an order of magnitude larger than the size of the scattering centres (the snow crystals) within the snowpack (for the SoRaX campaign, the largest traditional grain size recorded was 3 mm, as shown in Section 6.3.2). Thus, the microwave emission emitted from the underlying frozen ground and from the snowpack itself is allowed to propagate through the snowpack with less scattering occurring than at 36.5 GHz (whose wavelength of 0.8 cm is a similar order of magnitude to the scattering centres within the snowpack).

From Figures 6.8 – 6.10, it can also be seen that different elevation angles produce variations in brightness temperature. As the elevation angle increased from  $-60^\circ$  to  $-30^\circ$ , the brightness temperature at horizontal polarization varied significantly, especially at the two lower frequencies of 18.7 and 21.0 GHz, whilst the variation of observed brightness temperatures at vertical polarizations remained small. This independence of elevation

angle at vertical polarization was also displayed by [Schanda and Mätzler \[1981\]](#) and [Mätzler \[1987\]](#), who shows that the brightness temperature is almost independent of elevation angle at vertical polarizations, but highly dependent at horizontal polarizations.

Table 6.1 shows the standard deviation values of brightness temperatures observed at set azimuth angles, across the multiple elevation angles. It is clear that the variations are larger at horizontal polarizations than at vertical polarizations, as previously described. It can also be seen that the variations decrease with increasing frequency, for horizontal polarizations, while the vertical polarization does not exhibit such a pattern. Table 6.2 shows the standard deviation values of brightness temperatures across the individual elevation angles (for all azimuth angles). Whilst the standard deviation values in Table 6.2 are smaller than the corresponding frequencies and polarizations in Table 6.1, the standard deviation values do show a similar pattern to those in Table 6.1; horizontal polarization standard deviation values are larger than the corresponding vertical polarization.

### 6.3.2 Snow Characteristic Observations

This subsection highlights the data collected using snow pit observation techniques, as well as the stratigraphy analysis from the NIR photography. The snow pit observations consisted of profiles of physical temperature, density (via the box cutter technique), SSA and  $D_{opt}$  (via the IceCube instrumentation), and traditional grain size (via macrophotography, as defined by [Leppänen et al. \[2016b\]](#) and [Fierz et al. \[2009\]](#)).

Tables 6.3 – 6.7 show the location of each completed profile of physical temperature, density, SSA and  $D_{opt}$ , traditional grain size, and manual stratigraphy observations respectively, completed as part of the SoRaX snow removal experiment. It can be seen that across all four trenches, the -40° and -50° trenches were observed with the most number of observation techniques. Whilst the SSA and  $D_{opt}$  profiles were completed at all snow pit locations (no snow pits took place at 0 m, 1 m, or 5 m in the -60° trench), and density profiles were completed at all but one snow pit (5 m at -50°), the other three observation techniques (physical temperature, traditional grain size, and manual stratigraphy analysis) were not observed as frequently.

Physical temperature profiles (Table 6.3) were recorded infrequently across all SoRaX trenches, with no SoRaX trench recording a full number of profiles. The infrequent temperature profile observations were a result of an assumption that the horizontal variability of physical temperature would be much smaller than the vertical variability across the snowpack (Dr. Nick Rutter, Personal Correspondence). Therefore, by recording at

**Table 6.1:** Standard deviation values of observed brightness temperatures (K) of different azimuth angles, at each observed frequency.

Frequency	Azimuth Angle										
	170°	172°	174°	176°	178°	180°	182°	184°	186°	188°	190°
18.7 H	20.861	20.582	20.077	19.495	19.076	18.811	18.627	18.304	18.078	17.909	14.195
18.7 V	0.806	0.818	1.024	1.281	1.484	1.556	1.717	1.898	2.114	2.367	2.203
21.0 H	10.703	11.582	13.121	14.525	15.963	17.040	17.760	17.830	17.432	16.850	13.194
21.0 V	3.113	3.242	2.672	2.017	1.516	1.207	1.135	1.041	1.023	0.830	0.473
36.5 H	9.956	10.290	10.901	11.255	11.240	10.957	10.473	9.954	9.516	9.361	8.313
36.5 V	1.944	2.258	2.825	3.014	2.966	2.673	2.192	1.782	1.603	1.466	1.069

**Table 6.2:** Standard deviation values of observed brightness temperatures (K) of different elevation angles, at each observed frequency.

Elevation Angle	Frequency (GHz)					
	18.7 H	18.7 V	21.0 H	21.0 V	36.5 H	
-30°	2.657	1.453	3.339	2.434	0.982	0.927
-40°	1.223	0.948	1.702	1.871	0.641	0.347
-50°	2.476	0.931	0.988	0.920	1.508	1.080
-60°	1.348	0.246	3.210	0.569	0.703	0.438

**Table 6.3:** Location of physical temperature profile observations.

Trench Elevation Angle	Snow pit Location along Trench					
	0 m	1 m	2 m	3 m	4 m	5 m
-30	X					
-40	X	X			X	X
-50			X	X		
-60					X	

**Table 6.4:** Location of density profile observations.

Trench Elevation Angle	Snow pit Location along Trench					
	0 m	1 m	2 m	3 m	4 m	5 m
-30	X	X	X	X	X	X
-40	X	X	X	X	X	X
-50	X	X	X	X	X	
-60			X	X	X	

**Table 6.5:** Location of SSA and  $D_{opt}$  profile observations.

Trench Elevation Angle	Snow pit Location along Trench					
	0 m	1 m	2 m	3 m	4 m	5 m
-30	X	X	X	X	X	X
-40	X	X	X	X	X	X
-50	X	X	X	X	X	X
-60			X	X	X	

**Table 6.6:** Location of traditional grain size profile observations.

Trench Elevation Angle	Snow pit Location along Trench					
	0 m	1 m	2 m	3 m	4 m	5 m
-30					X	
-40					X	
-50					X	
-60					X	

**Table 6.7:** Location of manual stratigraphy observations.

Trench Elevation Angle	Snow pit Location along Trench					
	0 m	1 m	2 m	3 m	4 m	5 m
-30	X	X	X			
-40	X	X			X	X
-50			X	X	X	
-60					X	

least one vertical profile of physical temperature in each SoRaX trench, the mean vertical profile of the physical temperature would provide a valid assumed profile for the entire trench.

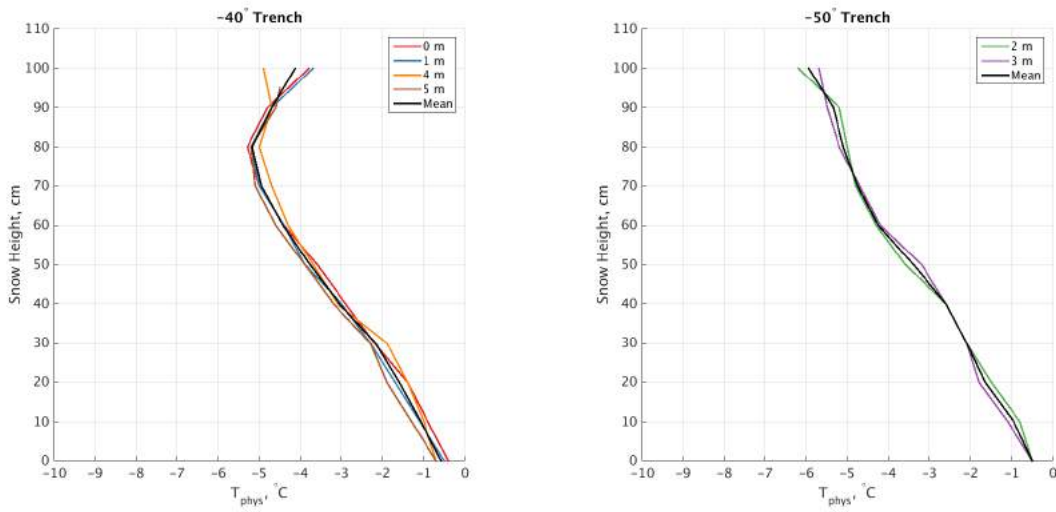
Traditional grain size profiles were also not recorded at every snowpit. In each SoRaX trench, traditional grain size was only recorded at the 3 m snowpit location. Similar to the assumptions regarding the physical temperature profiles, it was assumed that the horizontal spatial variability of traditional grain size did not vary as greatly as the vertical variability (Dr. Nick Rutter, Personal Correspondence). Therefore, by taking observations from a central snowpit, and assuming that the traditional grain size profile is representative of the entire trench, the traditional grain size of the other snowpits can be estimated.

The manual stratigraphy observations were subject to a different assumption to that of the physical temperature and traditional grain size observations. As each trench was individually recorded using NIR photography, in order to record the fine scaled horizontal and vertical stratigraphy, the manual stratigraphy observations acted as a way to check the NIR derived layer heights. The NIR photography analysis (discussed later in this section) proved to be difficult, as it was difficult to distinguish between the base of the snowpack and the snow-free ground. It was also difficult to distinguish the exact location of the snow-ground boundary, due to vegetation found under the snowpack. In these instances, the manual stratigraphy observations proved to be useful, as it allowed for the NIR derived layers to be adjusted to the correct heights, which in turn allowed for the ground to be distinguished. This was completed for all NIR derived stratigraphic layers, by assessing the heights of well-defined ice crusts within the snowpack via the manual stratigraphic observations where available. The corresponding ice crust layers within the NIR photographs were then adjusted to the correct heights, and thus allowing for the remaining stratigraphic layers to be calibrated.

From Tables 6.3 – 6.7, it is clear that the trenches associated with the -40° and -50° trenches have the most complete set of snow pit observations. It is for this reason that these two trenches will be discussed further in terms of their physical snow characteristics, in the section below.

Figures 6.11a and 6.11b show the physical temperature profiles of the -40° and -50° trenches respectively, along with the calculated mean temperature profile from the available data. From Figure 6.11a, it can be seen that the four profiles of physical temperature do not vary with increasing depth, with the exception of the upper-most 10 cm. This

closeness of the physical temperatures with height shows that the assumption regarding the horizontal spatial variability of physical temperature is valid. When simulating the brightness temperature of snowpits with no observed temperature profile (such as the 3 m snowpit in the -40° trench) with the n-HUT model (Section 6.4.3), the mean temperature profile of the individual trenches was assumed to be a valid representation.



(a) Physical temperature profiles of snow pits taken in the -40° trench. Snow pits were completed between 11:00 – 14:00 on 2nd March 2016.

(b) Physical temperature profiles of snow pits taken in the -50° trench. Snow pits were completed between 15:00 – 17:00 on 2nd March 2016.

**Figure 6.11:** Physical temperature profiles from the individual snow pits of the SoRaX campaign. Profiles observed at the 0 m (red), 1 m (blue), 2 m (green), 3 m (purple), 4 m (orange), and 5 m (brown) snow pits are shown, with the mean profile (black).

There are many similarities between the observed physical temperatures in the -40° and -50° trenches. Both trenches have a very similar ground temperature (-0.5 – -0.6°C), and both trenches experience a similar decrease of physical temperature with increasing height, up to 80 cm in depth. In the upper 30 cm, the two trenches differ; with the -40° trench experienced an increase in physical temperature with height, whilst the -50° trench experienced further decrease of physical temperature with height. The two trenches were observed and characterised on the same day, but at different times of the day; the -40° was characterised between 11:00 and 14:00 local time, and the -50° trench was characterised between 15:00 and 17:00 local time.. As the snow pit observations took place at different times, the dry bulb air temperature at the times of observation were different, as shown by Figure 6.12. Figure 6.12 shows the dry bulb air temperature, taken from the IOA Automatic Weather Station (via a Vaisala PT100 Thermometer) from 00:00 on the 01/03/16 to 00:00 on the 03/03/16 (local time). Highlighted on Figure 6.12 is the final SoRaX radiometric observation period (shown in the grey shading), as

well as the times of the -40° (shaded red) and the -50° (shaded blue) trenches. It can be seen when comparing the -40° and -50° trench air temperatures that the -50° trench experienced a lower air temperature (mean of -6.77°C) than that of the -40° trench (mean of -5.11°C). As snow is comprised of both air and ice crystals, the air within the snow will try to thermally equalise with its surroundings. However, as snow is a good thermal insulator ([Rees \[2006\]](#)), only the upper section of the snowpack responds to the changing air temperature. This explains the differing temperatures of the upper 30 cm in the two trenches, as well as the differing observations in the upper 10 cm across the -40° trench in the snow pits observed first in the observation period (snow pits at 0 m and 1 m) and those observed last (snow pits at 4 m and 5 m).

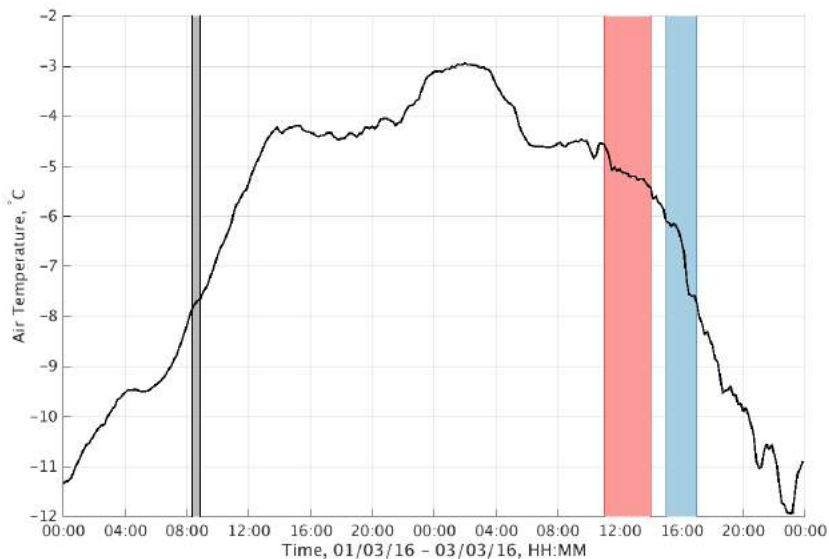
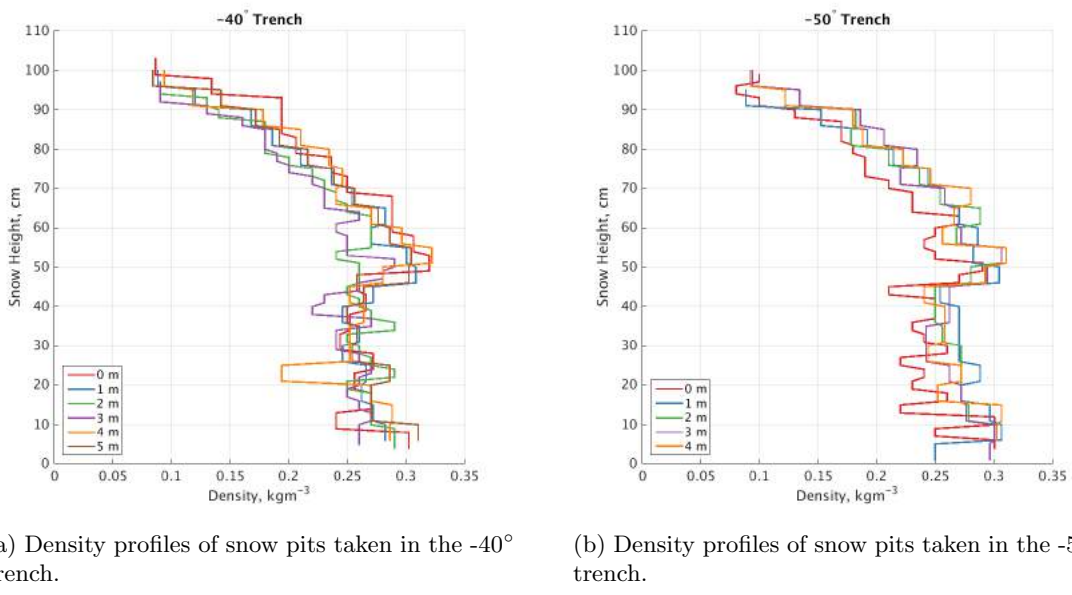


**Figure 6.12:** Dry bulb air temperature, measured using the PT100 sensor at the IOA AWS. Region shaded in grey, red, and blue mark the last SoRaX radiometer observation period, the -40° trench observation, and the -50° trench observation respectively.

Figures 6.13a and 6.13b show the observed density profiles of the -40° and -50° trenches respectively. A mean density profile was not calculated, as observations of density took place at all snowpits with the exception of one (-50°, 5 m). When comparing the density observations in both the -40° and -50° trenches, it can be seen that there is little horizontal spatial variability, as all profiles are very similar to one another. All profiles, unlike the physical temperature profiles, exhibit the same pattern of profile; less dense snow being found at the surface, with a densification of the snowpack in the upper 40 cm until a snow height of 60 cm. From 60 cm to the base, the density decreases from a maximum observed density of  $322 \text{ kg m}^{-3}$  to a minimum of  $194 \text{ kg m}^{-3}$  across all profiles. This variation in density across the entire snowpack is present due to the varying snow

types through metamorphism with age. The less dense snow found at the surface of the snow is new/fresh snow (as shown in Tables 6.8 and 6.9), characterised by small grain sizes (shown later in Figure 6.16). As the snow ages, the density of the snow increases, as it is compacted as newer snow settles above it. The lower layers of the snowpack are comprised of large crystallised depth hoars, which have a lower density than that of the faceted snow found above it. It should be noted that, like with the box cutter observations of the ASMEx slabs (Section 3.5.3), the box cutters used in the SoRaX snow removal experiment had a larger vertical dimension, and thus resolution (3 cm and 5 cm, depending upon the type of box cutter used, Figures 6.7a and 6.7b) than the thinner ice crust layers within the snowpack (as displayed by the NIR analysis of stratigraphic layers, Figure 6.18). In these instances, the precise observation of density of the ice crusts cannot be made, as the resolution of the box cutters are too large to measure their density effectively.

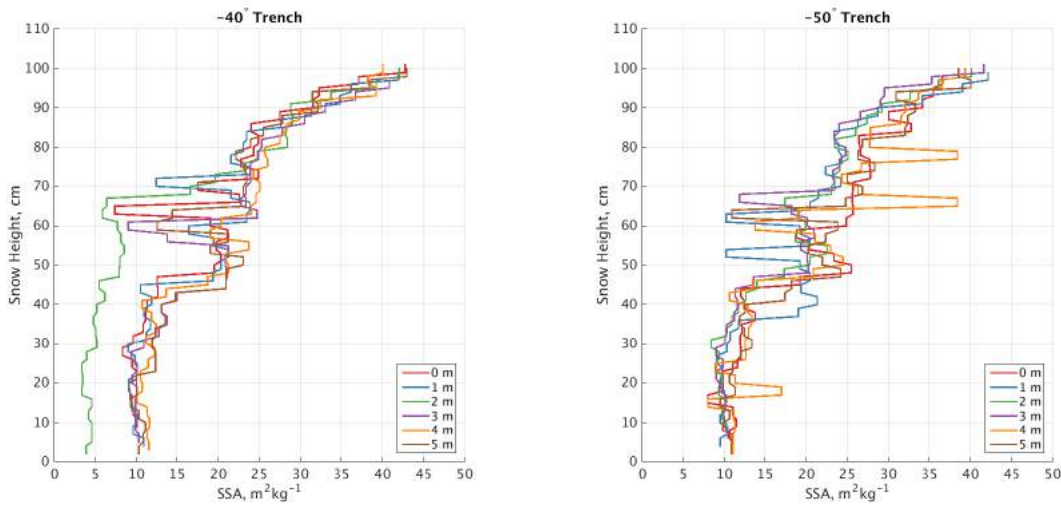


(a) Density profiles of snow pits taken in the  $-40^\circ$  trench. (b) Density profiles of snow pits taken in the  $-50^\circ$  trench.

**Figure 6.13:** Density profiles from the individual snow pits of the SoRaX campaign. Profiles observed at the 0 m (red), 1 m (blue), 2 m (green), 3 m (purple), 4 m (orange), and 5 m (brown) snow pits are shown.

Figures 6.14a and 6.14b show the observed SSA profiles of the  $-40^\circ$  and  $-50^\circ$  trenches respectively, using the IceCube instrument. While it is clear from both figures that a common pattern can be seen within the SSA profiles, some interesting points should be discussed. The general pattern of the SSA profiles are thus; SSA tends to be larger at the surface (synonymous with fresh snow) with a tendency of decreasing SSA as snow height decreases (due to the metamorphism altering the shape and crystal size) until the bottom of the snowpack (as the bottom of the snowpack is comprised of depth hoar, with

the smallest SSA values). Where layers are present within the snowpack, the SSA values drop dramatically, before immediately returning to prior values of SSA. A prime example of this can be seen in the  $-40^{\circ}$  trench for the 0 m snow pit profiles. At 63 - 66 cm, a much lower SSA value ( $\approx 7.5 \text{ m}^2 \text{ kg}^{-1}$ ) is found between two larger values of SSA. This suggests that a stratigraphic layer is present at this snow depth.



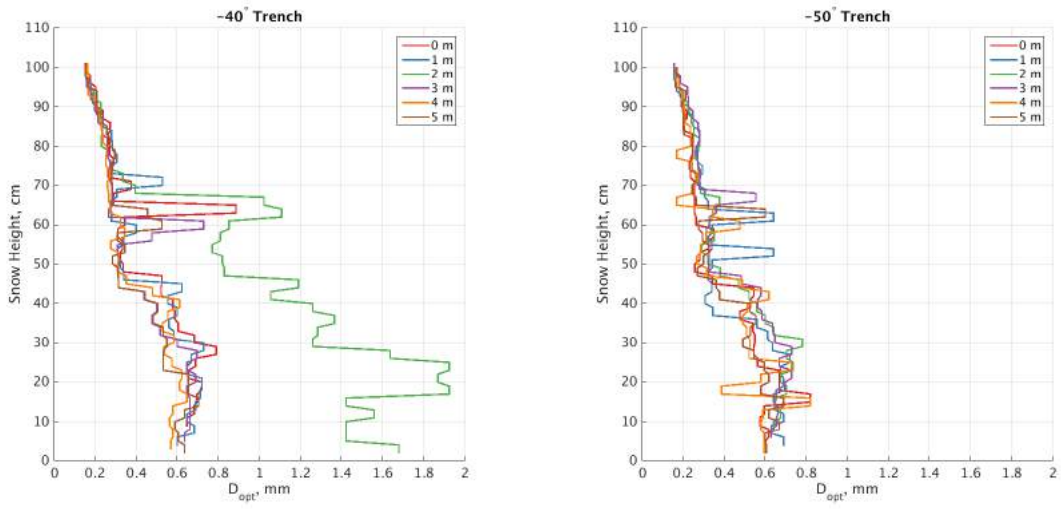
(a) SSA profiles of snow pits taken in the  $-40^{\circ}$  trench.

(b) SSA profiles of snow pits taken in the  $-50^{\circ}$  trench.

**Figure 6.14:** SSA profiles from the individual snow pits of the SoRaX campaign. Profiles observed at the 0 m (red), 1 m (blue), 2 m (green), 3 m (purple), 4 m (orange), and 5 m (brown) snow pits are shown.

One profile exhibits a different profile pattern than that of the other profiles. The SSA profile collected at the 2 m snow pit in the  $-40^{\circ}$  trench produced a different SSA profile to those collected across the same trench. The upper 30 cm produced similar values to those of the surrounding snow pits, however below 70 cm of snow height, the IceCube machine produced much lower observed values of SSA. It appears that the profile amplitude has been affected, as a similar pattern is produced (seen at the 45 – 60 cm in the 2 m profile), but at a much lower value of SSA. It was suspected that this occurred due to snow becoming trapped within the integrating sphere of the IceCube apparatus, and thus providing an incorrect value of the SSA at the lower 60 cm of the profile (Dr. Nick Rutter, personal correspondence). It is for this reason that the 2 m snow pit in the  $-40^{\circ}$  trench was not used for n-HUT model simulations in Section 6.4.

Figures 6.15b and 6.15b show the calculated values of  $D_{opt}$  across the  $-40^{\circ}$  and  $-50^{\circ}$  trenches respectively. As  $D_{opt}$  is inversely proportional of SSA (Eqn. 2.19), any patterns present in the SSA profile are inverted in the  $D_{opt}$  profiles. This explains the pattern of small  $D_{opt}$  values at the surface, with increasing values of  $D_{opt}$  being found as the

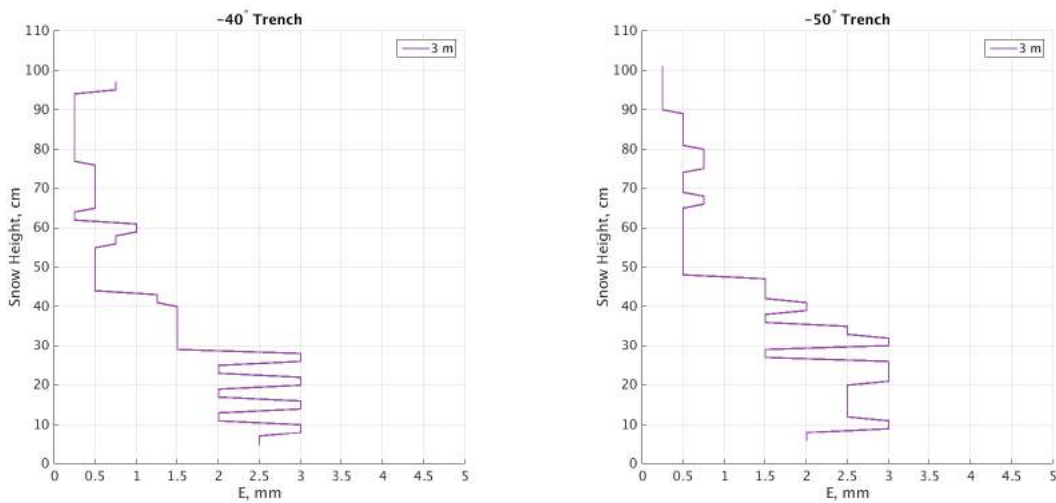


(a)  $D_{opt}$  profiles of snow pits taken in the  $-40^\circ$  trench.  
 (b)  $D_{opt}$  profiles of snow pits taken in the  $-50^\circ$  trench.

**Figure 6.15:**  $D_{opt}$  profiles from the individual snow pits of the SoRaX campaign. Profiles observed at the 0 m (red), 1 m (blue), 2 m (green), 3 m (purple), 4 m (orange), and 5 m (brown) snow pits are shown.

snow height decreases. Where stratigraphic layers are found and observed, spikes in  $D_{opt}$  are found within the profile. Using the same profile as with the SSA as an example, the 0 m snowpit in the  $-40^\circ$  trench exhibits a spike in calculated  $D_{opt}$  at 63 – 66 cm of snow height, due to the stratigraphic layer found at this approximate height. Similar to the SSA profiles, the 2 m snowpit in the  $-40^\circ$  trench produces an outlier calculation of  $D_{opt}$ , as the underestimation of SSA produces a large overestimation in  $D_{opt}$ . Thus, as the newly derived extinction coefficient produced in Section 5.4 uses  $D_{opt}$  as an input parameter, the large (incorrect) values of  $D_{opt}$  calculated from the 2 m  $-40^\circ$  snowpit would produce incorrect amounts of extinction within the n-HUT model. Therefore, the 2 m snowpit in the  $-40^\circ$  trench was not used for the HUT simulations. Similar to the box cutter observations, the observations of SSA (and calculations of  $D_{opt}$ ) are at a coarser resolution than some of the stratigraphic layers present within the snowpack. Again, in these instances, precise observations of the SSA (and calculations of  $D_{opt}$ ) for the thin layers are not possible.

Figures 6.16a and 6.16b show the observed values of traditional grain size (as defined by Fierz et al. [2009]), through macrophotography analysis of snow crystals, taken from the IceCube sampler. As only one profile of traditional grain size was completed in each trench, each profile only shows the single profile. It can be seen that, for both snow pits, the top of the snowpack is comprised of small snow grains (commonly found with fresh snow), with snow grain size increasing with decreasing snow height, until it reaches the



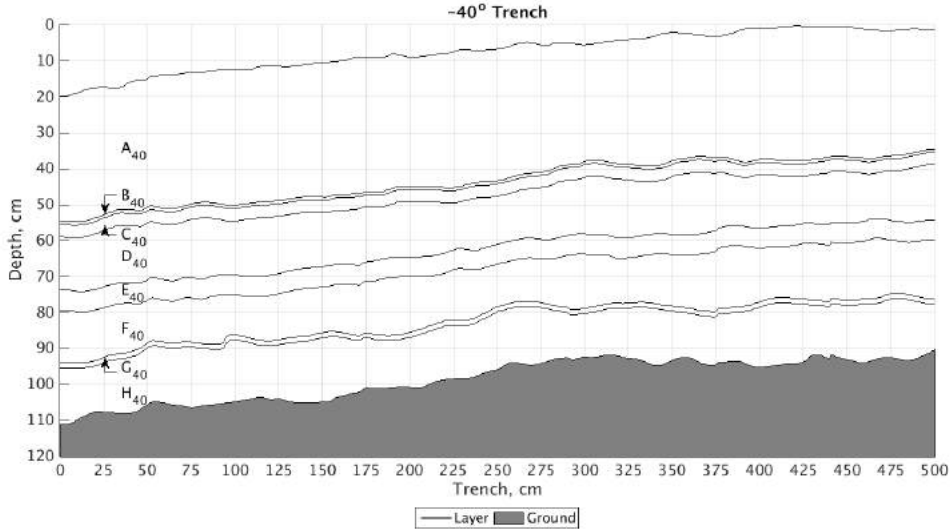
(a) Traditional grain size ( $E$ ) profile of the 3 m snowpit taken in the  $-40^\circ$  trench.

(b) Traditional grain size ( $E$ ) profile of the 3 m snowpit taken in the  $-50^\circ$  trench.

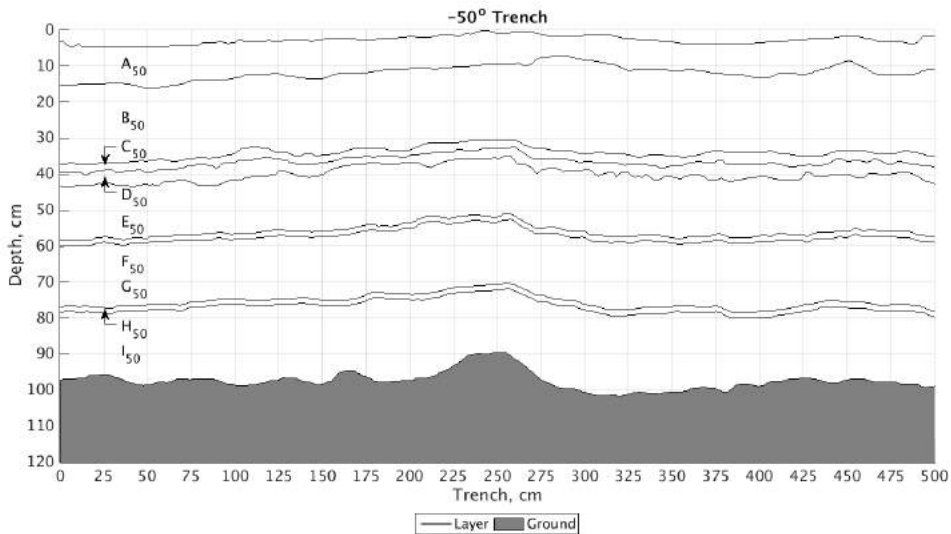
**Figure 6.16:** Traditional grain size profiles from the individual snow pits of the SoRaX campaign. Profile observed at the 3 m (purple) snowpit is shown.

maximum grain size in the bottom most layer of the snowpack, being comprised of depth hoar. As only one snowpit in each trench completed traditional grain size observations, it was assumed that the traditional grain size had a much smaller horizontal spatial variability than that of its vertical variability. Thus, it was assumed that the traditional grain size within individual layers would not vary within the boundaries of the internal layers. By combining the analysis of the NIR photography with the traditional grain size macrophotography, it is possible to estimate the traditional grain size across the entirety of the trenches.

Figures 6.17a and 6.17b show the uncorrected stratigraphic layer heights observed through the NIR photography technique. It shows the location of the NIR derived stratigraphic layers, with the NIR derived location of the ground layer. It can be seen that there are numerous different layers within each trench observation. Each individual layer has been labelled by a letter, and the trench elevation angle (such that layer A<sub>40</sub> is the topmost layer of the  $-40^\circ$  trench). Across both trenches, the thickness of each individual layer does not vary by a large amount. As previously stated, the NIR analysis underestimated the thickness of the bottom-most layer, as the base of the snowpack is difficult to distinguish from the frozen, relatively snow free ground and vegetation. To solve this, the manual stratigraphic observations made at different positions across each trench (Table 6.7) were used to correct the NIR stratigraphic height, using the manual stratigraphy observations to correct the bottom-most layers. Each individual snowpit in the  $-40^\circ$  and



(a) Raw NIR derived stratigraphic layers across the -40° trench.

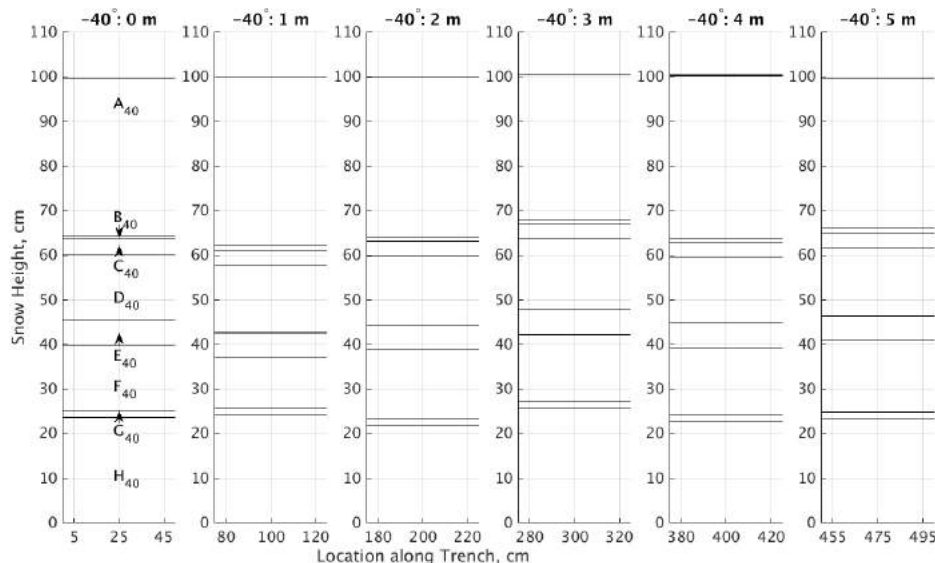


(b) Raw NIR derived stratigraphic layers across the -50° trench.

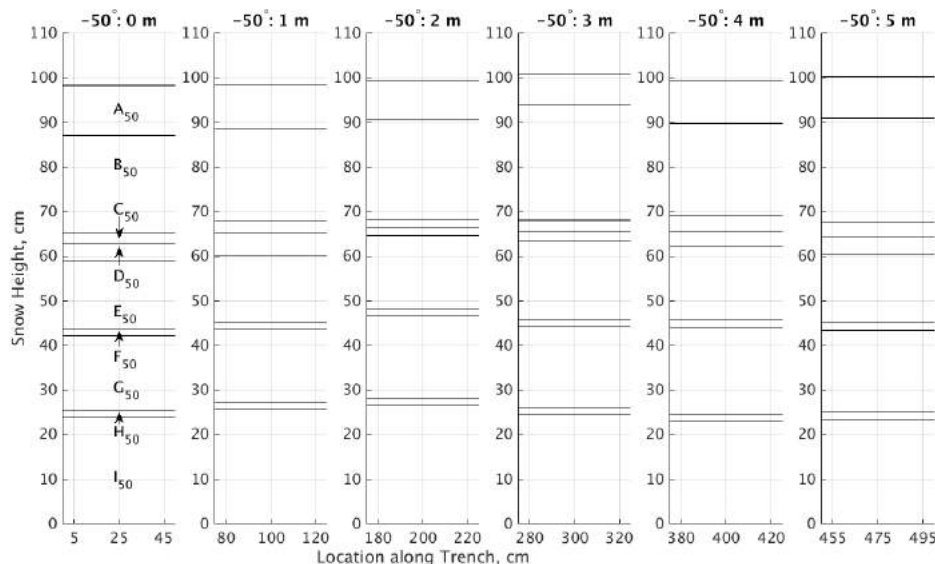
**Figure 6.17:** Raw NIR derived stratigraphic layers of the SoRaX trenches. Individual stratigraphic layers from each SoRaX trench are highlighted.

-50° trenches are shown in Figures 6.18a and 6.18b, showing the horizontal spatial variability of the individual layers. It can be seen that the -50° trench has an additional layer when compared to the -40° trench. The top-most NIR derived layer for the -40° trench (layer A<sub>40</sub>) is depicted as being two separate layers in the -50° NIR derived layer analysis (layers A<sub>50</sub> and B<sub>50</sub>). The layers as depicted in Figures 6.18a and 6.18b were used to define the layer boundaries for the simulations with the n-HUT model in Section 6.4.

As mentioned when discussing the traditional grain size observations, the NIR stratigraphic analysis was used to help estimate the traditional grain size across the individual



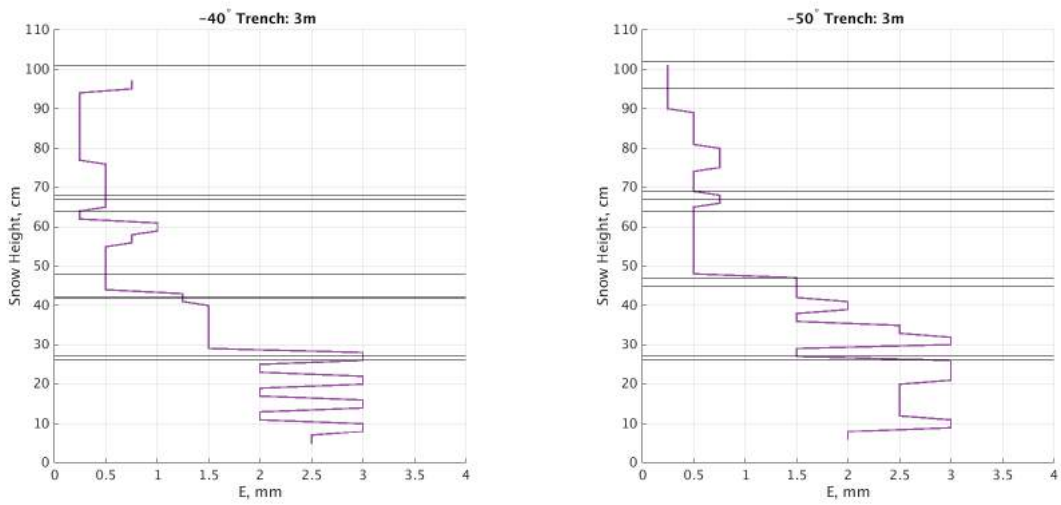
(a) Corrected NIR derived stratigraphic layers across the  $-40^\circ$  trench snowpits.



(b) Corrected NIR derived stratigraphic layers across the  $-50^\circ$  trench snowpits.

**Figure 6.18:** Corrected NIR derived stratigraphic layers of the SoRaX trenches, using the manual stratigraphy observations to calibrate the NIR stratigraphic layer locations. Individual stratigraphic layers from each SoRaX trench are highlighted.

trenches. As it is assumed that the horizontal spatial variability of the traditional grain size was small, it can be estimated that the layers depicted in Figures 6.19a and 6.19b would exhibit similar characteristics across the trench. Thus, by calculating the mean traditional grain size at 3 m for each layer, it would be possible to estimate the traditional grain size for each layer across the entire trench. Figures 6.19a and 6.19b show the traditional grain size observations (similar to Figures 6.16a and 6.16b), with the layer heights shown at the 3 m snowpit overlaid from Figure 6.18. Tables 6.8 and 6.9 show the mean traditional grain size of each layer of the two SoRaX trenches, as well as the snow grain types associated with each layer.



(a) Traditional Grain Size (E) observations for the 3 m snowpit in the  $-40^{\circ}$  trench, with NIR derived stratigraphic layers overlaid.

(b) Traditional Grain Size (E) observations for the 3 m snowpit in the  $-40^{\circ}$  trench, with NIR derived stratigraphic layers overlaid.

**Figure 6.19:** Traditional Grain size profiles of the 3 m snowpit, with corrected NIR derived stratigraphic layers.

## 6.4 HUT Simulations of the SoRaX Trenches

### 6.4.1 Aligning SoRaX Radiometric Data with Snowpit Observations

As mentioned in Section 6.3.2, the SoRaX snow removal experiment involved snowpits located as close as possible to the elevation and azimuth angle scans of the natural snowpack. By identifying what combination of elevation and azimuth angles corresponds to the closest snowpit observation, it was possible to use the observed snowpit parameters with both the original and the adapted n-HUT models, to produce simulated brightness temperatures of the snowpack. The simulated brightness temperature were then compared to the corresponding observed brightness temperatures, much like the comparison

**Table 6.8:** Stratigraphic layers, as observed using the NIR photography technique, for the -40° trench. Grain shape codes follow those by [Fierz et al. \[2009\]](#).

Layer	Traditional Grain Size (mm)	Grain Shape Code
A <sub>40</sub>	0.38	RGsr
B <sub>40</sub>	0.50	RG
C <sub>40</sub>	0.44	MFcr
D <sub>40</sub>	0.59	RGxf
E <sub>40</sub>	0.71	RGxf
F <sub>40</sub>	1.66	RG
G <sub>40</sub>	3.00	FC
H <sub>40</sub>	2.53	DH

**Table 6.9:** Stratigraphic layers, as observed using the NIR photography technique, for the -50° trench. Grain shape codes follow those by [Fierz et al. \[2009\]](#).

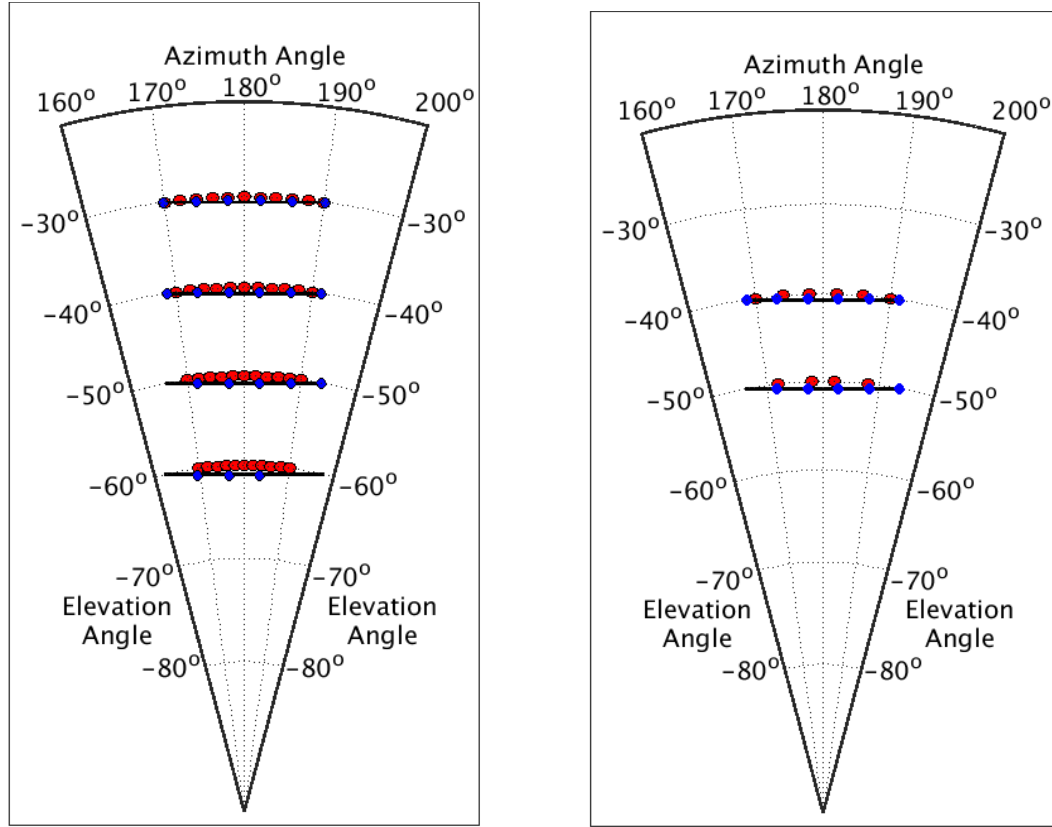
Layer	Traditional Grain Size (mm)	Grain Shape Code
A <sub>50</sub>	0.25	RGsr
B <sub>50</sub>	0.50	RGxf
C <sub>50</sub>	0.67	RGxf
D <sub>50</sub>	0.63	RGxf
E <sub>50</sub>	0.56	RGxf
F <sub>50</sub>	1.50	MFpc
G <sub>50</sub>	1.97	FC
H <sub>50</sub>	2.25	FC
I <sub>50</sub>	2.64	DH

of the ASMEx snow slab simulations and observed brightness temperatures in Section 4.3.

The location of the SoRaX trenches was previously shown in Figure 6.4, with the SoRaX radiometer scans and footprints being shown in Figure 6.3. Figure 6.20 combines the locations of the centre of the SoRaX radiometer scans use for the comparison with the location of all trenches and completed snow pits.

It is clear from Figure 6.2 that, by comparing the elevation and azimuth angles of the SoRaX scans with approximate snowpit locations, it was possible to match radiometer scans with the corresponding snowpit. It should be noted that, as the radiometer footprints (Figure 6.3b) cover a larger region than that observed by the snowpit profiles, the radiometric footprint may be affected by more than one profile. However, this influence is assumed to be small, as the horizontal variability of the observed snowpit parameters are small. As the focus of this study lies with the -40° and -50° trenches, Figure 6.20b shows the -40° and -50° trenches, with the completed snow pits and nearest SoRaX radiometric scans overlaid. Table 6.10 shows the SoRaX azimuth angle required to observe the brightness temperature corresponding to the relevant snowpit.

The snow pits at 0 m and 5 m in the -50° trench are not located with any SoRaX



(a) Completed SoRaX snow pits (blue), trenches (black lines), and SodRad1 azimuth and elevation centres (red).

(b) Completed SoRaX snow pits (blue), in the  $-40^\circ$  and  $-50^\circ$  trenches (black lines), and SodRad1 azimuth and elevation centres (red).

**Figure 6.20:** SoRaX snowpit and SodRad1 azimuth and elevation centres. The SodRad1 azimuth and elevation scans of Figure 6.20b are shown in detail in Table 6.10.

Snowpit location						
Elevation Angle	0 m	1 m	2 m	3 m	4 m	5 m
$-40^\circ$	$190^\circ$	$186^\circ$	$182^\circ$	$178^\circ$	$174^\circ$	$170^\circ$
$-50^\circ$	N/A	$188^\circ$	$182^\circ$	$178^\circ$	$172^\circ$	N/A

**Table 6.10:** Azimuth angles for the  $-40^\circ$  and  $-50^\circ$  snow pits. Snow pits marked with N/A show snowpit locations out of the range of the azimuth scans.

radiometer scans. This is due to the trench length being fixed (at 5 m), regardless of the elevation scan being observed. The radiometer scan arc, however, does vary in Cartesian co-ordinate space, but not in spherical co-ordinate space. The SoRaX radiometer scans take place over an azimuth range of  $20^\circ$ , regardless of the elevation angle. When comparing in Cartesian co-ordinates, the azimuth range of  $20^\circ$  is reduced from 5 m at  $-30^\circ$  of elevation to 3 m at  $-60^\circ$  of elevation (Figure 6.2). Thus, some snowpits can be found outside the SoRaX radiometer scan, and thus cannot be observed or compared to simulations.

## 6.4.2 n-HUT Model Parameter Selection

### 6.4.2.1 Extinction Coefficient Selection

For the original and adapted n-HUT models to accurately simulate the brightness temperature values of the observed SoRaX snow pits, many different parameters and initial values must be set. These parameters and initial settings include setting the underlying ground conditions (as shown in Figures 2.10 and 5.15), as well as setting specific model parameters prior to snowpack simulation.

As the n-HUT model is now capable of simulating the extinction of the snowpack using both the traditional grain size ([Hallikainen et al. \[1987\]](#), [Pullainen et al. \[1999\]](#), and [Lemmettyinen et al. \[2010\]](#)), and by using the optical diameter (as proposed in Section 5.4.5), two sets of brightness temperature simulations were produced; one using the original extinction coefficient (with traditional grain size as an input parameter), and one using the newly derived extinction coefficient (with optical diameter as an input parameter). This will allow for a comparison, not just between the observed brightness temperature and those simulated using the original n-HUT model, but also between the original and adapted n-HUT model simulations.

The comparison of simulated brightness temperatures between the original and adapted n-HUT models demonstrates the influence that the new extinction coefficient has upon the n-HUT model. An improvement in simulated brightness temperature values would infer that an improvement has been made to the n-HUT model, thus reaching the third and final thesis aim of evaluation of the new extinction coefficient.

### 6.4.2.2 Ground Parameter Selection

Both the original and adapted n-HUT models require that certain ground parameters be input, in order to simulate the underlying ground surface in terms of its microwave emission and the reflectivity of the underlying surface. These processes are calculated from values of the physical temperature of the ground, the height variations of the ground (input as root mean squared (rms) height variations), and the ground permittivity.

The ground physical temperature was not measured as part of the SoRaX snow removal trench observations, as the IOA houses numerous automatic sensors, capable of recording soil, snow, and air conditions, as part of the continuous monitoring of the IOA. As part of this sensor array, the ground temperature (5 cm below the ground surface) was observed using an automatic Stevens Hydra Probe II, which recorded hourly ground tem-

perature measurements. The ground physical temperature probe was located underneath the SoRaX snow removal trenches. Observations were made during the SoRaX observations. During the -40° and -50° trench observations, the ground temperature sensor was measured to be  $-0.81^{\circ}\text{C} \pm 0.01^{\circ}\text{C}$  and  $-0.82^{\circ}\text{C} \pm 0.01^{\circ}\text{C}$  respectively.

The rms height variations, unlike the ground physical temperature observations, were measured as part of the SoRaX snow removal trench observations. By manipulating the NIR-derived stratigraphic layers, it was possible to calculate the rms height variations from the ground position, across the individual snow pits. Table 6.11 shows the calculated rms height variation of each snowpit, calculated from the NIR-derived ground layer.

**Table 6.11:** RMS height variations (mm) of the ground layer at each of the snowpit locations in the -40° and -50° trenches, as calculated from the NIR derived ground layer.

Elevation Angle	Snowpit location					
	0 m	1 m	2 m	3 m	4 m	5 m
-40°	3.458	2.251	3.952	1.037	1.549	2.640
-50°	2.539	2.156	5.020	4.584	2.752	1.882

The ground permittivity, like the ground physical temperature, was not measured as part of the SoRaX snow removal trench observations. Thus, the default value for frozen soil (as given by [Pulliaisen et al. \[1999\]](#)) of 6 - 1j was used.

#### 6.4.2.3 Snow Parameter Selection

After the determination of the ground layer of the SoRaX trenches, the snowpack was then inputted into the two n-HUT models for simulation. It should be noted that the n-HUT model requires the angle of incidence to be defined, in order to calculate the correct path length through the layers of the snowpack (Section 2.5.4.2). Thus, the elevation angles were converted to angles of incidence via:

$$\theta_I = 90 + \theta_E \quad (6.1)$$

where  $\theta_I$  is the angle of incidence and  $\theta_E$  is the angle of elevation defined by the SodRad platform (both in degrees). Each individual snowpack in the -40° and -50° trenches were parameterised as a series of separate layers, with the layer boundaries being determined by the NIR-derived stratigraphic layers. Within each stratigraphic layer, the bulk characteristics were calculated from the profiles of physical temperature, density, SWE (using the bulk density and layer thickness values with Eqn. 2.17), as well as both the traditional grain size and the optical diameter (from the SSA profile, using Eqn. 2.19).

The snowpack was then input as a series of layers (with a base layer equal to that of the frozen ground) into the n-HUT models.

### 6.4.3 Original and Adapted n-HUT Model Simulation

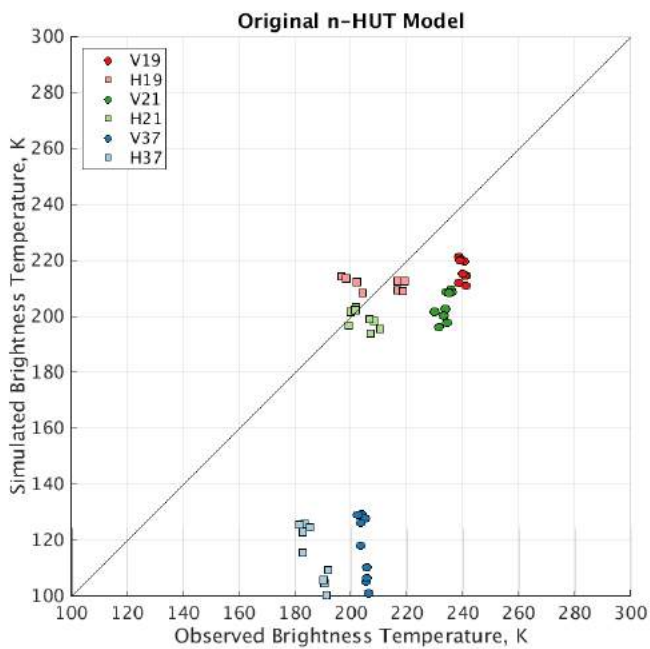
Figure 6.21 shows the simulated brightness temperature of the SoRaX snow pits, at 18.7, 21.0, and 36.5 GHz, at both horizontal and vertical polarizations. Figure 6.21a shows the original n-HUT model simulations, while Figure 6.21b shows the adapted n-HUT model simulations. Values of observed brightness temperatures and corresponding simulated brightness temperatures are shown in Appendix D.

The setup and parameterisation of the two HUT model runs are almost identical in nature, as they have almost the same initiation parameters and snow input parameters. The only difference between the two sets of simulations is the inclusion of the newly derived extinction coefficient model, and the inclusion of the optical grain size rather than the traditional grain size (as previously shown when comparing the two HUT model schematics in Figure 2.10 and 5.15). The microstructure parameter (traditional grain size or optical grain size) is only used by the n-HUT models to calculate the extinction coefficient (Eqns. 2.53 and 5.48 respectively). Thus, any differences between the two simulations results is purely a result of the differing extinction coefficient models being used (thus giving differing levels of extinction and scattering within the snowpack). From the brightness temperature values of the two sets of simulations, RMSE and bias values (displayed in Tables 6.12 and 6.13 respectively). This allows for a direct comparison between the two simulations, and thus a direct comparison between the two extinction coefficient models within the n-HUT models.

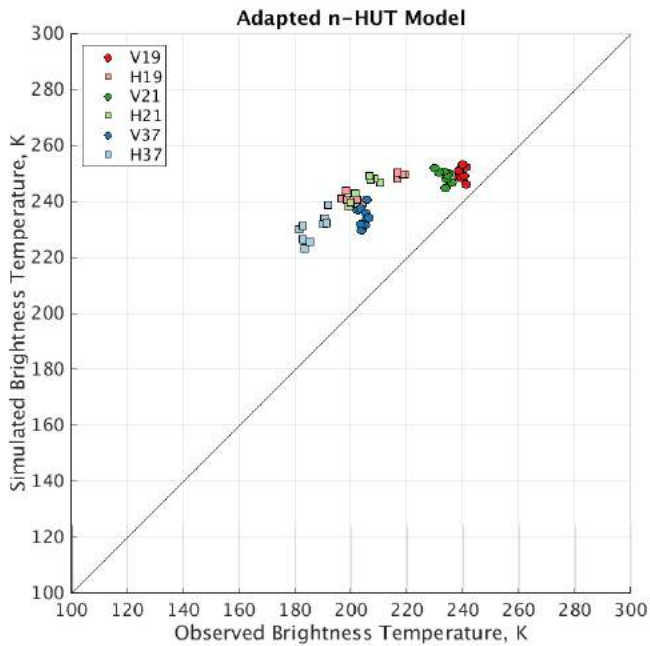
**Table 6.12:** RMSE values for the simulated brightness temperatures (K) of the SoRaX snow pits, from both the original and adapted n-HUT models.

Frequency (GHz)	Original		Adapted	
	H-Pol	V-Pol	H-Pol	V-Pol
18.7	11.13	23.46	37.54	10.87
21.0	7.75	30.15	39.68	15.60
36.5	72.68	88.16	44.09	30.40

Both simulation outputs show the same expected pattern; that the lower frequency brightness temperature simulations are larger than those corresponding to the higher frequency simulations. This is expected, as both extinction coefficient models used (Eqns. 2.53 and 5.48) use frequency as an input parameter; as the scattering (and therefore the total extinction) is highly dependent on frequency of radiation observed ([Hallikainen et al.](#)



(a) Simulated brightness temperatures from the original n-HUT model, using the [Hallikainen et al. \[1987\]](#) extinction coefficient and traditional grain size.



(b) Simulated brightness temperatures from the adapted n-HUT model, using the derived extinction coefficient and optical diameter, as shown in Section 5.4.5.

**Figure 6.21:** Original and adapted n-HUT model simulations plotted against observed brightness temperatures of the SoRaX snow pits. Simulations were produced at 18.7 (red), 21.0 (green), and 36.5 (blue) GHz, at horizontal (square) and vertical (circle) polarizations.

**Table 6.13:** Bias values for the simulated brightness temperatures (K) of the SoRaX snow pits, from both the original and adapted n-HUT models.

Frequency (GHz)	Original		Adapted	
	H-Pol	V-Pol	H-Pol	V-Pol
18.7	4.08	-23.08	37.12	10.62
21.0	-4.56	-29.88	39.63	15.17
36.5	-71.47	-87.36	43.98	30.22

[1987], Roy et al. [2004], Kontu and Pulliainen [2010], Chang et al. [1987], Rees [2006], and Grody [2008]). It can also be seen that both sets of simulations do not model the difference in brightness temperature between the horizontal and vertical polarization brightness temperatures. The difference is clearly visible in the observed brightness temperatures, as shown in Table 6.14.

**Table 6.14:** Brightness temperature polarization difference (K) for the observed brightness temperatures ( $T_{b,obs}$ ), along with the HUT simulations using the Hallikainen et al. [1987] extinction coefficient ( $T_{b,Hall}$ ) and the extinction coefficient derived in Section 5.4.5 ( $T_{b,New}$ ).

Frequency [GHz]	$T_{b,Obs}$	$T_{b,Hall}$	$T_{b,New}$
18.7	31.96	4.80	5.46
21.0	29.74	4.42	5.29
36.5	18.01	2.12	4.26

This suggests that the n-HUT models, regardless of the extinction coefficient model used, have problems in simulating the polarization difference. The lack of polarization difference in the simulated brightness temperatures may be a result of the assumptions made within the n-HUT model. The n-HUT model assumes that the extinction within the snowpack is independent of polarization, as the extinction coefficient does not include polarization as a determining factor. Therefore, polarization only makes a significant difference with regards to the interface reflectivity calculations. The new derived extinction coefficient also does not include polarization as a variable, as it only used  $\gamma_{sv}$  as part of deriving the empirical scattering coefficient model.

The simulation outputs differ in many ways. Firstly, the original n-HUT model simulations generally produce an underestimation of brightness temperature, whilst the adapted n-HUT model simulation produces an overestimation of brightness temperature. This is most apparent at 36.5 GHz, where the original n-HUT model produced a large underestimation (Bias = -77.47K / -87.36 K at horizontal/vertical polarizations), whilst the adapted n-HUT model produced an overestimation (Bias = 43.98 K / 30.40 K at horizontal/vertical polarizations). The fact that, for all frequencies and polarizations,

the values of RMSE are very similar to the magnitude of the bias, and thus a significant part of this error is due to the persistent bias that is present. This can be statistically shown, by subtracting the persistent bias from the simulated brightness temperatures, and calculating new RMSE values. Table 6.15 shows the adapted RMSE values, once the bias has been removed. The adapted RMSE values are much smaller, showing that a large portion of the RMSE values are due to the persistent bias.

**Table 6.15:** Adapted RMSE values for the simulated brightness temperatures (K) of the SoRaX snow pits. The adapted RMSE values are calculated from the simulated brightness temperatures, once the mean bias from Table 6.13 has been removed.

Hallikainen et al. [1987]				Section 5.4.5	
	H	V		H	V
18.7	10.35	4.24		5.58	2.33
21.0	6.27	3.97		1.97	3.63
36.5	13.25	11.85		3.29	3.31

The large underestimation produced by the original n-HUT model at 36.5 GHz is present due to the larger grain sizes found at the base of the snowpack. Tables 6.16 and 6.17 show the bulk layer traditional grain sizes and optical diameters for the 3 m snowpit at the -40° and -50° trenches respectively. It can be seen that, at the bases of both snowpacks, the grain sizes are larger than the snow crystals at the surface. The large grain sizes produce larger scattering coefficients, as shown by Tables 6.16 and 6.17. These larger extinction coefficients overpower the signal that would come from the upper part of the snowpack, due to the fact that the surface has much smaller magnitudes of scattering coefficient. The scattering coefficient contribution of the Hallikainen et al. [1987] extinction coefficient was calculated by subtracting the theoretical absorption coefficient (Eqn. 2.42) from the empirical extinction coefficient. The scattering coefficient from the newly derived extinction coefficient was calculated from the second term of Eqn. 5.48.

**Table 6.16:**  $k_s$  values calculated using the Hallikainen et al. [1987] extinction coefficient ( $k_{s,Hall}$ ) and the extinction coefficient calculated in Section 5.4.5 ( $k_{s,Mas}$ ) for each layer of the snowpit observed at 3 m in the -40° trench.

Layer	Microstructure		18.7 GHz		21.0 GHz		36.5 GHz	
	E [mm]	D <sub>opt</sub> [mm]	k <sub>s,Hall</sub>	k <sub>s,Mas</sub>	k <sub>s,Hall</sub>	k <sub>s,Mas</sub>	k <sub>s,Hall</sub>	k <sub>s,Mas</sub>
A <sub>40</sub>	0.38	0.23	0.172	0.183	0.244	0.234	1.245	0.740
B <sub>40</sub>	0.50	0.28	0.310	0.292	0.438	0.372	2.201	1.181
C <sub>40</sub>	0.44	0.28	0.222	0.291	0.316	0.370	1.636	1.175
D <sub>40</sub>	0.59	0.36	0.446	0.444	0.627	0.566	3.119	1.805
E <sub>40</sub>	0.71	0.34	0.682	0.409	0.953	0.521	4.651	1.658
F <sub>40</sub>	1.66	0.52	4.083	0.894	5.659	1.142	26.765	3.663
G <sub>40</sub>	3.00	0.76	13.497	1.581	18.687	2.020	88.030	6.496
H <sub>40</sub>	2.52	0.66	9.498	1.427	13.153	1.823	62.016	5.858

**Table 6.17:**  $k_s$  values calculated using the Hallikainen et al. [1987] extinction coefficient ( $k_{s,Hall}$ ) and the extinction coefficient calculated in Section 5.4.5 ( $k_{s,New}$ ) for each layer of the snowpit observed at 3 m in the -50° trench.

Layer	Microstructure		18.7 GHz		21.0 GHz		36.5 GHz	
	E [mm]	D <sub>opt</sub> [mm]	k <sub>s,Hall</sub>	k <sub>s,New</sub>	k <sub>s,Hall</sub>	k <sub>s,New</sub>	k <sub>s,Hall</sub>	k <sub>s,New</sub>
A <sub>50</sub>	0.25	0.18	0.069	0.106	0.099	0.136	0.518	0.430
B <sub>50</sub>	0.50	0.26	0.323	0.234	0.453	0.298	2.248	0.945
C <sub>50</sub>	0.67	0.28	0.614	0.282	0.857	0.356	4.167	1.143
D <sub>50</sub>	0.62	0.28	0.507	0.289	0.711	0.368	3.500	1.168
E <sub>50</sub>	0.56	0.35	0.389	0.437	0.549	0.557	2.760	1.774
F <sub>50</sub>	1.50	0.32	3.297	0.397	4.575	0.505	21.717	1.603
G <sub>50</sub>	1.97	0.50	5.771	0.814	7.997	1.039	37.776	3.329
H <sub>50</sub>	2.25	0.65	7.563	1.362	10.475	1.740	49.408	5.595
I <sub>50</sub>	2.64	0.64	10.427	1.491	14.440	1.905	68.076	6.1218

It should be noted that both the original and adapted n-HUT model simulations are subject to a number of small, yet unavoidable, errors. The radiometer and snowpit observations occurred at different times. It is therefore unlikely that the snowpack would have identical physical characteristics during both sets of observations. The density and microstructure parameters are unlikely to have significantly varied between the two sets of observations, as no snowfall or melting periods occurred between the two sets of observations. The dry bulb air temperature did vary between the two sets of observations, as can be seen in Figure 6.12. The mean dry bulb air temperature during the radiometer observations was -7.74°C, whilst it was -5.11°C and -6.77°C for the -40° and -50° trenches respectively. It has previously been shown that the top most 20 – 30 cm of the snowpack was susceptible to changes in dry bulb air temperature (Figure 6.11). To investigate the impact of the different air temperature present during the different times, the snowpack profiles were altered to simulate that of the snowpack during the radiometric observation. This was done by altering the top most 30 cm of the snowpack. The surface of the snow was set to be equal to that of the mean air temperature during the SoRaX radiometric observations. The top most 30 cm was then set to linearly decrease with depth, until the temperature of the snowpack at 40 cm was equal to that of the snowpack during the SoRaX snow removal observations.

When both of the SoRaX snowpacks were set to model the temperature during the radiometric observations, the original and adapted n-HUT models did not produce simulated brightness temperatures that varied significantly from the original simulations shown in Figure 6.21. The RMSE and bias values of both sets of simulations varied in the range of -0.16 K to +0.36 K of the values in Table 6.12, and by -0.04 K to -0.36 K of the values in Table 6.13. Thus the effects of the upper layer snow temperatures are shown to be

negligible.

## 6.5 Discussion

The reduced RMSE and bias values produced by the n-HUT model when using the new extinction coefficient model instead of the original extinction coefficient model ([Hallikainen et al. \[1987\]](#)) at vertical polarization presents an important improvement in the capability and usability of the n-HUT model. As the operational capability was increased tremendously by the inclusion of additional microstructure parameters ( $D_{opt}$ , shown in [Section 5.4.6](#)), the increased accuracy of the simulated brightness temperatures compared to observed brightness temperatures from a multiple layer snowpack show that the n-HUT model has been further improved.

This increase in accuracy in the n-HUT model at vertical polarization has several implications, each significant in their own right. The adapted n-HUT model can be used in place of the original n-HUT model in future snowpack observation campaigns, as the simulated brightness temperature from the adapted n-HUT model has been shown to be more accurate than the original n-HUT model ([Table 6.12](#) and [6.13](#)).

The adapted n-HUT model can also be used in place of the original n-HUT model in the satellite retrieval of snowpack parameters, such as snow mass and snow water equivalent estimations. The increased accuracy of simulations of brightness temperature with the adapted n-HUT model would reduce the large errors in snow water equivalent estimations, thus producing more accurate estimations of snow water equivalent and snow mass.

These more accurate estimations of snow mass and snow water equivalent are vital for hydrological forecasts and models. A more accurate estimation of the amount of water that is available as snow (through the use of remote sensing in conjunction with the adapted n-HUT model) would ultimately produce more accurate hydrological forecasts. The increased accuracy in snow mass estimates are also vital for meteorological and climatological studies, as the relationships between snow mass, snow extent, and global and local scale meteorological processes can be better understood.

## 6.6 Chapter Summary

The research behind Chapter 6 set out with the aim of testing the adapted n-HUT model (with the derived extinction coefficient model calculated in Section 5.4.5), and comparing the simulated brightness temperatures with those produced by the original n-HUT model (Hallikainen et al. [1987] and Lemmetyinen et al. [2010]), as well as against observed brightness temperatures of a natural snowpack. This section will summarise how each of the research goals of the third thesis aim (described in Section 1.3) have been individually reached, the main conclusions from this chapter, and any limitations and assumptions that should be taken into consideration.

**Aim 3: Goal 1: Analyse data collected as part of the Sodankylä Radiometer Experiment (SoRaX), to assess the usability of the SoRaX snowpit observations.**

Radiometric observations of the snowpack within the FMI ARC IOA took place at 18.7, 21.0, and 36.5 GHz. The SoRaX snow removal experiment assessed the same IOA snowpack, in terms of its physical temperature, density, traditional grain size, specific surface area, optical diameter, and internal stratigraphy. While not all observations were completed at all snowpit locations across each of the individual trenches, the horizontal and vertical spatial variability of the snowpack was adequately quantified. The SoRaX snow removal experiment produced snow parameter observations of sufficient quality to test the original and adapted n-HUT model.

**Aim 3: Goal 2: Simulate the brightness temperature, using both the original and the newly derived extinction coefficients.**

Using the data collected as part of the SoRaX field campaign, along with knowledge of the horizontal and vertical spatial variability of snowpack parameters, the natural snowpack was able to be used with both the original and the adapted n-HUT models to produce brightness temperature simulations. Both the original extinction coefficient model (Hallikainen et al. [1987]) and the newly derived extinction coefficient model (Section 5.4.5) were utilized in the simulations, allowing for both the traditional grain size and the optical diameter to serve as important input parameters.

**Aim 3: Goal 3: Compare and contrast the brightness temperature errors from both extinction coefficient models.**

The simulated brightness temperatures from both the original and the adapted n-HUT model were compared and contrasted, with respect to the observed SoRaX brightness temperatures at 18.7, 21.0, and 36.5 GHz, at both horizontal and vertical polarizations. It was shown that the original n-HUT model, using subjective observations of traditional grain size, produced large underestimations at vertical polarizations (bias = -23.08 K, -29.88 K, and -87.36 K at 18.7, 21.0, and 36.5 GHz respectively at vertical polarizations), whilst the adapted n-HUT model, using objective observations of SSA (and thus calculated values of  $D_{opt}$ ), produced overestimations of a smaller magnitude (bias = 10.62 K, 15.17 K, and 30.22 K at 18.7, 21.0, and 36.5 GHz respectively at vertical polarizations). The RMSE values from the overestimations and underestimations respectively were found to be of a comparable magnitude, a feature which suggests that a significant portion of the RMSE error was due to the persistent bias present. Once the persistent bias was removed (by directly removing the bias from the outputted brightness temperatures), the adapted multiple layer HUT snow emission model produced smaller RMSE values across all three frequencies and all polarizations. The overall underestimation by the original multiple layer HUT snow emission model was a result of the large grain sizes found in the base of the natural snowpack, as shown by the calculated scattering coefficients in Tables 6.16 and 6.17.

The lower magnitude values of RMSE and bias values that were produced when using the adapted n-HUT model (with objective observations of SSA and calculated values of  $D_{opt}$ ) instead of the original n-HUT model (with subjective observations of traditional grain size) prove that the newly derived extinction coefficient model is a significant breakthrough in brightness temperature simulation. By improving the RMSE and bias values of the n-HUT model, the derived extinction coefficient increases the accuracy of the simulated brightness temperatures, especially at 36.5 GHz where scattering is dominant.

The inclusion of a different microstructure parameter ( $D_{opt}$ ) also increases the operational capacity of the n-HUT model, as objective SSA observation techniques, such as observations with DUFISS, IceCube, and  $\mu$ CT analysis, can now be included as potential observations techniques that are capable of being used by the n-HUT model. This also reduces the need for subjective observations of traditional grain size to be taken when characterising a snowpack, if observations of SSA are also present.

## Chapter 7:

# Conclusion

## 7.1 Summary of Main Findings

The overall aim of this thesis was to produce a new extinction coefficient model for use within the n-HUT model, using modern observation techniques to measure snow properties. This overall aim was reached by completing three separate thesis aims, summarised below, detailing the key findings from each section of work.

### **Aim 1: Creation of the Arctic Snow Microstructure Experiment (ASME) dataset; comprising of radiometric and snow characteristic properties of snow slabs, extracted from the natural snowpack.**

The Arctic Snow Microstructure Experiment (ASME) was designed to make observations of homogeneous snow slabs, extracted from the natural snowpack. Microwave brightness temperatures of the snow slabs upon two bases (a perfect reflector and perfect absorber) were observed at 18.7, 21.0, 36.5, 89.0, and 150.0 GHz, at both horizontal and vertical polarizations. Snow parameters, such as physical temperature, density, specific surface area, and traditional grain size were observed for each of the 14 slabs. Three different observation categories (traditional snowpit techniques, SMP, and  $\mu$ CT analysis) were utilized as part of the ASME campaign.

14 snow slabs were analysed and observed in the manner described in Chapter 3, with the dataset visually shown in Chapter 4. The full dataset can be found in Appendix A and B. As snow slabs were taken from various depths in the snowpack, at different times throughout the winter and spring (including fresh snow slabs from the surface and depth hoar slabs from the base), a range of physical temperatures, densities, specific surface areas, and traditional grain sizes were observed, using traditional snowpit observations,

as well as from modern instrumentation like the SMP and through  $\mu$ CT analysis. From observations of density and SSA, calculated values of optical diameter and exponential correlation lengths were made. It was shown that, for the ASMEEx campaign, the values observed with the SMP instrument were inaccurate, when compared to those made with traditional techniques and from the  $\mu$ CT analysis. Therefore, the SMP observations were not used for the derivation of extinction coefficient. The observations from the  $\mu$ CT analysis were chosen to be used for the extinction coefficient calculation in Chapter 5. The high resolution observations from the  $\mu$ CT analysis allowed for the homogeneity of each slab to be assessed. Of the 14 ASMEEx slabs, four were shown to be non-homogeneous, with one additional slab being deemed wet.

The ASMEEx dataset was initially used to compare simulated brightness temperatures to observed brightness temperature values, for all dry slabs and all dry homogeneous slabs, using the original n-HUT model. For both sets of simulations, the RMSE and bias values are of a similar magnitude, suggesting that a significant portion of the RMSE is due to the persistent bias that was present. When restricting the slab dataset from all dry slabs to all dry homogeneous slabs, the RMSE and bias magnitudes were shown to reduce.

## **Aim 2: Derivation of a new extinction coefficient model, using the ASMEEx dataset.**

The ASMEEx dataset was used in conjunction with a flux coefficient model (as described in Section 5.2, [Wiesmann et al. \[1998\]](#) and [Toure et al. \[2008\]](#)), in order to calculate the two- and six-flux absorption and scattering coefficients. The absorptive flux coefficients were shown to be comparable to the theoretical absorption coefficient calculated within the n-HUT model. The scattering flux coefficients were shown to have a polarization difference, with horizontal polarizations having the larger scattering coefficients. After a preliminary analysis looking into the effect of anisotropy of the snow crystals on the scattering coefficient, it was decided that the vertical polarization scattering coefficient would be used for the calculation of the extinction coefficient.

The vertical polarization six-flux scattering coefficients were used to calculate an empirical formulae of scattering coefficients, using both frequency and optical diameter as dependant variables. The homogeneity of the slabs were shown to have little effect on the frequency dependency calculations, as the influence of the number of observations that occurred at each frequency played a larger role in the derivation of power exponents. The extinction coefficient, listed below, used the theoretical absorption coefficient (calculated

within the HUT model) together with the empirical formula for scattering coefficients.

$$k_{e,ASMEx} = (4\pi F \times 10^9) (\sqrt{\mu_0 \epsilon_0 \epsilon'_{snow}}) \left( \sqrt{0.5 \left( \sqrt{1 + \left( \frac{\epsilon''_{snow}}{\epsilon'_{snow}} \right)^2} \right)} - 1 \right) + 0.0065(D_o)^{2.12}(F^{2.12}) \quad (7.1)$$

**Aim 3: Validate the new extinction coefficient with independent natural snowpack data.**

After the implementation of the new extinction coefficient model with the n-HUT model, the adapted n-HUT model (Figure 5.15) was compared to the original n-HUT model, to test the effect of the differing extinction coefficients. This was completed via comparison of simulated brightness temperatures against observed brightness temperatures, using the Sodankylä Radiometer Experiment (SoRaX), as detailed in Chapter 6. Snowpit data collected through the SoRaX campaign consisted of numerous snowpit observations, which were discussed throughout both Chapters 3 and 6.

The n-HUT model simulated brightness temperatures of the SoRaX snowpits using both the original extinction coefficient ([Hallikainen et al. \[1987\]](#)) and the derived extinction coefficient from Chapter 5. It could be seen that the original n-HUT model underestimated the brightness temperatures at all frequencies at vertical polarizations, whilst the adapted n-HUT model produced smaller overestimations at both horizontal and vertical polarizations. This was most obvious at 36.5 GHz, where the adapted n-HUT model (RMSE = 30.40 K, bias = 30.22 K) produced smaller magnitude errors than that of the original n-HUT model (RMSE = 88.16 K, bias = -87.36 K).

## 7.2 Research Significance

The creation of a new extinction coefficient to be used within the adapted n-HUT model presents a significant improvement in the simulation of the microwave signature of the snowpack, as well as an improvement to the application of the n-HUT model. The adapted n-HUT model has been amended to be able to use another microstructure measurement as an input parameter; the original n-HUT model was initially designed to use traditional grain size. This inclusion of another microstructure parameter has expanded the capability of the n-HUT model. As the optical diameter is calculated directly from values of specific surface area, techniques that measure SSA (such as the

IceCube instrument,  $\mu$ CT analysis, and the SMP instrumentation) can be utilized with the n-HUT model.

The inclusion of additional observation techniques also improves the usability of the n-HUT model, as observations of SSA with the IceCube instrument are more objective than observations of traditional grain size. This objectivity is increased further if the SMP instrument (once correct calibration curves have been produced) or  $\mu$ CT analysis have been used. As the SMP required very little in the way of prior experience to use, it would be the ideal instrument to quantify large areas of snow cover quickly, as a snowpit observation is not needed.

The adapted n-HUT model is also an improvement upon the original n-HUT model, as the simulated brightness temperatures were more accurate than those using the original n-HUT model. This means that the new extinction coefficient model is more accurate than the [Hallikainen et al. \[1987\]](#) extinction coefficient model, within the n-HUT model. However, as an overestimation is present within the n-HUT model (as shown by the bias calculations of the SoRaX campaign, Table 6.13), work can be made towards a further improvement.

The adapted n-HUT model also provides an improvement over the original n-HUT model for use with remote sensing of snow with passive microwaves. By producing more accurate simulations in brightness temperature, the adapted n-HUT model would produce more accurate estimations of snow mass and snow water equivalent, when compared to those achieved using the original n-HUT model. This improvement in snow mass and snow water equivalent estimates would be advantageous for hydrological forecasts, irrigation management schemes, and global meteorological and climatological studies.

### 7.3 Research Limitations

Although the adapted n-HUT model is an improvement over the n-HUT model, the research has been limited by a number of assumptions and limitations. These assumptions and limitations are listed below:

- Problems with the radiometers during the ASMEEx campaign lead to an incomplete radiometric dataset, as Table 3.6 shows that, of the 14 slabs, only six were measured at all five possible frequencies. If the ASMEEx campaign had a complete radiometric dataset, the calculation of extinction coefficient would be strengthened, as the frequency and optical diameter dependencies would be more accurate.

- Problems with the SMP instrumentation lead to the data collected with the SMP instrument being neglected from the extinction coefficient calculation. This leads to the  $\mu$ CT analysis being the only set of modern high-resolution data. Having available SMP data would allow for an extension to the ASMEx dataset.
- The flux coefficient model introduced a polarization difference in the six-flux scattering coefficients that, while present in previous work ([Wiesmann et al. \[1998\]](#) and [Toure et al. \[2008\]](#)), was unaccounted for, and leads to the neglection of the scattering coefficients in the horizontal polarization. This neglection of the horizontal polarization may be the reason behind the greater RMSE and bias values in the horizontal polarization simulations with the adapted n-HUT model.

## 7.4 Future Work

Examples of potential future work that is possible as a result from the research presented in this thesis is listed below:

- Comparison of the adapted n-HUT model against the original n-HUT model and observed brightness temperatures for other snowpit observations would lead to further testing and evaluation of the adapted n-HUT model.
- Further work towards understanding the polarization difference in the six-flux scattering coefficients would allow for a more accurate extinction coefficient to be produced, thus improving the accuracy of the simulated brightness temperatures.
- Using the adapted n-HUT model with space-based passive microwave radiometers, in order to assess the accuracy of new global snow mass and snow water equivalent estimations.

**Appendix A:**

# ASME<sub>x</sub> Radiometric Data

**Table A.1:** Description of column headers in Table A.2. Std is the absolute value of the standard deviation.

Header	Abreviation	Description
Ref.		Slab Reference
Date		Date [ddmmyy]
$T_{air}$		Air Temperature [K]
$T_{Ephys}$		Physical temperature of the empty absorber set-up [K]
Freq		Frequency [GHz]
Pol		Polarization
Setup		Set-up design number
$T_{BA}$		$T_B$ of the snow on the absorbing base [K]
$\delta T_{BA}$		SEM of $T_B$ of the snow on the absorbing base [K]
$T_{BM}$		$T_B$ of the snow on the reflecting base [K]
$\delta T_{BM}$		SEM of $T_B$ of the snow on the reflecting base [K]
$T_{BA,S}$		Sky $T_B$ referring to the absorbing base [K]
$\delta T_{BA,S}$		SEM of sky $T_B$ referring to the absorbing base [K]
$T_{BM,S}$		Sky $T_B$ referring to the reflecting base [K]
$\delta T_{BM,S}$		SEM of sky $T_B$ referring to the reflecting base [K]
$T_{BE}$		$T_B$ of the empty absorber set-up [K]
$\delta T_{BE}$		SEM of $T_B$ of the empty absorber set-up [K]

---

Table A.2: Radiometric Data. (See Table A.1 for description of column

Ref.	Date	$T_{air}$	$T_{Ephys}$	Freq.	Pol.	Setup	$T_{BA}$	$\delta T_{BA}$	$T_{BA,S}$	$\delta T_{BA,S}$	$T_{BM}$	$\delta T_{BM}$	$T_{BM,S}$	$\delta T_{BM,S}$	$T_{BE}$	$\delta T_{BE}$
A01	140113	262.0	254.0	18.7	H	1	243.27	0.012	22.94	0.020	14.01	0.012	18.06	0.046	253.66	0.016
A01	140113	262.0	254.0	18.7	V	1	258.27	0.011	23.43	0.027	13.24	0.011	17.90	0.047	259.37	0.014
A01	140113	262.0	254.0	21.0	H	1	238.51	0.020	30.42	0.030	18.59	0.015	24.11	0.051	255.19	0.019
A01	140113	262.0	254.0	21.0	V	1	257.81	0.019	30.87	0.024	18.47	0.016	24.01	0.047	259.46	0.018
A01	140113	262.0	254.0	36.5	H	1	243.80	0.015	51.66	0.072	25.23	0.025	38.21	0.093	258.52	0.017
A01	140113	262.0	254.0	36.5	V	1	257.82	0.013	52.13	0.078	25.51	0.026	38.58	0.117	260.65	0.017
A02	140114	247.0	244.0	21.0	H	1	153.52	0.013	46.41	0.014	14.39	0.018	15.22	0.015	242.46	0.019
A02	140114	247.0	244.0	21.0	V	1	217.99	0.015	54.53	0.015	14.85	0.021	15.83	0.016	245.98	0.013
A02	140114	247.0	244.0	36.5	H	1	144.62	0.023	93.71	0.013	22.21	0.022	23.89	0.042	243.93	0.017
A02	140114	247.0	244.0	36.5	V	1	192.49	0.020	115.81	0.014	23.29	0.012	24.98	0.013	246.56	0.013
A03	140211	274.0	273.3	18.7	H	2	255.18	0.011	37.28	0.016	19.57	0.013	19.57	0.013	272.51	0.011
A03	140211	274.0	273.3	18.7	V	2	272.08	0.011	35.96	0.016	19.83	0.012	19.83	0.012	274.43	0.008
A03	140211	274.0	273.3	21.0	H	2	257.10	0.010	50.94	0.009	32.01	0.013	32.01	0.013	274.47	0.009
A03	140211	274.0	273.3	21.0	V	2	272.19	0.014	50.87	0.017	32.13	0.011	32.13	0.011	275.14	0.012
A04	140213	273.0	272.0	18.7	H	3	221.22	0.012	77.45	0.017	19.30	0.025	19.30	0.025	273.00	NaN
A04	140213	273.0	272.0	18.7	V	3	254.11	0.010	79.14	0.009	19.16	0.026	19.16	0.026	273.00	NaN
A04	140213	273.0	272.0	21.0	H	3	217.65	0.011	111.81	0.012	29.17	0.026	29.17	0.026	273.00	NaN
A04	140213	273.0	272.0	21.0	V	3	248.46	0.012	111.96	0.011	29.09	0.030	29.09	0.030	273.00	NaN

Ref.	Date	$T_{air}$	$T_{Ephys}$	Freq.	Pol.	Setup	$T_{BA}$	$\delta T_{BA}$	$T_{BA,S}$	$\delta T_{BA,S}$	$T_{BM}$	$\delta T_{BM}$	$T_{BM,S}$	$\delta T_{BM,S}$	$T_{BE}$	$\delta T_{BE}$
A05	140303	272.5	271.2	18.7	H	3	225.19	0.015	47.95	0.014	19.79	0.019	19.43	0.010	269.46	0.014
A05	140303	272.5	271.2	18.7	V	3	262.16	0.012	48.96	0.013	18.51	0.016	17.84	0.012	271.17	0.010
A05	140303	272.5	271.2	21.0	H	3	239.14	0.011	63.11	0.008	29.36	0.011	28.63	0.010	271.16	0.009
A05	140303	272.5	271.2	21.0	V	3	263.03	0.014	64.68	0.013	29.46	0.014	28.70	0.009	271.50	0.011
A05	140303	272.5	271.2	89.0	H	3	193.85	0.024	188.79	0.035	65.79	0.167	54.13	0.111	273.23	0.037
A05	140303	272.5	271.2	89.0	V	3	202.99	0.036	201.66	0.022	65.02	0.156	53.37	0.128	274.24	0.027
A05	140303	272.5	271.2	150.0	H	3	205.65	0.031	205.16	0.031	109.70	0.137	96.23	0.116	267.37	0.051
A05	140303	272.5	271.2	150.0	V	3	212.11	0.032	212.83	0.033	111.87	0.210	100.98	0.162	270.14	0.034
A06	140318	267.5	258.0	18.7	H	3	228.19	0.009	28.54	0.013	8.29	0.022	7.40	0.016	263.36	0.015
A06	140318	267.5	258.0	18.7	V	3	256.50	0.010	31.80	0.009	9.89	0.010	9.11	0.010	265.23	0.013
A06	140318	267.5	258.0	21.0	H	3	235.55	0.008	41.92	0.009	13.46	0.009	12.63	0.010	264.82	0.014
A06	140318	267.5	258.0	21.0	V	3	256.59	0.010	45.64	0.011	12.77	0.012	12.23	0.008	265.77	0.009
A06	140318	267.5	258.0	89.0	H	3	185.05	0.022	177.19	0.025	29.58	0.019	29.48	0.023	267.13	0.037
A06	140318	267.5	258.0	89.0	V	3	198.34	0.025	192.06	0.027	27.76	0.026	27.36	0.023	268.73	0.030
A06	140318	267.5	258.0	150.0	H	3	184.20	0.043	181.88	0.049	47.66	0.037	42.61	0.050	253.95	0.021
A06	140318	267.5	258.0	150.0	V	3	189.46	0.026	188.24	0.034	35.22	0.038	34.88	0.032	262.55	0.036
A07	140320	270.0	266.0	18.7	H	3	229.06	0.012	27.34	0.011	10.58	0.016	9.78	0.010	265.46	0.010
A07	140320	270.0	266.0	18.7	V	3	258.48	0.027	27.94	0.009	11.00	0.012	10.20	0.010	266.85	0.010
A07	140320	270.0	266.0	21.0	H	3	224.12	0.013	37.85	0.009	14.55	0.012	13.80	0.009	266.60	0.012

Ref.	Date	$T_{air}$	$T_{Ephys}$	Freq.	Pol.	Setup	$T_{BA}$	$\delta T_{BA}$	$T_{BA,S}$	$\delta T_{BA,S}$	$T_{BM}$	$\delta T_{BM}$	$T_{BM,S}$	$\delta T_{BM,S}$	$T_{BE}$	$\delta T_{BE}$
A07	140320	270.0	266.0	21.0	V	3	257.64	0.013	38.03	0.011	14.59	0.008	14.40	0.009	266.87	0.009
A07	140320	270.0	266.0	89.0	H	3	168.96	0.031	165.43	0.031	30.17	0.033	30.17	0.033	269.05	0.038
A07	140320	270.0	266.0	89.0	V	3	186.30	0.022	183.30	0.034	30.54	0.021	30.54	0.021	269.54	0.027
A07	140320	270.0	266.0	150.0	H	3	174.46	0.031	175.07	0.032	45.36	0.048	45.36	0.048	262.52	0.032
A07	140320	270.0	266.0	150.0	V	3	187.88	0.037	186.75	0.023	39.93	0.030	39.93	0.030	263.53	0.030
B01	150202	261.0	261.5	18.7	H	4	246.71	0.022	18.73	0.017	11.04	0.039	10.87	0.031	257.62	0.028
B01	150202	261.0	261.5	18.7	V	4	257.23	0.018	18.33	0.017	9.74	0.009	9.82	0.026	260.05	0.026
B01	150202	261.0	261.5	21.0	H	4	245.98	0.024	28.69	0.026	17.83	0.021	17.92	0.016	260.22	0.025
B01	150202	261.0	261.5	21.0	V	4	258.02	0.019	28.29	0.032	17.46	0.020	17.49	0.037	261.36	0.027
B01	150202	261.0	261.5	36.5	H	4	241.77	0.022	42.71	0.022	21.58	0.025	21.99	0.099	255.79	0.023
B01	150202	261.0	261.5	36.5	V	4	254.49	0.024	44.08	0.038	21.81	0.047	22.48	0.051	259.67	0.022
B02	150205	259.3	259.3	18.7	H	4	229.52	0.018	20.60	0.040	7.51	0.035	8.66	0.014	259.95	0.011
B02	150205	259.3	259.3	21.0	V	4	251.64	0.029	19.30	0.027	6.49	0.022	8.21	0.017	262.14	0.021
B02	150205	259.3	259.3	36.5	H	4	231.56	0.026	30.56	0.017	11.77	0.022	13.69	0.022	262.95	0.020
B02	150205	259.3	259.3	36.5	V	4	252.80	0.012	28.61	0.021	11.65	0.020	13.72	0.031	263.90	0.021
B02	150205	259.3	259.3	36.5	H	4	228.46	0.023	54.75	0.038	19.49	0.019	24.00	0.029	259.71	0.019
B02	150205	259.3	259.3	36.5	V	4	247.58	0.037	54.55	0.025	19.86	0.032	24.27	0.036	262.70	0.034
B03	150219	271.0	271.8	18.7	H	5	234.63	0.016	24.64	0.012	13.35	0.024	13.33	0.015	268.59	0.016
B03	150219	271.0	271.8	18.7	V	5	264.86	0.020	23.74	0.018	11.48	0.013	11.84	0.020	272.89	0.018

Ref.	Date	$T_{air}$	$T_{Ephys}$	Freq.	Pol.	Setup	$T_{BA}$	$\delta T_{BA}$	$T_{BA,S}$	$\delta T_{BA,S}$	$T_{BM}$	$\delta T_{BM}$	$T_{BM,S}$	$\delta T_{BM,S}$	$T_{BE}$	$\delta T_{BE}$
B03	150219	271.0	271.8	21.0	H	5	243.67	0.022	37.70	0.035	23.15	0.020	23.79	0.017	271.60	0.020
B03	150219	271.0	271.8	21.0	V	5	265.30	0.030	36.85	0.021	23.13	0.028	23.76	0.042	274.14	0.019
B03	150219	271.0	271.8	36.5	H	5	241.55	0.033	57.32	0.052	24.26	0.023	25.16	0.027	266.24	0.022
B03	150219	271.0	271.8	36.5	V	5	263.11	0.023	56.63	0.060	25.41	0.021	26.32	0.043	272.46	0.022
B04	150311	267.0	268.3	18.7	H	5	229.91	0.014	24.78	0.018	9.64	0.020	10.38	0.027	266.79	0.019
B04	150311	267.0	268.3	18.7	V	5	261.78	0.025	22.95	0.038	9.03	0.027	9.12	0.042	271.66	0.018
B04	150311	267.0	268.3	21.0	H	5	232.52	0.017	31.14	0.030	13.30	0.019	13.61	0.016	271.52	0.034
B04	150311	267.0	268.3	21.0	V	5	260.89	0.022	30.06	0.018	13.29	0.023	13.61	0.022	273.62	0.032
B04	150311	267.0	268.3	36.5	H	5	229.18	0.020	64.69	0.025	21.21	0.030	21.54	0.051	268.00	0.030
B04	150311	267.0	268.3	36.5	V	5	255.05	0.039	63.53	0.034	21.67	0.024	21.80	0.021	272.16	0.020
B05	150312	268.9	271.2	18.7	H	5	233.71	0.019	35.56	0.026	8.01	0.023	7.71	0.025	269.03	0.014
B05	150312	268.9	271.2	18.7	V	5	255.74	0.012	33.28	0.017	8.29	0.015	8.02	0.015	273.07	0.019
B05	150312	268.9	271.2	21.0	H	5	242.98	0.033	43.27	0.024	14.28	0.031	13.73	0.017	272.54	0.028
B05	150312	268.9	271.2	21.0	V	5	257.92	0.022	41.96	0.028	13.40	0.020	12.75	0.023	274.34	0.027
B05	150312	268.9	271.2	36.5	H	5	226.33	0.035	85.16	0.021	20.84	0.022	20.57	0.026	267.56	0.021
B05	150312	268.9	271.2	36.5	V	5	241.98	0.034	88.68	0.020	21.94	0.020	21.87	0.024	271.86	0.030
B05	150312	268.9	271.2	89.0	H	5	180.40	NaN	164.50	NaN	37.40	NaN	36.50	NaN	265.00	NaN
B05	150312	268.9	271.2	89.0	V	5	177.10	NaN	163.60	NaN	37.90	NaN	35.80	NaN	275.00	NaN
B05	150312	268.9	271.2	150.0	H	5	196.60	NaN	200.60	NaN	53.60	NaN	53.30	NaN	257.00	NaN

Ref.	Date	$T_{air}$	$T_{Ephys}$	Freq.	Pol.	Setup	$T_{BA}$	$\delta T_{BA}$	$T_{BA,S}$	$\delta T_{BA,S}$	$T_{BM}$	$\delta T_{BM}$	$T_{BM,S}$	$\delta T_{BM,S}$	$T_{BE}$	$\delta T_{BE}$
B05	150312	268.9	271.2	150.0	V	5	187.00	NaN	188.50	NaN	58.30	NaN	54.90	NaN	271.00	NaN
B06	150324	266.2	266.0	18.7	H	5	238.45	0.022	22.89	0.031	9.11	0.022	9.02	0.024	265.92	0.019
B06	150324	266.2	266.0	18.7	V	5	260.81	0.025	22.31	0.027	8.27	0.014	8.43	0.024	268.77	0.018
B06	150324	266.2	266.0	21.0	H	5	239.06	0.030	30.09	0.027	11.49	0.019	12.46	0.022	268.17	0.027
B06	150324	266.2	266.0	21.0	V	5	261.53	0.026	28.78	0.017	11.37	0.019	12.46	0.020	270.33	0.026
B06	150324	266.2	266.0	36.5	H	5	236.89	0.018	63.62	0.021	19.95	0.043	19.83	0.020	264.44	0.029
B06	150324	266.2	266.0	36.5	V	5	258.01	0.029	62.54	0.036	21.39	0.026	21.34	0.033	268.62	0.029
B06	150324	266.2	266.0	89.0	H	5	208.27	0.035	195.41	0.037	30.43	0.052	28.96	0.039	266.59	0.040
B06	150324	266.2	266.0	89.0	V	5	210.84	0.033	200.85	0.058	31.09	0.032	30.05	0.044	271.43	0.071
B06	150324	266.2	266.0	150.0	H	5	202.49	0.023	201.43	0.069	45.18	0.071	47.82	0.122	261.59	0.039
B06	150324	266.2	266.0	150.0	V	5	193.59	0.046	194.45	0.037	43.68	0.040	44.46	0.033	267.37	0.052
B07	150325	263.3	265.5	18.7	H	5	209.77	0.015	55.39	0.015	10.08	0.013	10.18	0.014	264.14	0.019
B07	150325	263.3	265.5	18.7	V	5	242.70	0.022	55.25	0.016	9.50	0.020	9.65	0.018	267.25	0.022
B07	150325	263.3	265.5	21.0	H	5	214.42	0.028	62.84	0.018	11.23	0.024	11.72	0.014	267.09	0.021
B07	150325	263.3	265.5	21.0	V	5	243.58	0.019	64.10	0.021	11.74	0.031	12.22	0.024	268.78	0.018
B07	150325	263.3	265.5	36.5	H	5	195.59	0.038	124.04	0.019	19.83	0.026	19.12	0.032	262.13	0.022
B07	150325	263.3	265.5	36.5	V	5	211.41	0.024	131.10	0.031	20.91	0.023	20.80	0.020	267.20	0.031
B07	150325	263.3	265.5	89.0	H	5	167.85	0.036	167.92	0.042	27.02	0.076	29.24	0.039	259.39	0.035
B07	150325	263.3	265.5	89.0	V	5	165.21	0.036	165.34	0.053	27.93	0.052	29.18	0.048	269.11	0.042

Ref.	Date	$T_{air}$	$T_{Ephys}$	Freq.	Pol.	Setup	$T_{BA}$	$\delta T_{BA}$	$T_{BA,S}$	$\delta T_{BA,S}$	$T_{BM}$	$\delta T_{BM}$	$T_{BM,S}$	$\delta T_{BM,S}$	$T_{BE}$	$\delta T_{BE}$
B07	150325	263.3	265.5	150.0	H	5	189.56	0.047	190.38	0.077	36.66	0.221	42.67	0.124	250.25	0.070
B07	150325	263.3	265.5	150.0	V	5	179.63	0.054	180.01	0.072	44.31	0.051	45.89	0.045	264.57	0.038

## Appendix B:

# ASME<sub>x</sub> Physical Slab Data

**Table B.1:** Description of column headers in Tables B.2 – B.6. SEM is the standard error of the mean.

Header	Abreviation	Description
Ref.		Slab Reference
Date		Date
<i>Thick</i>		Slab Thickness [mm]
$\delta\text{Thick}$		SEM of Slab Thickness [mm]
$T_{phys}$		Physical Snow Temperature [K]
$\delta T_{phys}$		SEM of Physical Snow Temperature [K]
$E$		Observed Grain Size [mm]
$\delta E$		SEM of Observed Grain Size [mm]
$\rho_s$		Density measured with traditional methods [ $\text{kgm}^{-3}$ ]
$\delta\rho_s$		SEM of Density measured with traditional methods [ $\text{kgm}^{-3}$ ]
$\rho_{SMP}$		Snow density measured with the SMP [ $\text{kgm}^{-3}$ ]
$\delta\rho_{SMP}$		SEM of snow density measured with the SMP [ $\text{kgm}^{-3}$ ]
$\rho_\mu$		Snow density measured with $\mu$ CT [ $\text{kgm}^{-3}$ ]
$\delta\rho_\mu$		SEM of snow density measured with $\mu$ CT [ $\text{kgm}^{-3}$ ]
$SSA_s$		SSA measured with the IceCube [ $\text{mm}^{-1}$ ]
$\delta SSA_s$		SEM of SSA measured with IceCube [ $\text{mm}^{-1}$ ]
$SSA_{SMP}$		SSA measured with the SMP [ $\text{mm}^{-1}$ ]
$\delta SSA_{SMP}$		SEM of SSA measured with the SMP [ $\text{mm}^{-1}$ ]
$SSA_\mu$		SSA measured with $\mu$ CT [ $\text{mm}^{-1}$ ]
$\delta SSA_\mu$		SEM of SSA measured with $\mu$ CT [ $\text{mm}^{-1}$ ]
$P_{exs}$		Exp. Corr. Length calculated with IceCube SSA [mm]
$\delta P_{exs}$		SEM of Exp. Corr. Length calculated with IceCube SSA [mm]
$P_{exSMP}$		Exp. Corr. Length measured with the SMP [mm]
$\delta P_{exSMP}$		SEM of Exp. Corr. Length measured with the SMP [mm]
$P_{exp}$		Exp. Corr. Length measured with $\mu$ CT [mm]
$\delta P_{exp}$		SEM of Exp. Corr. Length measured with $\mu$ CT [mm]
$D_{opts}$		Optical Diameter calculated with IceCube SSA [mm]
$\delta D_{opts}$		SEM of Optical Diameter calculated with IceCube SSA [mm]
$D_{optSMP}$		Exp. Corr. Length calculated with SMP SSA [mm]
$\delta D_{optSMP}$		SEM of Exp. Corr. Length calculated with SMP SSA [mm]
$D_{opt\mu}$		Exp. Corr. Length calculated with $\mu$ CT SSA values [mm]
$\delta D_{opt\mu}$		SEM Exp. Corr. Length calculated with $\mu$ CT SSA values [mm]

**Table B.2:** Physical Slab Data (See Table B.1 for description of column headings).

Ref.	Date	Thick	$\delta Thick$	$T_{phys}$	$\delta T_{phys}$	$E$	$\delta E$
A01	140113	168.57	2.377	259.95	0.029	0.45	0.03
A02	140114	150.03	1.039	250.82	0.189	0.69	0.06
A03	140211	157.31	1.082	272.75	0.029	0.62	0.07
A04	140213	164.98	2.510	272.55	0.029	0.93	0.08
A05	140303	148.91	0.539	272.17	0.055	0.88	0.06
A06	140318	136.06	1.182	265.40	0.334	0.75	0.06
A07	140320	139.63	1.116	267.92	1.765	0.92	0.05
B01	150202	136.60	0.501	259.80	0.449	0.68	0.05
B02	150205	149.17	0.562	262.10	0.091	0.85	0.08
B03	150219	140.01	0.697	270.40	0.178	0.75	0.07
B04	150311	160.13	0.723	267.97	0.315	0.72	0.02
B05	150312	49.94	0.941	269.80	0.261	1.81	0.06
B06	150324	144.93	1.451	267.65	0.155	0.84	0.07
B07	150325	151.60	0.529	269.32	0.197	1.73	0.07

**Table B.3:** Slab Density Data (See Table B.1 for description of column headings).

Ref.	Data	$\rho_s$	$\delta \rho_s$	$\rho_{SMP}$	$\delta \rho_{SMP}$	$\rho_\mu$	$\delta \rho_\mu$
A01	140113	135.50	8.184	145.69	2.240	93.48	2.465
A02	140114	284.17	6.230	296.44	2.459	98.80	8.208
A03	140211	227.67	12.095	199.90	1.796	200.56	2.960
A04	140213	225.67	12.095	272.04	2.552	310.01	4.171
A05	140303	286.67	10.541	250.94	2.283	284.19	3.432
A06	140318	280.00	4.292	265.44	2.064	273.88	1.831
A07	140320	284.83	6.766	254.09	1.215	279.20	4.084
B01	150202	139.50	6.977	229.54	1.739	141.89	3.677
B02	150205	160.33	9.844	217.17	1.619	182.98	3.969
B03	150219	234.00	6.928	223.83	0.951	251.80	2.264
B04	150311	268.17	7.586	227.91	2.921	269.96	2.537
B05	150312	337.50	4.500	258.66	2.685	319.81	5.913
B06	150324	315.00	5.060	287.52	1.244	318.87	1.797
B07	150325	282.50	4.949	261.92	3.067	307.06	2.743

**Table B.4:** Slab SSA Data (See Table B.1 for description of column headings).

Ref.	Data	$SSA_s$	$\delta SSA_s$	$SSA_{SMP}$	$\delta SSA_{SMP}$	$SSA_\mu$	$\delta SSA_\mu$
A01	140113	32.84	1.735	35.29	0.295	27.14	0.254
A02	140114	14.15	1.704	19.87	0.199	12.04	0.398
A03	140211	16.53	1.312	25.98	0.240	15.02	0.309
A04	140213	10.33	0.653	17.19	0.356	8.58	0.128
A05	140303	NaN	NaN	19.98	0.299	9.02	0.176
A06	140318	NaN	NaN	22.04	0.185	11.72	0.126
A07	140320	NaN	NaN	22.59	0.113	9.85	0.104
B01	150202	33.38	1.329	23.98	0.205	25.46	0.249
B02	150205	33.39	2.316	25.51	0.157	23.25	0.218
B03	150219	20.68	1.213	24.71	0.130	15.21	0.083
B04	150311	19.45	0.587	24.30	0.318	14.68	0.137
B05	150312	9.49	0.115	17.02	0.441	7.62	0.079
B06	150324	15.85	0.730	19.24	0.104	11.69	0.059
B07	150325	8.57	0.134	20.61	0.314	7.28	0.041

**Table B.5:** Slab  $P_{ex}$  Data (See Table B.1 for description of column headings).

Ref.	Data	$P_{exs}$	$\delta P_{exs}$	$P_{exSMP}$	$\delta P_{exSMP}$	$P_{exp}$	$\delta P_{exp}$
A01	140113	0.0779	0.0062	0.0726	0.0005	0.1006	0.0006
A02	140114	0.1463	0.0179	0.1139	0.0110	0.0808	0.0071
A03	140211	0.1364	0.0130	0.0917	0.0006	0.1669	0.0022
A04	140213	0.2190	0.0181	0.1468	0.0083	0.2445	0.0042
A05	140303	NaN	NaN	0.1205	0.0050	0.2501	0.0048
A06	140318	NaN	NaN	0.0976	0.0005	0.1851	0.0021
A07	140320	NaN	NaN	0.0963	0.0003	0.2167	0.0021
B01	150202	0.0762	0.0049	0.0948	0.0006	0.1009	0.0007
B02	150205	0.0741	0.0069	0.0902	0.0004	0.1044	0.0007
B03	150219	0.1080	0.0071	0.0921	0.0003	0.1438	0.0007
B04	150311	0.1091	0.0045	0.0956	0.0010	0.1462	0.0009
B05	150312	0.1998	0.0036	0.1370	0.0059	0.2579	0.0024
B06	150324	0.1242	0.0061	0.1074	0.0003	0.1682	0.0008
B07	150325	0.2421	0.0057	0.1097	0.0020	0.2760	0.0018

**Table B.6:** Slab  $D_{opt}$  Data (See Table B.1 for description of column headings).

Ref.	Data	$D_{opts}$	$\delta D_{opts}$	$D_{optSMP}$	$\delta D_{optSMP}$	$D_{opt\mu}$	$\delta D_{opt\mu}$
A01	140113	0.20	0.01	0.19	0.00	0.25	0.00
A02	140114	0.46	0.06	0.38	0.04	0.64	0.03
A03	140211	0.40	0.03	0.26	0.00	0.47	0.01
A04	140213	0.63	0.04	0.46	0.03	0.83	0.02
A05	140303	NaN	NaN	0.37	0.02	0.82	0.02
A06	140318	NaN	NaN	0.30	0.00	0.57	0.01
A07	140320	NaN	NaN	0.29	0.00	0.72	0.03
B01	150202	0.20	0.01	0.28	0.00	0.26	0.00
B02	150205	0.20	0.01	0.26	0.00	0.29	0.00
B03	150219	0.32	0.02	0.27	0.00	0.43	0.00
B04	150311	0.34	0.01	0.28	0.00	0.45	0.00
B05	150312	0.69	0.01	0.42	0.02	0.88	0.02
B06	150324	0.41	0.02	0.34	0.00	0.56	0.00
B07	150325	0.76	0.01	0.34	0.01	0.91	0.01

## Appendix C:

# Two- to- Six-Flux Coefficient conversion

The two-flux coefficients (Eqns. 5.30 and 5.31) are described as:

$$\gamma'_a = \gamma \frac{1 - r_0}{1 + r_0} \quad (\text{C.1})$$

$$\gamma'_b = (\gamma + \gamma'_a) \frac{r_0}{1 - r_0} \quad (\text{C.2})$$

and the two solid angles (Eqns. 5.32 and 5.33) are described as:

$$\Omega_1 = 2\pi \left( 1 - \sqrt{\frac{\epsilon - 1}{\epsilon}} \right) \quad (\text{C.3})$$

$$\Omega_2 = 2\pi \sqrt{\frac{\epsilon - 1}{\epsilon}} \quad (\text{C.4})$$

The relationship between the two solid body angles is written as (Eq. 5.35)

$$F = \frac{2\gamma_c}{\gamma_b} = \frac{\Omega_2}{\Omega_1} = \frac{\left( \sqrt{\frac{\epsilon - 1}{\epsilon}} \right)}{\left( 1 - \sqrt{\frac{\epsilon - 1}{\epsilon}} \right)} \quad (\text{C.5})$$

where  $\gamma_b$  is the six-flux scattering coefficient in the backward direction, and  $\gamma_c$  is the six-flux scattering coefficient for scattering by about  $90^\circ$  (scattering perpendicular to the direction of travel). By rearranging Eqn. C.5 into the form  $\gamma_c = \frac{F\gamma_b}{2}$ , and inserting it into Eqn. C.2:

$$\gamma'_b = \gamma_b + \frac{4(\frac{F\gamma_b}{2})^2}{\gamma_a + 2(\frac{F\gamma_b}{2})} = \gamma_b + \frac{F^2\gamma_b^2}{\gamma_a + F\gamma_b} \quad (\text{C.6})$$

$$\Rightarrow (\gamma'_b - \gamma_b) = \frac{F^2\gamma_b^2}{\gamma_a + F\gamma_b} \Rightarrow \gamma_a + F\gamma_b = \frac{F^2\gamma_b^2}{(\gamma'_b - \gamma_b)} \Rightarrow \gamma_a = F\gamma_b \left( \frac{F\gamma_b}{(\gamma'_b - \gamma_b)} - 1 \right) \quad (\text{C.7})$$

The result of Eqn. C.7 can be inserted into Eqn. C.1 to get:

$$\gamma'_a = \left( \frac{F^2\gamma_b^2}{(\gamma'_b - \gamma_b)} - F\gamma_b \right) \left( 1 + \frac{4\gamma_c}{\left( \frac{F^2\gamma_b^2}{(\gamma'_b - \gamma_b)} - F\gamma_b \right) + 2\gamma_c} \right) \quad (\text{C.8})$$

Eqn. C.5 can be inserted into Eqn. C.8, in the form  $\gamma_c = \frac{F\gamma_b}{2}$ , to remove  $\gamma_a$  from the expression:

$$\gamma'_a = \left( \frac{F^2\gamma_b^2}{(\gamma'_b - \gamma_b)} - F\gamma_b \right) \left( 1 + \frac{4\left(\frac{F\gamma_b}{2}\right)}{\left( \frac{F^2\gamma_b^2}{(\gamma'_b - \gamma_b)} - F\gamma_b \right) + 2\left(\frac{F\gamma_b}{2}\right)} \right) \quad (\text{C.9})$$

$$\Rightarrow \gamma'_a = \left( \frac{F^2\gamma_b^2}{(\gamma'_b - \gamma_b)} - F\gamma_b \right) \left( 1 + \frac{2F\gamma_b}{\left( \frac{F^2\gamma_b^2}{(\gamma'_b - \gamma_b)} \right)} \right) \quad (\text{C.10})$$

$$\Rightarrow \gamma'_a = \frac{F^2\gamma_b^2}{(\gamma'_b - \gamma_b)} + 2F\gamma_b - F\gamma_b - 2(\gamma'_b - \gamma_b) \quad (\text{C.11})$$

$$\Rightarrow 0 = F^2\gamma_b^2 + 2F\gamma_b(\gamma'_b - \gamma_b) - F\gamma_b(\gamma'_b - \gamma_b) - 2(\gamma'_b - \gamma_b)(\gamma'_b - \gamma_b) - \gamma'_a(\gamma'_b - \gamma_b) \quad (\text{C.12})$$

$$\Rightarrow -F^2\gamma_b^2 - 2F\gamma_b\gamma'_b + 2F\gamma_b^2 + F\gamma_b\gamma'_b - F\gamma_b^2 + 2\gamma'^2_b - 4F\gamma_b\gamma'_b + 2\gamma_b^2 + \gamma'_a\gamma'_b - \gamma'_a\gamma_b = 0 \quad (\text{C.13})$$

A quadratic equation for  $\gamma_b$  can be found, and some manipulation of Eqn. C.13. The quadratic equation is in the form:

$$a\gamma_b^2 + b\gamma_b + c = 0 \quad (\text{C.14})$$

where

$$a = 2 + F - F^2; b = -(\gamma'_a + 4\gamma'_b + F\gamma'_b); c = \gamma'_b(\gamma'_a + 2\gamma'_b) \quad (\text{C.15})$$

Eqn. C.14 can be solved for  $\gamma_b$ , via the quadratic equation:

$$\gamma_b = \frac{-b + \sqrt{b^2 + 4ac}}{2a} \quad (\text{C.16})$$

Then, by substituting this solution into Eqn. C.7, a solution for  $\gamma_a$  can be found. A solution for  $\gamma_c$  can be found by inserting the solution of  $\gamma_b$  into Eqn. C.5. Finally, a solution for  $\gamma_s$  can be found via Eqn. 5.34.

## Appendix D:

# SoRaX Radiometric Data

**Table D.1:** Description of column headers in Table D.2.

Header Abreviation	Description
Ele	SodRad Elevation Angle [°]
Azi	SodRad Azimuth Angle [°]
Pit	Snowpit location [m]
Inc	n-HUT model Incidence Angle [°]
Pol	Polarization
18.7so	Observed $T_B$ at 18.7 GHz [K]
21.0so	Observed $T_B$ at 21.0 GHz [K]
36.5so	Observed $T_B$ at 36.5 GHz [K]
18.7ad	Simulated $T_B$ at 18.7 GHz with the adapted n-HUT model [K]
21.0ad	Simulated $T_B$ at 21.0 GHz with the adapted n-HUT model [K]
36.5ad	Simulated $T_B$ at 36.5 GHz with the adapted n-HUT model [K]
18.7or	Simulated $T_B$ at 18.7 GHz with the original n-HUT model [K]
21.0or	Simulated $T_B$ at 21.0 GHz with the original n-HUT model [K]
36.5or	Simulated $T_B$ at 36.5 GHz with the original n-HUT model [K]

---

Table D.2: SoRaX  $T_B$  Radiometric Data. (See Table D.1 for description of column headings).

Ele	Azi	Pit	Inc	Pol	18.7so	21.0so	36.5so	18.7or	21.0or	36.5or	18.7ad	21.0ad	36.5ad
-40	190	0	50	H	196.7	241.1	214.5	201.7	239.4	203.4	183.4	223.3	126.0
-40	190	0	50	V	238.4	249.0	221.6	235.7	247.1	210.0	203.6	229.7	129.5
-40	186	1	50	H	198.7	240.9	213.6	201.7	239.5	202.5	185.3	225.6	124.7
-40	186	1	50	V	239.2	248.6	220.4	236.1	247.0	208.9	205.0	231.7	128.0
-40	178	3	50	H	203.9	239.4	208.7	199.2	238.3	197.0	182.6	226.7	115.7
-40	178	3	50	V	241.0	246.4	214.8	233.6	245.1	202.6	203.5	232.0	118.2
-40	174	4	50	H	202.0	240.9	212.5	199.9	240.0	201.8	181.4	230.2	125.8
-40	174	4	50	V	240.5	249.2	219.9	234.1	248.1	208.7	202.4	236.9	129.2
-40	170	5	50	H	198.2	244.0	213.9	201.3	242.9	202.5	182.8	231.6	123.1
-40	170	5	50	V	238.8	251.3	220.3	235.1	250.0	208.4	203.4	237.4	126.1
-50	188	1	40	H	216.5	248.2	209.7	210.5	246.9	195.7	190.4	234.0	104.5
-50	188	1	40	V	238.7	251.0	212.1	234.4	249.6	197.9	205.4	236.0	105.4
-50	182	2	40	H	219.2	250.0	212.6	208.2	248.2	198.4	190.3	232.1	105.9
-50	182	2	40	V	240.7	252.5	214.8	233.1	250.7	200.4	205.7	233.9	106.7
-50	178	3	40	H	218.7	249.7	209.1	206.9	248.0	194.2	191.0	232.4	100.4
-50	178	3	40	V	241.0	252.3	211.3	231.6	250.5	196.2	206.3	234.3	101.2
-50	172	4	40	H	216.6	250.3	212.7	206.5	249.3	199.4	191.7	238.8	109.6
-50	172	4	40	V	239.8	253.3	215.3	229.9	252.2	201.6	205.7	240.9	110.5

# References

- J. Amlien. Remote Sensing of Snow with Passive Microwave Radiometers - A review of current algorithms. In *Report No. 1019*, page 52. Norsk Regnesentral, Oslo, 2008. ISBN 978-82-539-0529-7.
- R. Anty and R. Cole. Dielectric Properties of Ice and Solid D<sub>2</sub>O. *Journal of Chemical Physics*, 20(8):1309–1314, 1952. doi: 10.1063/1.1700726.
- T. Aoki, H. Motoyoshi, Y. Kodama, T. Yasunari, and K. Sugiura. Variations of the snow physical parameters and their effects on albedo in Sapporo , Japan. *Annals of Glaciology*, pages 375–381, 2007.
- R. Armstrong and M. Brodzik. Recent northern hemisphere snow extent: A comparison of data derived from visible and microwave satellite sensors. *Geophysical Research Letters*, 28(19):3673–3676, oct 2001. doi: 10.1029/2000GL012556.
- R. Armstrong, A. Rango, and E. Josberger. Snow depths and grain-size relationships with relevance for passive microwave studies. *Annals of Glaciology*, 17:171–176, 1993. doi: 10.1017/S0260305500012799.
- A. Arslan. *Microwave Models of Snow Characteristics for Remote Sensing*. PhD thesis, Helsinki University of Technology, 2006.
- J. Barnes, C. Bowley, M. Smallwood, and J. Willand. The application of Heat Capacity Mapping Mission (HCMM) thermal data to snow hydrology. [Salt Verde Watershed and the southern Sierra Nevada. Technical report, NASA, Concord, Mass., mar 1981.
- T. Barnett, J. Adam, and D. Lettenmaier. Potential impacts of a warming climate on water availability in snow-dominated regions. *Nature*, 438(7066):303–9, nov 2005. doi: 10.1038/nature04141.
- R. Barry. The parameterization of surface albedo for sea ice and its snow cover. *Progress in Physical Geography*, 20(1):63–79, 1996. doi: 10.1177/030913339602000104.
- A. Benson and R. Williams. Cost of early snowmelt in terms of reduced irrigation deliveries. *Journal of Natural Resources Policy Research*, 5(2-3):79–89, apr 2013.
- P. Bernier. Microwave Remote Sensing of Snowpack Properites: Potential and Limitations. *Nordic Hydrology*, 18:1 – 20, 1987.
- O. Beser. *Determination of snow water equivalent over the eastern part of Turkey using passive microwave data*. Doctoral dissertation, Middle East Technical University, 2011.
- H. Blanford. On the Connexion of the Himalaya Snowfall with Dry Winds and Seasons of Drought in India. *Proceedings of the Royal Society of London*, 37:3–22, 1884. doi: 10.1098/rspl.1884.0003.
- R. Brown, B. Brasnett, and D. Robinson. Gridded North American monthly snow depth and snow water equivalent for GCM evaluation. *Atmosphere-Ocean*, 41(1):1–14, mar 2003. doi: 10.3137/ao.410101.

- E. Burakowski and M. Magnusson. Climate Impacts on the Winter Tourism Economy in the United States. Technical report, Natural Resources Defense Council, New Hampshire, 2012.
- T. Carroll, D. Cline, E. Berkowitz, and D. Savage. Snow economics and the NOHRSC Snow Information System (SNOW-INFO) for the United States. In *EGS - AGU - EUG Joint Assembly*, 2003.
- A. Chang. Nimbus-7 SMMR Snow Cover Data. *Glaciological Data*, GD-18:181–187, 1986.
- A. Chang, P. Gloersen, T. Schmugge, T. Wilheit, and H. Zwally. Microwave emission from snow and glacier ice. *Journal of Glaciology*, 16(74):23 –39, 1976. doi: 10.1017/S0022143000031415.
- A. Chang, J. Foster, and D. Hall. Nimbus-7 SMMR derived global snow cover parameters. *Annals of Glaciology*, 9:39 – 44, 1987. doi: 10.1017/S0260305500000355.
- A. Chang, J. Foster, D. Hall, B. Goodison, A. Walker, J. Metcalfe, and A. Harby. Snow parameters derived from microwave measurements during the BOREAS winter field campaign. *Journal of Geophysical Research*, 102(D24):29663–29671, dec 1997. doi: 10.1029/96JD03327.
- A. Chang, R. Kelly, E. Josberger, R. Armstrong, J. Foster, and N. Mognard. Analysis of Ground-Measured and Passive-Microwave-Derived Snow Depth Variations in Midwinter across the Northern Great Plains. *Journal of Hydrometeorology*, 6:20–33, 2005. doi: 10.1175/JHM-405.1.
- E. Chang and Y. Guo. Is the number of North Atlantic tropical cyclones significantly underestimated prior to the availability of satellite observations? *Geophysical Research Letters*, 34(14):L14801, 2007. doi: 10.1029/2007GL030169.
- S. Colbeck. Theory of metamorphism of dry snow. *Journal of Geophysical Research: Oceans*, 88(C9):5475–5482, jun 1983. doi: 10.1029/JC088iC09p05475.
- S. Colbeck. The Layered Character of Snow Covers. *Reviews of Geophysics*, 29(1):81–96, 1991. doi: 10.1029/90RG02351.
- M. Collins, R. Knutti, JM Arblaster, J.-L. Dufresne, T. Fichefet, P. Friedlingstein, X. Gao, W. Gutowski, T. Johns, G. Krinner, M. Shongwe, C. Tebaldi, A. Weaver, and M. Wehner. Long-term climate change: projections, commitments and irreversibility. In *Climate Change 2013: The Physical Science Basis. Contribution of Working Group I to the Fifth Assessment Report of the Intergovernmental Panel on Climate Change.*, chapter 12, pages 1029–1136. Cambridge University Press, Cambridge, 2013.
- K. Cuffey and W. Patterson. *The Physics of Glaciers*. Butterworth Heinemann, Oxford, 4th edition, 2010. ISBN 9780080919126.
- I. Davenport, M. Sandells, and R. Gurney. The effects of variation in snow properties on passive microwave snow mass estimation. *Remote Sensing of Environment*, 118(1): 168–175, mar 2012. doi: 10.1016/j.rse.2011.11.014.
- N. Doesken and A. Judson. *The Snow Booklet, A Guid to the Science, Climatology, and Measurement of Snow in the United States*. Colorado State University, 2nd edition, 1997. ISBN 978-0965105620.
- J. Dozier, S. Schneider, and D. McGinnis Jr. Effect of Grain Size and Snowpack Water Equivalence on Visable and Near-Infrared Satellite Observations of Snow. *Water Resources Research*, 17(4):1213–1221, 1981.

- C. Fierz, R. Armstrong, Y. Durand, P. Etchevers, E. Greene, D. McClung, K. Nishimura, P. Satyawali, and S. Sokratov. The International Classification for Seasonal Snow on the Ground. In *IHP-VII Technical Documents in Hydrology*, pages 1 – 80, 2009.
- J. Foster, D. Hall, A. Chang, and A. Rango. An overview of passive microwave snow research and results. *Reviews of Geophysics*, 22(2):195, 1984. doi: 10.1029/RG022i002p00195.
- J. Foster, D. Hall, and A. Chang. Remote sensing of snow. *Eos, Transactions American Geophysical Union*, 68(32):682, 1987. doi: 10.1029/EO068i032p00682-01.
- J. Foster, A. Chang, D. Hall, and A. Rango. Derivation of Snow Water Equivalent in Boreal Forests Using Microwave Radiometry. *Arctic*, 44(5):147–152, jan 1991. ISSN 1923-1245.
- J. Foster, C. Sun, J. Walker, R. Kelly, A. Chang, J. Dong, and H. Powell. Quantifying the uncertainty in passive microwave snow water equivalent observations. *Remote Sensing of Environment*, 94(2):187–203, 2005. doi: 10.1016/j.rse.2004.09.012.
- A. Frei and D. Robinson. Northern Hemisphere snow extent: Regional variability 1972–1994. *International Journal of Climatology*, 19(14):1535–1560, 1999. doi: 10.1002/(SICI)1097-0088(19991130)19:14<1535::AID-JOC438>3.0.CO;2-J.
- A. Frei, M. Tedesco, S. Lee, J. Foster, D. Hall, R. Kelly, and D. Robinson. A review of global satellite-derived snow products. *Advances in Space Research*, 50(8):1007–1029, 2012. doi: 10.1016/j.asr.2011.12.021.
- J. Gallet, F. Dominé, C. Zender, and G. Picard. Measurement of the specific surface area of snow using infrared reflectance in an integrating sphere at 1310 and 1550 nm. *The Cryosphere*, 3(2009):167–182, 2009. doi: 10.5194/tc-3-167-2009.
- N. Grody. Relationship between snow parameters and microwave satellite measurements: Theory compared with Advanced Microwave Sounding Unit observations from 23 to 150 GHz. *Journal of Geophysical Research*, 113(D22):D22108, nov 2008. doi: 10.1029/2007JD009685.
- M. Hallikainen and P. Jolma. Retrieval of the Water Equivalent of Snow Cover in Finland by Satellite Microwave Radiometry. *IEEE Transactions on Geoscience and Remote Sensing*, GE-24(6):855–862, nov 1986. doi: 10.1109/TGRS.1986.289700.
- M. Hallikainen, F. Ulaby, and M. Abdelrazik. Dielectric Properties of Snow in the 3 to 37 GHz range. *IEEE Transactions on Antennas and Propagation*, AP-34(11):1329 – 1340, 1986. doi: 10.1109/TAP.1986.1143757.
- M. Hallikainen, F. Ulaby, and T. Van Deventer. Extinction Behavior of Dry Snow in the 18- to 90- GHz Range. *IEEE Transactions on Geoscience and Remote Sensing*, GE-25 (6):737–745, 1987. doi: 10.1109/TGRS.1987.289743.
- M. Heggli, E. Frei, and M. Schneebeli. Snow replica method for three-dimensional X-ray microtomographic imaging. *Journal of Glaciology*, 55(192):631–639, 2009. doi: 10.3189/002214309789470932.
- J. Hollinger, J. Peirce, and G. Poe. SSM/I Instrument Evaluation. *IEEE Transactions on Geoscience and Remote Sensing*, 28(5):781 – 790, 1990. doi: 10.1109/36.58964.
- G. Hufford. A Model for the Complex Permittivity of Ice at Frequencies below 1 THz. *International Journal of Infrared and Millimeter Waves*, 12(7):677–682, 1991. doi: 10.1007/BF01008898.

- A. Ishimaru. *Wave Propagation and Scattering in Random Media, Volume 1: Single Scattering and Transport Theory*. Academic Press, New York, 1 edition, 1978. ISBN 978-0-12-374701-3.
- B. Jimenez Cisneros, T. Oki, N. Arnell, G. Benito, J. Cogley, P. Doll, T. Jiang, and S. Mwakalila. Freshwater resources. In *Climate Change 2014: Impacts, Adaptation, and Vulnerability. Part A: Global Sectoral Aspects. Contribution of Working Group II to the Fifth Assessment Report of the Intergovernmental Panel of Climate Change*, chapter 3, pages 229–269. Cambridge University Press, Cambridge, cambridge edition, 2014.
- A. Judson and N. Doesken. Density of Freshly Fallen Snow in the Central Rocky Mountains. *Bulletin of the American Meteorological Society*, 81(7):1577–1587, 2000. doi: 10.1175/1520-0477(2000)081<1577:DOFFSI>2.3.CO;2.
- R. Kelly, A. Chang, L. Tsang, and J. Foster. A Prototype AMSR-E Global Snow Area and Snow Depth Algorithm. *IEEE Transactions on Geoscience and Remote Sensing*, 41(2):230 – 242, 2003. doi: 10.1109/TGRS.2003.809118.
- T. Koike and T. Suhama. Passive-microwave remote sensing of snow. *Annals of Glaciology*, 18:305–308, 1993. doi: 10.1017/S0260305500011691.
- M Konig, J. Winther, and E. Isaksson. Measuring Snow and Ice Properties from Satellite. *Reviews of Geophysics*, 39(1):1–27, 2001.
- A. Kontu and J. Pulliaisen. Simulation of Spaceborne Microwave Radiometer Measurements of Snow Cover Using In Situ Data and Brightness Temperature Modeling. *IEEE Transactions on Geoscience and Remote Sensing*, 48(3):1031–1044, mar 2010. doi: 10.1109/TGRS.2009.2030499.
- A. Kulkarni, S. Randhawa, B. Rathore, I Bahuguna, and R. Sood. Snow and glacier melt runoff model to estimate hydropower potential. *Journal of the Indian Society of Remote Sensing*, 30(4):221–228, dec 2002. doi: 10.1007/BF03000365.
- K. Kunzi, S. Patil, and H. Rott. Snow-Cover Parameters Retrieved from Nimbus-7 Scanning Multichannel Microwave Radiometer (SMMR) Data. *IEEE Transactions on Geoscience and Remote Sensing*, 20(4):452 – 467, 1982. doi: 10.1109/TGRS.1982.350411.
- J. Lamb. Measurements of the Dielectric Properties of Ice. *Trans. Faraday Soc.*, 42A: 238–244, 1946. doi: 10.1109/IGARSS.1993.322667.
- D. Leathers and D. Robinson. The association between extremes in North American snow cover extent and United States temperatures. *Journal of Climate*, 6(7):1345–1355, 1993. doi: 10.1175/1520-0442(1993)006<1345:TABEIN>2.0.CO;2.
- L. Legagneux, A. Cabanes, and F. Dominé. Measurement of the specific surface area of 176 snow samples using methane adsorption at 77 K. *Journal of Geophysical Research*, 107(D17):4335, 2002. doi: 10.1029/2001JD001016.
- S. Leinss, H. Löwe, M. Proksch, J. Lemmetyinen, A. Wiesmann, and I. Hajnsek. Anisotropy of seasonal snow measured by polarimetric phase differences in radar time series. *The Cryosphere*, 10:1771–1797, 2016. doi: 10.5194/tc-10-1771-2016.
- J. Lemmetyinen, J. Pulliaisen, A. Rees, A. Kontu, Y. Qiu, and C. Derksen. Multiple-layer adaptation of HUT snow emission model: Comparison with experimental data. *IEEE Transactions on Geoscience and Remote Sensing*, 48(7):2781–2794, 2010. doi: 10.1109/TGRS.2010.2041357.

- L. Leppänen, A. Kontu, J. Lemmetyinen, K. Rautiainen, and J. Pulliaisen. Sodankylä Radiometer Experiment SoRaX, 2016a.
- Leena Leppänen, Anna Kontu, Henna-Reetta Hannula, Heidi Sjöblom, and Jouni Pulliainen. Sodankylä manual snow survey program. *Geoscientific Instrumentation, Methods and Data Systems*, 5(1):163–179, may 2016b. ISSN 2193-0864. doi: 10.5194/gi-5-163-2016.
- H. Löwe and A. van Herwijnen. A Poisson shot noise model for micro-penetration of snow. *Cold Regions Science and Technology*, 70:62–70, jan 2012. doi: 10.1016/j.coldregions.2011.09.001.
- H. Löwe, F. Riche, and M. Schneebeli. A general treatment of snow microstructure exemplified by an improved relation for thermal conductivity. *Cryosphere*, 7(5):1473–1480, 2013. doi: 10.5194/tc-7-1473-2013.
- A. Mary, M. Dumont, J. Dedieu, Y. Durand, P. Sirguey, H. Milhem, O. Mestre, H. Negi, A. Kokhanovsky, M. Lafaysse, and S. Morin. Intercomparison of retrieval algorithms for the specific surface area of snow from near-infrared satellite data in mountainous terrain , and comparison with the output of a semi-distributed snowpack model. *The Cryosphere*, 7:741–761, 2013. doi: 10.5194/tc-7-741-2013.
- W. Maslanka, L. Leppänen, A. Kontu, M. Sandells, J. Lemmetyinen, M. Schneebeli, M. Proksch, M. Matzl, H-R. Hannula, and R. Gurney. Arctic Snow Microstructure Experiment for the development of snow emission modelling. *Geoscientific Instrumentation, Methods and Data Systems*, 5:85–94, 2016. doi: 10.5194/gi-5-85-2016.
- M. Matzl and M. Schneebeli. Measuring specific surface area of snow by near-infrared photography. 52, 52(176):558–564, 2006. doi: 10.3189/172756506781828412.
- C. Mätzler. Applications of the Interaction of Microwaves with the Natural Snow Cover. *Remote Sensing Reviews*, 2(2):259–387, 1987. doi: 10.1080/02757258709532086.
- C. Mätzler. Passive Microwave Signatures of Landscapes in Winter. *Meteorology and Atmospheric Physics*, 54:241–260, 1994. doi: 10.1007/BF01030063.
- C. Mätzler. Microwave permittivity of dry snow. *IEEE Transactions on Geoscience and Remote Sensing*, 34(2):573–581, mar 1996. doi: 10.1109/36.485133.
- C. Mätzler. Autocorrelation functions of granular media with free arrangement of spheres, spherical shells, or ellipsoids. *Journal of Applied Physics*, 81(3):1509–1517, 1997. doi: 10.1063/1.363916.
- C. Mätzler. Microwave Properties of Ice and Snow. In B. Schmitt, C. De Bergh, and M. Festou, editors, *Solar System Ices: Based on Reviews Presented at the International Symposium Solar System Ices held in Toulouse, France, on March 2730, 1995*, volume 227, chapter Physics an, pages 241–257. Springer Netherlands, Dordrecht, 1 edition, 1998. ISBN 978-94-010-6209-1.
- C. Mätzler. Relation between grain-size and correlation length of snow. *Journal of Glaciology*, 48(162):461 – 466, 2002. doi: 10.3189/172756502781831287.
- C. Mätzler. *Thermal Microwave Radiation : Applications for Remote Sensing*. The Institution of Engineering and Technology, 2006. ISBN 978-0-36341-573-9.
- C. Mätzler and U. Wegmüller. Dielectric properties of fresh-water ice at microwave frequencies. *Journal of Physics D: Applied Physics*, 20:1623–1630, 1987. doi: 10.1088/0022-3727/20/12/013.

- C. Merchant and P. Le Borgne. Retrieval of Sea Surface Temperature from Space, Based on Modeling of Infrared Radiative Transfer: Capabilities and Limitations. *Journal of Atmospheric and Oceanic Technology*, 21(11):1734–1746, 2004. doi: 10.1175/JTECH1667.1.
- O. Mishima, DD. Klug, and E. Wahlley. The far-infrared spectrum of ice Ih in the range 8–25cm-1. Sound waves and difference bands, with application to Saturn’s rings. *Journal of Chemical Physics*, 78:6399–6404, 1983. doi: 10.1063/1.444700.
- B. Montpetit, A. Royer, A. Langlois, M. Chum, P. Cliche, A. Roy, N. Champollion, G. Picard, F. Dominé, and R. Obbard. In-situ Measurements for Snow Grain Size and Shape Characterization Using Optical Methods. In *68th Eastern Snow Conference*, pages 173–188, 2011.
- B. Montpetit, A. Royer, A. Langlois, P. Cliche, A. Roy, N. Champollion, G. Picard, F. Domine, and R. Obbard. Instruments and Methods New shortwave infrared albedo measurements for snow specific surface area retrieval. *Journal of Glaciology*, 58(211): 941 – 952, 2012. doi: 10.3189/2012JoG11J248.
- B. Montpetit, A. Royer, A. Roy, A. Langlois, and C. Derksen. Snow Microwave Emission Modeling of Ice Lenses Within a Snowpack Using the Microwave Emission Model for Layered Snowpacks. *IEEE Transactions on Geoscience and Remote Sensing*, 51(9): 4705–4717, sep 2013. doi: 10.1109/TGRS.2013.2250509.
- J. Muñoz, J. Infante, T. Lakhankar, R. Khanbilvardi, P. Romanov, N. Krakauer, and A. Powell. Synergistic Use of Remote Sensing for Snow Cover and Snow Water Equivalent Estimation. *British Journal of Environment & Climate Change*, 3(34):612–627, 2013. doi: 10.9734/BJECC/2013/7699.
- Y. Orsolini and N. Kvamstø. Impact of Eurasian snow cover on the northern hemisphere winter circulation. In *ECMWF / GLASS Workshop on Land Surface Modelling*, pages 177–184, 2009.
- D Polder and J. Van Santen. The effective permeability of mixtures of solids. *Physica*, 12(5):257–271, 1946. doi: 10.1016/S0031-8914(46)80066-1.
- M. Proksch, H. Löwe, and M. Schneebeli. Density, specific surface area and correlation length of snow measured by high-resolution penetrometry. *J. Geophys. Res.-Earth Surface*, 120(2):346–362, 2015. doi: 10.1002/2014JF003266.
- M. Proksch, N. Rutter, C. Fierz, and M. Schneebeli. Intercomparison of snow density measurements: bias, precision, and vertical resolution. *The Cryosphere*, 10:371–384, 2016. doi: 10.5194/tc-10-371-2016/.
- J. Pulliainen. Mapping of snow water equivalent and snow depth in boreal and sub-arctic zones by assimilating space-borne microwave radiometer data and ground-based observations. *Remote Sensing of Environment*, 101(2):257–269, mar 2006. doi: 10.1016/j.rse.2006.01.002.
- J. Pulliainen and M. Hallikainen. Retrieval of Regional Snow Water Equivalent from Space-Borne Passive Microwave Observations. *Remote Sensing of Environment*, 75: 76–85, 1997.
- J. Pulliainen, J. Grandell, and M. Hallikainen. HUT snow emission model and its applicability to snow water equivalent retrieval. *IEEE Transactions on Geoscience and Remote Sensing*, 37(3):1378–1390, 1999. doi: 10.1109/36.763302.

---

## References

---

- X. Qu and A. Hall. On the persistent spread in snow-albedo feedback. *Climate Dynamics*, 42(1-2):69–81, 2014. doi: 10.1007/s00382-013-1774-0.
- A. Rango, A. Chang, and J. Foster. The Utilization of Spaceborne Microwave Radiometers for Monitoring Snowpack Properties. *Hydrology Research*, 10(1):25–40, 1979.
- A Rees. *Physical principles of remote sensing*. Cambridge University Press, Cambridge, 3rd edition, 2012. ISBN 9780521181167.
- A. Rees, C. Derksen, M. English, A. Walker, C. Duguay, A. Rees, and W. Laurier. Uncertainty in snow mass retrievals from satellite passive microwave data in lake-rich high-latitude environments. *Hydrological Processes*, 20:1019–1022, 2006. doi: 10.1002/hyp.6076.
- A. Rees, J. Lemmetyinen, C. Derksen, J. Pullainen, and M. English. Observed and modelled effects of ice lens formation on passive microwave brightness temperatures over snow covered tundra. *Remote Sensing of Environment*, 114(1):116–126, 2010. doi: 10.1016/j.rse.2009.08.013.
- A. Rees, M. English, C. Derksen, P. Toose, and A. Silis. Observations of late winter Canadian tundra snow cover properties. *Hydrological Processes*, 28(12):3962–3977, jun 2014. doi: 10.1002/hyp.9931.
- W. Rees. *Remote Sensing of Snow and Ice*. Taylor & Francis, Cambridge, 2006. ISBN 978-0-415-29831-5.
- D. Robinson, A. David, T. Estilow, and NOAA CDR Program. NOAA Climate Data Record (CDR) of Northern Hemisphere (NH) Snow Cover Extent (SCE), Version 1., 2012.
- Th. Rose and H. Czekala. RPG-XCH-DP X Frequency, Dual Polarization Radioemters Operating Manual, 2011.
- H. Rott. Prospects of Microwave Remote Sensing for Snow Hydrology. In *Hydrologic Applications of Space Technology (Proceedings of the Cocoa Beach Workshop, Florida)*, volume 160, pages 215–224, 1986.
- H. Rott, K. Sturm, and H. Miller. Active and passive microwve signatures of Antarctic firn by means of field measurements and satellite data. *Annals of Glaciology*, 17(7): 337–343, 1993. doi: 10.3198/1993AoG17-1-337-343.
- V. Roy, K. Goita, A. Royer, A. Walker, and B. Goodison. Snow water equivalent retrieval in a Canadian boreal environment from microwave measurements using the HUT snow emission model. *IEEE Transactions on Geoscience and Remote Sensing*, 42(9):1850–1859, sep 2004. doi: 10.1109/TGRS.2004.832245.
- E. Schanda. *Physical Fundamentals of Remote Sensing*. Springer-Verlag, Berlin, 1 edition, 1986. ISBN 978-3-642-48733-0.
- E. Schanda and C. Mätzler. Optimum characteristics for snow pack evaluation by microwave radiometry. *Advances in Space Research*, 1(10):151–162, 1981. doi: 10.1016/0273-1177(81)90390-2.
- M. Schneebeli and J. Johnson. A constant-speed penetrometer for high-resolution snow stratigraphy. *Annals of Glaciology*, 26(5):107–111, 1998. doi: 10.3198/1998AoG26-1-107-111.

- M. Schneebeli and S. Sokratov. Tomography of temperature gradient metamorphism of snow and associated changes in heat conductivity. *Hydrological Processes*, 18(18): 3655–3665, 2004. doi: 10.1002/hyp.5800.
- M. Schneebeli, C. Pielmeier, and J. Johnson. Measuring Snow Microstructure and Hardness using a High Resolution Penetrometer. *Cold Regions Science and Technology*, 30 (1):305–311, 1999. doi: 10.1016/S0165-232X(99)00030-0.
- M. Schneebeli, V. Smith, D. Schmid, and S. Bourgeois. Casting Snow Samples with Phthalate. Technical report, WSL Institute for Snow and Avalanche SLF, 2008.
- M. Schwank, A. Wiesmann, C. Werner, C. Mätzler, D. Weber, A. Murk, I. Völksch, and U. Wegmüller. ELBARA II, an L-Band Radiometer System for Soil Moisture Research. *Sensors*, 10(1):584–612, jan 2010. doi: 10.3390/s100100584.
- G. Seidler, L. Atkins, E. Behne, U. Noomnarm, S. Koehler, R. Gustafson, and W. McKEAN. Applications of synchrotron X-Ray Microtomography to Mesoscale Materials. *Advances in Complex Systems*, 4(4):481–490, dec 2001. doi: 10.1142/S0219525901000371.
- E. Sharkov. *Passive Microwave Remote Sensing of the Earth*. Springer, Berlin, 1st edition, 2003. ISBN 978-3-540-43946-2.
- A. Sihvola. Mixing Rules with Complex Dielectric Coefficients. *Subsurface Sensing Technologies and Applications*, 1(4):393–415, 2000. doi: 10.1023/A:1026511515005.
- A. Sorman and O. Beser. Determination of snow water equivalent over the eastern part of Turkey using passive microwave data. *Hydrological Processes*, 27(14):1945–1958, jul 2013. ISSN 08856087. doi: 10.1002/hyp.9267.
- Ph. Stanzel, U. Haberl, and H. Nachtnebel. Modelling snow accumulation and snow melt in a continuous hydrological model for real-time flood forecasting. *IOP Conference Series: Earth and Environmental Science*, 4(1):012016, nov 2008. doi: 10.1088/1755-1307/4/1/012016.
- M. Sturm, J. Holmgren, and G. Liston. A Seasonal Snow Cover Classification System for Local to Global Applications. *Journal of Climate*, 8:1261 – 1283, 1995. doi: 10.1175/1520-0442(1995)008<1261:ASSCCS>2.0.CO;2.
- A. Tait. Estimation of Snow Water Equivalent Using Passive Microwave Radiation Data. *Remote Sensing of Environment*, 64(3):286 – 291, 1998. doi: 10.1016/S0034-4257(98)00005-4.
- M. Takala, J. Pulliaisen, S. Metsamaki, and J. Koskinen. Detection of snowmelt using spaceborne microwave radiometer data in Eurasia from 1979 to 2007. *IEEE Transactions on Geoscience and Remote Sensing*, 47(9):2996–3007, 2009. doi: 10.1109/TGRS.2009.2018442.
- M. Takala, K. Luojus, J. Pulliaisen, C. Derksen, J. Lemmetyinen, J-P. Kärnä, J. Koskinen, and B. Bojkov. Estimating northern hemisphere snow water equivalent for climate research through assimilation of space-borne radiometer data and ground-based measurements. *Remote Sensing of Environment*, 115(12):3517–3529, 2011. doi: 10.1016/j.rse.2011.08.014.
- K. Tape, N. Rutter, H. Marshall, R. Essery, and M. Sturm. Instruments and methods recording microscale variations in snowpack layering using near-infrared photography. *Journal of Glaciology*, 56(195):75–80, apr 2010. doi: 10.3189/002214310791190938.

- M. Tedesco and E. Kim. Intercomparison of Electromagnetic Models for Passive Microwave Remote Sensing of Snow. *IEEE Transactions on Geoscience and Remote Sensing*, 44(10):2654–2666, oct 2006. doi: 10.1109/TGRS.2006.873182.
- M Tedesco and A A Kokhanovsky. The semi-analytical snow retrieval algorithm and its application to MODIS data. *Remote Sensing of Environment*, 111:228–241, 2007. doi: 10.1016/j.rse.2007.02.036.
- A. Toure, K. Goïta, A. Royer, C. Mätzler, and M. Schneebeli. Near-infrared digital photography to estimate snow correlation length for microwave emission modeling. *Applied Optics*, 48(36):6723–6733, 2008. doi: 10.1364/AO.47.006723.
- L. Tsang. Dense media radiative transfer theory for dense discrete random media with spherical particles of multiple sizes and permittivities. In *Progress In Electromagnetics Research*, pages 181–230. Elsevier, New York, 1992.
- F. Ulaby, R. Moore, and A. Fung. *Microwave Remote Sensing, Active and Passive, Volume 1: Microwave Remote Sensing Fundamentals and Radiometry*. Artech House Publishers, 1986a. ISBN 978-0890061909.
- F. Ulaby, R. Moore, and A. Fung. *Microwave Remote Sensing, Active and Passive, Volume 3: From Theory to Applications*. Artech House Publishers, 1986b. ISBN 0890061920.
- A. Walker and B. Goodison. Discrimination of a wet snow cover using passive microwave satellite data. *Annals of Glaciology*, 17:307–311, 1993. doi: 10.1017/S026030550001301X.
- S. Warren. Optical Properties of Snow. *Reviews of Geophysics and Space Physics*, 20(1): 67 – 89, 1982. doi: 10.1029/RG020i001p00067.
- U. Wegmüller and C. Mätzler. Rough bare soil reflectivity model. *IEEE Transactions on Geoscience and Remote Sensing*, 37(3):1391–1395, may 1999. doi: 10.1109/36.763303.
- T. Weise. *Radiometric and Structural Measurements of Snow*. Phd. thesis, University of Bern, 1996.
- A. Wiesmann, C. Mätzler, and T. Weise. Radiometric and Structural Measurements of Snow Samples. *Radio Science*, 33(2):273 – 289, 1998. doi: 10.1029/97RS02746.
- N. Zuanon. IceCube, a portable and reliable instrument for snow specific surface area measurement in the field. In *International Snow Science Workshop Grenoble - Chamonix Mont-Blanc*, pages 1020–1023, 2013.